Carbon-Rich Silicon Oxycarbide (SiOC) and Silicon Oxycarbide/Element (SiOC/X, X= Si, Sn) Nano-Composites as New Anode Materials for Li-Ion Battery Application

Vom Fachbereich Material- und Geowissenschaften der Technischen Universität Darmstadt
Zur Erlangung des akademischen Grades Doktor-Ingenieur (Dr.-Ing.)
Genehmigte kumulative Dissertation von Dipl.-Ing. Jan H. Kaspar
Geboren am 5. Mai 1984 in Heppenheim
April 2014 – Darmstadt – D17

TECHNISCHE
UNIVERSITÄT
DARMSTADT

Disperse
Feststoffe

Carbon-Rich Silicon Oxycarbide (SiOC) and Silicon Oxycarbide/Element (SiOC/X, X= Si, Sn)
Nano-Composites as New Anode Materials for Li-Ion Battery Application

Genehmigte kumulative Dissertation von Jan H. Kaspar, geboren in Heppenheim.
1. Gutachten: Prof. Dr. Ralf Riedel
2. Gutachten: Prof. Dr. Gian Domenico Soraràù

Tag der Einreichung: 22.04.2014
Tag der Prüfung: 04.07.2014

Darmstadt - D 17

Gewidmet

Irmgard I. R. Kaspar

The presented cumulative dissertation summarizes the essential scientific findings, which were reported to the scientific community in the following peer-reviewed journals. The reports itself [1] – [7] are enclosed in the Chapter *Publications* of this work.

[1] J. Kaspar, M. Graczyk-Zajac and R. Riedel, Carbon-rich SiOC anodes for lithium-ion batteries: Part II. Role of thermal cross-linking, *Solid State Ionics*, 225 **(2012)** 527-531

[2] J. Kaspar, M. Graczyk-Zajac and R. Riedel, Lithium insertion into carbon-rich SiOC ceramics: Influence of pyrolysis temperature on electrochemical properties, *Journal of Power Sources*, 244 **(2013)** 450-455

[3] G. Liu, J. Kaspar, L.M. Reinold, M. Graczyk-Zajac and R. Riedel, Electrochemical performance of DVB-modified SiOC and SiCN polymer-derived negative electrodes for lithium-ion batteries, *Electrochimica Acta*, 106 **(2013)** 101-108

[4] J. Kaspar, M. Graczyk-Zajac and R. Riedel, Determination of the Li-ion diffusion coefficient in carbon-rich SiOC by the electrochemical methods PITT, GITT and EIS, *Electrochimica Acta*, 155 **(2014)** 665-670

[5] E. Ionescu, C. Terzioglu, C. Linck, J. Kaspar, A. Navrotsky and R. Riedel, Thermodynamic control of phase composition and crystallization of metal-modified silicon oxycarbides, *Journal of the American Ceramic Society*, 96 **(2013)** 1899-1903

[6] J. Kaspar, M. Graczyk-Zajac, S. Lauterbach, H.-J. Kleebe and R. Riedel, Silicon oxycarbide/nano-silicon composite anodes for Li-ion batteries: Considerable influence of nano-crystalline vs. nano-amorphous silicon embedment on the electrochemical properties, *Journal of Power Sources*, 269 **(2014)** 164-172

[7] J. Kaspar, C. Terzioglu, E. Ionescu, M. Graczyk-Zajac, S. Hapis, H.-J. Kleebe and R. Riedel, Stable SiOC/Sn Nanocomposite Anodes for Lithium-Ion Batteries with Outstanding Cycling Stability, *Advanced Functional Materials,* 24 **(2014)** 4097-4104

Table of contents

Table of contents 1

List of abbrevations 3

1. ..... Introduction and motivation 5

2. ..... Fundamentals 7

- 2.1. Lithium-ion battery 7
  - 2.1.1. Basic concepts 7
  - 2.1.2. Electrochemical principles 8
  - 2.1.3. Material aspects 10
  - 2.1.4. Tin and silicon anodes 11
- 2.2. Polymer-derived ceramics 12
  - 2.2.1. General background 12
  - 2.2.2. Silicon oxycarbide 13
  - 2.2.3. Silicon oxycarbide as anode material 14

3. ..... Cumulative part of the thesis 17

- 3.1. Microstructural, electrochemical and electroanalytical characterization of polymer-derived carbon-rich silicon oxycarbide ceramics as prospective anode materials for Li-ion batteries 18
  - 3.1.1. Results and discussion 18
  - 3.1.2. Statement of personal contribution 26
- 3.2. Silicon oxycarbide/nano-silicon composite anodes for Li-ion batteries: Considerable influence of nano-crystalline versus nano-amorphous silicon embedment on the electrochemical properties 28
  - 3.2.1. Results and discussion 28
  - 3.2.2. Statement of personal contribution 33
- 3.3. An innovative single-source precursor approach towards SiOC/Sn nano-composites with high Li-ion storage capacity and enhanced cycling stability 34
  - 3.3.1. Results and discussion 34
  - 3.3.2. Statement of personal contribution 40

4. ..... Summary 41

5. ..... Outlook 44

References 45

Publications 53

Lebenslauf und Bildungsgang

Danksagung

Eidesstattliche Erklärung

List of abbrevations

AK	Arbeitskreis/Working group
$a_{ox/red}$	Chemical activity of the oxidized/reduced species of a redox-couple
C_a	Anode specific capacity
C_c	Cathode specific capacity
CNT	Carbon nano-tube
C_{irr}	Irreversible capacity
C_{rev}	Reversible capacity
C_{th}	Theoretical capacity
C_{total}	Total capacity of a Li-ion battery full-cell
D_{Li}^{+}	Diffusion coefficient of Li-ions
DMC	Dimethyl carbonate
DVB	Divinylbenzene
ΔE	Electromotive force/difference in half-cell potential
ΔE^0	Difference in standard cell potential
E	Young's modulus
$E^0{}_{a/c}$	Standard electrode potential of the anode/cathode
$E_{a/c}$	Electrode potential of the anode/cathode
EC	Ethylene carbonate
EDS	Energy-dispersive X-ray spectroscopy
EIS	Electrochemical impedance spectroscopy
EV	Electrical vehicle
F	Faraday's constant (96485.3365 C mol^{-1})
FTIR	Fourier transformed infrared spectroscopy
ΔG	Change in Gibb's free energy
ΔG^0	Change in standard Gibb's free energy
GCPL	Galvanostatic cycling with potential limitation
GITT	Galvanostatic intermittent titration technique
η	Coulombic efficiency
HEV	Hybrid electrical vehicle
HTT1800	Commercially available polyorganosilazane, Clariant GmbH, Germany
HRTEM	High-resolution transmission electron microscopy
I(t)	Current as a function of time
$LiPF_6$	Lithium hexafluorophosphate
MAS-NMR	Magic angle spinning nuclear magnetic resonance (spectroscopy)
NMP	N-methyl-2-pyrrolidone
NMR	Nuclear magnetic resonance (spectroscopy)

nSi	Nano-silicon
nSi_a	Amorphous nano-silicon
nSi_c	Crystalline nano-silicon
n/a	Not available
p	Specific power
PCGA	Potentiodynamic cycling with galvanostatic acceleration
PDC	Polymer-derived ceramic
PITT	Potentiostatic intermittent titration technique
PMS MK	Commercially available polyorganosilsesquioxane, Wacker-Belsil, Germany
PVDF	Polyvinylidene fluoride
q	Specific charge capacity
Q	Charge capacity
Q_m	Mass specific capacity contribution of the inactive components of a Li-ion battery full-cell, in $mAhg^{-1}$
R	Gas constant (8.314 $J\ mol^{-1}\ K^{-1}$)
Ref.	Reference
RD-684a	Commercially available polyorganosiloxane, Starfire Systems Inc, USA
SAED	Selected area electron diffraction
SiCN	Silicon carbonitrtide
SiOC	Silicon oxycarbide
$SiOC_T$	Silicon oxycarbide pyrolyzed at T, in °C
$SiOC_{MK}$	Silicon oxycarbide derived from *PMS MK* polymer
$SiOC_{RD}$	Silicon oxycarbide derived from *RD-684a* polymer
$Sn(ac)_2$	Tin(II)acetate
t	Time
T	Temperature
TEM	Transmission electron microscopy
T_{pyr}	Temperature of pyrolysis
U^0	Standard cell voltage
ΔV	Change in volume
w	Specific energy density
wt-%	Weight percent
XRD	X-ray diffraction
z	Number of electrons

1. Introduction and motivation

The history of batteries dates back into the year 1800, when the Italian Professor A. Volta at the University of Pavia, discovered the world's first primary cell, the so-called "Voltaic-pile". It was composed of an alternating stacking of copper and zinc plates, divided by brine soaked cotton-cloths, functioning as electrolyte. A current was produced by connecting the two ends of the stack in an external circuit. The driving force for the current was the difference in the electrochemical potential of the zinc and copper plates. Zinc cations were released into the brine by oxidation of zinc and electrons supplied to the electric circuit. At the copper plates, protons were consumed from the electrolyte and reduced to hydrogen-gas by uptake of the transferred electrons. In consequence, the brine was steadily consumed during cell-reactions, causing the battery to dry-out quickly. After the discovery of this first primary cell, it took about 60 years, until the French physicist G. Planté invented the world's first secondary or rechargeable cell, namely the lead-acid battery. The major advantage of the lead-acid battery, as it is known nowadays, is its relatively high power-density with an electromotive force of about 2 V per cell unit. The high power density reasons its application in motorized vehicles as energy storage component and to supply the high surge currents that are needed to start the engine. However, its high nominal weight and accordingly low gravimetric energy density were and are hindering its area-wide and multifunctional application [8].

In 1991, the tremendous success of the lightweight Lithium-ion battery started by its commercial release through Sony Energytech [9, 10]. Within a few years, Li-ion cells experienced an inimitable break-through as rechargeable power source for all kind of portable electronics and are still the energy source of choice for today's smartphones, laptops and electrified devices, which require an off-grid power supply. Compared to other rechargeable batteries, Li-ion cells exhibit several prominent advantages, namely high energy density by weight and volume, high working voltage, long service life-time, marginal self-discharge and an enhanced temperature range of operation [11, 12]. Presently, Li-ion batteries rapidly conquer the market of electric and hybrid electric driven vehicles (EVs/HEVs), as well as larger scale stationary energy storage and smart-grid technology [13-15].

Back in the 1990's, a Li-ion cell consisted of a graphite anode in combination with a lithium cobalt oxide cathode and a liquid electrolyte, not very different from the present cell design. But thanks to the scientific and technological progress, the performance, safety and lifetime of today's Li-ion cells significantly improved due to optimization and tailoring of the graphite anode, as well as the introduction and implementation of mixed-oxide compounds as cathode materials. Likewise the fundamental study and research for novel functional materials for electrode and electrolyte application contributed to this progress [11, 12].

In order to satisfy the steadily growing energy needs and power demands of our energy-based society and to further promote the development of eco-friendly EVs and HEVs, the search and design of next generation anode and cathode materials, as well as prospective electrolytes, with superior properties to the state of the art compounds are an essential issue in the 21st century. Consequently, innovative material solutions are granted the key to success for the future role of Li-ion technology in the market of multifunctional and omnipresent power-supply and energy-storage devices [16-19]. For instance, the stored energy in a cell can be enhanced in three different ways, all addressing material solutions: *i)* generating a larger chemical potential difference between the employed electrodes, *ii)* decreasing the mass (or volume) of the electrode reactants per exchanged electron or *iii)* ensuring that the battery's electrolyte is not consumed in the cell reactions, implying the use of electrolytes other than organic solvent-based ones [12].

In this context the working objective of this thesis is settled, namely the investigation of polyorganosiloxane derived carbon-rich silicon oxycarbide ceramics (SiOC) and silicon oxycarbide/element (SiOC/X, X=Si, Sn) nano-composites as novel and prospective anode materials for Li-ion battery application. Therefore, SiOC-based materials are synthesized and characterized by means of various chemical, structural, electrochemical and electroanalytical methods. The chemical composition and microstructure of the compounds are carefully analyzed and correlated with the materials electrochemical properties and performance. For pure carbon-rich SiOC, the lithium ion storage process is investigated, including the transport and mobility of lithium ions within the material.

2. Fundamentals

In this Chapter the fundamentals and basic principles underlying the scientific findings in this thesis are introduced, with respect to the latest research developments.

2.1. Lithium-ion battery

2.1.1. Basic concepts

A battery is a device that stores and converts chemical energy into electrical energy and vice versa. A typical cell is built of two electrodes, connected by an external circuit and an ionically conducting but electronically insulating medium, called electrolyte. In the case of a Li-ion cell, electrode processes occur by the reversible insertion and extraction of Li-ions in and out of the electrode compounds by redox reaction. Per definition for cell-discharge, the negative electrode is denoted anode and the positive one cathode. A schematic representation of a Li-ion cell is shown is Figure 1. When a consumer load, i.e. a negative current, is applied to the charged cell, the anode (e.g. graphite/Li_xC_6) is oxidized upon the release of Li-ions into the electrolyte and electrons supplied to the external circuit. Both charge species transfer to the cathode (e.g. $Li_{1-x}CoO_2$/$LiCoO_2$), which is reduced upon the electron flow and uptake of Li-ions from the electrolyte. Equation 1 a) and 1 b) present the electrode reactions for discharge conditions, employing a graphite anode and $LiCoO_2$ cathode. The electrolyte in a Li-ion cell is typically comprised of a Li-containing salt, solved in a mixture of organic solvents (e.g. $LiPF_6$ in EC : DMC). To (re-)charge the cell, an external voltage of positive sign is applied to the electrodes, reversing the chemical reactions and hence the direction of the Li-ion and electron flow, c.f. Figure 1.

$$LiC_6 \xrightarrow{discharge} Li_{1-x}C_6 + xLi^+ + xe^- \qquad \text{Eq. 1 a)}$$

$$Li_{1-x}CoO_2 + xLi^+ + xe^- \xrightarrow{discharge} LiCoO_2 \qquad \text{Eq. 1 b)}$$

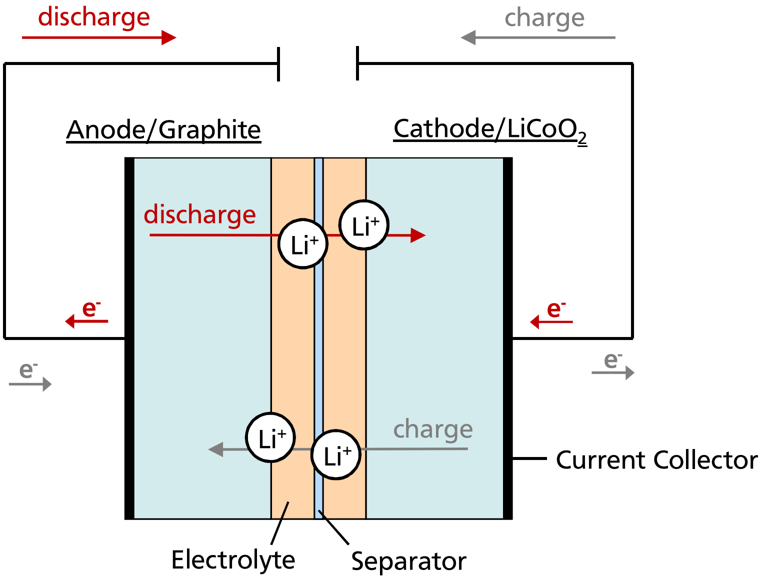

Figure 1 Schematic presentation of a Li-ion cell. The Li-ions shuttle between the electrodes through the electrolyte, while electrons transfer in the external circuit.

2.1.2. Electrochemical principles

The driving force for Li-ion shuttling between the anode and cathode is expressed by the change in Gibbs free energy per mole of reaction (ΔG), dictated by the chemistry that occurs at each electrode. According to Eq. 2, the change in Gibbs free energy directly relates to the electromotive force (ΔE) of the cell, which describes the difference in cell potential between both electrodes of the corresponding half-cell reactions (Eq. 3). In Eq. 2, F denotes Faraday's constant, z is the number of electrons transferred per mole of reaction and in Eq. 3, E_c and E_a present the half-cell potentials of the cathode and anode, respectively [8].

$$\Delta_R G = -zF\,\Delta E \qquad \text{Eq. 2}$$

$$\Delta E = E_c - E_a \qquad \text{Eq. 3}$$

When cell conditions are different than that of the standard state, the half-cell potential is described by the Nernst-Equation (Eq. 4), taking into account that the potential depends on the chemical activity of the reactants involved in the redox process (a_{ox}, a_{red}). Here R denotes the gas constant, T the temperature and E_c^0 and E_a^0 are the standard half-cell potentials of the cathode and anode, respectively.

$$E_{c,a} = E_{c,a}^0 - \frac{RT}{zF}\ln\left(\frac{a_{ox}}{a_{red}}\right) \qquad \text{Eq. 4}$$

In the case of a full cell, the Nernst-Equation turns into Eq. 5, for the schematic chemical reaction in Eq. 6. Here p, q, r, s denote the stoichiometric coefficients of the involved chemical species A, B, C, D and ΔE^0 quantifies the difference in standard cell potential of both half-cells.

$$\Delta E = \Delta E^0 - \frac{RT}{zF} \ln\left(\frac{a_C^r a_D^s}{a_A^p a_B^q}\right) \qquad \text{Eq. 5}$$

$$pA + qB \leftrightarrow rC + sD \qquad \text{Eq. 6}$$

When all reactants are at the equilibrium state, the difference in cell potential equals the difference in standard cell potential and Eq. 2 turns into Eq. 7.

$$\Delta_R G^0 = -zF \cdot \Delta E^0 \qquad \text{Eq. 7}$$

Accordingly, the corresponding cell voltage U^0 can be expressed for standard conditions by rearrangement of Eq. 7 into Eq. 8.

$$U^0 = \Delta E^0 = \frac{-\Delta_R G^0}{zF} \qquad \text{Eq. 8}$$

The charge capacity Q of an electrochemical cell is given by Eq. 9 and defined as the antiderivative of the current as function of time $I(t)$, i.e. the maximum charge obtainable from the cell. The unit of Q is amper-hour (Ah).

$$Q = \int_{t_1}^{t_2} I(t)dt \qquad \text{Eq. 9}$$

Another important parameter is the specific charge capacity q, which quantifies how much charge is stored per mass (m) of reactants, according to Eq. 10. The unit of q is amper-hour per kilogram ($Ah \cdot kg^{-1}$).

$$q = \frac{zF}{m} \qquad \text{Eq. 10}$$

The specific energy density w in turn, is derived from the change in Gibbs free energy per mol of reaction, divided by the mass of the reactants, Eq. 11. The unit of w is watt-hour per kilogram ($Wh \cdot kg^{-1}$).

$$w = \frac{zF \cdot \Delta E^0}{m} \qquad \text{Eq. 11}$$

The specific power p that an electrochemical cell can deliver per mass is defined by Eq. 12. The unit of p is watt per kilogram ($W \cdot kg^{-1}$).

$$p = \frac{I \cdot U}{m} \qquad \text{Eq. 12}$$

2.1.3. Material aspects

The most studied and commercially employed cathode materials in a Li-ion battery are lithium based *i)* layered-oxides (e.g. $LiMO_2$, M= Ni, Mn, Co; C_{th}= 130-140 $mAhg^{-1}$), *ii)* spinel-structures (e.g. $LiMn_2O_4$; C_{th}= 148 $mAhg^{-1}$) and *iii)* olivine-type phosphates (e.g. $LiFePO_4$; C_{th}= 170 $mAhg^{-1}$) [17, 20, 21]. In addition, lithium orthosilicates (e.g. Li_2MSiO_4, M= Fe, Mn, Co, Ni; $C_{th}\approx$ 330 $mAhg^{-1}$), are recently receiving increasing attention, since they provide the potential for an extraction of 2 Li-ions per formula unit and thus enable a higher theoretical capacity than lithium layered-oxides, spinel- and olivine-structures [17, 18].

At the anode side, graphite is the most popular compound in commercial application. Li-ions can intercalate in-between the basal-planes of the crystal structure. The highest stoichiometry that can form at room temperature is LiC_6, providing a theoretical capacity of 372 $mAhg^{-1}$ [8].

The total capacity (C_{total}) of a Li-ion full cell is expressed by a function of the cathode (C_c) and anode (C_a) specific capacity, including a mass specific contribution (Q_m in $mAhg^{-1}$) of the inactive cell components (electrolyte, separator, current collectors, housing, etc.), according to Eq. 8. Figure 2, presents the dependency of the total capacity of a 18650 Li-ion cell as a function of the anode specific capacity, assuming a cathodic contribution of 140 $mAhg^{-1}$ (i.e. $LiCoO_2$) and 170 $mAhg^{-1}$ (i.e. $LiFePO_4$), while Q_m amounts 130.4 $mAhg^{-1}$, as reported elsewhere [22].

$$C_{total} = \left(\frac{1}{C_a} + \frac{1}{C_c} + \frac{1}{Q_m}\right)^{-1} \qquad \text{Eq. 8}$$

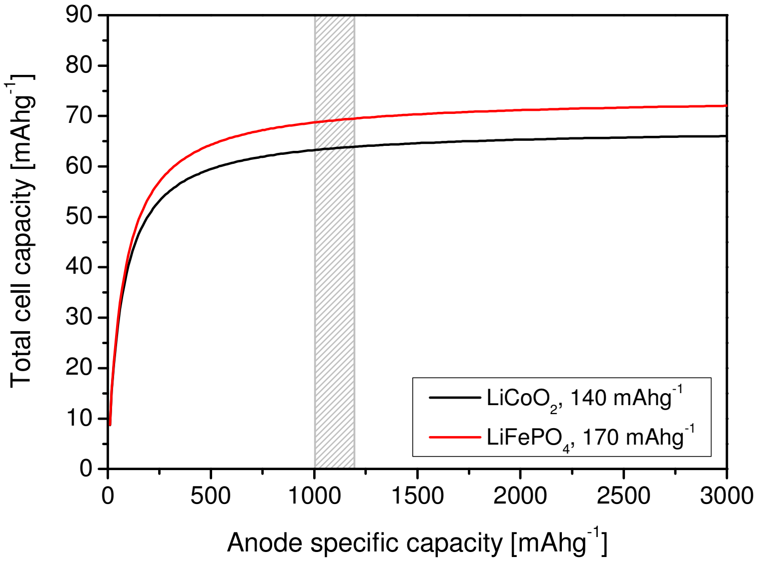

Figure 2 Total capacity of a 18650 Li-ion cell as a function of the anode specific capacity according to Eq. 8, shown for a cathodic contribution of 140 $mAhg^{-1}$ ($LiCoO_2$) and 170 $mAhg^{-1}$ ($LiFePO_4$) [22].

In order to increase the total cell capacity, it is either possible to increase the cathode or anode specific capacity or to decrease the mass of the inactive cell components. However, a significant and real-time breakthrough in the commercial production process and implementation of high capacity cathode compounds is considered as less likely [22]. Therefore, the most promising way to increase C_{total} is rationalized by the implementation of next generation anode materials, with a high specific capacity in the range of 1000 – 1200 $mAhg^{-1}$. A further enhancement would not have significance on the total cell capacity, as recognizable by the curve saturation in Figure 2 [22].

2.1.4. Tin and silicon anodes

One class of materials considered as next generation anodes are compounds, which store lithium via alloying processes [23-31]. Lithium-tin (Li-Sn) and lithium-silicon (Li-Si) for instance provide a sufficient high theoretical capacity of 994 $mAhg^{-1}$ for $Sn/Li_{22}Sn_5$ and 3579 $mAhg^{-1}$ for $Si/Li_{15}Si_4$, which is about three to ten times higher than the theoretical one of graphite (372 $mAhg^{-1}$). However, the major drawback related to alloy-forming anodes is their poor cycling stability, which emerges from large volume changes during the alloying and dealloying process: For $Sn/Li_{22}Sn_5$ $\Delta V \approx 260$ % and for $Si/Li_{15}Si_4$ $\Delta V \approx 280$ % [32-35]. The huge volume changes create strong internal mechanical stresses, which cause the particles to crack and to pulverize. In consequence, the electrical contact throughout the electrode breaks down, with the result of electrode failure and short cycle life-time [33, 36-38].

To overcome this drawback, huge research efforts have been in progress, in order to compensate and to avoid the occurring degradation of tin and silicon based anodes, Sn: [32, 39-41], Si: [34, 35, 42-56]. For both compounds, a size reduction to the nano-metric scale is intensively explored as a possible pathway to overcome the electrode failure, e.g. for Sn: [57-60] and for Si: [61-65]. In addition various studies have shown a considerable increase in the reversible capacity and lifetime for silicon thin-films [66, 67], silicon nano-wires [68-74] and silicon nano-tubes [75, 76]. Likewise for Sn, nano-cone arrays [60] and coated nano-pillars [58] were outlined to effectively enhance the cycling-stability of Sn-comprising electrodes. Another approach follows the optimization and tailoring of electrode binders, in order to alleviate mechanical degradation and hold the electrode particles together upon alloying and dealloying expansion and contraction [77-83]. Last but not least, a very promising and efficient way for utilizing tin and silicon for anode purposes is demonstrated by the preparation of Sn/carbon and Si/carbon composites or selective carbon-coating methods, e.g. for Sn/C: [57, 59] and Si/C: [84-97].

2.2. Polymer-derived ceramics

2.2.1. General background

The term polymer-derived ceramic (PDC) classifies compounds which are prepared by a thermal conversion of inorganic polymer precursors under controlled atmosphere. The initial development of the fabrication method dates back into the 1960's when Ainger and Herbert [98] and Chantrell and Popper [99] reported on the preparation of non-oxide ceramics from molecular precursors for the very first time. A milestone in the field was accomplished almost one decade later, when Verbeek, Winter and Mansmann [100-102] succeeded in the synthesis of small-diameter Si_3N_4/SiC ceramic fibers by the thermolysis of polysilazane, polysiloxane and polycarbosilane precursors. At the same time in the 1970's, Yaijma et al. came up with a new innovative preparation route of SiC based ceramic fibers, by thermal conversion of polycarbosilanes [103-105]. Since this pioneering work in the field of PDCs, further advancements were achieved by the development of new synthesis routes for polymer precursors with controlled molecular structure and chemical composition and the application of improved PDC processing techniques during the 1980's [106-108].

Beyond the early studies on the ternary PDCs SiOC and SiCN, a large variety of quaternary and multi-nary ceramics were explored by introduction of additional constituents to the ternary framework, such as Al, B, Hf, Ti or Zr [109-128]. Their introduction lead to a significant enhancement of the compounds high temperature properties, including mechanical stability, creep and oxidation resistance.

Since the microstructure and chemical composition of PDCs strongly correlate with the molecular structure and chemical composition of the starting polymer, the processing of PDCs bears several advantages in contrast to conventional ceramic manufacturing. Ceramic products and properties can be designed and tailored towards certain application demands by choosing suitable polymers without using any additives or sintering agents. Moreover, various polymer forming techniques that are well-established in the plastics industry can be utilized for preceramic shaping, such as polymer infiltration pyrolysis, injection molding, coating from solvent, extrusion or resin transfer molding. Consequently, the ceramic fabrication from inorganic polymers results in highly homogeneous compounds, with excellent functional properties like enhanced mechanical integrity or thermal resistance. Last but not least, silicon based ternary or multi-nary PDCs, like SiOC and SiCN, are not accessible by traditional processing methods and can only be prepared by a polymer precursor to ceramic conversion [129-133].

2.2.2. Silicon oxycarbide

The term silicon oxycarbide stands for a chemical structure in which silicon is simultaneously bonded to carbon and oxygen, forming tetrahedral structural units of $SiO_{4-x}C_x$ (x= 1-4) mixed bonds. The units itself build up an amorphous and heterogeneous Si-O-C network phase, in which free carbon might be dispersed; likewise SiO_2-enriched regions can form. The replacement of two-valent oxygen atoms by four-fold carbon atoms mechanically strengthens the structure and enhances its thermal integrity [134, 135]. The prefix “carbon-rich” further classifies silicon oxycarbides, in which the content of carbon exceeds 20 wt-% [131]. The microstructure of carbon-rich SiOC is composed of two interpenetrating phases: *i)* the amorphous $SiO_{4-x}C_x$ (x= 1-4) network and/or silica phase and *ii)* a free carbon phase comprised of amorphous carbon [133, 136-139]. Depending on the amount of segregated carbon, either carbon nano-domains (lower amount of free C) or a carbon percolation network (higher amount of free C) exists, as demonstrated by electrical conductivity measurements and TEM analysis [140-142]. Carbon-rich SiOC exhibits additional advantageous properties over stoichiometric or near stoichiometric compositions, namely an enhanced temperature resistance and high temperature crystallization integrity [136-138, 141, 143].

Besides the preparation of silicon oxycarbides starting from polyorganosiloxanes, a second important fabrication method is widely recognized, namely Sol-Gel processing. Hereby, functionalized silicon monomers are reacted to form a gel, which is thermally converted into ceramic SiOC. Research efforts in this field were initiated in the end of the 1980’s and followed up during the 1990’s by various scientists [134, 135, 144-152], amongst others by Sorarù et al. [153-166]. Nevertheless this method presents a serious disadvantage as it cannot be applied in industrial scale processing.

Figure 3 illustrates the preparation route of carbon-rich SiOC from polyorganosiloxane, including a scheme of the resultant microstructure for a pyrolysis temperature of 1100 °C.

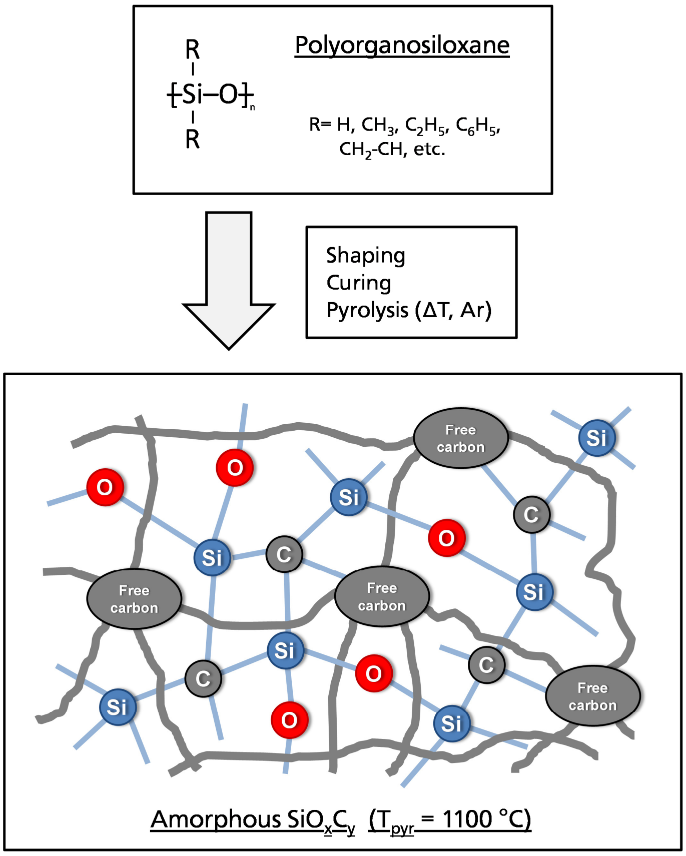

Figure 3 Preparation route for carbon-rich SiOC, including a scheme of the microstructure of the correspondent ceramic obtained at a pyrolysis temperature of 1100 °C.

2.2.3. Silicon oxycarbide as anode material

The electrochemical properties of polymer- and Sol-Gel-derived silicon oxycarbide ceramics were analyzed in the middle of the 1990's for the first time and SiOC identified as potential host material for Li-ions [167-172]. Since that time SiOC compounds with various chemical compositions were examined and stoichiometries with an exceptionally high content of free carbon were identified as perspective anode materials, with respect to gravimetric capacity, rate capability and cycling behavior [173-191]. In addition, investigations on SiOC-CNT composite were addressed by Shen et al. [192] and Bhandavat et al. [193, 194] and the synthesis and electrochemical properties of Sol-Gel derived SiOC/Si composites reported by Liu et al. [195]. Electroanalytical examinations of SiOC of specific chemical composition $SiO_{0.85}C_{1.98}$ were accomplished by D. Ahn [196] and Weidman et al. [190]. First attempts of modeling carbon-rich SiOC and the Li-ion insertion into the ceramic microstructure were presented by P. Kroll [197-200].

Table 1 summarizes the state of the art of various carbon-rich SiOC stoichiometries that were electrochemically studied. For comparison, the chemical composition, amount of free carbon, first cycle reversible (C_{rev}) and irreversible capacity (C_{irr}), coulombic efficiency (η), applied cycling current and if available capacity retention upon continuous cycling are listed. All selected samples were prepared a by polymer to ceramic conversion at a final pyrolysis temperature of 1000 °C and fulfill the requirement of comprising at least 20 wt-% of free carbon within their microstructure.

Table 1 Overview of various SiOC compounds and their electrochemical characteristics reported in literature. The chemical composition, free carbon content, first cycle reversible (C_{rev}) and irreversible capacity (C_{irr}), coulombic efficiency (η), cycling current and if available capacity retention upon continuous cycling are given.

Chemical Composition	Free C [wt-%]	C_{rev} [mAhg^{-1}]	C_{irr} [mAhg^{-1}]	η [%]	Current [mAg^{-1}]	Capacity retention	Ref.
$SiOC_{2.9}$	36.6	560	300	65	14.8	n/a	[167]
$SiO_{1.5}C_{3.9}$	44.3	640	340	65	14.8	n/a	[167]
$SiO_{0.61}C_{6.22}$	59.0	573	290	65	32.7	n/a	[175]
$SiO_{0.51}C_{7.78}$	65.2	608	259	70	32.7	95% after 40 cycles	[175]
$SiO_{0.61}C_{2.74}$	34.7	523	270	66	32.7	n/a	[178]
$SiO_{0.29}C_{5.07}$	54.1	520	272	72	32.7	n/a	[178]
$SiO_{1.63}C_{11.49}$	70.7	498	250	67	32.7	93% after 40 cycles	[179]
$SiO_{1.56}C_{7.36}$	64.3	580	267	68	32.7	93% after 40 cycles	[179]
$SiO_{2.78}C_{13.1}$	70.5	469	266	64	32.7	86% after 40 cycles	[188]
$SiO_{1.96}C_{3.46}$	40.9	732	381	66	32.7	not stable	[188]
$SiO_{0.85}C_{1.99}$	25.9	794	370	68	100	n/a	[174]
$SiO_{0.90}C_{4.40}$	48.5	568	330	63	18	cycling stable	[189]
$SiO_{0.98}C_{2.47}$	32.0	605	325	65	18	cycling stable	[191]
$SiO_{1.39}C_{0.68}$	21.8	322	400	45	18.6	n/a	[201]

Despite, this summary provides a comprehensive overview of the charge storage capability of various SiOC stoichiometries, it cannot capture the correlation between the microstructure, chemical composition and electrochemical properties of each single material as a whole. Especially the microstructural development and chemical composition are strongly relying on the employed polymers in the material preparation.

Within this context, a matter of debate within the scientific community is concerned with the nature of the electrochemically active Li-ion storage sites in carbon-rich SiOC and two different theories are argued. Raj et al. explain the microstructure of carbon-rich SiOC by the so-called "nanodomain model". According to this model, carbon-rich SiOC consists of clusters of silica tetrahedrons that are encased by Si-O-C mixed bond tetrahedrons, denoted as "interdomain-walls". These units in turn are embedded in a cage-like network of graphene sheets that form an interconnected sp^2 carbon network [202]. Based on several theoretical considerations, Raj et al. outline the tetrahedral voids in the Si-O-C mixed bonds within the interdomain-walls as electrochemically active sites, which can reversibly host the Li-ions. The graphene network is attributed a minor role in the active storage process [174, 176, 182]. Consequently, Raj et al. attribute the high capacity of polysiloxane-derived ceramics to the unique mixed coordination between silicon, carbon and oxygen [174].

A more established understanding of the microstructure of carbon-rich SiOC was presented in Chapter 2.2.2, characterizing the material as amorphous Si-O-C-mixed bond network that is interpenetrated by an amorphous free carbon phase. In consistence with this microstructural understanding, Fukui et al. identified three electrochemically active sites for Li-ions within carbon-rich SiOC by ^{7}Li-MAS-NMR measurements: *i)* Major Li-ion host sites are interstitial spaces and edges of the graphene layers within the free carbon phase and a minor contribution to the reversible capacity is assigned to *ii)* less ionic Li-species that can be stored in micropores and *iii)* diamagnetic Li-species that are directly or indirectly stored in the amorphous Si-O-C network [173, 175, 178-180, 187, 188]. Moreover, the comparison of the voltage profiles of carbon-rich SiOC and disordered carbon anodes reveals significant similarities in the potential dependency, which additionally confirms the Li-ion insertion within the free carbon phase and consequently its electrochemical activity [175].

3. Cumulative part of the thesis

Within the cumulative part of this thesis the major scientific findings, which are reported in publication [1] – [7] are summarized and correlated.

The initial work presented in Chapter 3.1 relates to the chemical, microstructural, electrochemical and electroanalytical study of carbon-rich silicon oxycarbide, derived from commercially available polyorganosiloxane *RD-684a*, as prospective anode material for Li-ion batteries. The following Chapters 3.2 and 3.3 focus on the examination of silicon oxycarbide/nano-silicon (SiOC/nSi) and silicon oxycarbide/tin (SiOC/Sn) composites, in which the relevance of an additional electrochemical active phase, precipitated within SiOC as host matrix, is evaluated. The study of the composites follows two major objectives: *i)* to analyze the impact of the incorporation of lithium-alloy forming elements (Li-X, X= Si, Sn) on the microstructure and electrochemical properties of the composites and *ii)* to improve the intrinsically poor cycling stability of Si- and Sn-based anodes via embedment within SiOC. In Chapter 3.2, the preparation of SiOC/nSi composites via ex-situ mixing of polyorganosiloxane *RD-684a* and nano-silicon powder, followed by thermal treatment, is introduced, whereas in Chapter 3.3, an innovative single-source precursor approach is presented for the synthesis of SiOC/Sn compounds. In this case, polyorganosiloxane *RD-684a* and *PMS MK* are chemically modified with tin(II)acetate in order to yield in-situ Sn-precipitates within SiOC upon thermolysis.

3.1. Microstructural, electrochemical and electroanalytical characterization of polymer-derived carbon-rich silicon oxycarbide ceramics as prospective anode materials for Li-ion batteries

The content of this Chapter is published in:

[1] J. Kaspar, M. Graczyk-Zajac and R. Riedel, Carbon-rich SiOC anodes for lithium-ion batteries: Part II. Role of thermal cross-linking, *Solid State Ionics*, 225 **(2012)** 527-531

[2] J. Kaspar, M. Graczyk-Zajac and R. Riedel, Lithium insertion into carbon-rich SiOC ceramics: Influence of pyrolysis temperature on electrochemical properties, *Journal of Power Sources*, 244 **(2013)** 450-455

[3] G. Liu, J. Kaspar, L.M. Reinold, M. Graczyk-Zajac and R. Riedel, Electrochemical performance of DVB-modified SiOC and SiCN polymer-derived negative electrodes for lithium-ion batteries, *Electrochimica Acta*, 106 **(2013)** 101-108

[4] J. Kaspar, M. Graczyk-Zajac and R. Riedel, Determination of the Li-ion diffusion coefficient in carbon-rich SiOC by the electrochemical methods PITT, GITT and EIS, *Electrochimica Acta*, 155 **(2014)** 665-670

In the present Chapter the correlation between the microstructural development of carbon-rich SiOC in dependence of pyrolysis temperature and its corresponding electrochemical properties are presented. The nature of the free carbon phase is characterized and investigated with respect to its Li-ion storing properties. In addition a further increase of the carbon content by chemical modification of polyorganosiloxane *RD-684a* with divinylbenzene is addressed. The influence of the carbon-enrichment on the maximum achievable capacity and cycling stability of the resulting ceramics is analyzed. Finally the chemical diffusion coefficient of Li-ions within SiOC is determined by the well-established electroanalytical methods: Potentiostatic intermittent titration technique (PITT), Galvanostatic intermittent titration technique (GITT) and Electrochemical impedance spectroscopy (EIS).

3.1.1. Results and discussion

Carbon-rich silicon-oxycarbide ceramics were prepared via pyrolysis of commercially available polyorganosiloxane *RD-684a* (Starfire Systems Inc., USA) under inert atmosphere. Prior to pyrolysis, the polymer was thermally cross-linked at 400 °C for 3 h. Cross-linking and pyrolysis were carried out under a steady flow of purified argon and heating rates adjusted to 50 °C h^{-1} for cross-linking and 100 °C h^{-1} for pyrolysis. The final ceramization temperature ranged from 900 - 2000 °C, with a holding time of 3 h. For chemical and microstructural characterization, elemental analysis, X-ray powder diffraction, Raman- and FTIR-spectroscopy were applied.

XRD analysis reveals the amorphous nature of the samples prepared between 900 - 1200 °C, while in the materials annealed above 1200 °C crystalline silicon carbide is detected. The SiC intensities are found to increase with temperature of pyrolysis (T_{pyr}) and peaks get more distinct. This development is related to a partitioning and the decomposition of the structural Si-O-C network by the carbothermal reaction of silicon and accompanied by loss of oxygen, as confirmed by elemental analysis. At 2000 °C additional peaks for graphitic carbon appear in the pattern, indicating a partial graphitization of the free carbon phase.

The recorded Raman-spectra confirm the disordered nature of the free carbon phase, due to the presence of strong D- and less intense G-bands, Figure 4 a). With increasing temperature of pyrolysis, the D- and G-bands get more narrow and distinct, relying on *i)* a decreasing number of intrinsic defect sites, *ii)* the disappearance of residual C-H bonds, especially present at lower T_{pyr} and *iii)* the vanishing of dangling bonds. Simultaneously, the intensities of the 2D vibrations, the overtones of the D-band, strongly increase, emphasizing an overall increasing structural organization of the free carbon and partial graphitization towards 2000 °C [203-207].

Within the recorded FTIR-spectra (Figure 4 b)) vibrational modes assigned to Si-O and Si-C are present, stemming from the $SiO_{4-x}C_x$ (x= 1-4) mixed bonds in the amorphous Si-O-C network phase and silicon carbide. With increasing temperature of pyrolysis the intensities of the Si-O vibrations significantly diminish in contrast to the Si-C modes. This development illustrates the progressive degradation of the Si-O-C network by the carbothermal reaction of silicon and well correlates with the results from XRD analysis. In addition, this development is reflected by the changing chemical composition of the samples, emphasized by elemental analysis by means of strongly diminishing oxygen content with increasing T_{pyr}. At 2000 °C almost no oxygen and likewise Si-O intensities in the FTIR-spectrum are registered anymore.

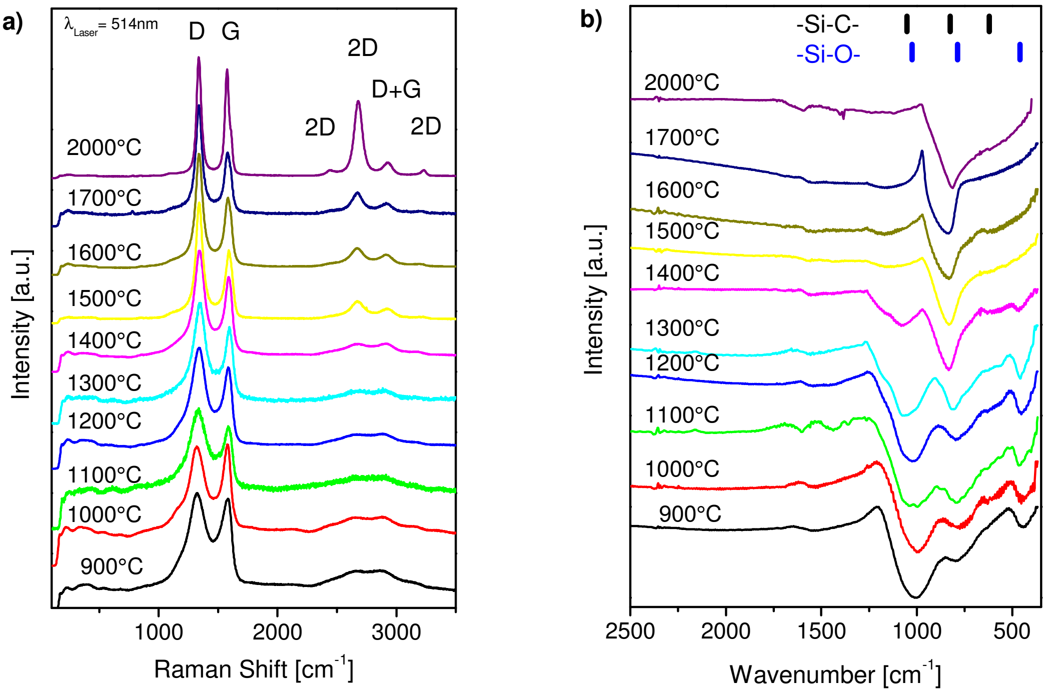

Figure 4 a) Raman spectra and b) FTIR spectra of SiOC pyrolyzed between 900 - 2000 °C.

For analyzing the Li-ion uptake and electrochemical characteristics, the first cycle voltage-profiles of $SiOC_{1100}$ and $SiOC_{1300}$ are presented in Figure 5. These samples are exemplarily chosen due to their similar chemical composition (both $SiO_{0.93}C_{3.46}$), but different microstructural features, i.e. a higher carbon organization and presence of crystalline SiC for the pyrolysis temperature of 1300 °C. $SiOC_{1100}$ demonstrates the higher reversible capacity with 521 $mAhg^{-1}$, whereas 367 $mAhg^{-1}$ are recovered for $SiOC_{1300}$. Both materials show solid-electrolyte-interface formation at potentials between 1.1 and 0.5 V for the first Li-ion uptake, running into an extended sloping plateau below potentials of 0.5 V. The well-developed sloping plateau in the lower potential region is highly indicative for the Li-ion insertion within the free carbon phase present in the SiOC microstructure. In the anodic branches, most of the charge is continuously recovered below 1.5 V, with a similar curve progression as reported for disordered soft and hydrogen-containing carbons [208-210]. Accordingly, the high capacity and excellent lithium-ion storage ability can be attributed to the presence and nature of the free carbon phase within SiOC. The carbon itself offers a large variety of Li-ion storing sites, namely edges of graphene sheets, interstitial spaces between graphene layers, micro- and nano-pores, intercalation into graphite nano-crystallites, adsorption at carbon-crystallite surfaces and defect sites [175, 178-180, 185, 187-189] and [210-215].

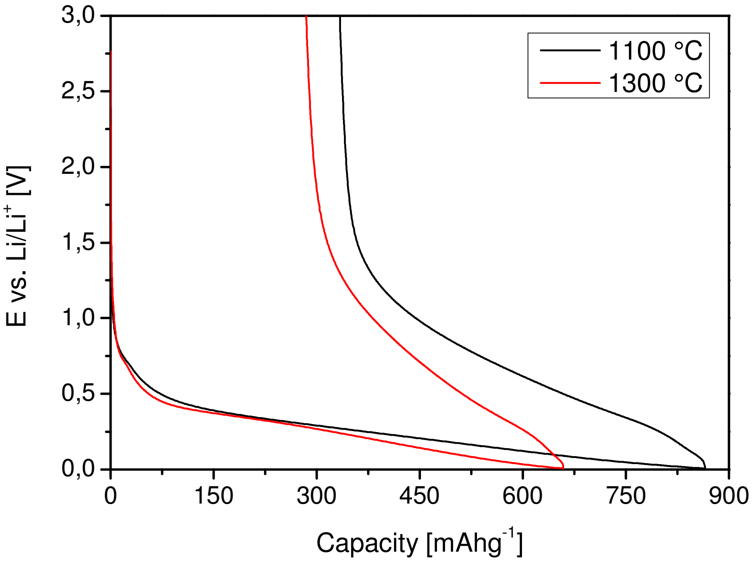

Figure 5 First cycle voltage profile for SiOC pyrolyzed at 1100 and 1300 °C, current rate 37 mAg^{-1}.

Figure 6 compares the average reversible capacity of SiOC prepared between 900 - 2000 °C for different cycling currents. As indicated by the comparison of the 1100 and 1300 °C samples, the average reversible capacity strongly diminishes with increasing temperature of pyrolysis. On the one hand, the increasing organization of the free carbon, as revealed by Raman-spectroscopy, accounts for a reducing amount of Li-ion storing sites, since higher ordered carbons can generally host less Li-ions than orderless configurations [216]. Hence, at higher temperatures of pyrolysis the corresponding capacities are necessarily lower than at lower pyrolysis temperatures. On the other hand, the partitioning of the Si-O-C amorphous network reduces the structural stability of the segregated free carbon. In addition the formation of electrochemically inactive SiC likewise contributes to the result of decreasing capacities with increasing T_{pyr}.

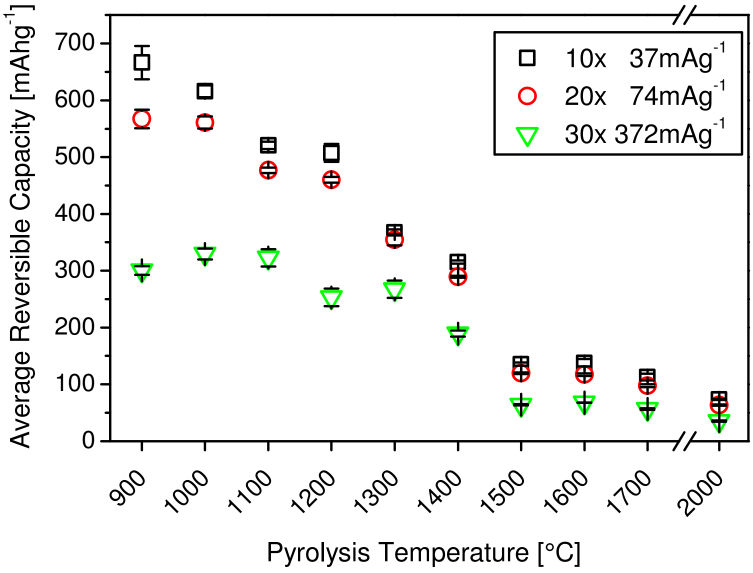

Figure 6 SiOC average reversible capacity in dependence of temperature of pyrolysis. Average values were calculated from 10 cycles at 37 mAg^{-1}, 20* x 74 mAg^{-1} and 30 x 372 mAg^{-1}. The error bars indicate the standard deviation from the average value (* for $SiOC_{1100}$, 30 x 74 mAg^{-1}).

Among the investigated samples, SiOC prepared at 900 °C reveals the highest reversible capacity, but significant fading upon continuous cycling. Within ten cycles at 37 mAg^{-1}, the recovered charge diminishes from 738 to 644 mAhg^{-1}. In particular, between the first and second cycle 40 mAhg^{-1} are lost. Most probably, this decay relates to a large amount of residual hydrogen (about 1.1 wt-%) within the sample, especially within the free carbon phase in form of C-H bonds, stemming from the initial polymer precursor. According to Dahn et al., Li-ion storage in H-containing carbons occurs via Li-binding in the vicinity of H atoms [208]. During Li-ion extraction, the original C-H bonds reform. When this reforming is disturbed or incomplete, the recovered capacity continuously decays [208, 217].

Among the sample series, SiOC pyrolyzed at 1000 and 1100 °C are identified as most promising and suitable anode materials, due to their superior electrochemical performance in terms of high reversible capacity in combination with excellent rate capability and cycling stability. At a current rate of 37 and 74 mAg^{-1}, an average reversible capacity of 615 mAhg^{-1} and 561 mAhg^{-1} is registered for $SiOC_{1000}$ and 512 mAhg^{-1} and 477 mAhg^{-1} for $SiOC_{1100}$, while at a current rate of 372 mAg^{-1}, both registered values are similar with 330 and 323 mAhg^{-1}. In general the excellent rate capability is explained by the beneficial nano-structure of the samples that kinetically boosts the Li-ions due to shorten diffusion path ways [218-220]. For visualization of the applied cycling procedure, the capacity performance in dependence of cycle number is exemplarily shown for $SiOC_{1100}$ in Figure 7.

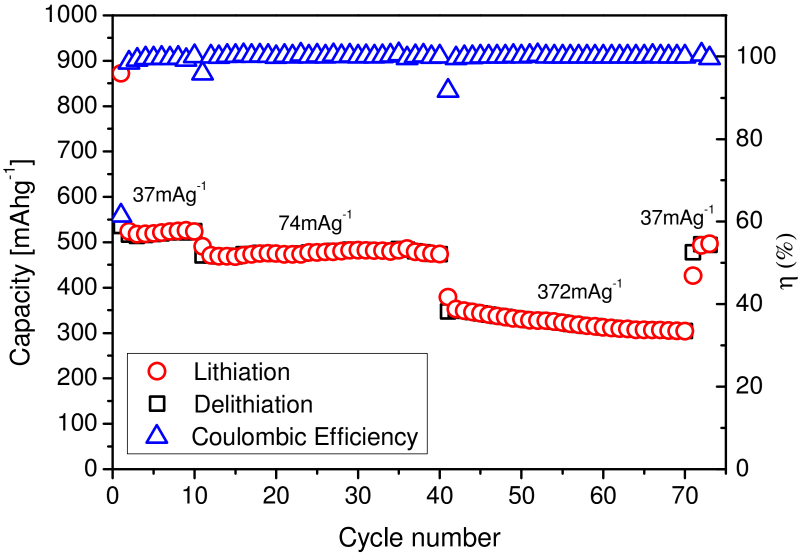

Figure 7 Capacity behavior and coulombic efficiency of SiOC pyrolyzed at 1100 °C upon continuous cycling at different current rates.

The introduction of additional carbon-rich side groups to the polymer-precursor, via chemical modification of polyorganosiloxane *RD-684a* with divinylbenzene (DVB) by hydrosilylation reaction, was considered to further enhance the amount of segregated carbon within the SiOC microstructure, Figure 8. Therefore, modification was carried out with lower, equal and higher stoichiometric ratio of Si-H to C=C groups, present in the polymer and DVB, respectively. An analogous modification was accomplished for polyorganosilazane *HTT1800* (Clariant GmbH, Germany), which converts into a low-carbon (< 10 wt-% free carbon) silicon carbonitride ceramic (SiCN) [221, 222].

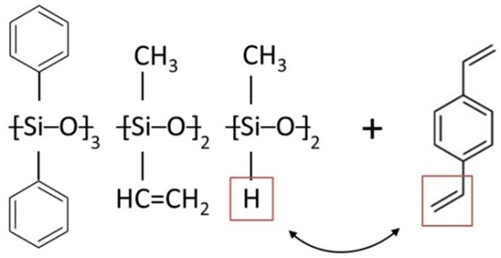

Figure 8 Scheme of hydrosilylation: Polyorganosiloxane *RD-684a* and DVB.

For pyrolyzed SiOC and SiCN samples (T_{pyr} = 1100 °C), the carbon content was found to increase upon precursor modification. The most significant increase in the yield of free carbon was obtained for the SiCN system with the highest amount of DVB addition, i.e. 49.3 wt-% free carbon after modification. Accordingly, this sample demonstrated the highest increase in electrochemical capacity among the SiCN series. On the contrary, for already intrinsically carbon-rich SiOC the first cycle lithium uptake was found to only increase in the case of modification with stoichiometric amount of DVB, namely from 521 $mAhg^{-1}$ up to 603 $mAhg^{-1}$. Especially the highest amount of DVB addition lead to a significantly lower reversible capacity, i.e. 344 $mAhg^{-1}$ in the first cycle. For all carbon enriched SiOC compounds, the cycling stability strongly decayed, compared to the unmodified state. In conclusion, a further enhancement of the carbon content for already intrinsically carbon-rich pre-ceramic polymers appears of disadvantage regarding the electrochemical properties of the corresponding ceramics. When the amount of carbon exceeds a certain threshold, the amorphous Si-O-C network cannot provide sufficient stabilizing conditions towards the formed free carbon phase, which impairs the cycling stability of the material.

The presented results emphasize the excellent electrochemical properties of carbon-rich SiOC not only in terms of capacity, which is attributed to the advantageous nature of the free carbon phase embedded in the ceramic network, but also in terms of rate capability. In the following, the attempt to rationalize the reasons for this excellent performance, in the view of lithium ion transport rate and mobility, was addressed. A new material batch was prepared under optimized processing conditions at T_{pyr} of 1100 °C. The specific chemical composition of the obtained sample was $SiO_{0.95}C_{3.72}$. The Li-ion diffusivity within the material was evaluated by three independent electroanalytical methods, namely potentiostatic intermittent titration technique (PITT), galvanostatic intermittent titration technique (GITT) and electrochemical impedance spectroscopy (EIS). PITT and EIS revealed a similar order of magnitude for the Li-ion diffusion coefficient in the relevant potential range of $E < 1$ V (vs. Li/Li^+) with $D_{Li^+} = 10^{-9} - 10^{-10}$ $cm^2\,s^{-1}$, whereas GITT based calculations suggested D_{Li^+} in the range of $10^{-10} - 10^{-11}$ $cm^2\,s^{-1}$. A graphical comparison of D_{Li^+} as a function of the potential is presented in Figure 9.

All three methods reveal Li-ion diffusivities similar to disordered carbon ($10^{-10} - 10^{-11}$ $cm^2\,s^{-1}$ [210, 223]), well emphasizing the insertion of Li-ions into the free carbon phase present in the SiOC microstructure. The Li-ion diffusivity in SiOC of specific chemical composition $SiO_{0.85}C_{1.98}$, analyzed by PITT and GITT, was reported by D. Ahn with $D_{Li^+} = 10^{-7} - 10^{-10}$ $cm^2\,s^{-1}$, one to two orders of magnitude higher than the diffusivity determined in the present work [196]. However, controversially Weideman et al. evaluated the Li-ion diffusivity within SiOC of the same composition ($SiO_{0.85}C_{1.98}$) by GITT to $D_{Li^+} = 1.8 - 4.2 \cdot 10^{-14}$ $cm^2\,s^{-1}$ [190], revealing a difference between these studis in the order of magnitude of $10^{-4} - 10^{-7}$ $cm^2\,s^{-1}$.

According to this deviation, the validity of these reports should be critically questioned. For comparison, the Li-ion diffusion coefficient in graphite is calculated to 10^{-9} - 10^{-13} $cm^2 s^{-1}$ [223-225].

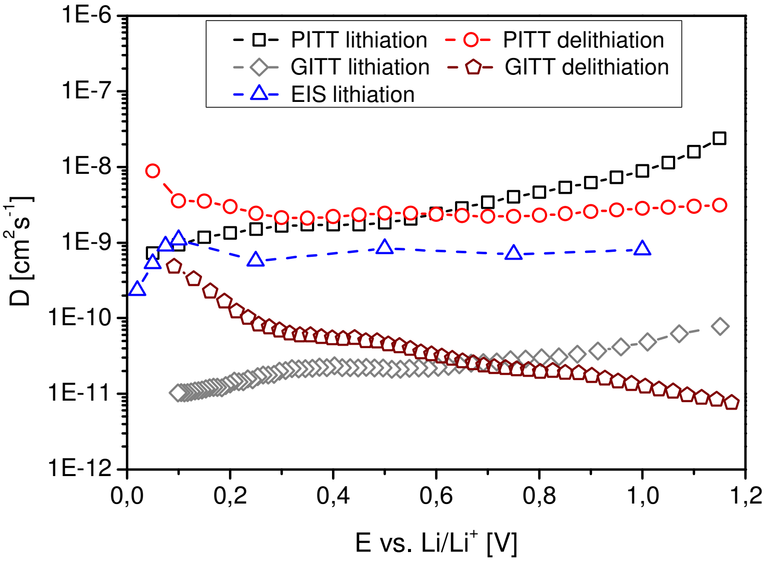

Figure 9 Comparison of the Li-ion diffusion coefficient calculated by PITT, GITT and EIS as a function of the potential.

In contrast to graphite and disordered carbon, the *D vs. E* curves obtained for carbon-rich $SiO_{0.95}C_{3.72}$ demonstrate a constant behavior, Figure 9. Neither significant minima, as known for graphite [225], nor comparable maxima to those registered for disordered carbon are present [210]. A similar independence of D_{Li^+} of the electrode potential was shown by D. Ahn for $SiO_{0.85}C_{1.98}$, but not further addressed in his work [196]. To explain this finding, some unique microstructural features of carbon-rich SiOC must be emphasized: *i)* the lateral flake size of the free carbon, which amounts about 50 Å [2] and *ii)* the embedding of the free carbon within the stabilizing Si-O-C network. On the one hand, the present flake size is large enough to support local distortions around adsorbed Li-ions, since the critical healing length of the distortions is about 5 Å. This leads to weak attractive interactions among the adsorbed ions. On the other hand, coulombic repulsion forces exists between the ionic species, since the carbon flake size is too small to shield the charge completely, as it is the case for graphite with an ideal infinitive length of its graphene layers (c.f. reference [210] and references therein). Accordingly, the attractive and repulsive interactions can counteract each other, excluding the presence of any significant minima or maxima in the *D vs. E* curves. The second feature to emphasize is the transition regime between the Si-O-C network and the free carbon phase. At the interface, there is a change from oxygen-rich towards carbon-rich $SiO_{4-x}C_x$ (x= 1-4) structural units, leading to local bond distortions [133]. In consequence there is an enrichment of voids and defect-sites within this transition regime that offers continuous and potential independent diffusion pathways into the bulk of the material.

3.1.2. Statement of personal contribution

[1] J. Kaspar, M. Graczyk-Zajac and R. Riedel, Carbon-rich SiOC anodes for lithium-ion batteries: Part II. Role of thermal cross-linking, *Solid State Ionics*, 225 **(2012)** 527-531

All experimental work related to the material synthesis and preparation was carried out by myself. All applied chemical and microstructural characterization methods were performed by myself, except XRD measurements, which were done by Dipl.-Ing. Jean-Christophe Jaud (AK Prof. Donner). Dipl.-Ing. Claudia Fasel and Dr. Gabriela Mera (both AK Prof. Riedel) gave me an initial assist with the elemental analysis and Raman-spectroscopy. The electrode processing and all electrochemical characterization was accomplished by myself. The manuscript was written by myself and revised and approved of by Dr. Magdalena Graczyk-Zajac and Prof. Ralf Riedel.

[2] J. Kaspar, M. Graczyk-Zajac and R. Riedel, Lithium insertion into carbon-rich SiOC ceramics: Influence of pyrolysis temperature on electrochemical properties, *Journal of Power Sources*, 244 **(2013)** 450-455

All experimental work related to the material synthesis and preparation was carried out by myself. All applied chemical and microstructural characterization methods were performed by myself, except XRD measurements, which were done by Dipl.-Ing. Jean-Christophe Jaud (AK Prof. Donner). The electrode processing and all electrochemical characterization was done by myself. The manuscript was written by myself and revised and approved of by Dr. Magdalena Graczyk-Zajac and Prof. Ralf Riedel. Dr. Magdalena Graczyk-Zajac particularly contributed to the discussion on the voltage profiles.

[3] G. Liu, J. Kaspar, L.M. Reinold, M. Graczyk-Zajac and R. Riedel, Electrochemical performance of DVB-modified SiOC and SiCN polymer-derived negative electrodes for lithium-ion batteries, *Electrochimica Acta*, 106 **(2013)** 101-108

The idea behind this work was developed by myself as a result of various scientific discussions with my former colleague Dr. Mahdi Seifollahi Bazarjani. The experimental proceeding for the study was developed with Dr. Magdalena Graczyk-Zajac and Dipl.-Ing. Mirko Reinold. Most of the experimental work was carried out by Dr. Guanwei Liu, at that time M.Sc. and a visiting student in our group. Dr. Guanwei Liu worked under my supervision concerning all work related to the SiOC system. The part relating to SiCN ceramics was coordinated by Dipl.-Ing. Mirko Reinold. In particular, I supported the sample preparation, microstructural characterization (except XRD, Dipl.-Ing. Jean-Christophe Jaud, AK Prof. Donner), electrode processing, electrochemical measurements, as well as data evaluation and interpretation. The elemental analysis of all samples was carried out by myself. The manuscript was initially written by M.Sc. Guanwei Liu and primarily revised by Dr. Magdalena Graczyk-Zajac. Secondary revision was accomplished by myself and Dipl.-Ing. Mirko Reinold. Prof. Ralf Riedel revised and approved of the manuscript before publication.

[4] J. Kaspar, M. Graczyk-Zajac and R. Riedel, Determination of the Li-ion diffusion coefficient in carbon-rich SiOC by the electrochemical methods PITT, GITT and EIS, *Electrochimica Acta*, 155 **(2014)** 665-670

All experimental work and data analysis, including the performed estimations, was carried out by myself, except the determination of the particle-size distribution, which was done by Dipl.-Ing. Alexander Uhl. The manuscript was written by myself and revised and approved of by Dr. Magdalena Graczyk-Zajac and Prof. Ralf Riedel.

3.2. Silicon oxycarbide/nano-silicon composite anodes for Li-ion batteries: Considerable influence of nano-crystalline versus nano-amorphous silicon embedment on the electrochemical properties

The content of this Chapter is published in:

[6] J. Kaspar, M. Graczyk-Zajac, S. Lauterbach, H.-J. Kleebe and R. Riedel, Silicon oxycarbide/nano-silicon composite anodes for Li-ion batteries: Considerable influence of nano-crystalline vs. nano-amorphous silicon embedment on the electrochemical properties, *Journal of Power Sources*, 269 **(2014)** 164-172

In Chapter 3.2 the preparation of silicon oxycarbide/nano-silicon composites by ex-situ mixing of either crystalline or amorphous nano-silicon particles with polyorganosiloxane *RD-684a*, followed by thermal conversion, is presented. The influence of the silicon particle morphology on the composites structural evolution, as well as electrochemical properties, is analyzed and discussed. From the perspective of silicon, the potential and benefits of an embedding SiOC host matrix, by means of increasing the intrinsically poor cycling stability and cycle life-time of silicon-based anodes, is addressed.

3.2.1. Results and discussion

Silicon oxycarbide/nano-silicon composites (SiOC/nSi) were prepared by mixing of either crystalline nano-silicon (nSi_c, 30-50 nm; Nanostructured & Amorphous Materials Inc., USA) or amorphous nano-silicon (nSi_a, ~36 nm; Strem Chemicals Inc., Germany) particles with polyorganosiloxane *RD-684a* (Starfire Systems Inc., USA) and subsequent pyrolysis of the mixture at 1100 °C. The amount of Si addition to the polymer was adjusted to generate a composite with a weight-ration of Si to SiOC phase of 20:80, as considered preferential for silicon-based composites anode [48].

The microstructural characterization of the prepared compounds was accomplished by means of XRD, Raman-spectroscopy and TEM analysis and revealed the composites composed of four major phases: *i)* the amorphous Si-O-C phase, *ii)* free carbon segregation, *iii)* crystalline silicon and *iv)* crystalline silicon carbide. In Figure 10, TEM micrographs and the SAED pattern of composite SiOC/nSi_c and likewise in Figure 11 for SiOC/nSi_a are shown.

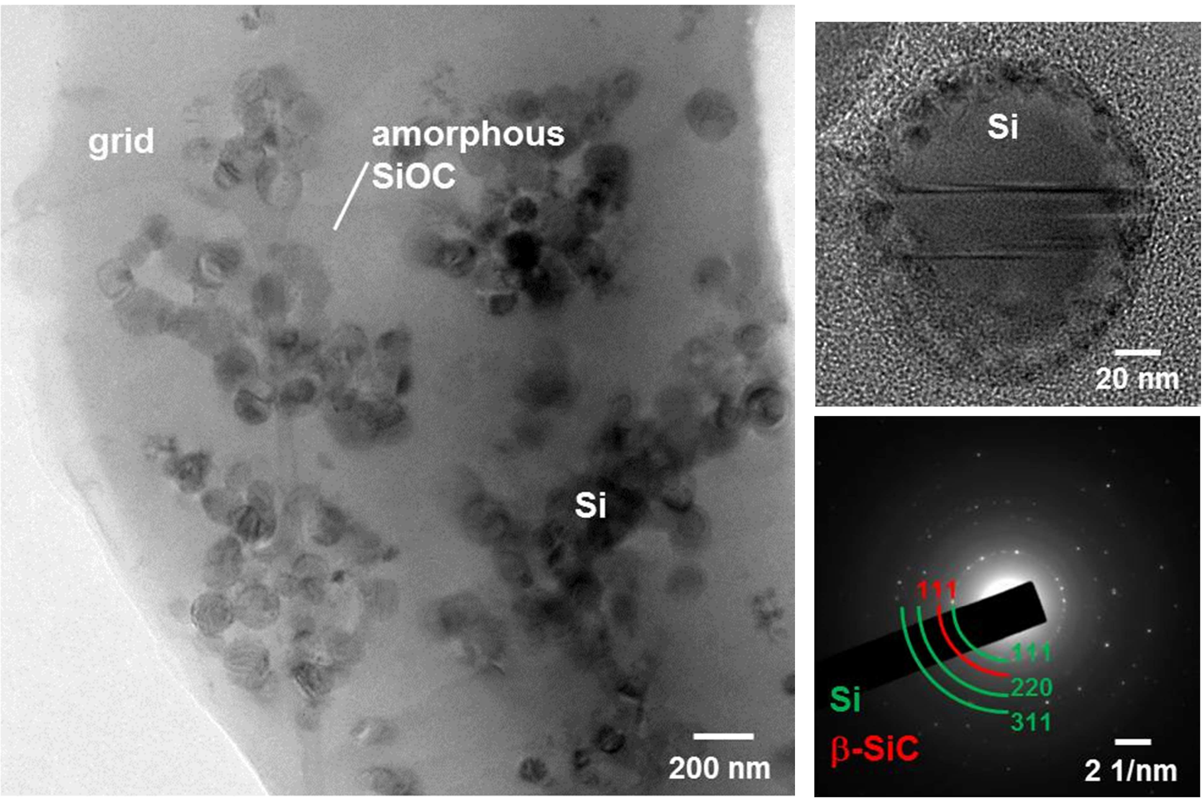

Figure 10 TEM micrographs and SAED pattern of SiOC/nSi_c.

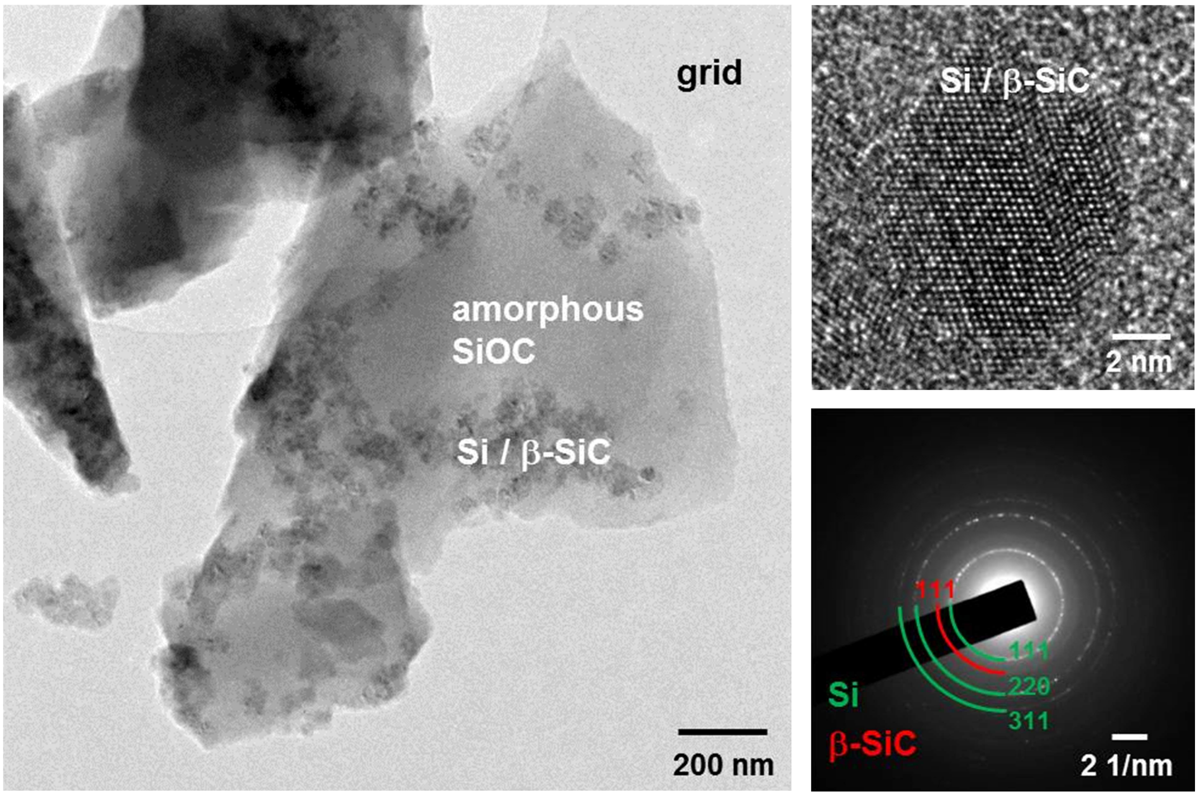

Figure 11 TEM micrographs and SAED pattern of SiOC/nSi_a.

Note that for both samples, the silicon distribution within the matrix is inhomogeneous, as a result of the applied ex-situ mixing during sample preparation. In the case of SiOC/nSi_c, silicon particles up to 100 nm in diameter are well visible, surrounded by the amorphous Si-O-C. For SiOC/nSi_a the microstructure appears different. The initial amorphous nSi particles crystallized into Si and SiC grains of ~10 nm in diameter. Due to the similar lattice parameter of Si and SiC, HRTEM is not able to clearly distinguish between both phases.

The electrochemical performance of both samples upon galvanostatic cycling with 74 mAg^{-1} is compared in Figure 12. For SiOC/nSi_c the initial reversible capacity amounts 804 $mAhg^{-1}$ and increases during the first 10 cycles up to 905 $mAhg^{-1}$. Around cycle 15 a continuous capacity decrease sets on and after 50 cycles only 314 $mAhg^{-1}$ are recovered. The coulombic efficiency within one cycle amounts 94 - 98 %. The reason for the observed capacity fading is the progressive degradation and failure of the embedding SiOC matrix, which is not able to withstand and accommodate the generated mechanical stress by Li-Si alloying expansion and dealloying contraction. At a certain point the matrix ruptures irreversibly and electrically insulated fragments cannot further contribute to Li-ion storage. In addition, the differential capacity plot for SiOC/nSi_c (Figure 13 a)) confirms this circumstance and reflects the extended cycling behavior in Figure 12.

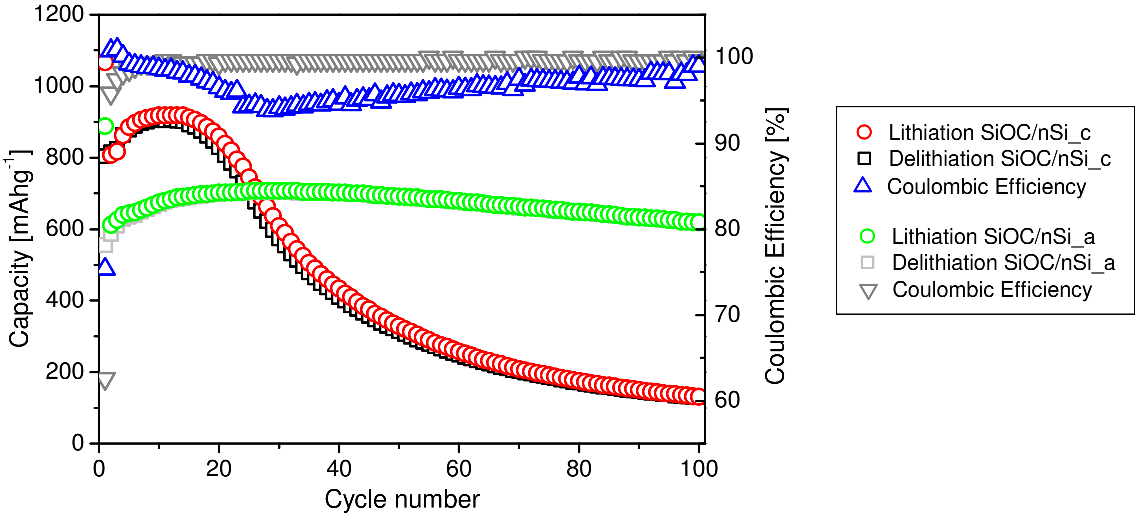

Figure 12 Comparison of the cycling behavior and coulombic efficiency of SiOC/nSi_c and SiOC/nSi_a in dependence of cycle number at a current rate of 74 mAg^{-1}.

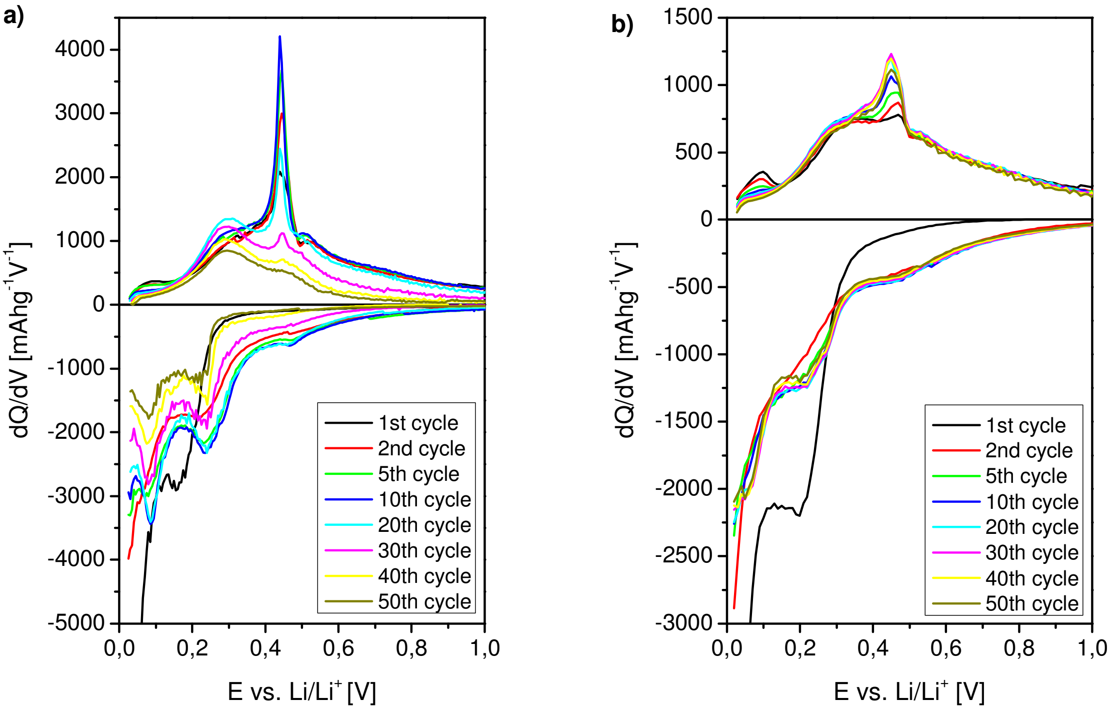

Figure 13 Differential capacity curves for a) SiOC/nSi_c and b) SiOC/nSi_a.

When following the intensity development of the Li-Si alloying/dealloying signals in Figure 13 a), at 0.22 and 0.08 V for alloying and at 0.30 and 0.45 V for dealloying, an initial intensity increase is recognized, followed by rapid decreasing intensity after cycle 10. The initial capacity increase relates to a cycle-wise silicon activation, suggesting that not all silicon phase present in the composite is contributing to Li-ion storage right from the beginning. Accordingly, the observed capacity increase in Figure 12 can be explained by this step-wise activation. In addition to silicon activity, signals from SiOC matrix activity are present in the differential capacity plots in Figure 13. Typically SiOC activity is traced around 0.45, 0.1 and 0.02 V in the cathodic branch and around 0.08, 0.34 and 0.68 V and in the anodic branch [4]. Note that not all SiOC related signals are well pronounced and clearly visible, but rather broadened and overlapping with the ones from silicon.

For SiOC/nSi_a, the initial registered capacity is lower compared to SiOC/nSi_c (Figure 12), due to the loss of nSi active phase upon SiC crystallization. The recovered capacity slightly increases with the cycle number from 555 mAhg^{-1} up to a maximum of 704 mAhg^{-1} and demonstrates a rather stable cycling behavior during the 100 measured cycles. Characteristic fading and matrix failure as observed for SiOC/nSi_c does not occur. The coulombic efficiency after the 5th cycle is continuously higher than 99.5 %. In addition, the differential capacity at the afore mentioned potentials for Li-Si alloying/dealloying remains constant after cycle 10, Figure 13 b). This superior behavior relies on the different microstructure and enhanced matrix integrity of the SiOC/nSi_a sample. On the one hand, the smaller size of the nSi crystallites (~10 nm) causes absolute minor volume changes upon Li-Si alloying/dealloying and in consequence less mechanical stress appliance to the matrix. On the other hand the significant presence of SiC phase is considered to increase the intrinsically electrical conductivity of the composite and supports the internal electrical contact (σ_{SiC}= ~10^1 – 10 Sm^{-1} depended on its form and size, σ_{Si}= 10^{-3} Sm^{-1}, σ_{SiOC}= 7.14 Sm^{-1} [142, 226]). Accordingly, matrix destruction combined with capacity fading, as found in the case of sample SiOC/nSi_c, is not observed for composite SiOC/nSi_a.

In Figure 14, the cycling performance of both composites is compared with respect to pure SiOC (c.f. Figure 7, Chapter 3.1, rate 74 mAg^{-1}) and a pure nSi_c reference, representing the general cycling behavior of both, pure nSi_c and nSi_a reference electrodes. The capacity of the nSi reference drops instantly and after 10 cycles only ~10 % of the initial capacity is recovered. Pure SiOC on the contrary demonstrates a stable performance with 477 $mAhg^{-1}$ in average. For pure silicon, rapid degradation is a reported phenomenon and is rationalized by the tremendous volume changes upon Li-Si alloying/dealloying process ($Si/Li_{15}Si_4$ $\Delta V \approx$ 280 %) that provoke the amorphization and pulverization of the electrode [33-38].

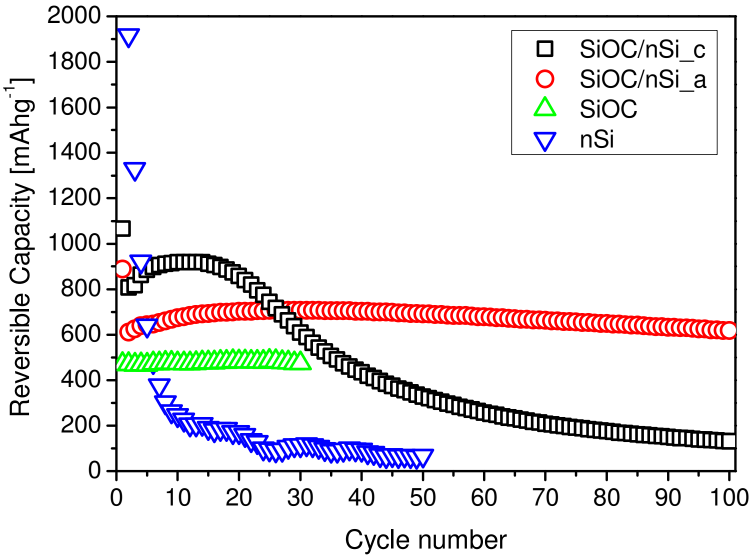

Figure 14 Comparison of the reversible capacity in dependence of cycle number for SiOC/nSi_c, SiOC/nSi_a, pure SiOC (c.f. Figure 7, Chapter 3.1, rate 74 mAg^{-1}) and a pure nSi reference at a current rate of 74 mAg^{-1}.

Concerning both SiOC/nSi composites, from the perspective of the embedding SiOC phase, the incorporation of additional electrochemically active silicon enhances the composites capacity, i.e. up to 905 mAhg^{-1} for SiOC/nSi_c and up to 704 mAhg^{-1} for SiOC/nSi_a. However, in the case of SiOC/nSi_c, cycling stability and electrode life-time significantly diminish, due to SiOC matrix failure upon Li-Si alloying/dealloying expansion and contraction. From the perspective of silicon, SiOC appears as suitable host to mechanically stabilize the incorporated nSi-grains upon Li-uptake and release and accounts for an improved cycling stability, compared to the pure nSi reference. Particularly for SiOC/nSi_a, the presence of significant smaller nSi grains and an enhanced intrinsically electrical conductivity by the presence of in-situ formed SiC phase helps to prevent matrix degradation and failure of the stabilizing SiOC host.

3.2.2. Statement of personal contribution

[6] J. Kaspar, M. Graczyk-Zajac, S. Lauterbach, H.-J. Kleebe and R. Riedel, Silicon oxycarbide/nano-silicon composite anodes for Li-ion batteries: Considerable influence of nano-crystalline vs. nano-amorphous silicon embedment on the electrochemical properties, *Journal of Power Sources*, 269 **(2014)** 164-172

All experimental work related to material synthesis and preparation was carried out by myself. All applied chemical and microstructural characterization methods were performed by myself, except XRD (Dipl.-Ing. Jean-Christophe Jaud, AK Prof. Donner) and TEM (Dr. Stefan Lauterbach, AK Prof. Kleebe). The electrode processing and all electrochemical characterization was performed by myself. The manuscript was written by myself and revised and approved of by Dr. Magdalena Graczyk-Zajac, Dr. Stefan Lauterbach, Prof. Hans-Joachim Kleebe, and Prof. Ralf Riedel.

3.3. An innovative single-source precursor approach towards SiOC/Sn nano-composites with high Li-ion storage capacity and enhanced cycling stability

The content of this Chapter is published in:

[5] E. Ionescu, C. Terzioglu, C. Linck, J. Kaspar, A. Navrotsky and R. Riedel, Thermodynamic control of phase composition and crystallization of metal-modified silicon oxycarbides, *Journal of the American Ceramic Society*, 96 **(2013)** 1899-1903

[7] J. Kaspar, C. Terzioglu, E. Ionescu, M. Graczyk-Zajac, S. Hapis, H.-J. Kleebe and R. Riedel, Stable SiOC/Sn Nanocomposite Anodes for Lithium-Ion Batteries with Outstanding Cycling Stability, *Advanced Functional Materials,* 24 **(2014)** 4097-4104

In the present Chapter, the synthesis of novel ceramic/tin nano-composites via an innovative single-source-precursor approach is introduced. In-situ formed tin nano-particles finely dispersed within a SiOC ceramic matrix were obtained by chemical modification of polyorganosilsesquioxane *PMS MK* and polyorganosiloxane *RD-684a* with tin(II)acetate, followed by thermolysis. The microstructure of the composites is carefully characterized and materials studied with respect to their electrochemical performance and properties. Especially the impact of the mechanical properties of the embedding SiOC, namely carbon-poor and therefore stiff and brittle vs. carbon-rich and therefore mechanically less brittle, is addressed. In addition an assessment based on the thermodynamic fundamentals prevalent during pyrolysis conditions is presented, emphasizing the question why in the case of tin-organic precursor modification nonvalent metallic precipitates are formed within the SiOC, whereas the modification with other metal-organic compounds results in the segregation of metal-oxide, -silicide or -carbide species.

3.3.1. Results and discussion

The synthesis of SiOC/Sn nano-composites was accomplished by chemical modification of polyorganosilsesquioxane *PMS MK* (MK, Wacker-Belsil, Germany) and polyorganosiloxane *RD-684a* (RD, Starfire Systems Inc., USA) with tin(II)acetate ($Sn(ac)_2$, Sigma-Aldrich, Germany), followed by thermal conversion at 1000 °C. The final tin content in the samples amounted 21.0 wt-% for $SiOC_{MK}/Sn$ and 27.5 wt-% for $SiOC_{RD}/Sn$. The major difference between both materials is represented by the chemical composition of the SiOC host.

Polyorganosilsesquioxane *PMS MK* transforms into a carbon-poor and therefore stiff and brittle SiOC with low content of free carbon (~6 wt-%) and a Young's modulus of 85-96 GPa, whereas polyorganosiloxane *RD-684a* converts into a carbon-rich (> 40 wt-% free carbon) and consequently softer SiOC with a lower value of the Young's modus of 66 GPa [142, 227].

TEM micrographs of both samples reveal the presence of spherical crystalline Sn inclusions within the amorphous SiOC host. In the case of $SiOC_{MK}$/Sn (Figure 15) a large number of highly homogeneous dispersed, ultrafine Sn grains with sizes below 10 nm and a few ones with larger size that tend to agglomerate are found. For $SiOC_{RD}$/Sn (Figure 16), Sn grains with an average diameter of 45 nm are analyzed, likewise homogeneously distributed throughout the matrix. In addition few ones with lager diameter are present as well. For both composites, the EDS inset in the high resolution image outlines the amorphous matrix as composed of Si, O and C. The Cu-signal relates to the support grid. The absence of Sn intensity is explained by a too low electron acceleration voltage to stimulate the emission of X-rays from Sn atoms.

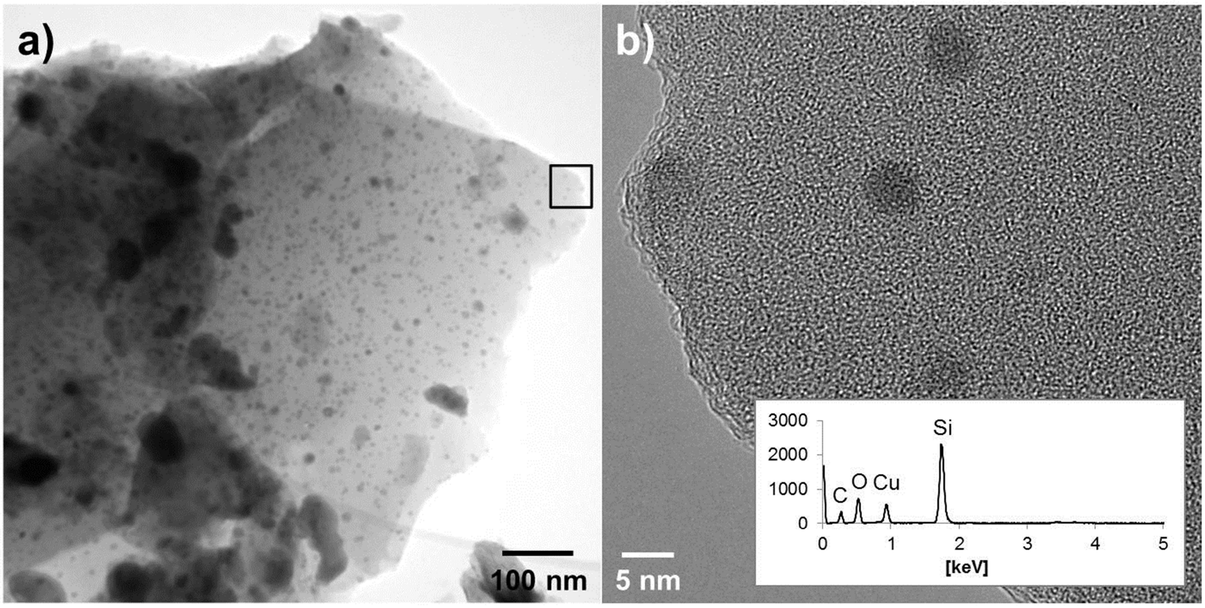

Figure 15 a) TEM micrograph of $SiOC_{MK}$/Sn and b) high-resolution image with EDS pattern of the amorphous SiOC matrix phase (insertion in a)).

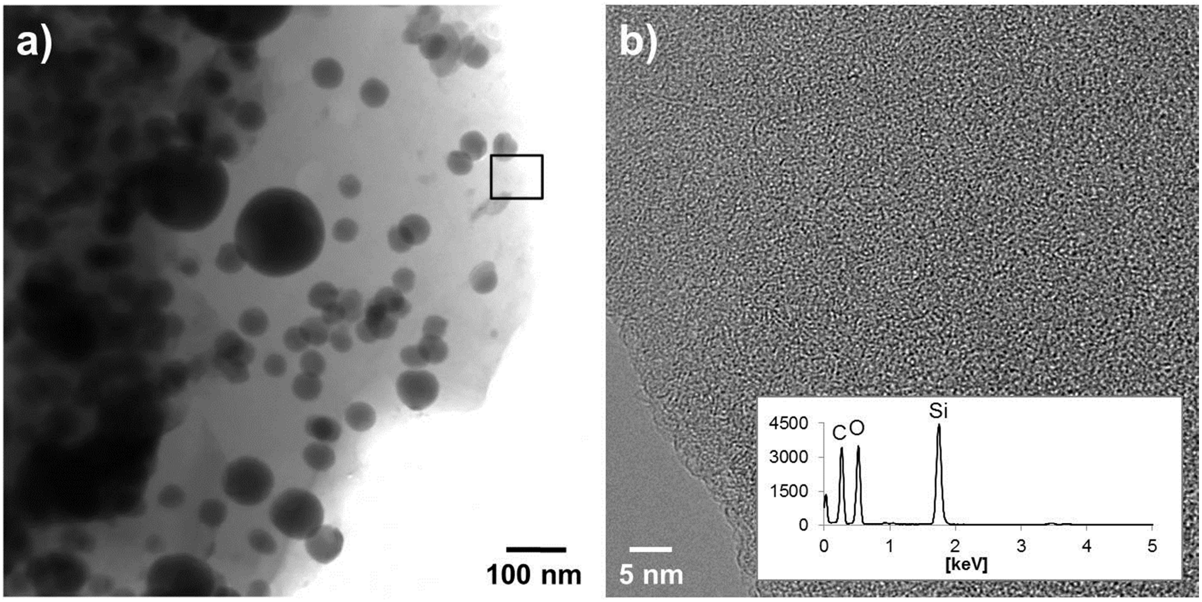

Figure 16 a) TEM micrograph of $SiOC_{RD}$/Sn and b) high-resolution image with EDS pattern of the amorphous SiOC matrix phase (insertion in a)).

In both cases the thermal conversion of the Sn-organic modified polymers leads to the formation of metallic Sn precipitates. This poses the question, why the nonvalent state is thermodynamically favored over the precipitation of Sn-oxide, -silicide or -carbide species. In order to answer this question, a comprehensive study about the underling thermodynamic principles that govern the conversion of organometallic-modified polysiloxane was addressed, employing *PMS MK* polymer. The study revealed that in the lower temperature regime of pyrolysis the formation of metal-oxide intermediates is energetically favored and generally expectable. Upon reaching a final pyrolysis temperature of 1100 - 1300 °C, a reduction of the metal-oxides to the nonvalent state by free carbon present in the SiOC matrix is possible, if thermodynamically preferential; likewise a further reaction to metal-silicide or metal-carbide species. A thermodynamic assessment in order to predict the phase composition of metal-modified silicon oxycarbide was developed on the basis of change in Gibb's free energy calculations and illustrated by Ellingham diagrams. The correspondent plots for the system Sn/SnO and Si/SiO_2 with respect to C/CO are shown in Figure 17 (data taken from [228]). Particularly in the case of Sn-organics, the precipitation of Sn-metal is favored, since the Sn/SnO phase equilibrium lies above the C/CO tie-line for temperatures exceeding 600 °C. For silicon-organic modified SiOC the formation of SiO_2 would be energetically favored, since the Si/SiO_2 equilibrium is continuously below the C/CO equilibrium. Accordingly, an in-situ precipitation of nonvalent silicon from silicon-organic modified polysiloxane cannot be expected in analogy to SiOC/Sn.

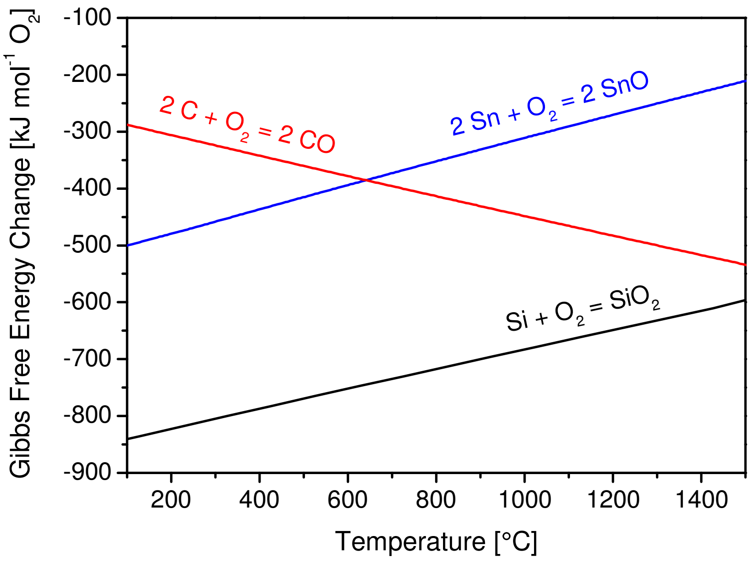

Figure 17 Ellingham diagram showing the Gibbs free energy change of Si/SiO_2 and Sn/SnO with respect to the system C/CO. SnO, with Gibbs free energy located above the C/CO line will get reduced by carbon upon CO gas release, whereas SiO_2 located below the C/CO line will be stable against its reduction (data taken from [228]).

The electrochemical activity of the prepared SiOC/Sn composites was traced by differential capacity plots, shown in Figure 18. For both samples, the cathodic branches of cycle two and five demonstrate strong and characteristic signals for different Li-Sn alloying stages: For $SiOC_{MK}$/Sn at 0.64 V (LiSn) and 0.38 V ($Li_{22}Sn_5$) and for $SiOC_{RD}$/Sn at 0.66 V (LiSn) and 0.42 V (Li_7Sn_2) [32]. For $SiOC_{MK}$/Sn the highest alloy stoichiometry $Li_{22}Sn_5$ is reached, whereas for $SiOC_{RD}$/Sn alloying stops with Li_7Sn_2 phase. In the anodic branches, several signals for Li-Sn dealloying appear, which indicate that dealloying occurs via multifold reactions and cannot simply be considered as the reverse reaction-path of the observed alloying process [32].

The suppression of $Li_{22}Sn_5$ phase in the case of $SiOC_{RD}$/Sn relies on the restriction of the alloy expansion in the embedding matrix. The volume increase for Li_7Sn_2 only amounts 75 %, as compared to $Li_{22}Sn_5$ resulting in less mechanical stress transference to the matrix. This lower load can be well accommodated by the carbon-rich and soft $SiOC_{RD}$ without degradation. The stiff and brittle $SiOC_{MK}$ on the contrary, is not able to withstand the alloy expansion and contraction and thus ruptures and pulverizes during cycling. Due to the available unlimited free volume for alloy expansion, the highest known Li-Sn stoichiometry $Li_{22}Sn_5$ can form.

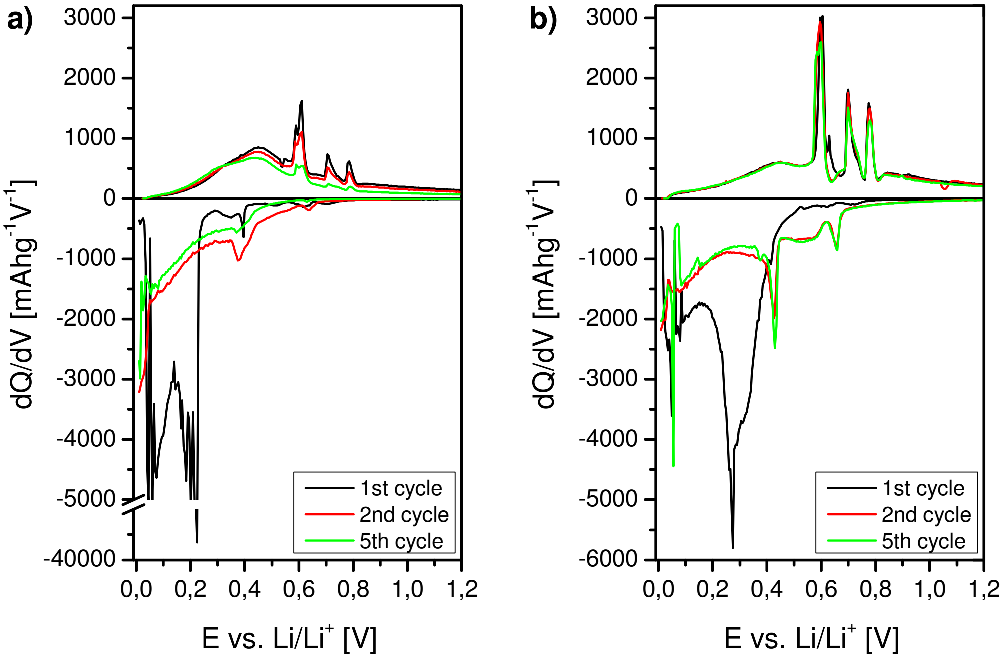

Figure 18 Differential capacity plot for a) $SiOC_{MK}/Sn$ and b) $SiOC_{RD}/Sn$, cycles 1, 2 and 5 are shown.

Figure 19 compares the galvanostatic cycling performance of both composites at different current rates and illustrates their cycling stability. For $SiOC_{MK}/Sn$, the initial lithiation amounts 1190 mAhg^{-1}, while 566 mAhg^{-1} are recovered in the first extraction, with a coulombic efficiency of 48 %. Upon continuous cycling, $SiOC_{MK}/Sn$ demonstrates significant capacity fading and at a current of 744 mAg^{-1} almost no electrochemical activity is found. The coulombic efficiency within the first 5 cycles does not exceed 90 %, revealing large irreversible losses by two interplaying processes. First, the permanent solid electrolyte interface formation, since new surface is steadily created when electrode particles crack and pulverize and second the irreversible Li-ion trapping within once broken and electrically insulated electrode pieces. For $SiOC_{RD}/Sn$ on the contrary, the initial Li-ion uptake is slightly lower with 1022 mAhg^{-1}, but 651 mAhg^{-1} are recovered reversibly. The first cycle efficiency amounts 64 %. Upon continuous cycling at different current rates, the registered capacity remains stable and even at a high current of 744 mAg^{-1} an average reversible capacity of 133 mAhg^{-1} is traced.

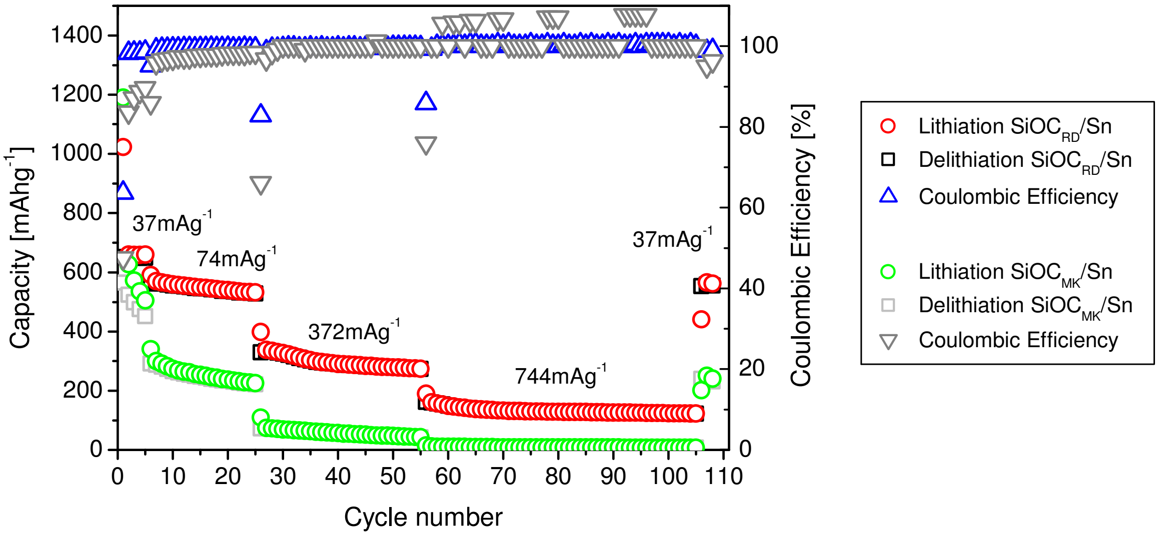

Figure 19 Comparison of the capacity performance and coulombic efficiency of $SiOC_{RD}$/Sn and $SiOC_{MK}$/Sn at different current rates.

The superior cycling stability of $SiOC_{RD}$/Sn relies on the beneficial properties of the $SiOC_{RD}$ matrix host. To recall, $SiOC_{RD}$ represents a soft (E= 66 GPa), electrochemically active ceramic with an intrinsically high content of free carbon (> 40 wt-%). Scarmi et al. reported the model structures of carbon-poor and carbon-rich amorphous ceramics [229]. According to their model, carbon-rich SiOC consists of a cellular network of graphene sheets of sp^2 carbon, where nano-domains of silica are sequestered within cells created by the graphene sheets. Carbon-poor SiOC on the contrary, is represented by nano-domains of sp^2 carbon, discontinuously dispersed in silica. Accordingly, in the former one, the graphene-like network can accommodate the volume change of the Sn nanoparticles upon Li-alloying/dealloying, as it can elastically deform. Consequently, the volume expansion of Sn does not lead to matrix rupture for the $SiOC_{RD}$/Sn composite. In the case of low-carbon $SiOC_{MK}$/Sn this is not the case. The induced stresses upon Sn-Li alloy expansion exceed the critical fracture strength of the matrix material, which irreversibly cracks and ruptures, with the result of decreasing capacity retention. A similar matrix failure, causing poor cycling stability was identified for the SiOC/nSi_c composite, discussed in Chapter 3.2.

3.3.2. Statement of personal contribution

[5] E. Ionescu, C. Terzioglu, C. Linck, J. Kaspar, A. Navrotsky and R. Riedel, Thermodynamic control of phase composition and crystallization of metal-modified silicon oxycarbides, *Journal of the American Ceramic Society*, 96 **(2013)** 1899-1903

The experimental work of this study was performed by various persons working under the supervision of Dr. Emanuel Ionescu. My particular contribution is related to the data interpretation and discussion of the Sn, Fe and Mn modified samples. The manuscript was written by Dr. Emanuel Ionescu and revised and approved of by Dipl.-Ing. Christoph Linck, by myself, by Prof. Alexandra Navrotsky and by Prof. Ralf Riedel.

[7] J. Kaspar, C. Terzioglu, E. Ionescu, M. Graczyk-Zajac, S. Hapis, H.-J. Kleebe and R. Riedel, Stable SiOC/Sn Nanocomposite Anodes for Lithium-Ion Batteries with Outstanding Cycling Stability, *Advanced Functional Materials,* 24 **(2014)** 4097-4104

The idea behind this work was developed by myself as a result of various scientific discussions with my former colleague Dr. Benjamin Papendorf. The experimental proceeding of the study was developed with Dr. Emanuel Ionescu and Dr. Magdalena Graczyk-Zajac. The experimental work related to the composite synthesis and electrode preparation was carried out by M.Sc. Caglar Terzioglu, who worked as a master student under Dr. Emanuel Ionescu's and my supervision. Concerning the material characterization, FTIR was accomplished by M.Sc. Caglar Terzioglu, XRD performed by Dipl.-Ing. Christoph Linck and TEM imaging conducted by M.Sc. Stefania Hapis (AK Prof. Kleebe). SEM imaging was performed by myself, as well as the elemental analysis of all samples, except for the Sn content, which was analyzed at "Mikroanalytisches Labor Pascher". The presented electrochemical experiments were performed and evaluated by myself. The manuscript was written by myself and revised and approved of by Dr. Emanuel Ionescu, Dr. Magdalena Graczyk-Zajac, Prof. Hans-Joachim Kleebe and Prof. Ralf Riedel.

4. Summary

Within the scope of this thesis, carbon-rich silicon oxycarbide ceramics derived from polyorganosiloxane and silicon oxycarbide/element (SiOC/X, X=Si, Sn) nano-composites were studied as potential anode material for Li-ion battery application. Chemical, structural, electrochemical and electroanalytical characterization methods were applied in order to investigate the prepared compounds.

The first part of the work was devoted to carbon-rich SiOC derived from commercially available polyorganosiloxane *RD-684a*. The used polymer exhibits a high amount of carbon within its molecular structure and consequently provides an exceptionally high amount of free carbon (> 40 wt-%) within the ceramic after thermal conversion. A strong correlation between the electrochemical characteristics and microstructural properties of the Si-O-C network and free carbon phase were detected for samples pyrolyzed between 900 - 2000 °C. The Si-O-C network phase decomposed with increasing T_{pyr} by carbothermal reaction, with the result of silicon-carbide crystallization, loss of oxygen and SiC domain growth. In addition, the organization of the free carbon steadily increased towards higher ordered structures with partial graphitization at 2000 °C. Both findings were identified as the reason for strongly diminishing capacities with increasing T_{pyr}, rationalized by *i)* the loss of the stabilizing function of the Si-O-C network towards the segregated carbon and *ii)* the fact that higher ordered carbons can naturally host less Li-ions than orderless configurations. Among the sample series, the pyrolysis temperatures of 1000 °C and 1100 °C were identified as preferential, since both silicon oxycarbides demonstrated high reversible capacities of 615 and 521 $mAhg^{-1}$ in combination with good rate capability and cycling stability. The results from this study were presented to the scientific community in publication [1] and [2].

In a next step the amount of free carbon within the SiOC microstructure was attempted to increase, based on the assumption that a further enhancement would likewise increase the Li-ion storage capacity. The results of this study demonstrated that such enhancement only initially enhances the charge storage capacity, but significantly reduces the compounds cycling stability. The introduction of additional carbon was considered to hinder the formation of the continuous amorphous Si-O-C network, accompanied by the loss of its stabilizing function towards the segregated carbon. The results of this study were reported within publication [3].

In the following, the Li-ion diffusion within SiOC pyrolyzed at 1100 °C was analyzed by three independent electroanalytical methods, namely PITT, GITT and EIS. All three techniques revealed D_{Li^+} in the order of magnitude 10^{-9} - 10^{-11} cm^2 s^{-1}, in a similar range reported for disordered carbons (10^{-10} - 10^{-11} cm^2 s^{-1}) and in average faster than for graphite (10^{-9} - 10^{-13} cm^2 s^{-1}). Interestingly, the analyzed diffusion coefficient was found less potential dependent, when comparing to disordered carbon and graphite, rationalized by: *i)* the characteristic properties of the segregated carbon phase, with flake-sizes of ~50 Å and *ii)* the beneficial bi-phasic network-structure of carbon-rich SiOC that offers an enhanced amount of voids and defect sites within the transition regime of the Si-O-C network and free carbon phase, supporting a steady and potential independent Li-ion transport into the bulk of SiOC grains. The findings from this study gave rise to publication [4].

The second part of the thesis was concerned with the study of silicon oxycarbide/element (SiOC/X, X=Si, Sn) nano-composites. SiOC/nSi samples were synthesized in the weight-ratio 80:20 via ex-situ mixing of polyorganosiloxane *RD-684a* and nano-silicon particles, followed by thermolysis. High gravimetric capacities of 905 $mAhg^{-1}$ and 704 $mAhg^{-1}$ were registered for nano-crystalline and nano-amorphous silicon particle embedment, respectively. However, strong capacity fading disqualified the SiOC/nSi_c composite for practical application, whereas SiOC/nSi_a showed superior electrochemical properties and a reliable cycling behavior. Fundamental microstructural differences were identified as the reason for this difference. In the case of SiOC/nSi_c, crystalline silicon grains of up to 100 nm in diameter are present within the SiOC matrix, while in the case of SiOC/nSi_a the amorphous starting particles crystallized into silicon and silicon carbide grains of ~10 nm in size. Due to the smaller size of the nSi grains, the absolute volume expansion of the formed Li-Si alloy is less significant, as in the case of the bigger grains, with the result of minor stress appliance to the SiOC matrix. In consequence critical fracture strength within the SiOC host phase and therefore mechanical degradation are avoided. In addition, the presence of a high amount of SiC phase beneficially enhances the intrinsically electrical contact within the SiOC/nSi_a composite. The results from this study are discussed within publication [6], which is presently under review.

Silicon oxycarbide/tin nano-composites (SiOC/Sn) were derived from single-source precursors, which were prior synthesized upon chemical modification of polyorganosilsesquioxane *PMS MK* and polyorganosiloxane *RD-684a* with tin(II)acetate. The advantage of the chosen processing route is reflected in a highly homogeneous and in-situ precipitation of Sn grains within the formed matrices. The electrochemical characteristics of the prepared samples was analyzed with respect to the matrix properties, i.e. *PMS MK* transforming into a carbon-poor and therefore stiff and brittle SiOC ceramic, whereas *RD-*

684a yields a carbon-rich and therefore softer host phase. Accordingly, $SiOC_{RD}/Sn$ reveals a high reversible capacity of 651 $mAhg^{-1}$ and stable cycling behavior, whereas for $SiOC_{MK}/Sn$ only 566 $mAhg^{-1}$ and a poor cycling stability are registered. In addition, different Li-Sn alloy stoichiometries could be identified in the fully lithiated state, namely Li_7Sn_2 and $Li_{22}Sn_5$ for $SiOC_{RD}/Sn$ and $SiOC_{MK}/Sn$, respectively. Carbon-rich $SiOC_{RD}$ well accommodates the transferred mechanical load upon Li-Sn alloy expansion and contraction without degradation and alloying stops with Li_7Sn_2 stoichiometry. On the contrary the stiff and brittle $SiOC_{MK}$ ruptures, since the induced stresses exceeded the critical fracture strength of the ceramic. In consequence, the alloy can expand up to $Li_{22}Sn_5$ phase. The week cycling stability of the $SiOC_{MK}/Sn$ material finally relates to matrix failure upon prolonged cycling. The findings from this study were reported to the scientific community in publication [7].

The thermodynamic principles governing the thermal conversion of tin-organically modified polysiloxanes were addressed and illuminated by a general assessment concerning the conversion of metal-organically modified polyorganosilsesquioxane *PMS MK* on the basis of change in Gibb's free energy calculations with respect to the system C/CO. The results and findings from this study were illustrated by Ellingham diagrams and presented in publication [5].

In summary for the investigated SiOC/X (X= Si, Sn) composites, the incorporation of an additional electrochemically active and alloy-forming phase within the ceramic microstructure allows for the following conclusions, hierarchically addressed by their importance: *First*, carbon-rich SiOC represents a suitable host phase for compounds that store lithium via alloying process, whereas carbon-poor SiOC is less applicable ($SiOC_{RD}/Sn$ vs. $SiOC_{MK}/Sn$). *Second*, a highly homogeneous distribution of the alloy-forming grains is of major importance, in order to minimize and prevent the mechanical degradation and failure of the SiOC matrix, due to the volume-expansion of the formed alloy ($SiOC_{RD}/Sn$ vs. SiOC/nSi_c, both reveal a comparable inclusion diameter). And *third*, a reduction of the inclusion size strongly enhances the mechanical integrity and cycle life-time of the composite, since critical stress intensities, which exceed the critical fracture strength of the SiOC matrix, are avoided and therefore prevent an irreversible damaging and failure of the matrix (SiOC/nSi_a vs. SiOC/nSi_c).

5. Outlook

Besides the excellent capacity performance and Li-ion storing kinetics of polyorganosiloxane derived carbon-rich SiOC, one serious drawback of the material is its relatively low first cycle coulombic efficiency, of about 66 %. Accordingly, future work on these PDC-systems should focus on the reduction of this first cycle irreversible capacity, which presents one major hindrance for commercial application. One possibility could be a prelithiation step or in-situ Li-doping of the material during ceramization by prior chemical modification of the polymer-precursor with Li-organic species, similar to the proceeding in the preparation of SiOC/Sn composites.

Concerning methodological aspects, in-situ Raman-spectroscopy represents an appropriate method to directly trace the Li-ion uptake within the free carbon phase in the SiOC microstructure and to additionally prove that the Li-ions are certainly stored within the segregated carbon. Moreover, the great chance of in-situ monitoring is reflected by the possibility of identifying and directly correlating characteristic Li-ion storage sites with the electrochemical cycling profile during Li-ion insertion and extraction.

Another challenging but highly interesting task is the in-situ precipitation of free silicon in addition to free carbon within the SiOC microstructure. This could be realized by either mixing of polymer-precursors with suitable reactive compounds or by chemical modification of the starting-polymer. However, the success of the latter approach appears less likely, relying on the thermodynamic principles valid during pyrolysis (c.f. Chapter 3.3.1, Figure 16). But the former one appears promising, since an internal study recently revealed that the thermolysis of mixtures of $MgSi_2$ with *PMS MK* and *RD-684a* leads to the precipitation of free silicon and MgO within the generated SiOC. Accordingly the question arises, if other metal-silicides behave in the same way. In an ideal case, the correspondingly formed metal-oxide would show electrochemical activity as well. For instance $TiSi_2$ could be a candidate, due to the high oxygen affinity of titanium in order to form TiO_2. There is already one study in the literature, in which the precipitation of traces of crystalline Si upon the calcination of mixtures of $TiSi_2$ and *PMS MK* is reported [230].

Last but not least, similar considerations might be addressed for the future preparation of Li-ion battery cathode materials by utilizing PDC-technology. Here the question arises, if Si-based polymers can be simultaneously modified with Li-organic and metal-organic species (e.g. M=Mn, Co or Fe) and thermally processed into $Li_2(M)SiO_4$ materials.

References

[1] J. Kaspar, M. Graczyk-Zajac, R. Riedel, Solid State Ionics, 225 (2012) 527-531.

[2] J. Kaspar, M. Graczyk-Zajac, R. Riedel, Journal of Power Sources, 244 (2013) 450-455.

[3] G. Liu, J. Kaspar, L.M. Reinold, M. Graczyk-Zajac, R. Riedel, Electrochimica Acta, 106 (2013) 101-108.

[4] J. Kaspar, M. Graczyk-Zajac, R. Riedel, Electrochimica Acta, 115 (2014) 665-670.

[5] E. Ionescu, C. Terzioglu, C. Linck, J. Kaspar, A. Navrotsky, R. Riedel, Journal of the American Ceramic Society, 96 (2013) 1899-1903.

[6] J. Kaspar, M. Graczyk-Zajac, S. Lauterbach, H.J. Kleebe, R. Riedel, Journal of Power Sources, 269 (2014) 164-172.

[7] J. Kaspar, C. Terzioglu, E. Ionescu, M. Graczyk-Zajac, S. Hapis, H.J. Kleebe, R. Riedel, Advanced Functional Materials, 24 (2014) 4097-4104.

[8] J.-K. Park, Principles and Applications of Lithium Secondary Batteries, Wiley-VCH, Weihnheim, 2012.

[9] T. Nagaura, M. Nagamine, I. Tanabe, N. Miyamoto, Progress in Batteries & Solar Cells, 8 (1989) 84-88.

[10] T. Nagaura, K. K. Tozawa, Progress in Batteries & Solar Cells, 9 (1990) 209-214.

[11] J.M. Tarascon, M. Armand, Nature, 414 (2001) 359-367.

[12] M. Armand, J.M. Tarascon, Nature, 451 (2008) 652-657.

[13] H. Kawamoto, Science and Technology Trends, 36 (2010) 34-34.

[14] G.L. Soloveichik, Annual Review of Chemical and Biomolecular Engineering, 2 (2011) 503-527.

[15] J. Liu, Advanced Functional Materials, 23 (2013) 924-928.

[16] B. Scrosati, J. Garche, Journal of Power Sources, 195 (2010) 2419-2430.

[17] C.M. Hayner, X. Zhao, H.H. Kung, Annual Review of Chemical and Biomolecular Engineering, 3 (2012) 445-471.

[18] J. Chen, Materials, 6 (2013) 156-183.

[19] R. Wagner, N. Preschitschek, S. Passerini, J. Leker, M. Winter, Journal of Applied Electrochemistry, 43 (2013) 481-496.

[20] J.W. Fergus, Journal of Power Sources, 195 (2010) 939-954.

[21] B. Xu, D. Qian, Z. Wang, Y.S. Meng, Material Science and Engineering: R: Reports 73 (2012) 51-65.

[22] U. Kasavajjula, C. Wang, A.J. Appleby, Journal of Power Sources, 163 (2007) 1003-1039.

[23] J.O. Besenhard, J. Yang, M. Winter, Journal of Power Sources, 68 (1997) 87-90.

[24] R.A. Huggins, Journal of Power Sources, 81-82 (1999) 13-19.

[25] P. Limthongkul, Y.-I. Jang, N.J. Dudney, Y.-M. Chiang, Journal of Power Sources, 119-121 (2003) 604-609.

[26] M.N. Obrovac, L. Christensen, D.B. Le, J.R. Dahn, Journal of the Electrochemical Society, 154 (2007) A849-A855.

[27] D. Larcher, S. Beattie, M. Morcrette, K. Edström, J.-C. Jumas, J.-M. Tarascon, Journal of Materials Chemistry, 17 (2007) 3759-3772.

[28] J. Hassoun, S. Panero, B. Scrosati, Fuel Cells, 9 (2009) 277-283.

[29] C.-M. Park, J.-H. Kim, H. Kim, H.-J. Sohn, Chemical Society Reviews, 39 (2010) 3115-3141.

[30] W.-J. Zhang, Journal of Power Sources, 196 (2011) 13-24.

[31] W.-J. Zhang, Journal of Power Sources, 196 (2011) 877-885.

[32] M. Winter, J.O. Besenhard, Electrochimica Acta, 45 (1999) 31-50.

[33] L.Y. Beaulieu, K.W. Eberman, R.L. Turner, L.J. Krause, J.R. Dahn, Electrochemical and Solid State Letters, 4 (2001) A137-A140.

[34] M.N. Obrovac, L. Christensen, Electrochemical and Solid State Letters, 7 (2004) A93-A96.

[35] J. Li, J.R. Dahn, Journal of the Electrochemical Society, 154 (2007) A156-A161.

[36] X.H. Liu, L. Zhong, S. Huang, S.X. Mao, T. Zhu, J.Y. Huang, ACS Nano, 6 (2012) 1522-1531.

[37] Y.F. Gao, M. Zhou, Journal of Power Sources, 230 (2013) 176-193.

[38] Z. Ma, T. Li, Y.L. Huang, J. Liu, Y. Zhou, D. Xue, RSC Advances, 3 (2013) 7398-7402.

[39] M. Wachtler, J.O. Besenhard, M. Winter, Journal of Power Sources, 94 (2001) 189-193.

[40] A.D.W. Todd, P.P. Ferguson, M.D. Fleischauer, J.R. Dahn, International Journal of Energy Research, 34 (2010) 535-555.

[41] F.M. Courtel, Y. Abu-Lebdeh, Tin-Based Anode Materials for Lithium-Ion Batteries, in: Nanotechnology for Lithium-Ion Batteries, Springer, 2013, pp. 67-83.

[42] H. Jung, M. Park, Y.-G. Yoon, G.-B. Kim, S.-K. Joo, Journal of Power Sources, 115 (2003) 346-351.

[43] P. Limthongkul, Y.-I. Jang, N.J. Dudney, Y.-M. Chiang, Acta Materialia, 51 (2003) 1103-1113.

[44] A. Netz, R.A. Huggins, Solid State Ionics, 175 (2004) 215-219.

[45] T.D. Hatchard, J.R. Dahn, Journal of the Electrochemical Society, 151 (2004) A838-A842.

[46] W.-R. Liu, Z.-Z. Guo, W.-S. Young, D.-T. Shieh, H.-C. Wu, M.-H. Yang, N.-L. Wu, Journal of Power Sources, 140 (2005) 139-144.

[47] M.N. Obrovac, L.J. Krause, Journal of the Electrochemical Society, 154 (2007) A103-A108.

[48] S.D. Beattie, D. Larcher, M. Morcrette, B. Simon, J.M. Tarascon, Journal of the Electrochemical Society, 155 (2008) A158-A163.

[49] N. Ding, J. Xu, Y.X. Yao, G. Wegner, X. Fang, C.H. Chen, I. Lieberwirth, Solid State Ionics, 180 (2009) 222-225.

[50] B. Key, R. Bhattacharyya, M. Morcrette, V. Seznec, J.M. Tarascon, C.P. Grey, Journal of the American Chemical Society, 131 (2009) 9239-9249.

[51] V.L. Chevrier, J.R. Dahn, Journal of the Electrochemical Society, 156 (2009) A454-A458.

[52] V.L. Chevrier, J.W. Zwanziger, J.R. Dahn, Canadian Journal of Physics, 87(6) (2009) 625-632.

[53] B. Key, M. Morcrette, J.-M. Tarascon, C.P. Grey, Journal of the American Chemical Society, 133 (2010) 503-512.

[54] Y. Oumellal, N. Delpuech, D. Mazouzi, N. Dupre, J. Gaubicher, P. Moreau, P. Soudan, B. Lestriez, D. Guyomard, Journal of Materials Chemistry, 21 (2011) 6201-6208.

[55] J.-H. Trill, C. Tao, M. Winter, S. Passerini, H. Eckert, Journal of Solid State Electrochemistry, 15 (2011) 349-356.

[56] S.S. Suh, W.Y. Yoon, C.G. Lee, S.U. Kwon, J.H. Kim, Y. Matulevich, Y.U. Kim, Y. Park, C.U. Jeong, Y.Y. Chan, Journal of the Electrochemical Society, 160 (2013) A751-A755.

[57] G. Derrien, J. Hassoun, S. Panero, B. Scrosati, Advanced Materials, 19 (2007) 2336-2340.

[58] L. Bazin, S. Mitra, P.L. Taberna, P. Poizot, M. Gressier, M.J. Menu, A. Barnabe, P. Simon, J.M. Tarascon, Journal of Power Sources, 188 (2009) 578-582.

[59] J. Hassoun, K.-S. Lee, Y.-K. Sun, B. Scrosati, Journal of the American Chemical Society, 133 (2011) 3139-3143.

[60] Z. Du, S. Zhang, Y. Xing, X. Wu, Journal of Power Sources, 196 (2011) 9780-9785.

[61] J. Graetz, C.C. Ahn, R. Yazami, B. Fultz, Electrochemical and Solid State Letters, 6 (2003) A194-A197.

[62] M. Holzapfel, H. Buqa, L.J. Hardwick, M. Hahn, A. Wursig, W. Scheifele, P. Novak, R. Kotz, C. Veit, F.M. Petrat, Electrochimica Acta, 52 (2006) 973-978.

[63] D. Arquier, G. Calleja, G. Cerveau, R.J.P. Corriu, Comptes Rendus Chimie, 10 (2007) 795-802.

[64] J.R. Szczech, S. Jin, Energy & Environmental Science, 4 (2011) 56-72.

[65] C.-F. Sun, K. Karki, Z. Jia, H. Liao, Y. Zhang, T. Li, Y. Qi, J. Cumings, G.W. Rubloff, Y. Wang, ACS Nano, 7 (2013) 2717-2724.

[66] J.P. Maranchi, A.F. Hepp, P.N. Kumta, Electrochemical and Solid State Letters, 6 (2003) A198-A201.

[67] V. Baranchugov, E. Markevich, E. Pollak, G. Salitra, D. Aurbach, Electrochemistry Communications, 9 (2007) 796-800.

[68] C.K. Chan, H. Peng, G. Liu, K. McIlwrath, X.F. Zhang, R.A. Huggins, Y. Cui, Nature Nanotechnology, 3 (2008) 31-35.

[69] C.K. Chan, R. Ruffo, S.S. Hong, R.A. Huggins, Y. Cui, Journal of Power Sources, 189 (2009) 34-39.

[70] L.-F. Cui, R. Ruffo, C.K. Chan, H. Peng, Y. Cui, Nano Letters, 9 (2009) 491-495.

[71] Y.F. Gao, M. Zhou, Journal of Applied Physics, 109 (2011) 014310.

[72] A. Vlad, A.L.M. Reddy, A. Ajayan, N. Singh, J.-F. Gohy, S. Melinte, P.M. Ajayan, Proceedings of the National Academy of Sciences, 109 (2012) 15168-15173.

[73] M. Ge, J. Rong, X. Fang, C. Zhou, Nano Letters, 12 (2012) 2318-2323.

[74] X.H. Liu, F. Fan, H. Yang, S. Zhang, J.Y. Huang, T. Zhu, ACS Nano, 7 (2013) 1495-1503.

[75] Y. Fan, Q. Zhang, Q. Xiao, X. Wang, K. Huang, Carbon, 59 (2013) 264-269.

[76] Z. Wen, G. Lu, S. Mao, H. Kim, S. Cui, K. Yu, X. Huang, P.T. Hurley, O. Mao, J. Chen, Electrochemistry Communications, 29 (2013) 37-70.

[77] L. Chen, X. Xie, J. Xie, K. Wang, J. Yang, Journal of Applied Electrochemistry, 36 (2006) 1099-1104.

[78] J. Li, R.B. Lewis, J.R. Dahn, Electrochemical and Solid State Letters, 10 (2007) A17-A20.

[79] N.S. Hochgatterer, M.R. Schweiger, S. Koller, P.R. Raimann, T. Wohrle, C. Wurm, M. Winter, Electrochemical and Solid State Letters, 11 (2008) A76-A80.

[80] D. Mazouzi, B. Lestriez, L. Roue, D. Guyomard, Electrochemical and Solid State Letters, 12 (2009) A215-A218.

[81] J.S. Bridel, T. Azais, M. Morcrette, J.M. Tarascon, D. Larcher, Chemistry of Materials, 22 (2010) 1229-1241.

[82] I. Kovalenko, B. Zdyrko, A. Magasinski, B. Hertzberg, Z. Milicev, R. Burtovyy, I. Luzinov, G. Yushin, Science, 334 (2011) 75-79.

[83] J.S. Kim, W. Choi, K.Y. Cho, D. Byun, J. Lim, J.K. Lee, Journal of Power Sources, 244 (2013) 521-526.

[84] N. Dimov, S. Kugino, M. Yoshio, Journal of Power Sources, 136 (2004) 108-114.

[85] Y. Liu, K. Hanai, J. Yang, N. Imanishi, A. Hirano, Y. Takeda, Solid State Ionics, 168 (2004) 61-68.

[86] M. Holzapfel, H. Buqua, W. Scheifele, P. Novak, F.M. Petrat, Chemical Communications, 12 (2005) 1566-1568.

[87] S.H. Ng, J.Z. Wang, D. Wexler, K. Konstantinov, Z.P. Guo, H.K. Liu, Angewandte Chemie International Edition, 45 (2006) 6896-6899.

[88] X.L. Yang, Z.Y. Wen, X.X. Xu, B. Lin, Z.X. Lin, Journal of the Electrochemical Society, 153 (2006) A1341-A1344.

[89] J. Saint, M. Morcrette, D. Larcher, L. Laffont, S. Beattie, J.P. Peres, D. Talaga, M. Couzi, J.M. Tarascon, Advanced Functional Materials, 17 (2007) 1765-1774.

[90] M. Alias, O. Crosnier, I. Sandu, G. Jestin, A. Papadimopoulos, F. Le Cras, D.M. Schleich, T. Brousse, Journal of Power Sources, 174 (2007) 900-904.

[91] R. Demir Cakan, M.-M. Titirici, M. Antonietti, G. Cui, J. Maier, Y.-S. Hu, Chemical Communications, 37 (2008) 3759-3761.

[92] C. Martin, M. Alias, F. Christien, O. Crosnier, D. Belanger, T. Brousse, Advanced Materials, 21 (2009) 4735-4741.

[93] Z. Luo, D. Fan, X. Liu, H. Mao, C. Yao, Z. Deng, Journal of Power Sources, 189 (2009) 16-21.

[94] Y.N. Jo, Y. Kim, J.S. Kim, J.H. Song, K.J. Kim, C.Y. Kwag, D.J. Lee, C.W. Park, Y.J. Kim, Journal of Power Sources, 195 (2010) 6031-6036.

[95] H. Xiang, K. Zhang, G. Ji, J.Y. Lee, C. Zou, X. Chen, J. Wu, Carbon, 49 (2011) 1787-1796.

[96] R. Yi, F. Dai, M.L. Gordin, S. Chen, D. Wang, Advanced Energy Materials, 3 (2013) 295-300.

[97] R. Yi, F. Dai, M.L. Gordin, H. Sohn, D. Wang, Advanced Energy Materials, 11 (2013) 1507-1515.

[98] F.W. Ainger, J.M. Herbert, Special Ceramics, (1960) 168-168.

[99] P.G. Chantrell, P. Popper, Special Ceramics, (1965) 67-67.

[100] W. Verbeek, 1973, Ger. Pat. No. 2218960, U.S. Pat. No. 3853567

[101] W. Verbeek, G. Winter, 1974, Ger. Pat. No. 2236078

[102] G. Winter, W. Verbeek, M. Mansmann, 1974, Ger. Pat. No. 2243527

[103] S. Yajima, J. Hayashi, M. Omori, Chemistry Letters, 4 (1975) 931-934.

[104] S. Yajima, J. Hayashi, M. Omori, K. Okamura, Nature, 261 (1976) 683-685.

[105] S. Yajima, K. Okamura, J. Hayashi, M. Omori, Journal of the American Ceramic Society, 59 (1976) 324-327.

[106] R. West, L.D. David, P.I. Djurovich, Y.U. Hyuk, R. Sinclair, American Ceramic Society Bulletin, 62 (1983) 899-903.

[107] D. Seyferth, G.H. Wiseman, C. Prud'homme, Journal of the American Ceramic Society, 66 (1983) C13-C13.

[108] K.J. Wynne, R.W. Rice, Annual Review of Materials Science, 14 (1984) 297-334.

[109] G. Pouskouleli, Ceramics International, 15 (1989) 213-229.

[110] M. Peuckert, T. Vaahs, M. Brück, Advanced Materials, 2 (1990) 398-404.

[111] S. Dire, F. Babonneau, C. Sanchez, J. Livage, Journal of Materials Chemistry, 2 (1992) 239-244.

[112] G.D. Soraru, M. Mercadini, R.D. Maschio, F. Taulelle, F. Babonneau, Journal of the American Ceramic Society, 76 (1993) 2595-2600.

[113] A.M. Wootton, M. Rappensberger, M.H. Lewis, S. Kitchin, A.P. Howes, R. Dupree, Journal of Non-Crystalline Solids, 204 (1996) 217-227.

[114] R. Riedel, A. Kienzle, W. Dressler, L. Ruwisch, J. Bill, F. Adlinger, Nature, 382 (1996) 796-796.

[115] R. Riedel, L.M. Ruswisch, L. An, R. Raj, Journal of the American Ceramic Society, 81 (1998) 3341-3344.

[116] S. Dire, R. Ceccato, S. Gialanella, F. Babonneau, Journal of the European Ceramic Society, 19 (1999) 2849-2858.

[117] Z.-C. Wang, F. Aldinger, R. Riedel, Journal of the American Ceramic Society, 84 (2001) 2179-2183.

[118] A. Zimmermann, A. Bauer, M. Christ, Y. Cai, F. Aldinger, Acta Materialia, 50 (2002) 1187-1196.

[119] F. Hönack, R. Riedel, Advanced Engineering Materials, 5 (2003) 122-125.

[120] R. Harshe, C. Balan, R. Riedel, Journal of the European Ceramic Society, 24 (2004) 3471-3482.

[121] S. Bernard, K. Ayadi, M.-P. Berthet, F. Chassagneux, D. Cornu, J.-M. Letoffe, P. Miele, Journal of Solid State Chemistry, 177 (2004) 1803-1810.

[122] M.A. Schiavon, C. Gervais, F. Babonneau, G.D. Soraru, Journal of the American Ceramic Society, 87 (2004) 203-208.

[123] S. Bernard, M. Weinmann, P. Gerstel, P. Miele, F. Aldinger, Journal of Materials Chemistry, 15 (2005) 289-299.

[124] E. Ionescu, B. Papendorf, H.-J. Kleebe, F. Poli, K. Müller, R. Riedel, Journal of the American Chemical Society, 93 (2010) 1774-1782.

[125] E. Ionescu, B. Papendorf, H.-J. Kleebe, R. Riedel, Journal of the American Chemical Society, 93 (2010) 1783-1789.

[126] E. Ionescu, C. Linck, C. Fasel, M. Müller, H.-J. Kleebe, R. Riedel, Journal of the American Ceramic Society, 93 (2010) 241-250.

[127] B. Papendorf, K. Nonnenmacher, E. Ionescu, H.-J. Kleebe, R. Riedel, Small, 7 (2011) 970-978.

[128] E. Ionescu, B. Papendorf, H.-J. Kleebe, H. Breitzke, K. Nonnenmacher, G. Buntkowsky, R. Riedel, Journal of the European Ceramic Society, 32 (2012) 1873-1881.

[129] R. Riedel, G. Mera, R. Hauser, A. Klonczynski, Journal of the Ceramic Society of Japan, 114 (2006) 425-444.

[130] P. Colombo, R. Riedel, G.D. Soraràu, H.J. Kleebe, Polymer Derived Ceramics: From Nano-Structure to Applications, DEStech Publications Inc., Lancaster (PA), USA, 2010.

[131] P. Colombo, G. Mera, R. Riedel, G.D. Soraru, Journal of the American Ceramic Society, 93 (2010) 1805-1837.

[132] E. Ionescu, H.-J. Kleebe, R. Riedel, Chemical Society Reviews, 41 (2012) 5032-5052.

[133] G. Mera, A. Navrotsky, S. Sen, H.-J. Kleebe, R. Riedel, Journal of Material Chemistry A, 1 (2013) 3826-3836.

[134] H. Zhang, C.G. Pantano, Journal of the American Ceramic Society, 73 (1990) 958-963.

[135] C.G. Pantano, A.K. Singh, H. Zhang, Journal of Sol-Gel Science and Technology, 14 (1999) 7-25.

[136] Y.D. Blum, D.B. MacQueen, H.-J. Kleebe, Journal of the European Ceramic Society, 25 (2005) 143-149.

[137] H.-J. Kleebe, G. Gregori, Y.D. Blum, F. Babonneau, International Journal of Materials Research, 97 (2006) 699-709.

[138] G. Gregori, H.-J. Kleebe, Y.D. Blum, F. Babonneau, International Journal of Materials Research, 97 (2006) 710-720.

[139] S.J. Widgeon, S. Sen, G. Mera, E. Ionescu, R. Riedel, A. Navrotsky, Chemistry of Materials, 22 (2010) 6221-6228.

[140] J. Cordelair, P. Greil, Journal of the European Ceramic Society, 20 (2000) 1947-1957.

[141] H.-J. Kleebe, Y.D. Blum, Journal of the European Ceramic Society, 28 (2008) 1037-1042.

[142] S. Martínez-Crespiera, E. Ionescu, H.-J. Kleebe, R. Riedel, Journal of the European Ceramic Society, 31 (2011) 913-919.

[143] R.M. Morcos, A. Navrotsky, T. Varga, Y. Blum, D. Ahn, F. Poli, K. Müller, R. Raj, Journal of the American Ceramic Society, 91 (2008) 2969-2974.

[144] F. Babonneau, K. Thorne, J.D. Mackenzie, Chemistry of Materials, 1 (1989) 554-558.

[145] J. Livage, F. Babonneau, C. Sanchez, Some Aspects of the Chemistry of Transition Metal Oxide Gels, in: J. Harrod, R. Laine (Eds.) Inorganic and Organometallic Oligomers and Polymers, Springer Netherlands, 1991, pp. 217-228.

[146] G.M. Renlund, S. Prochazka, R.H. Doremus, Journal of Materials Research, 6 (1991) 2723-2734.

[147] G.M. Renlund, S. Prochazka, R.H. Doremus, Journal of Materials Research, 6 (1991) 2716-2722.

[148] F. Babonneau, L. Bois, J. Livage, Journal of Non-Crystalline Solids, 147 (1992) 280-284.

[149] F. Babonneau, L. Bois, C.Y. Yang, L.V. Interrante, Chemistry of Materials, 6 (1994) 51-57.

[150] L. Bois, J. Maquet, F. Babonneau, H. Mutin, D. Bahloul, Chemistry of Materials, 6 (1994) 796-802.

[151] L. Bois, J. Maquet, F. Babonneau, D. Bahloul, Chemistry of Materials, 7 (1995) 975-981.

[152] R.J.P. Corriu, D. Leclercq, P.H. Mutin, A. Vioux, Journal of Materials Science, 30 (1995) 2313-2318.

[153] F. Babonneau, G.D. Soraru, G. D'Andrea, S. Dire, L. Bois, Materials Research Society Symposium Proceedings, 271 (1992) 789-794.

[154] G.D. Soraru, Journal of Sol-Gel Science and Technology, 2 (1994) 843-848.

[155] G.D. Soraru, G. D'Andrea, R. Campostrini, F. Babonneau, G. Mariotto, Journal of the American Ceramic Society, 78 (1995) 379-387.

[156] G.D. Soraru, E. Dallapiccola, G. D'Andrea, Journal of the American Ceramic Society, 79 (1996) 2074-2080.

[157] G.D. Soraru, R. Campostrini, S. Maurina, F. Babonneau, Journal of the American Ceramic Society, 80 (1997) 999-1004.

[158] G.D. Soraru, D. Suttor, Journal of Sol-Gel Science and Technology, 14 (1999) 69-74.

[159] T. Rouxel, G. Massouras, G.-D. SorarÃ¹, Journal of Sol-Gel Science and Technology, 14 (1999) 87-94.

[160] T. Rouxel, J.-C. Sanglebf, J.-P. Guin, V. Keryvin, G.-D. Soraru, Journal of the American Ceramic Society, 84 (2001) 2220-2224.

[161] C. Turquat, H.-J. Kleebe, G. Gregori, S. Walter, G.D. Soraru, Journal of the American Ceramic Society, 84 (2001) 2189-2196.

[162] H.-J. Kleebe, C. Turquat, G.D. Soraru, Journal of the American Ceramic Society, 84 (2001) 1073-1080.

[163] G.D. Soraru, S. Modena, E. Guadagnino, P. Colombo, J. Egan, C. Pantano, Journal of the American Ceramic Society, 85 (2002) 1529-1536.

[164] G.D. Soraru, L. Pederiva, J. Latournerie, R. Raj, Journal of the American Chemical Society, 85 (2002) 2181-2187.

[165] G. Trimmel, R. Badheka, F. Babonneau, J. Latournerie, P. Dempsey, D. Bahloul-Houlier, J. Parmentier, G.D. Soraru, Journal of Sol-Gel Science and Technology, 26 (2003) 279-283.

[166] H. Brequel, J. Parmentier, S. Walter, R. Badheka, G. Trimmel, S. Masse, J. Latournerie, P. Dempsey, C. Turquat, A. Desmartin-Chomel, L. Le Neindre-Prum, U.A. Jayasooriya, D. Hourlier, H.J. Kleebe, G.D. Soraru, S. Enzo, F. Babonneau, Chemistry of Materials, 16 (2004) 2585-2598.

[167] A.M. Wilson, J.N. Reimers, E.W. Fuller, J.R. Dahn, Solid State Ionics, 74 (1994) 249-254.

[168] W. Xing, A.M. Wilson, G. Zank, J.R. Dahn, Solid State Ionics, 93 (1997) 239-244.

[169] W. Xing, A.M. Wilson, K. Eguchi, G. Zank, J.R. Dahn, Journal of the Electrochemical Society, 144 (1997) 2410-2416.

[170] A.M. Wilson, G. Zank, K. Eguchi, W. Xing, B. Yates, J.R. Dahn, Chemistry of Materials, 9 (1997) 1601-1606.

[171] A.M. Wilson, G. Zank, K. Eguchi, W. Xing, J.R. Dahn, Journal of Power Sources, 68 (1997) 195-200.

[172] A.M. Wilson, W. Xing, G. Zank, B. Yates, J.R. Dahn, Solid State Ionics, 100 (1997) 259-266.

[173] H. Fukui, H. Ohsuka, T. Hino, K. Kanamura, Chemistry Letters, 38 (2009) 86-87.

[174] D. Ahn, R. Raj, Journal of Power Sources, 195 (2010) 3900-3906.

[175] H. Fukui, O. Hisashi, T. Hino, K. Kanamura, ACS Applied Materials & Interfaces, 4 (2010) 998-1008.

[176] P.E. Sanchez-Jimenez, R. Raj, Journal of the American Ceramic Society, 93 (2010) 1127-1135.

[177] J. Shen, R. Raj, Journal of Power Sources, 196 (2011) 5945-5950.

[178] H. Fukui, H. Ohsuka, T. Hino, K. Kanamura, Journal of Power Sources, 196 (2011) 371-378.

[179] H. Fukui, H. Ohsuka, T. Hino, K. Kanamura, Journal of the Electrochemical Society, 158 (2011) A550-A555.

[180] H. Fukui, N. Nakata, K. Dokko, B. Takemura, H. Ohsuka, T. Hino, K. Kanamura, ACS Applied Materials & Interfaces, 3 (2011) 2318-2322.

[181] X. Liu, M.-C. Zheng, K. Xie, Journal of Power Sources, 196 (2011) 10667-10672.

[182] D. Ahn, R. Raj, Journal of Power Sources, 196 (2011) 2179-2186.

[183] X. Liu, K. Xie, C.-m. Zheng, J. Wang, Z. Jing, Journal of Power Sources, 214 (2012) 119-123.

[184] P. Dibandjo, M. Graczyk-Zajac, R. Riedel, V.S. Pradeep, G.D. Soraru, Journal of the European Ceramic Society, 32 (2012) 2495-2503.

[185] M. Graczyk-Zajac, L. Toma, C. Fasel, R. Riedel, Solid State Ionics, 225 (2012) 522-526.

[186] R. Bhandavat, Z. Pei, G. Singh, Nanomaterials and Energy, 1 (2012) 324-337.

[187] H. Fukui, K. Eguchi, H. Ohsuka, T. Hino, K. Kanamura, Journal of Power Sources, 243 (2013) 152-158.

[188] H. Fukui, H. Ohsuka, T. Hino, K. Kanamura, Journal of the Electrochemical Society, 160 (2013) A1276-A1281.

[189] V.S. Pradeep, M. Graczyk-Zajac, M. Wilamowska, R. Riedel, G.D. Soraru, Solid State Ionics, (2013) in press, doi: 10.1016/j.ssi.2013.1008.1043.

[190] P.D. Weidman, D. Ahn, R. Raj, Journal of Power Sources, 249 (2014) 219-230.

[191] V.S. Pradeep, M. Graczyk-Zajac, R. Riedel, G.D. Soraru, Electrochimica Acta, 119 (2014) 78-85.

[192] J. Shen, D. Ahn, R. Raj, Journal of Power Sources, 196 (2011) 2875-2878.

[193] R. Bhandavat, M. Cologna, G. Singh, Nanomaterials and Energy, 1 (2012) 57-61.

[194] R. Bhandavat, G. Singh, Journal of Physical Chemistry C, 117 (2013) 11899-11905.

[195] X. Liu, K. Xie, J. Wang, C. Zheng, Y. Pan, Journal of Materials Chemistry, 22 (2012) 19621-19624.

[196] D. Ahn, in, University of Colorado Boulder, CO, 2010.

[197] P. Kroll, Journal of Materials Chemistry, 13 (2003) 1657-1668.

[198] P. Kroll, Journal of Non-Crystalline Solids, 351 (2005) 1121-1126.

[199] P. Kroll, Journal of Materials Chemistry, 20 (2010) 10528-10534.

[200] P. Kroll, MRS Proceedings, 1313 (2011).

[201] X. Liu, M.-C. Zheng, K. Xie, J. Liu, Electrochimica Acta, 59 (2012) 304-309.

[202] A. Saha, R. Raj, D.L. Williamson, Journal of the American Chemical Society, 89 (2006) 2188-2195.

[203] L.G. Cancado, K. Takai, T. Enoki, M. Endo, Y.A. Kim, H. Mizusaki, A. Jorio, L.N. Coelho, R. Magalhaes-Paniago, M.A. Pimenta, Applied Physics Letters, 88 (2006) 163106-163106.

[204] M.A. Pimenta, G. Dresselhaus, M.S. Dresselhaus, L.G. Cancado, A. Jorio, R. Saito, Physical Chemistry Chemical Physics, 9 (2007) 1276-1290.

[205] A.C. Ferrari, Solid State Communications, 143 (2007) 47-57.

[206] N. Larouche, B.L. Stansfield, Carbon, 48 (2010) 620-629.

[207] M.S. Dresselhaus, A. Jorio, R. Saito, Annual Review Condensed Matter Physics, 1 (2010) 89-108.

[208] J.R. Dahn, T. Zheng, Y. Liu, J.S. Xue, Science, 270 (1995) 590-593.

[209] T. Zheng, W.R. McKinnon, J.R. Dahn, Journal of the Electrochemical Society, 143 (1996) 2137-2145.

[210] J.S. Gnanaraj, M.D. Levi, E. Levi, G. Salitra, D. Aurbach, J.E. Fischer, A. Claye, Journal of the Electrochemical Society, 148 (2001) A525-A536.

[211] Y. Matsumura, S. Wang, J. Mondori, Carbon, 33 (1995) 1457-1462.

[212] A. Claye, J.E. Fischer, Electrochimica Acta, 45 (1999) 107-120.

[213] Y.F. Reynier, R. Yazami, B. Fultz, Journal of the Electrochemical Society, 151 (2004) A422-A426.

[214] M. Letellier, F. Chevallier, F. Béguin, E. Frackowiak, J.N. Rouzaud, Journal of Physics and Chemistry of Solids, 65 (2004) 245-251.

[215] D. Pan, S. Wang, B. Zhao, M. Wu, H. Zhang, Y. Wang, Z. Jiao, Chemistry of Materials, 21 (2009) 3136-3142.

[216] H. Azuma, H. Imoto, S.i. Yamada, K. Sekai, Journal of Power Sources, 81-82 (1999) 1-7.

[217] T. Zheng, Q. Zhong, J.R. Dahn, Journal of the Electrochemical Society, 142 (1995) L211-L214.

[218] C.J. Wen, B.A. Boukamp, R.A. Huggins, W. Weppner, Journal of the Electrochemical Society, 126 (1979) 2258-2266.

[219] A.S. Arico, P. Bruce, B. Scrosati, J.-M. Tarascon, W. van Schalkwijk, Nature Materials 4(2005) 366-377.

[220] P.G. Bruce, B. Scrosati, J.-M. Tarascon, Angewandte Chemie International Edition, 47 (2008) 2930-2946.

[221] M. Graczyk-Zajac, C. Fasel, R. Riedel, Journal of Power Sources, 196 (2011) 6412-6418.

[222] M. Wilamowska, M. Graczyk-Zajac, R. Riedel, Journal of Power Sources, 244 (2013) 80-86.

[223] D. Aurbach, J.S. Gnanaraj, M.D. Levi, E.A. Levi, J.E. Fischer, A. Claye, Journal of Power Sources, 97-98 (2001) 92-96.

[224] M.D. Levi, D. Aurbach, The Journal of Physical Chemistry B, 101 (1997) 4641-4647.

[225] E. Markevich, M.D. Levi, D. Aurbach, Journal of Electroanalytical Chemistry, 580 (2005) 231-237.

[226] C. Haluschka, C. Engel, R. Riedel, Journal of the European Ceramic Society, 20 (2000) 1365-1374.

[227] C. Moysan, R. Riedel, R. Harshe, T. Rouxel, F. Augereau, Journal of the European Ceramic Society, 27 (2007) 397-403.

[228] M.W. Chase, NIST-JANAF Thermochemical Tables, American Chemical Society, 1998.

[229] A. Scarmi, G.D. Soraru, R. Raj, Journal of Non-Crystalline Solids, 351 (2005) 2238-2243.

[230] J.D. Torrey, R.K. Bordia, Journal of Materials Research, 22 (2007) 1959-1966.

Publications

[1] J. Kaspar, M. Graczyk-Zajac and R. Riedel, Carbon-rich SiOC anodes for lithium-ion batteries: Part II. Role of thermal cross-linking, *Solid State Ionics*, 225 **(2012)** 527-531

[2] J. Kaspar, M. Graczyk-Zajac and R. Riedel, Lithium insertion into carbon-rich SiOC ceramics: Influence of pyrolysis temperature on electrochemical properties, *Journal of Power Sources*, 244 **(2013)** 450-455

[3] G. Liu, J. Kaspar, L.M. Reinold, M. Graczyk-Zajac and R. Riedel, Electrochemical performance of DVB-modified SiOC and SiCN polymer-derived negative electrodes for lithium-ion batteries, *Electrochimica Acta*, 106 **(2013)** 101-108

[4] J. Kaspar, M. Graczyk-Zajac and R. Riedel, Determination of the Li-ion diffusion coefficient in carbon-rich SiOC by the electrochemical methods PITT, GITT and EIS, *Electrochimica Acta*, 155 **(2014)** 665-670

[5] E. Ionescu, C. Terzioglu, C. Linck, J. Kaspar, A. Navrotsky and R. Riedel, Thermodynamic control of phase composition and crystallization of metal-modified silicon oxycarbides, *Journal of the American Ceramic Society*, 96 **(2013)** 1899-1903

[6] J. Kaspar, M. Graczyk-Zajac, S. Lauterbach, H.-J. Kleebe and R. Riedel, Silicon oxycarbide/nano-silicon composite anodes for Li-ion batteries: Considerable influence of nano-crystalline vs. nano-amorphous silicon embedment on the electrochemical properties, *Journal of Power Sources*, 269 **(2014)** 164-172

[7] J. Kaspar, C. Terzioglu, E. Ionescu, M. Graczyk-Zajac, S. Hapis, H.-J. Kleebe and R. Riedel, Stable SiOC/Sn Nanocomposite Anodes for Lithium-Ion Batteries with Outstanding Cycling Stability, *Advanced Functional Materials,* 24 **(2014)** 4097-4104

Solid State Ionics 225 (2012) 527–531

Contents lists available at SciVerse ScienceDirect

Solid State Ionics

journal homepage: www.elsevier.com/locate/ssi

Carbon-rich SiOC anodes for lithium-ion batteries: Part II. Role of thermal cross-linking

Jan Kaspar *, Magdalena Graczyk-Zajac, Ralf Riedel

Institut für Materialwissenschaft, Technische Universität Darmstadt, Petersenstr., 32, 64287 Darmstadt, Germany

ARTICLE INFO

Article history:
Received 10 September 2011
Received in revised form 16 January 2012
Accepted 18 January 2012
Available online 11 February 2012

Keywords:
Li-Ion battery
Anode
Silicon oxycarbide
SiOC
Polymer-derived ceramic
High capacity

ABSTRACT

This paper presents the study of lithium insertion into carbon-rich polymer-derived silicon oxycarbide (SiOC) ceramics, synthesized by a thermal treatment of commercially available polysiloxane at 400 °C, followed by pyrolysis at 1100 and 1300 °C. The investigated samples demonstrate a similar chemical composition and provide a high amount of free carbon as separate phase within their microstructure. XRD- and Raman-measurements led us to identify the free carbon phase as a mixture of disordered carbon, nano-crystalline graphite and graphene sheets. This advantageous composition offers a large variety of Li-Ion storage sites, providing high lithiation capacities and reliable cycling behavior. In particular the 1100 °C sample demonstrates a stable reversible capacity of 521 $mAhg^{-1}$ at a cycling current of 37 mAg^{-1}, which is significantly higher than the theoretical capacity of graphite. The inferior performance of the 1300 °C sample with 367 $mAhg^{-1}$ at 37 mAg^{-1} is attributed to a changed microstructure, namely an increased carbon organization within the free carbon phase and SiC crystallization at this temperature. In both cases, the thermal cross-linking leads to much better electrochemical properties than observed for directly pyrolyzed samples.

1. Introduction

Li-Ion batteries are well commercialized and widely used as energy source for all kinds of portable electronics. However, there is still a need for higher energy and power density devices, e.g. as power sources for electrically driven cars or large scale stationary energy storage. Consequently, new high capacity materials need to be found [1,2].

One alternative class of materials is polymer-derived ceramics (PDC), which provide a high amount of free carbon as a separate phase within the microstructure [3-8]. Since the early work of Dahn's group on silicon-oxycarbide anodes [9-13], continuous research was done in order to establish SiOC on the anode side. In the last years, those efforts got further pushed by industry, e.g. by Dow Corning Toray Company, one of the global players in silicone business [8,14-16]. The lithiation capacity of SiOC ceramics is closely related to their microstructure and phase composition, which can be systematically designed by selecting suitable precursors, chemical modification and variable processing techniques [17,18]. Stable reversible capacities for SiOC-based anodes up to 600 $mAhg^{-1}$ have already been reported [8]. Concerning the microstructure of carbon-rich SiOC, different models are discussed in the literature. First, a nanodomain model, which describes a structural graphene network with embedded domains of SiO_2 and an interdomain boundary between both phases, consisting of SiOC mixed-bonds [19,20]. In a second model, a continuous amorphous SiOC phase is discussed, excluding SiO_2 formation but suggesting free carbon segregation [8,21-23]. Cordelair et al. studied carbon segregation within SiOC for different polysiloxane precursors by electrical conductivity measurements. Their results suggest an initial formation of carbon clusters at lower temperatures of pyrolysis, followed by the formation of carbon percolation networks at higher temperatures [24]. In addition, TEM investigations on carbon-rich SiOC approved the presence of carbon percolation networks for different polysiloxane precursors and suggested turbostratic organization [25-27].

We report here on the electrochemical performance of carbon-rich SiOC derived from commercially available polysiloxane Polyramics RD-684 ($SiOC_{RD684}$). Solid state MAS-NMR already demonstrated that the ceramic microstructure is composed of an amorphous Si–O–C network of interconnected $SiO_{4-x}C_x$ ($x=1$–4) structural units and free carbon [21]. Additionally, Martínez-Crespiera et al. approved carbon percolation network formation for $SiOC_{RD684}$ by electrical conductivity measurements and TEM studies [25]. A reversible capacity of 650 $mAhg^{-1}$ has been announced for $SiOC_{RD684}$ based anodes by Graczyk-Zajac et al. for UV-cross-linked polymer precursor [28]. However this cross-linking method makes the material preparation much more expensive and time consuming. In this work, we focus on thermal polymer cross-linking (holding at 400 °C before pyrolysis) in order to influence the final carbon organization and preserve its high amount.

---

* Corresponding author. Tel.: +49 6151 16 6343; fax: +49 6151 16 6346.
E-mail address: kaspar@materials.tu-darmstadt.de (J. Kaspar).

0167-2738/$ – see front matter © 2012 Elsevier B.V. All rights reserved.
doi:10.1016/j.ssi.2012.01.026

2. Experimental part

2.1. Sample preparation

Carbon-rich $SiOC_{RD684}$ was prepared by a thermal conversion of commercially available polysiloxane Polyramics RD-684 (Starfire Systems Inc., USA) (Fig. 1). The polymer was first cross-linked at 400 °C and then pyrolyzed at 1000, 1100, 1200, 1300 and 1400 °C in argon atmosphere. Dwell-time was 3 h and heating rates $50°Ch^{-1}$ for cross-linking and $100°Ch^{-1}$ for pyrolysis. The samples prepared at 1100 °C (SiOC_1100) and 1300 °C (SiOC_1300) were chosen for electrochemical studies.

2.2. Characterization methods

For material characterization, X-ray powder diffraction (XRD) was carried out at a Bruker D8 Advance (Bruker, USA), using Ni-filtered Cu-K^{α} radiation. Micro-Raman spectra were taken with a confocal micro-Raman spectrometer Horiba HR 800 (Horiba, Japan), using an Ar-Ion laser with wavelength 514.5 nm. For elemental analysis, a carbon analyzer Leco-200 (Leco Corporation, USA) was used to determine the carbon content and an N/O analyzer, Leco TC-436 (Leco Corporation, USA) to determine the oxygen content of the samples. The silicon fraction was calculated as the difference to 100 wt-% of the sum of the wt-%-values of carbon and oxygen, assuming a negligibly small amount of hydrogen in the analyzed samples and no other elements present.

2.3. Electrode preparation and electrochemical testing

For electrode preparation, samples were hand-ground to a fine powder and processed in the following way: 85 wt-% sample material (active mass) were mixed with 5 wt-% Carbon black SuperP® (Timcal Ltd., Switzerland) and 10 wt-% polyvinylidene fluoride (PVdF, SOLEF Solvay, Germany) solved in N-methyl-2-pyrrolidone (NMP, BASF, Germany). The obtained slurry was homogenized and tape casted on the rough side of 10 μm thin copper foil (SE-Cu58, Schlenk Metallfolien, Germany). Wet-film thickness was adjusted to 130 μm. The loading of active material after solvent evaporation was about 3.3 mg cm^{-2}. In a next step circular electrodes were cut and dried under vacuum in a Buchi oven at 80 °C for 24 h, before being transferred to an argon filled glove-box, H_2O/ O_2<1 ppm (MBraun Glove Box Systems, Germany).

Measuring cells of two-electrode Swagelok® type were assembled, using a metallic lithium foil (99.9% purity, Alfa Asear, USA) as reference/counter electrode, 1 M $LiPF_6$ in EC:DMC, ratio 1:1 (LP30, Merck KGaA, Germany) as electrolyte and Whatman™ glass fiber filter (Whatman™, UK) as separator.

Hermetically closed cells were connected to a VMP multipotentiostat (BioLogic Science Instruments, France) and studied by galvanostatic cycling with potential limitation (GCPL). GCPL measurements were performed between 0.005 and 3 V (E vs. Li/ Li^{+}) at charging/discharging rates of 37, 74 and 372 mAg^{-1}. Within one GCPL cycle, current rates were chosen similar and capacities recalculated to the initial amount of active mass.

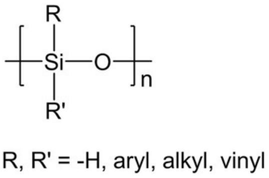
$$\left[-Si(R)(R')-O-\right]_n$$

Fig. 1. Structure of polysiloxane Polyramics RD-684, as provided by the producer.

3. Material characterization

3.1. X-ray powder diffraction

Fig. 2 presents the X-ray diffraction patterns of $SiOC_{RD684}$ prepared between 1000 and 1400 °C.

In all patterns, there is a weak but distinct reflex at 26.5° and a broad one at around 43°. Both are related to carbon segregations within the SiOC microstructure. According to Bragg's equation, the signal at 26.5° corresponds to the interlayer distance of graphite (0.335 nm) and suggests a minor fraction of the carbon phase composed of graphitic carbon [29]. The broad signal at 43° originates from arbitrary diffraction related to graphene sheets, characteristic for amorphous, disordered carbons [14]. Since the intensity of the graphitic signal is comparably weak, the free carbon phase is predominantly of amorphous and disordered nature. At lower temperatures (1000–1200 °C) there are no further peaks visible in the pattern. This finding correlates well with the reported microstructure for $SiOC_{RD684}$ by Widgeon et al. [21]. At higher temperatures (1300 and 1400 °C) crystalline SiC is formed [30,31].

The preliminary electrochemical examination following the XRD study allowed us to choose the samples prepared at 1100 and 1300 °C as representing the "boundary" properties and the most perspective electrochemical performance. In consequence only these two samples are further discussed.

3.2. Raman spectroscopy

Micro-Raman measurements were performed to analyze the carbon phase in more detail. Fig. 3 presents the spectra for $SiOC_{RD684}$ pyrolyzed at 1100 and 1300 °C.

In both spectra strong D and G bands are present, characteristic for carbonaceous materials. The D mode (1350 cm^{-1}) presents a disorder induced vibration of six-fold aromatic rings and its intensity correlates with the present amount of six-fold aromatic rings. The G mode (1580 cm^{-1}) originates from an in-plane bond stretching of sp^2 hybridized carbon atoms within aromatic ring or chain structures [32-34]. The intense D- and less intense G-bands in Fig. 3 demonstrate the carbon phase of predominant amorphous and disordered organization, as already suggested by XRD. This finding is in good agreement with the Raman data on $SiOC_{RD684}$ by Martínez-Crespiera et al. [25].

For the 1300 °C sample, the D-mode is right located at 1350 cm^{-1}, whereas it is slightly shifted to 1330 cm^{-1} for the 1100 °C sample. The G-mode on the contrary is shifted for the 1300 °C sample to 1600 cm^{-1}, whereas it is right located for the 1100 °C sample at

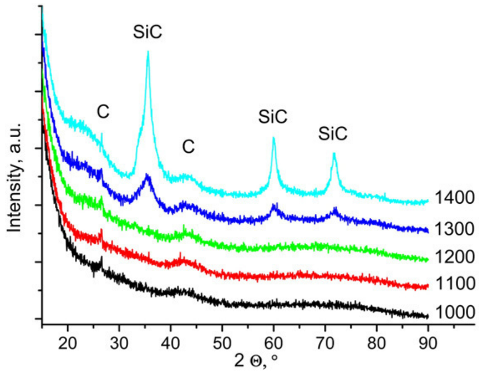

Fig. 2. X-ray powder diffraction patterns of $SiOC_{RD684}$, pyrolyzed between 1000 and 1400 °C.

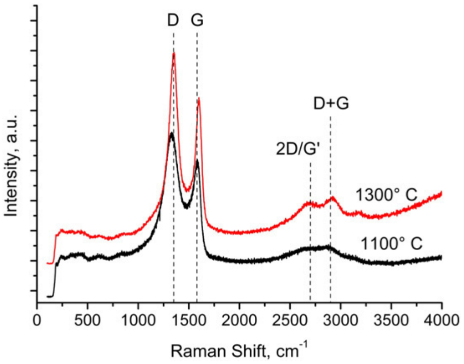

Fig. 3. Micro-Raman spectra of $SiOC_{RD684}$, pyrolyzed at 1100 and 1300 °C.

1580 cm^{-1}. According to the 3-stage model by Ferrari and Robertson, a G-band shift to higher wavenumbers indicates the presence of nano-crystalline graphite [34]. Additionally, the narrow width of the D-band demonstrates a narrow crystallite sizes distribution of these nano-crystallites [35].

The next important signal present in both spectra is the 2D-band (historically called G') at 2700 cm^{-1}. The 2D-band represents the second order of the D-mode and its intensity is related to the stacking order of graphene sheets along the c-axis [36-39]. In both spectra, the 2D-band is very broad and its intensity relatively weak, demonstrating a rather random graphene sheet distribution than distinct stacking. The evolution of the 2D-band at 1300 °C is associated with an increased ordering, e.g. multilayer graphene formation and graphite nano-crystallite growth [37]. The band at 2950 cm^{-1} is associated with a D + G combination mode and is also characteristic for disorder in carbonaceous materials [37].

For the estimation of carbon crystallite sizes (L_a), Ferrari and Robertson reported different formulas within their 3-stage-model [34]. Unfortunately, none of these formulae is straight applicable for the present type of PDC-carbon, as reported for carbon-rich SiCN before [6,7,40,41]. Based on the XRD- and Raman-data, the free carbon phase is rather a mixture of disordered carbon, nano-crystalline graphite and graphene sheets. Thus, it is more accurate to use a general valid equation to determine L_a, reported by Cancado et al. [35]. Accordingly, at 1100 °C L_a amounts 4.99 nm and at 1300 °C L_a amounts 6.25 nm. This increase in crystallite size perfectly matches the found increase in carbon organization at 1300 °C by means of the 2D-band.

3.3. Elemental analysis

Table 1 presents the results from elemental analysis for $SiOC_{RD684}$ prepared upon pyrolysis at 1100 and 1300 °C.

For both samples, the chemical composition is similar and the measured carbon-content exceptional high with 49.20 and 49.11 wt-%. According to Soraru et al. [42], based on the elemental composition a stoichiometric SiOC-formula can be derived and the amount of free carbon quantified. The total fraction of free carbon amounts 41.57 wt-% and 41.52 wt-% for SiOC_1100 and SiOC_1300, respectively.

Table 1
Elemental analysis of the $SiOC_{RD684}$ prepared upon pyrolysis at 1100 and 1300 °C. (*-normalized to one silicon atom).

Sample	Si (wt-%)	O (wt-%)	C (wt-%)	Empirical formula*	Free carbon (wt-%)
SiOC_1100	33.25	17.55	49.20	$SiO_{0.93}C_{3.46}$	41.57
SiOC_1300	33.24	17.65	49.11	$SiO_{0.93}C_{3.46}$	41.52

4. Electrochemical measurements

4.1. First lithiation/delithiation cycle

Fig. 4 presents the first galvanostatic lithiation/delithiation cycle for SiOC_1100 and SiOC_1300 with a current rate of 37 $mAhg^{-1}$. Table 2 summarizes the measured values for first charging capacity (C_{ch}), discharging capacity (C_{rev}), irreversible capacity (C_{irr}) and corresponding coulombic efficiency (η). C_{irr} represents the amount of charge, which is not recovered during the first delithiation process and η is the quantity of charge stored reversibly, estimated by the ratio $C_{rev}/C_{ch} \times 100\%$.

The measured lithiation capacities amount 866 $mAhg^{-1}$ and 658 $mAhg^{-1}$ for SiOC_1100 and SiOC_1300, whereas 532 $mAhg^{-1}$ and 374 $mAhg^{-1}$ are recovered during the first extraction. The observed irreversible loss is lower for SiOC_1100, with a coulombic efficiency of 61.5% compared to 56.8% for SiOC_1300. The amount of free carbon is similar for both samples (~41.5 wt-%), so that the difference observed in the electrochemical behavior has to be mostly attributed to the different microstructures at 1100 and 1300 °C, namely carbon organization and crystallization of electrochemically inactive SiC. Surprisingly, the performed thermal cross-linking did not lead to an increase in the final free carbon content in comparison to non-cross-linked samples from reference [28] (~45 wt-%).

When comparing the shape of both curves in Fig. 4, solid–electrolyte-interface (SEI) formation is seen between 1.1 and 0.5 V during the first Li-insertion. During the first extraction a significant amount of charge is continuously recovered between 0.005 and 1.5 V, as reported for disordered soft and hydrogen-containing carbon [43,44].

We attribute the good electrochemical performance of $SiOC_{RD684}$ to the excess carbon within the ceramic microstructure. Recently, Fukui et al. proposed a model for the lithium storage mechanism in Si–O–C based materials, emphasizing interstitial spaces between graphene layers, edges of graphene sheets and micropores as the major Li-storing sites, while the Si–O–C glass phase is attributed a minor role [8]. Additionally for $SiOC_{RD684}$, charge storage by intercalation into graphite nano-crystallites, deposition at carbon-crystallite surfaces and storage at defect sites must be considered [8,45-47]. Likewise for carbon-rich SiCN, free carbon domains within the amorphous Si–C–N network were recently reported as the major active sites for Li-Ion storage [6,7,48].

4.2. Extended galvanostatic cycling with increasing currents

Fig. 5a and b presents the extended cycling of SiOC_1100 and SiOC_1300 at different current rates.

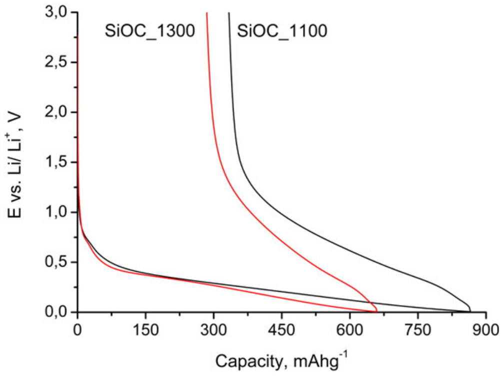

Fig. 4. Comparison of the first lithiation/delithiation cycle for $SiOC_{RD684}$ prepared at 1100 and 1300 °C at a current rate of 37 mAg^{-1}.

Table 2
Comparison of the first cycle charging/ discharging capacity, irreversible capacity and coulombic efficiency of sample SiOC_1100 and SiOC_1300.

Sample	C_{ch} (mAhg^{-1})	C_{rev} (mAhg^{-1})	C_{irr} (mAhg^{-1})	η (%)
SiOC_1100	866	532	333	61.5
SiOC_1300	658	374	285	56.8

For SiOC_1100 (Fig. 5a) cycled at 37 mAg^{-1}, the average reversible capacity amounts 521 mAhg^{-1} without significant fading over 10 cycles. When increasing the cycling current to 74 mAg^{-1}, capacity diminishes to 477 mAhg^{-1}, but is still remarkably stable over 30 cycles. At 372 mAg^{-1}, capacity initially reduces to 347 mAhg^{-1} and further diminishes to 304 mAhg^{-1} after 30 cycles. When slow currents are applied again, an average capacity of 492 mAhg^{-1} is recovered, demonstrating that the material is not significantly damaged during fast cycling. Similar observations are made for SiOC_1300 (Fig. 5b), when cycled at 37 and 74 mAg^{-1}. However, the corresponding capacities are significantly lower. At 372 mAhg^{-1}, SiOC_1300 does not show a fading as seen for SiOC_1100, but rather an initial decrease in capacity to a minimum of 246 mAhg^{-1} followed by a recovery up to 282 mAhg^{-1} after 30 cycles.

Table 3 summarizes the average capacities registered for the investigated samples in comparison with the values observed for non-cross-linked material from reference [28].

For SiOC_1100, the thermally cross-linked samples present much higher capacities than the material prepared by direct pyrolysis at all three cycling rates. For SiOC_1300 the tendency is the same, although the capacities recovered at 37 mAg^{-1} are comparable. This indicates that even if thermal cross-linking does not increase the yield of free carbon, it influences the final microstructure, resulting in much better cycling properties.

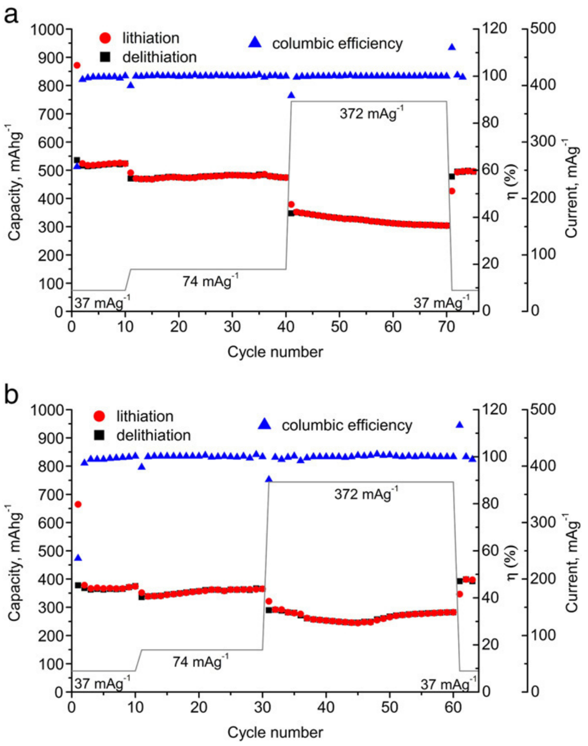

Fig. 5. Cycling performance and single cycle columbic efficiency for a) SiOC_1100 and b) SiOC_1300 at different current rates, indicated in the figures.

Table 3
Average discharge capacity for SiOC_1100 and SiOC_1300 at cycling currents of 37, 74 and 372 mAg^{-1}. In brackets the values found for not cross-linked material from reference [28].

	Average capacity at the following current rates		
Sample	37 mAg^{-1}	74 mAg^{-1}	372 mAg^{-1}
SiOC_1100	521 (458)	477 (291)	323 (146)
SiOC_1300	367 (369)	354 (321)	268 (85)

For the thermally cross-linked samples, SiOC_1100 provides superior capacities to SiOC_1300 at all cycling rates, even though both samples show a similar amount of free carbon (~41.5 wt-%). Again, this deviation is explained by the discussed microstructural differences, namely increased carbon organization and SiC crystallization at 1300 °C. Azuma et al. demonstrated that highly ordered carbons store less lithium ions than disordered carbon structures [29]. Moreover, a decrease in lithiation capacity with increasing temperature of thermal treatment was reported by Dahn et al. for disordered soft and hydrogen-containing carbon [43]. When the free carbon starts to organize, as observed by Raman 2D-band and carbon crystallites grow, less Li-storage sites remain available and capacity diminishes [47]. Another micro-structural difference is illustrated by the formation of SiC at 1300 °C, which is reported as electrochemically inactive and does not contribute to charge storage [9,49].

Since the free carbon phase is dominated by disordered carbon as the major Li-Ion host, the observed capacities can be compared with the ones reported for all kind of carbonaceous materials by Dahn et al. [43]. For soft carbons thermally treated at 1100 °C and 1300 °C, a reversible capacity of 300 mAhg^{-1} and 200 mAhg^{-1} is found. When comparing to SiOC$_{RD684}$, it is evident that the ceramic provides significantly higher capacities at both temperatures. We attribute this phenomenon to a stabilizing role of the Si–O–C network, enabling free carbon to intercalate lithium in a more efficient and stable way, namely 521 and 367 mAhg^{-1} for SiOC_1100 and SiOC_1300, respectively.

It has also been reported, that for SiOC based anodes the amount of oxygen within the material strongly affects the maximum achievable capacity of such systems [10]. A similar behavior was demonstrated for Si-containing disordered carbons, in which the present Si–O–C glass phase was found of major significance for reversible and irreversible capacity, both increasing with an increasing amount of oxygen [49].

5. Conclusion

We present here carbon-rich SiOC anode materials demonstrating advantageous electrochemical properties, prepared in a simple and inexpensive way. The prepared ceramics demonstrate high lithiation capacities and reliable cycling performance, with an average of 521 mAhg^{-1} for a final pyrolysis temperature of 1100 °C. The capacities registered for thermally cross-linked samples significantly exceed those found for directly pyrolyzed samples. Moreover, the advantageous composition of the free carbon phase within the SiOC microstructure was found to play the key role in Li-Ion storage, by offering a large variety of Li-storing sites. The free carbon itself was identified as a mixture of disordered carbon, nano-crystalline graphite and graphene sheets. The superior capacity performance of the 1100 °C sample was attributed to the less organization of the free carbon and absence of crystalline SiC.

We demonstrated that the thermal pretreatment and the final temperature of pyrolysis have a significant impact on the microstructure development, phase composition and especially degree of carbon organization, which directly correlates with the achievable capacity of carbon-rich SiOC.

Acknowledgments

The authors acknowledge the financial support by the Deutsche Forschungsgemeinschaft (DFG), Bonn, Germany within SPP1473 and SFB 595/A4 program.

JK thanks G. Mera, C. Fasel and J.-C. Jaud for their help in the material characterization.

References

[1] H. Kawamoto, Techno. Trends - Q. Rev. 36 (2010) 34.
[2] Y. Wang, H. Li, P. He, E. Hosono, H. Zhou, Nanoscale 2 (2010) 1294–1305.
[3] D. Ahn, R. Raj, J. Power Sources 196 (2011) 2179–2186.
[4] J. Shen, R. Raj, J. Power Sources 196 (2011) 5945–5950.
[5] P.E. Sanchez-Jimenez, R. Raj, J. Am. Ceram. Soc. 93 (2010) 9.
[6] J. Kaspar, G. Mera, A.P. Nowak, M. Graczyk-Zajac, R. Riedel, Electrochim. Acta 56 (2010) 174–182.
[7] M. Graczyk-Zajac, G. Mera, J. Kaspar, R. Riedel, J. Eur. Ceram. Soc. 30 (2010) 3235–3243.
[8] H. Fukui, O. Hisashi, T. Hino, K. Kanamura, Appl. Mater. Interface 4 (2010) 998–1008.
[9] A.M. Wilson, J.N. Reimers, E.W. Fuller, J.R. Dahn, Solid State Ionics 74 (1994) 249–254.
[10] W. Xing, A.M. Wilson, K. Eguchi, G. Zank, J.R. Dahn, J. Electrochem. Soc. 144 (1997) 2410–2416.
[11] W. Xing, A.M. Wilson, G. Zank, J.R. Dahn, Solid State Ionics 93 (1997) 239–244.
[12] A.M. Wilson, W. Xing, G. Zank, B. Yates, J.R. Dahn, Solid State Ionics 100 (1997) 259–266.
[13] A.M. Wilson, G. Zank, K. Eguchi, W. Xing, J.R. Dahn, J. Power Sources 68 (1997) 195–200.
[14] H. Fukui, H. Ohsuka, T. Hino, K. Kanamura, J. Electrochem. Soc. 158 (2011) A550–A555.
[15] H. Fukui, H. Ohsuka, T. Hino, K. Kanamura, J. Power Sources 196 (2011) 371–378.
[16] H. Fukui, H. Ohsuka, T. Hino, K. Kanamura, Chem. Lett. 38 (2009) 86–87.
[17] P. Colombo, G. Mera, R. Riedel, G.D. Soraru, J. Am. Ceram. Soc. 93 (2010) 1805–1837.
[18] R. Riedel, G. Mera, R. Hauser, A. Klonczynski, J. Ceram. Soc. Jpn. 114 (2006) 425–444.
[19] T. Varga, A. Navrotsky, J.L. Moats, R.M. Morcos, F. Poli, K. Müller, A. Saha, R. Raj, J. Am. Ceram. Soc. 90 (2007) 3213–3219.
[20] A. Saha, R. Raj, D.L. Williamson, J. Am. Ceram. Soc. 89 (2006) 2188–2195.
[21] S.J. Widgeon, S. Sen, G. Mera, E. Ionescu, R. Riedel, A. Navrotsky, Chem. Mater. 22 (2010) 6221–6228.
[22] P. Kroll, J. Mater. Chem. 20 (2010) 10528–10534.
[23] P. Kroll, J. Non-Cryst, Solids 351 (2005) 1121–1126.
[24] J. Cordelair, P. Greil, J. Eur. Ceram. Soc. 20 (2000) 1947–1957.
[25] S. Martínez-Crespiera, E. Ionescu, H.-J. Kleebe, R. Riedel, J. Eur. Ceram. Soc. 31 (2011) 913–919.
[26] H.-J. Kleebe, Y.D. Blum, J. Eur. Ceram. Soc. 28 (2008) 1037–1042.
[27] H.-J. Kleebe, G. Gregori, Y.D. Blum, F. Babonneau, Int. J. Mater. Res. 97 (2006) 710–720.
[28] M. Graczyk-Zajac, L. Toma, R. Riedel, Submitted to Solid State Ionics, Special Issue SSI-18, (2011).
[29] H. Azuma, H. Imoto, S.i. Yamada, K. Sekai, J. Power Sources 81–82 (1999) 1–7.
[30] R. Alonso, G. Mariotto, C. Gervais, F. Babonneau, G.D. Soraru, Chem. Mater. 19 (2007) 5694–5702.
[31] M.A. Schiavon, S.U.A. Redondo, S.R.O. Pina, I.V.P. Yoshida, J. Non-Cryst, Solids 304 (2002) 92–100.
[32] N. Larouche, B.L. Stansfield, Carbon 48 (2010) 620–629.
[33] M.S. Dresselhaus, A. Jorio, R. Saito, Annu. Rev. Condens. Matter Phys. 1 (2010) 89–108.
[34] A.C. Ferrari, J. Robertson, Phys. Rev. B 61 (2000) 14095–14107.
[35] L.G. Cancado, K. Takai, T. Enoki, M. Endo, Y.A. Kim, H. Mizusaki, A. Jorio, L.N. Coelho, R. Magalhaes-Paniago, M.A. Pimenta, Appl. Phys. Lett. 88 (2006) 163106.
[36] P. Poncharal, A. Ayari, T. Michel, J.L. Sauvajol, Phys. Rev. B 78 (2008) 113407.
[37] M.A. Pimenta, G. Dresselhaus, M.S. Dresselhaus, L.G. Cancado, A. Jorio, R. Saito, Phys. Chem. Chem. Phys. 9 (2007) 1276–1290.
[38] A.C. Ferrari, Solid State Commun. 143 (2007) 47–57.
[39] A.C. Ferrari, J.C. Meyer, V. Scardaci, C. Casiraghi, M. Lazzeri, F. Mauri, S. Piscanec, D. Jiang, K.S. Novoselov, S. Roth, A.K. Geim, Phys. Rev. Lett. 97 (2006) 187401.
[40] G. Mera, A. Tamayo, H. Nguyen, S. Sen, R. Riedel, J. Am. Ceram. Soc. 93 (2010) 1169–1175.
[41] G. Mera, R. Riedel, F. Poli, K. Müller, J. Eur. Ceram. Soc. 29 (2009) 2873–2883.
[42] G.D. Soraru, S. Modena, E. Guadagnino, P. Colombo, J. Egan, C. Pantano, J. Am. Ceram. Soc. 85 (2002) 1529–1536.
[43] J.R. Dahn, T. Zheng, Y. Liu, J.S. Xue, Science 270 (1995) 590–593.
[44] T. Zheng, W.R. McKinnon, J.R. Dahn, J. Electrochem. Soc. 143 (1996) 2137–2145.
[45] D. Pan, S. Wang, B. Zhao, M. Wu, H. Zhang, Y. Wang, Z. Jiao, Chem. Mater. 21 (2009) 3136–3142.
[46] L. Matzui, M. Semen'ko, M. Babich, L. Kapitanchuk, in: I.V. Barsukov, C.S. Johnson, J.E. Doninger, V.Z. Barsukov (Eds.), New Carbon Based Materials for Electrochemical Energy Storage Systems, Springer, Dordrecht, 2006, pp. 345–356.
[47] Y. Matsumura, S. Wang, J. Mondori, Carbon 33 (1995) 1457–1462.
[48] M. Graczyk-Zajac, C. Fasel, R. Riedel, J. Power Sources 196 (2011) 6412–6418.
[49] D. Larcher, C. Mudalige, A.E. George, V. Porter, M. Gharghouri, J.R. Dahn, Solid State Ionics 122 (1999) 71–83.

Journal of Power Sources 244 (2013) 450–455

Contents lists available at SciVerse ScienceDirect

Journal of Power Sources

journal homepage: www.elsevier.com/locate/jpowsour

Lithium insertion into carbon-rich SiOC ceramics: Influence of pyrolysis temperature on electrochemical properties

Jan Kaspar*, Magdalena Graczyk-Zajac, Ralf Riedel

Institut für Materialwissenschaft, Technische Universität Darmstadt, Petersenstr. 32, 64287 Darmstadt, Germany

HIGHLIGHTS

- ► Carbon-rich SiOC as anode material for Li-ion batteries.
- ► Influence of pyrolysis temperature (T_{pyr}) on electrochemical properties.
- ► Different microstructure development with T_{pyr}.
- ► Increasing carbon organization and Si—O—C network degradation.
- ► Reducing capacities and changing voltage profiles.

ARTICLE INFO

Article history:
Received 25 October 2012
Received in revised form
21 November 2012
Accepted 23 November 2012
Available online 30 November 2012

Keywords:
Li-ion battery
Anode
Carbon-rich SiOC
Influence of pyrolysis
Temperature
High capacity

ABSTRACT

Carbon-rich silicon oxycarbide ceramics (SiOC) prepared via thermal conversion of polyorganosiloxane demonstrate high lithiation capacity and reliable rate capability when used as anode material in Li-ion batteries. The electrochemical properties of carbon-rich SiOC are strongly related to microstructure and phase composition, dependent on final pyrolysis temperature. Both, the increasing organization of free carbon segregated within the microstructure and the gradual degradation of the amorphous Si—O—C network with increasing pyrolysis temperature (T_{pyr}) lead to reduced capacities and changing voltage profiles. Within our study, the highest registered capacity of 660 mAh g^{-1} for $T_{pyr} = 900$ °C dropped below 80 mAh g^{-1} for SiOC pyrolyzed at 2000 °C. A continuous decrease in capacity is observed, when increasing T_{pyr} stepwise by 100 °C, which can be explained by major microstructural changes. First, the free carbon within the ceramic microstructure organizes toward higher ordered configurations, as determined by Raman spectroscopy. Second, X-ray powder diffraction demonstrates a decomposition of the amorphous Si—O—C network resulting in SiC crystallization and growth of SiC domains. Simultaneously, FTIR spectroscopy shows a strong increase of Si—C vibration with T_{pyr}, while Si—O vibration diminishes and almost disappears after annealing at 1700–2000 °C. According to our study we find, that i) increasing carbon organization provides less Li-ion storing sites, ii) gradual Si—O—C network decomposition reduces the structural stability of the free carbon phase and iii) formation of electrochemically inactive SiC account for reduced capacities and changing voltage profiles with increasing T_{pyr}.

1. Introduction

Polymer-derived silicon oxycarbide ceramics (SiOC) containing a high amount of free carbon within their microstructure attracted attention as alternative anode material for Li-ion batteries [1–5]. Polymer derived SiOC is synthesized via pyrolysis of polyorganosiloxanes in protective atmosphere by a polymer precursor to ceramic conversion [6]. The lithiation capacity of carbon-rich SiOC is closely related to its microstructure and phase composition. The material consists of an amorphous Si—O—C network in coexistence with an interpenetrating free carbon network [7,8]. In this structure, the segregated carbon serves as Li-ion host, offering a large variety of Li-storing sites due to its disordered nature. Major storing sites are: Edges of graphene sheets, interstitial spaces between graphene layers, micro- and nanopores, graphite nano-crystallites, interfacial and defect sites. On the contrary, the amorphous Si—O—C network plays a stabilizing role toward the free carbon and does not actively contribute to Li-ion storage [1,4,5].

The results presented in this paper are along with our recent study on carbon-rich SiOC anodes derived from a commercial preceramic polymer, namely Polyramic® RD-684a [4,5]. Both studies suggest

---

* Corresponding author. Tel.: +49 6151 16 6343; fax: +49 6151 16 6346.
E-mail address: kaspar@materials.tu-darmstadt.de (J. Kaspar).

0378-7753/$ – see front matter © 2012 Elsevier B.V. All rights reserved.
http://dx.doi.org/10.1016/j.jpowsour.2012.11.086

an influence of i) the polymer pretreatment and ii) the final pyrolysis temperature on the electrochemical properties of $SiOC_{RD684}$ due to the attained microstructural features. For further clarification a comprehensive sample series was prepared within the temperature range between 900 and 2000 °C and systematically studied by means of XRD, Raman- and IR-spectroscopy and elemental analysis, as well as by electrochemical methods. The characterization of the samples prepared at 1100 and 1300 °C already discussed in reference [5] is for the coherence recalled in the present work. The collected data clearly outline a strong correlation between the final pyrolysis temperature, ceramic microstructure evolution and achievable electrochemical performance.

2. Experimental

2.1. Sample preparation

Ten samples of carbon-rich SiOC were prepared via pyrolysis of polyorganosiloxane Polyramic® RD-684a ($SiOC_{RD684}$, Starfire Systems Inc., USA) in protective atmosphere. Prior to pyrolysis, the polymer-precursors were thermally cross-linked at 400 °C for 3 h. Cross-linking and pyrolysis were carried out under a steady flow of purified argon and heating rates were adjusted to 50 °C h^{-1} for cross-linking and 100 °C h^{-1} for pyrolysis. The final ceramization temperature ranged from 900 to 2000 °C with a holding time of 3 h. For the treatment at 900–1100 °C a horizontal tube-furnace with standard Schlenk-technique was used. Pyrolysis between 1200 and 1700 °C was carried out in a horizontal alumina tube furnace and for the 2000 °C sample an Astro graphite furnace was used. In the following, samples are denoted according to their final pyrolysis temperature (T_{pyr}), e.g. $SiOC_{1100}$.

2.2. Characterization methods

XRD analysis was carried out at a Bruker D8 Advance (Bruker, USA), using Ni-filtered Cu K_α radiation. Mirco-Raman spectra were performed on a confocal micro-Raman spectrometer Horiba HR 800 (Horiba, Japan), using an Ar-Ion laser with a wavelength of 514.5 nm. Infrared spectra were recorded with a Bruker Vertex 70 FT-IR spectrometer (Bruker, USA) in transmission geometry, using KBr pellets. For elemental analysis, a carbon analyzer Leco-200 (Leco Corporation, USA) was used to determine the carbon content and an N/O analyzer Leco TC-436 (Leco Corporation, USA) to determine the oxygen content in the samples. The silicon fraction was calculated as the difference to 100 wt-% of the sum of the wt-% values of carbon and oxygen, assuming a negligibly small amount of hydrogen and no other elements present in the samples.

2.3. Electrode preparation

Pyrolyzed samples ($SiOC_{900}$–$SiOC_{2000}$) were hand-ground to a fine powder and processed in the following way: 85 wt-% sample material (referred to as active mass) were mixed with 5 wt-% Carbon black SuperP® (Timcal Ltd., Switzerland) and 10 wt-% polyvinylidene fluoride (PVdF, SOLEF Solvay, Germany) solved in N-methyl-2-pyrrolidone (NMP, BASF, Germany). The obtained slurry was homogenized and tape casted on the rough side of 10 μm thin copper foil (SECu58, Schlenk Metallfolien GmbH, Germany). Wet-film thickness was adjusted to 130 μm. The loading of active material after solvent evaporation was about 3.3 mg cm^{-2}. Circular electrodes were cut and dried under vacuum in a Buchi oven at 80 °C for 24 h, before transferred to an argon filled glove-box with H_2O/O_2 contamination < 1 ppm (MBraun Glove Box Systems, Germany). Measuring cells of two-electrode Swagelok® type were assembled, using metallic lithium foil (99.9% purity, Alfa Aesar, USA) as reference/counter electrode, 1 M $LiPF_6$ in EC:DMC, ratio 1:1 (LP30, Merck KGaA, Germany) as electrolyte and Whatman™ glass fiber filter (Whatman™, UK) as separator. Hermetically closed cells were connected to a VMP3 multipotentiostat (BioLogic Science Instruments, France) and studied by galvanostatic cycling with potential limitation (GCPL). GCPL measurements were performed between 0.005 and 3 V (E vs. Li/Li^+) at charging/discharging currents of 37, 74 and 372 mA g^{-1}. Within one charging–discharging cycle, the same current rates were applied and capacities were recalculated to the initial amount of active mass.

3. Results and discussion

3.1. X-ray powder diffraction

Fig. 1 presents the X-ray diffraction patterns prior reported for $SiOC_{900}$–$SiOC_{1400}$ [5], completed with samples prepared between 1500–2000 °C. From 900 to 1200 °C the samples remain X-ray amorphous [5], while from 1300 to 2000 °C SiC crystallization is detected in consequence of a carbothermal reaction of silica with carbon [9]. As a result, the amorphous Si–O–C network gradually decomposes. With increasing T_{pyr} from 1300 to 2000 °C, the diffraction intensity related to SiC increases and the signal width gets narrower, indicating growth of SiC domains. At lower temperatures, a weak signal appears at 26.5° related to diffraction at graphitic carbon within the free carbon phase. Furthermore, a broad hump around 43° is recognized, originating from arbitrary diffraction at graphene sheets, characteristic for disordered carbons [10,11]. Except for $SiOC_{2000}$, the graphite reflexes are weak, suggesting the segregated carbon of predominantly amorphous nature. The observed graphitization at 2000 °C is characteristic for disordered soft carbon and emphasizes the increasing carbon organization with T_{pyr} [12,13]. Both findings are in good agreement with the results obtained by Raman and FTIR spectroscopy, discussed in the following sections.

3.2. Raman-spectroscopy

Micro-Raman spectroscopy was performed to further analyze the structural development of the segregated carbon with

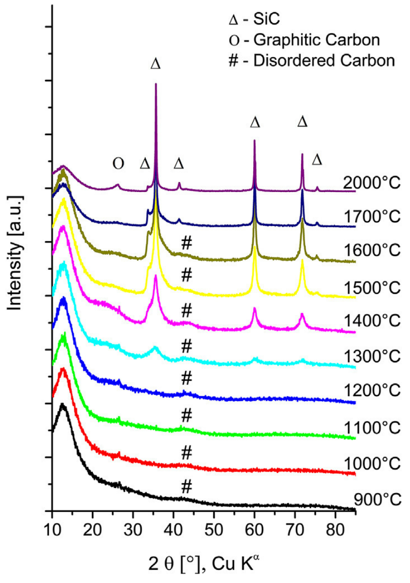

Fig. 1. XRD pattern of the samples SiOC 900–2000 °C.

increasing T_{pyr}. The recorded spectra are shown in Fig. 2. For all temperatures the characteristic carbon vibrations are present: The D-band around 1350 cm^{-1}, the G-band around 1580 cm^{-1}, the 2D vibrations at 2440, 2700 and 3200 cm^{-1} and the D + G combination mode at 2950 cm^{-1}. In all spectra the integral intensity of the D-band $I\ (A_D)$ is stronger than that of the $I\ (A_G)$, proving the disordered nature of the segregated carbon. Integral intensities were obtained by Lorentzian fit of D- and G-band within each spectrum [14]. With increasing T_{pyr}, the D- and G-band get more narrow and distinct due to i) a decreasing number of intrinsic defect sites, ii) disappearance of residual C–H bonds present at lower T_{pyr} and iii) vanishing of dangling bonds. Simultaneously, the intensity of the 2D vibrations strongly increases, demonstrating increasing structural carbon organization and graphitization toward 2000 °C [15–19]. In contrast, no trace of the Raman signal from SiC can be detected, probably because of both the relatively low level of SiC segregation and the reduced size of the formed SiC domains [9].

The integral intensities $I\ (A_D)$ and $I\ (A_G)$ for each temperature and the dimensions of the corresponding carbon crystallite sizes (L_a), calculated by the general valid equation (Eq. (1)) reported by Cancado et al. [15], with laser wavelength $\lambda = 514$ nm, are summarized in Table 1. The increase in carbon crystallite size with T_{pyr} perfectly matches the found increase in carbon organization by means of Raman 2D bands. The sample SiOC$_{900}$ shows a larger L_a than SiOC$_{1000}$ which is not in agreement with the general trend presented in Table 1. However, for this sample the pyrolysis temperature of 900 °C was most likely too low to eliminate residual C–H bonds within the carbon phase, as suggested by the D-band shoulder toward lower wavenumbers. This so called I-mode is representative for the presence of mixed sp^2–sp^3-hybridized carbon [14].

$$L_a(\mathrm{nm}) = \left(2.4\times10^{-10}\right)\lambda^4\left(\frac{(I\ (A_D))}{(I\ (A_G))}\right)^{-1} \qquad (1)$$

Eq. (1). Equation used for the estimation of the carbon crystallite size L_a [15].

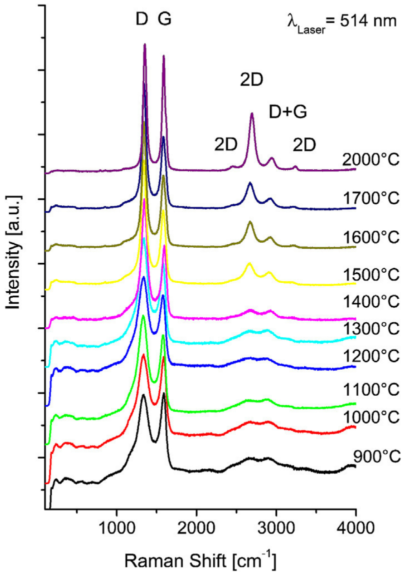

Fig. 2. Raman spectra of the samples SiOC 900–2000 °C.

Table 1
Estimated carbon crystallite size L_a in dependence of T_{pyr}, calculated by Eq. (1).

T_{pyr} [°C]	$I\ (A_D)$	$I\ (A_G)$	L_a [nm]
900	134	42	5.25
1000	142	42	4.95
1100	194	58	4.99
1200	143	50	5.86
1300	171	64	6.25
1400	114	47	6.91
1500	102	54	8.87
1600	89	51	9.60
1700	88	51	9.71
2000	71	54	12.74

3.3. FTIR-spectroscopy

Fig. 3 presents the FTIR spectra for SiOC$_{900}$–SiOC$_{2000}$. In all spectra characteristic bands for Si–O and Si–C vibrations are visible, originating from $SiO_{4-x}C_x$ (x = 1–4) mixed bonds as building units of the amorphous Si–O–C phase and form crystalline SiC formed at higher annealing temperatures. At 455 cm^{-1} Si–O–Si rocking vibration and around 790 cm^{-1} O–Si–O band bending, overlapping with Si–C stretching vibration at 830 cm^{-1}, is found. The weak absorption at 620 cm^{-1} is also due to Si–C vibration. The broad absorption in the range of 1000–1060 cm^{-1} originates from Si–O, similar to vitreous silica showing absorption at 1090 cm^{-1}. The shift to lower wavenumbers indicates that Si–O bonds are barely located in SiO_4 coordination but rather in random $SiO_{4-x}C_x$ mixed bonds [20–23].

With increasing temperature of pyrolysis the intensity of the Si–O bands at 455 cm^{-1} and 1000–1600 cm^{-1} strongly diminishes. Especially the band at 455 cm^{-1} completely disappears for SiOC$_{1500}$–SiOC$_{2000}$. Simultaneously, a significant intensity increase and a shift of the overlapping Si–O and Si–C vibration around 800 cm^{-1} are found. At 900 °C, the Si–O vibration is dominating with a characteristic absorption maximum at 790 cm^{-1}. But already for the sample annealed at 1300 °C, this maximum is shifted toward

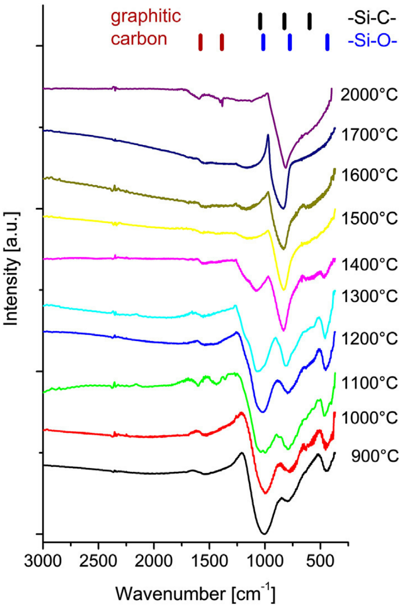

Fig. 3. FTIR spectra of the samples SiOC 900–2000 °C.

830 cm^{-1}, indicating a significant decrease of the Si–O contribution and a strong increase of Si–C vibration. For the samples $SiOC_{1700}$ and $SiOC_{2000}$, Si–C vibration at 830 cm^{-1} and 820 cm^{-1} is detected, exclusively.

The development of the Si–O and Si–C absorption bands with T_{pyr} outlines the progressive degradation of the Si–O–C network, characterized by the disappearance of Si–O intensity and increasing dominance of Si–C vibration. This result well correlates with the found SiC crystallization and SiC domain growth for the samples $SiOC_{1300}$–$SiOC_{2000}$ by means of XRD. For completeness, the bands located at 1350 and 1580 cm^{-1} for $SiOC_{2000}$ are related to graphitic carbon vibration [24].

3.4. Elemental analysis

Table 2 presents the results obtained from elemental analysis for representative samples from the series $SiOC_{900}$–$SiOC_{2000}$. Based on the chemical composition an empirical formula for the SiOC stoichiometry can be derived and the amount of free carbon segregated in the microstructure quantified (see Table 2) [25,26]. For $SiOC_{1000}$–$SiOC_{1400}$, the chemical composition is similar and the free carbon content is exceptionally high with about 41 wt-%. Up to an annealing temperature of 1300 °C, the amount of oxygen is stable, but starts to diminish significantly beyond 1400 °C due to oxygen outgassing in form of CO and SiO. This decrease in oxygen content illustrates the ongoing Si–O–C decomposition, as analyzed by XRD and FTIR spectroscopy. At 2000 °C almost no oxygen is present anymore. In consequence of the reduced oxygen amount, the carbon and silicon content increases for the samples heat-treated at 1400 °C and higher. On the contrary, the total amount of free carbon drops at higher T_{pyr}, due to the loss of CO.

3.5. Electrochemical performance

The characteristic first cycle lithiation/delithiation profiles for $SiOC_{900}$–$SiOC_{2000}$ are presented in Fig. 4, all recorded with a current rate of 37 mA g^{-1}. All cycles show significant hysteresis during Li-insertion/extraction with coulombic efficiencies between 61.5% ($SiOC_{1100}$) and 20.5% ($SiOC_{1700}$). The registered reversible capacities diminish with increasing T_{pyr} from 738 mAh g^{-1} for $SiOC_{900}$ to 75 mAh g^{-1} for $SiOC_{2000}$. Table 3 summarizes the measured values for the first charging capacity (C_{ch}), reversible capacity (C_{rev}), irreversible capacity (C_{irr}) and corresponding coulombic efficiency (η). The columbic efficiency has been calculated as the ratio $C_{rev}/C_{ch} \times 100\%$. The electrochemical behavior of the samples $SiOC_{1100}$ and $SiOC_{1300}$ has already been discussed in [5] within the context of the advantages of various cross-linking methods [4,5]. The potential vs. capacity curves for the mentioned samples are re-called in Fig. 4 for its completeness.

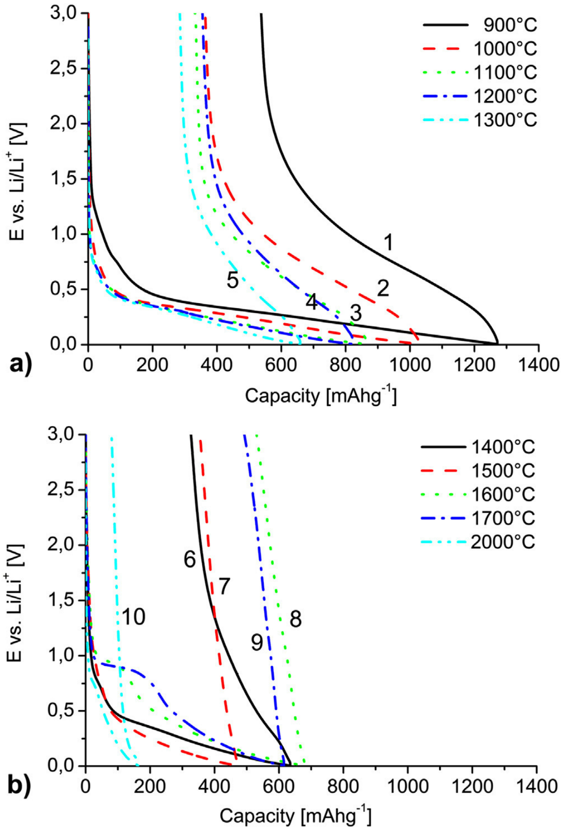

Fig. 4. First cycle lithiation/delithation profile for SiOC a) 900–1300 °C (curves 1–5) and b) 1400–2000 °C (curves 6–10).

In general, voltage profiles for $SiOC_{900}$–$SiOC_{1500}$ appear quite similar, showing a long sloping plateau between 0.4–0.005 V in the cathodic branch, which is related to Li-ion storage in the disordered carbon phase. In the anodic branch, most of the charge is continuously recovered below 1.5 V ($SiOC_{900}$–$SiOC_{1400}$). Similar voltage profiles were reported for carbon-rich SiOC and disordered soft or hydrogen containing carbon [1,4,5,12,27]. Voltage profiles of $SiOC_{1600}$ and $SiOC_{1700}$ appear different, showing an additional plateau at 0.95 V in the cathodic branch, followed by steeply sloping toward 0.5 V and further sloping to 0.005 V. Similar behavior has been reported and discussed for carbon-rich SiCN ceramics pyrolyzed at 2000 °C by Graczyk-Zajac et al. [28]. During the lithium extraction less than 160 mAh g^{-1} of charge is recovered for $SiOC_{1500}$–$SiOC_{1700}$ with coulombic

Table 2
Elemental analysis of $SiOC_{RD684}$ prepared upon pyrolysis between 900 °C and 2000 °C (* – normalized to one silicon atom).

T_{pyr} [°C]	Si [wt-%]	O [wt-%]	C [wt-%]	Empirical formula*	Free carbon [wt-%]
900	30.35	22.07	47.58	$SiO_{1.28}C_{3.67}$	42.88
1100	33.25	17.55	49.20	$SiO_{0.93}C_{3.46}$	41.57
1300	33.24	17.65	49.11	$SiO_{0.93}C_{3.46}$	41.52
1400	34.43	14.24	51.33	$SiO_{0.73}C_{3.49}$	41.95
1600	41.26	3.19	55.55	$SiO_{0.14}C_{3.15}$	39.10
2000	43.41	0.04	56.55	$SiC_{3.05}$	38.00

Table 3
Comparison of the first cycle charging capacity, reversible capacity, irreversible capacity and coulombic efficiency for the samples SiOC 900–2000 °C.

T_{pyr} [°C]	C_{ch} [mAh g^{-1}]	C_{rev} [mAh g^{-1}]	C_{irr} [mAh g^{-1}]	η [%]
900	1277	738	539	57.8
1000	1028	614	414	59.7
1100	866	532	334	61.5
1200	828	471	357	56.9
1300	658	374	284	56.8
1400	641	313	328	48.8
1500	471	141	330	29.9
1600	686	154	532	22.4
1700	621	128	493	20.6
2000	163	75	88	46.0

efficiencies < 30%. The sample pyrolyzed at 2000 °C demonstrates the lowest reversible capacity among the studied series (75 mAh g^{-1}), however the cycling efficiency again increases, from 20.6% for SiOC$_{1700}$ to 46.0% registered for SiOC$_{2000}$. Nevertheless, from a practical point of view, the significant hysteresis, low coulombic efficiency and low reversible capacity of the samples prepared between 1500 and 2000 °C clearly disqualifies these samples for battery application.

The registered charging and reversible capacity for the series SiOC$_{900}$–SiOC$_{1500}$ continuously decreases while voltage profiles remain similar. This diminution in charge storage is related to a decrease in available Li-ion storing sites within the free carbon phase. As found by Raman, the structural organization of the free carbon increases with temperature of pyrolysis. According to our previous reports [4,5] and findings of Azuma et al. [13], higher ordered carbons can host less Li-ions than order-less configurations, meaning that at lower T_{pyr} the corresponding capacities must be higher than at higher T_{pyr}.

Fig. 5 summarizes the average reversible capacity registered for SiOC$_{900}$–SiOC$_{2000}$ for continuous cycling at different current rates. The average values are calculated from 10 cycles with a current of 37 mA g^{-1}, 20 cycles with 74 mA g^{-1} and 30 cycles with 372 mA g^{-1}. The error bars in Fig. 5 indicate the standard deviation from the average value. Deviation comes from capacity fading during cycling or, for the samples showing stable cycling behavior (SiOC$_{1000}$, SiOC$_{1200}$) from temperature fluctuations in the laboratory where the cells were tested. Table 4 summarizes the calculated values. Between 900 and 1200 °C, the measured capacities of 666 - 460 mAh g^{-1} for cycling current 37 and 74 mA g^{-1} are much higher than the theoretical capacity of graphite (372 mAh g^{-1}). For SiOC$_{1300}$–SiOC$_{1400}$ the reversible capacity drops below 400 mAh g^{-1} and for the samples SiOC$_{1500}$–SiOC$_{2000}$ capacity of less than 140 mAh g^{-1} is recovered in average.

Among the studied materials, sample SiOC$_{900}$ shows the highest capacity, but also the largest fading during cycling. Within the first ten cycles at 37 mA g^{-1}, the recovered charge diminishes from initially 738 to 644 mAh g^{-1}. In particular between the first and second cycle 40 mAh g^{-1} are lost. Most probably, this decay is related to a large amount of residual hydrogen within the sample, especially within the free carbon phase in form of C–H bonds stemming from the initial polymer precursor. The H-content for a similar prepared sample at 900 °C was analyzed to 1.13 wt-% [29]. According to Dahn et al., Li-ion storage in H-containing carbons occurs by Li-binding in the vicinity of H atoms [12]. During Li extraction, the original C–H bonds reform. When this reforming is disturbed or incomplete, the cycling capacity slowly decays with continuous cycling [12,30].

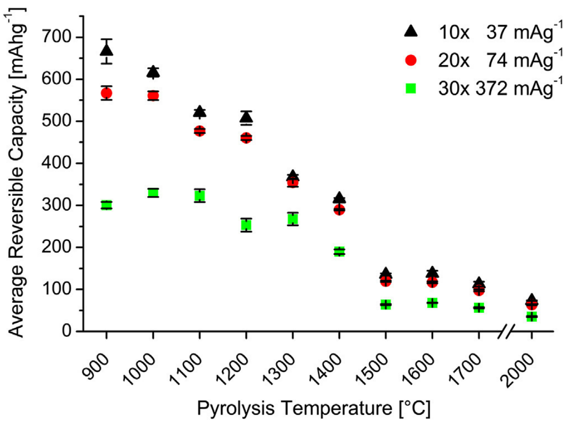

Fig. 5. SiOC average reversible capacity in dependence of temperature of pyrolysis. Average values were calculated from 10 cycles at 37 mA g^{-1}, 20 × 74 mA g^{-1} and 30 × 372 mA g^{-1}. Error bars indicate the standard deviation from the average value.

Table 4
SiOC average reversible capacity in dependence of temperature of pyrolysis, for the current rates: 37, 74 and 372 mA g^{-1}.

T_{pyr} [°C]	Average reversible capacity at the following current rates		
	37 mA g^{-1}	74 mA g^{-1}	372 mA g^{-1}
900	666	567	300
1000	615	561	330
1100	521	477	323
1200	507	460	253
1300	367	354	268
1400	315	289	190
1500	135	120	64
1600	138	117	68
1700	112	97	56
2000	73	64	35

Among the investigated sample series, SiOC$_{1000}$ and SiOC$_{1100}$ are the most perspective samples for potential application as anode material. Both present outstanding properties: High capacity in combination with good high rate stability. At 37 and 74 mA g^{-1}, the average reversible capacity of SiOC$_{1000}$ (615 mAh g^{-1}, 561 mAh g^{-1}) is approximately 100 mAh g^{-1} higher than that of the sample SiOC$_{1100}$ (512 mAh g^{-1}, 477 mAh g^{-1}). At a current rate of 372 mA g^{-1}, values are quite similar with 330 and 323 mAh g^{-1}. In general, the good high rate performance of SiOC$_{900}$–SiOC$_{1300}$ can be explained by the intrinsic nanostructure of the ceramics, which kinetically boosts the Li-ions due to shorten diffusion pathways [31–33]. Similar findings were reported for nano-structured, carbon-rich SiCN ceramics [34,35].

To summarize, the registered reversible capacities decrease with temperature of pyrolysis (cf. Fig. 5) by two major contributions: First, increasing structural organization of the segregated free carbon leads to less Li-ion storing sites. Second, continuous degradation of the Si–O–C network reduces the structural stability of the free carbon phase.

4. Conclusions

We demonstrated that the temperature of pyrolysis (T_{pyr}) has a significant impact on the electrochemical properties of carbon-rich, polyorganosiloxane derived SiOC ceramics. In particular the analyzed capacities were found to decrease by structural changes of the free carbon phase from highly disordered toward partially graphitized configurations. In consequence, the number of Li-storing sites diminishes, since higher ordered carbons can host less Li-ions than orderless configurations. Additionally, degradation of the stabilizing Si–O–C network occurs, by a solid state reaction of Si–O bonds with carbon, resulting in SiC crystallization, growth of SiC domains and oxygen-loss. This gradual decomposition reduces the structural stability of the free carbon phase, favoring reduced capacities and changing voltage profiles.

Acknowledgments

The authors acknowledge the financial support by the Deutsche Forschungsgemeinschaft (DFG), Bonn, Germany within SPP1473/JP8 and SFB 595/A4 program. Special thanks to G. Mera, C. Fasel and J.-C. Jaud for their support of the characterization of the materials and helpful discussion.

References

[1] H. Fukui, O. Hisashi, T. Hino, K. Kanamura, Appl. Mater. Interfaces 4 (2010) 998–1008.
[2] H. Fukui, H. Ohsuka, T. Hino, K. Kanamura, J. Power Sources 196 (2011) 371–378.
[3] P. Dibandjo, M. Graczyk-Zajac, R. Riedel, V.S. Pradeep, G.D. Soraru, J. Eur. Ceram. Soc. 32 (2012) 2495–2503.
[4] M. Graczyk-Zajac, L. Toma, C. Fasel, R. Riedel, Solid State Ionics 225 (2012) 522–526.
[5] J. Kaspar, M. Graczyk-Zajac, R. Riedel, Solid State Ionics 225 (2012) 527–531.
[6] P. Colombo, G. Mera, R. Riedel, G.D. Soraru, J. Am. Ceram. Soc. 93 (2010) 1805–1837.
[7] S.J. Widgeon, S. Sen, G. Mera, E. Ionescu, R. Riedel, A. Navrotsky, Chem. Mater. 22 (2010) 6221–6228.
[8] S. Martínez-Crespiera, E. Ionescu, H.-J. Kleebe, R. Riedel, J. Eur, Ceram. Soc. 31 (2011) 913–919.
[9] R. Alonso, G. Mariotto, C. Gervais, F. Babonneau, G.D. Soraru, Chem. Mater. 19 (2007) 5694–5702.
[10] F. Bonino, S. Brutti, M. Piana, S. Natale, B. Scrosati, L. Gherghel, K. Müllen, Electrochim. Acta 51 (2006) 3407–3412.
[11] C.L. Burket, R. Rajagopalan, H.C. Foley, Carbon 46 (2008) 501–510.
[12] J.R. Dahn, T. Zheng, Y. Liu, J.S. Xue, Science 270 (1995) 590–593.
[13] H. Azuma, H. Imoto, S.i. Yamada, K. Sekai, J. Power Sources 81–82 (1999) 1–7.
[14] A. Sadezky, H. Muckenhuber, H. Grothe, R. Niessner, U. Pöschl, Carbon 43 (2005) 1731–1742.
[15] L.G. Cancado, K. Takai, T. Enoki, M. Endo, Y.A. Kim, H. Mizusaki, A. Jorio, L.N. Coelho, R. Magalhaes-Paniago, M.A. Pimenta, Appl. Phys. Lett. 88 (2006) 163106.
[16] M.A. Pimenta, G. Dresselhaus, M.S. Dresselhaus, L.G. Cancado, A. Jorio, R. Saito, Phys. Chem. Chem. Phys. 9 (2007) 1276–1290.
[17] A.C. Ferrari, Solid State Commun. 143 (2007) 47–57.
[18] N. Larouche, B.L. Stansfield, Carbon 48 (2010) 620–629.
[19] M.S. Dresselhaus, A. Jorio, R. Saito, Annu. Rev. Condens. Matter Phys. 1 (2010) 89–108.
[20] G.M. Renlund, S. Prochazka, R.H. Doremus, J. Mater. Res. 6 (1991) 2723–2734.
[21] D. Gupta, B. Awasthy, S.P. Varma, J. Mater. Sci. 28 (1993) 1488–1490.
[22] Q. Liu, W. Shi, F. Babonneau, L.V. Interrante, Chem. Mater. 9 (1997) 2434–2441.
[23] Q.-S. Ma, Z.-H. Chen, W.-W. Zheng, H.-F. Hu, Ceram. Int. 31 (2005) 1045–1051.
[24] R.A. Friedel, G.L. Carlson, J. Phys. Chem. US 75 (1971) 1149–1151.
[25] G.D. Soraru, J. Sol-gel. Sci. Tech. 2 (1994) 843–848.
[26] G.D. Soraru, L. Pederiva, J. Latournerie, R. Raj, J. Am. Ceram. Soc. 85 (2002) 2181–2187.
[27] T. Zheng, W.R. McKinnon, J.R. Dahn, J. Electrochem. Soc. 143 (1996) 2137–2145.
[28] M. Graczyk-Zajac, G. Mera, J. Kaspar, R. Riedel, J. Eur. Ceram. Soc. 30 (2010) 3235–3243.
[29] J. Kaspar et al., unpublished data.
[30] T. Zheng, Q. Zhong, J.R. Dahn, J. Electrochem. Soc. 142 (1995) L211–L214.
[31] C.J. Wen, B.A. Boukamp, R.A. Huggins, W. Weppner, J. Electrochem. Soc. 126 (1979) 2258–2266.
[32] A.S. Arico, P. Bruce, B. Scrosati, J.-M. Tarascon, W. van Schalkwijk, Nat. Mater. 4 (2005) 366–377.
[33] G. Peter, B. Bruce, J.-M. Scrosati, Tarascon, Angew. Chem. Int. Ed. 47 (2008) 2930–2946.
[34] J. Kaspar, G. Mera, A.P. Nowak, M. Graczyk-Zajac, R. Riedel, Electrochim. Acta 56 (2010) 174–182.
[35] L.M. Reinold, M. Graczyk-Zajac, Y. Gao, G. Mera, R. Riedel, Carbon-rich SiCN ceramics as high capacity/high stability anode material for lithium ion batteries, J. Power Sources, Submitted for publication.

Electrochimica Acta 106 (2013) 101–108

Contents lists available at SciVerse ScienceDirect

Electrochimica Acta

journal homepage: www.elsevier.com/locate/electacta

Electrochemical performance of DVB-modified SiOC and SiCN polymer-derived negative electrodes for lithium-ion batteries

Guanwei Liu[a,b,c], Jan Kaspar[a], Lukas Mirko Reinold[a], Magdalena Graczyk-Zajac[a,*], Ralf Riedel[a]

[a] Fachbereich Material- und Geowissenschaften, Technische Universität Darmstadt, Petersenstr. 32, 64287 Darmstadt, Germany
[b] State Key Lab of New Ceramics and Fine Processing, Department of Materials Science and Engineering, Tsinghua University, Beijing 100084, PR China
[c] R&D Center for Vehicle Batteries and Energy Storage, General Research Institute for Nonferrous Metals, Beijing 100088, PR China

ARTICLE INFO

Article history:
Received 26 February 2013
Received in revised form 7 May 2013
Accepted 13 May 2013
Available online 23 May 2013

Keywords:
Polymer-derived ceramics
Lithium ion battery
Silicon oxycarbide
Silicon carbonitride
Anode

ABSTRACT

Chemical modification of commercially available polyorganosilazane (HTT1800) and polyorganosiloxane (Polyramic RD-684a) with divinylbenzene (DVB) is accomplished via hydrosilylation reaction. The incorporation of DVB leads to an increase of the free carbon amount after pyrolysis within the corresponding SiCN and SiOC ceramics. The modification is carried out with lower, equal and higher stoichiometric ratios of the Si—H to C═C groups present in the Si-based polymer and DVB. FTIR results indicate a complete consumption of the Si—H bonds in the case of the stoichiometric amount of DVB and polymer RD-684a, while for HTT1800 neither the stoichiometric ratio nor DVB excess leads to a complete consumption of the Si—H groups. For both SiCN and SiOC ceramics the carbon content is found to increase with the amount of DVB. However, the most significant increase in free carbon content is registered for SiCN samples, namely of ca. 40%. The carbon content changed from 9.9 wt.% in the pure HTT1800-derived material up to 49.3 wt.% for the SiCN ceramic obtained with the highest amount of DVB addition. Accordingly, Li-ion storage and therefore charge storage capacity are simultaneously increased, for the first cycle from 136 to 574 mAh g^{-1}, while columbic efficiency is raised by 10% up to 60.4%.

1. Introduction

Due to the increasing energy consumption and environmental aspects, there is a growing interest in new energy storage devices. Lithium-ion batteries are a promising candidate for this application and have received much attention in recent years because of a high energy and power density. Nevertheless, there is still a need for new electrode materials to face up growing safety, capacity and high rate capability requirements. Currently graphitic materials are used as anode due to low price and high charge reversibility despite relatively low capacity (372 mAh g^{-1}), instability during long-time cycling and inadequacy for high power applications [1,2].

In this scope, polymer-derived silicon oxycarbides (SiOC) and silicon carbonitrides (SiCN) have been studied as alternative electrode materials in the middle of nineties [3–7]. Polymer derived ceramics (PDC) exhibit numerous advantageous properties for application as anode material in lithium ion batteries. They are chemically inert with respect to battery components and are lightweight materials. Furthermore, their chemical and physical properties can be designed by varying the starting polymer composition. PDCs based on the SiOC and SiCN systems with high carbon content have been recently reported to exhibit electrochemical properties suitable for the storage of lithium ions [8–20]. The carbon content and its intrinsic structure are important issues for the electrochemical performance of SiOC and SiCN negative electrodes. The free carbon formed in the PDC route exhibits a 3D-percolating cage-like structure or isolated carbon clusters in carbon rich and carbon poor SiOC ceramics, respectively [21,22]. The sp^2-hybridized carbon cannot only offer effective lithium storage sites, but also electronic conducting paths throughout the material. According to recent investigations, disordered free carbons encapsulated in the ceramic matrix are the major lithium intercalating agent, while pores and the so called mixed bond configuration of the ceramic network (tetrahedrally coordinated silicon from SiC_4 via SiC_3O, SiC_2O_2 and $SiCO_3$ to SiO_4 for silicon oxycarbide) play a minor role [13].

In consequence, as free carbon is considered as a major Li-ion storing site, enhanced amount of free carbon within the ceramic matrix should lead to an enhancement in charge storage. Some routes for synthesizing Si-based and carbon-rich PDCs have already been reported:

---

[*] Corresponding author. Tel.: +49 6151166343; fax: +49 6151166346.
E-mail address: graczyk@materials.tu-darmstadt.de (M. Graczyk-Zajac).

0013-4686/$ – see front matter © 2013 Elsevier Ltd. All rights reserved.
http://dx.doi.org/10.1016/j.electacta.2013.05.064

i. Using phenyl-rich pre-ceramic Si-polymers [10,11]
ii. Addition of carbon or carbon precursor to Si-polymers [12–14,23,24]
iii. Chemical modification of pre-ceramic Si-polymers [18,25]

As a chemical method, hydrosilylation reaction is often used for modifying silicon based polymers [25–28]. Si—H groups within the polymer backbone can easily react with vinyl groups of the blending additive, e.g. divinylbenzene (DVB). In this way carbon-rich units are introduced to the polymer and the carbon content of the derived ceramic is increased. Liu et al. studied the electrochemical properties of SiOC prepared from Si-polymer–DVB hydrosilylation reaction [25], however mostly the influence of the pyrolysis conditions and post treatment on the final electrochemical properties have been analyzed. Chen et al. [24] choose another strategy, namely polysilazane, which provides carbon poor SiCN ceramics, was mixed with DVB. A specially designed procedure was applied to induce phase separation between DVB and polysilazane. Accordingly, the mixture of the two precursors was first thermally treated at 70 °C to crosslink DVB, which was supposed to act as a carbon precursor, followed by thermal treatment of the mixture at 120 °C to further crosslink the polysilazane. Finally, the solid mixture was pyrolyzed at 1200 °C. Such procedure should inhibit the hydrosilylation reaction, while leading to the formation of free carbon clusters spread within the ceramic matrix. However, no direct proof of the absence of hydrosilylation reaction, i.e. by means of FT-IR measurements of cross-linked material, was presented.

Within this work we investigate the influence of the amount of reacted DVB on the electrochemical performance of the ceramic. Therefore two different starting polymers providing an intrinsically low (Polysilazane, HTT1800) and high (Polysiloxane, Polyramic RD-684a) carbon content were chemically modified with DVB and thermally converted into SiCN and SiOC ceramics, respectively. For both, three different blending ratios were studied, namely (i) lower DVB content than the stoichiometric ratio with respect to Si—H/C═C groups, (ii) stoichiometric and (iii) excess amount of DVB. The reaction progress has been followed by FTIR spectroscopy; structure and chemical composition of the derived ceramics were analyzed by means of XRD, Raman spectroscopy and elemental analysis. The electrochemical performance of the synthesized samples has been studied by galvanostatic cycling with potential limitation. Finally the question is addressed, whether there is a maximum in carbon content, i.e. a threshold value, which once exceeded, reverses the positive influence in Li-ion storing properties and capacity enhancement.

2. Experimental

2.1. Raw materials and synthesis procedure

Commercially available polyorganosilazane HTT1800 (Clariant GmbH, Germany) and polyorganosiloxane Polyramic RD-684a (Starfire Systems Inc., USA) were used as starting precursors, in the following denoted as POLYR and HTT, respectively.

Hydrosilylation reaction was carried out in argon atmosphere using standard Schlenk techniques. First, different amounts of divinylbenzene (DVB, p-divinylbenzene, 85%, Sigma–Aldrich, UK) (Table 1) were added to 20 g RD/HTT under magnetic stirring, followed by dropping of 10 ppm platinum catalyst relative to POLYR/HTT amount. As platinum source Pt(0)-1,3-divinyl-1,1,3,3-tetramethyldisiloxane, diluted in xylene (Sigma–Aldrich, UK) was used. The mixture was kept at 120 °C for 12 h. The obtained cured material was placed in a horizontal tube-furnace with standard Schlenk-technique, first cross-linked at 230 °C for 2 h and finally pyrolyzed at 1100 °C for 2 h under argon atmosphere, with heating rate of 100 °C throughout the process.

Table 1
Amounts and ratio of DVB used to modify POLYR and HTT polymers.

	PD1	PD2	PD3
POLYR 20 g	1.5 g (50%)	3 g (100%)	8 g (266%)
	HD1	HD2	HD3
HTT 20 g	8 g (50%)	16 g (100%)	32 g (200%)

2.2. Preparation of electrodes and cells

The obtained ceramic powders were first ground in a mortar and then sieved through a 40 μm-mesh. Then 85 wt.% sample material (active mass) were mixed with 5 wt.% Carbon black SuperP® (Timcal Ltd., Switzerland) and 10 wt.% polyvinylidene fluoride (PVdF, SOLEF Solvay, Germany) dissolved in N-methyl-2-pyrrolidone (NMP, BASF, Germany). The obtained slurry was homogenized and tape casted on the rough side of 10 μm thin copper foil (SE-Cu58, Schlenk Metallfolien, Germany) using a hand blade coating technique. After drying at 80 °C for 24 h, electrodes were cut, weighted and dried under vacuum at 80 °C for 24 h in a Buchi oven. Vacuum dried electrodes were finally transferred to an argon filled glove box (MBraun Glove Box Systems) for testing-cell assembly.

Half-cells of two-electrode Swagelok® type were assembled for electrochemical tests, using a metallic lithium foil (99.9% purity, Alfa Asear, USA) as reference/counter electrode, 1 M $LiPF_6$ in EC:DMC, ratio 1:1 (LP30, Merck KGaA, Germany) as electrolyte and Whatman™ glass fiber filter (Whatman™, UK) as separator.

2.3. Electrochemical studies

Hermetically closed cells were connected to VMP3 multi-potentiostat (BioLogic Science Instruments, France) and studied by galvanostatic cycling with potential limitation (GCPL) between 0.005 V and 3 V (E vs. Li/Li^+). All the potentials within this manuscript are referred to potential of Li/Li^+ reaction. The following current rates were applied for lithium insertion/extraction: 2× C/20 ($18.6\,mA\,g^{-1}$), 10× C/10 ($37.2\,mA\,g^{-1}$), 20× C/5 = ($74.4\,mA\,g^{-1}$), 30× C/2 ($186\,mA\,g^{-1}$), 50× C ($372\,mA\,g^{-1}$) followed by 2× C/20 ($18.6\,mA\,g^{-1}$). The same rate was used for charge (C) and discharge (D) and measured capacities were recalculated to the initial amount of active mass for data analysis.

2.4. Characterization

The amorphous structure of the pyrolyzed ceramics was proven by X-ray powder diffraction (XRD) in transmission geometry with a STOE STADI P (STOE and Cie GmbH, Germany) equipped with Mo K_α radiation. Micro-Raman spectra were recorded with a confocal micro-Raman spectrometer Horiba HR800 (Horiba, Japan) with an Ar ion laser at a wavelength of 514 nm. For the chemical analysis of the samples, the carbon content was determined by a carbon analyzer (Leco C-200, Leco Corporation, USA) and the oxygen and nitrogen content measured by a N/O analyzer (Leco TC-436, Leco Corporation, USA). The silicon fraction was calculated as the difference to 100% of the sum of the wt.%-values of carbon, nitrogen and oxygen, assuming a negligibly small amount of hydrogen in the analyzed samples and no other elements present.

3. Results and discussion

3.1. Determination of the theoretical content of DVB

Although previous investigations [21,25–28] have confirmed the feasibility of modifying Si-polymers containing Si—H groups by DVB addition via a hydrosilylation reaction, only few studies considered the molar ratio of Si—H to vinyl groups [27]. In our work, we first calculated the stoichiometric amount of DVB required for a complete hydrosilylation reaction of the POLYR and HTT polymers in order to later determine the number of Si—H groups that have reacted with DVB. The molecular structure of POLYR, HTT and DVB are presented in Fig. 1. If considering one structural unit of POLYR as 1 mol, it contains 2 mol Si—H group. Accordingly, the mass of POLYR carrying 2 mol Si—H is 886 g/mol. For complete consumption of 2 mol of Si—H bonds, the theoretically required amount of DVB is 1 mol, namely 130 g. For the 20 g POLYR used in our work, the stoichiometric amount of DVB amounts 3.0 g. The content of DVB necessary for the reaction of all Si—H groups of 20 g HTT was calculated analogously and amounts 16 g.

In order to systematically investigate the hydrosilylation reaction between DVB and the Si-polymers, amounts of DVB lower/equal/higher than that of the stoichiometric ratio were used for POLYR and HTT modification, respectively (Table 1).

3.2. Hydrosilylation reaction of DVB with POLYR and HTT

After 8 h reaction time at 120 °C, the POLYR-DVB mixtures transformed from viscous, transparent liquids into translucent, gelled substances, while the HTT-DVB reaction formed a gel with a sticky, milky appearance. The cured materials were then examined by FTIR. The recorded spectra are presented in Fig. 2. For a quantitative comparison, the intensity of all bands is normalized to the $Si{-}CH_3$ band at 1250 cm^{-1}, which is considered inactive in the polymer modification reactions.

For the POLYR-DVB system, the main absorption bands are associated to Si—H (2160 cm^{-1}), $Si{-}CH{=}CH_2$ (1400, 1600 cm^{-1}), $Si{-}CH_3$ (1260 cm^{-1}), Si—O (1010, 1100 cm^{-1}), $-CH{=}CH_2$ (900 cm^{-1}), Si—C, Si—H and phenyl C—H bonds (overlapping at 800 cm^{-1}), as well as to Si—O—Si (500, 700 cm^{-1}) units (Fig. 2a) [28]. The difference between the mixture of POLYR with DVB after 0 and 8 h is the decrease in the intensity of the $-CH{=}CH_2$ vibration at 900 cm^{-1}. The decrease in vinyl-vibration is also in agreement with the vanishing of the Si—H band located at 2160 cm^{-1}. A slight residue of Si—H still remains after 8 h reaction time (sample PD1), due to the under-stoichiometric composition of the reaction agents, while the Si—H vibration disappears for the samples PD2 and PD3 (Fig. 2b) proving completed hydrosilylation. This result corresponds to the calculation of the critical amount of DVB for the complete consumption of Si—H groups in POLYR.

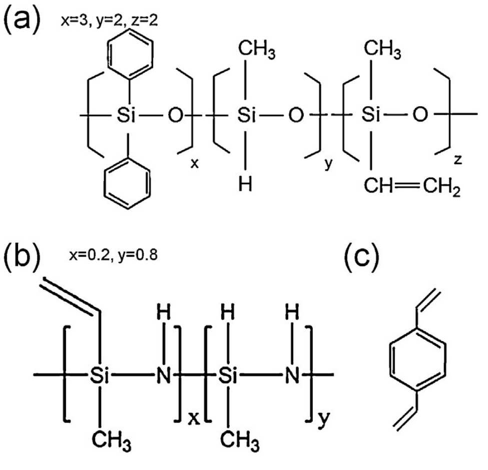

Fig. 1. Structure of the (a) POLYR, (b) HTT and (c) DVB.

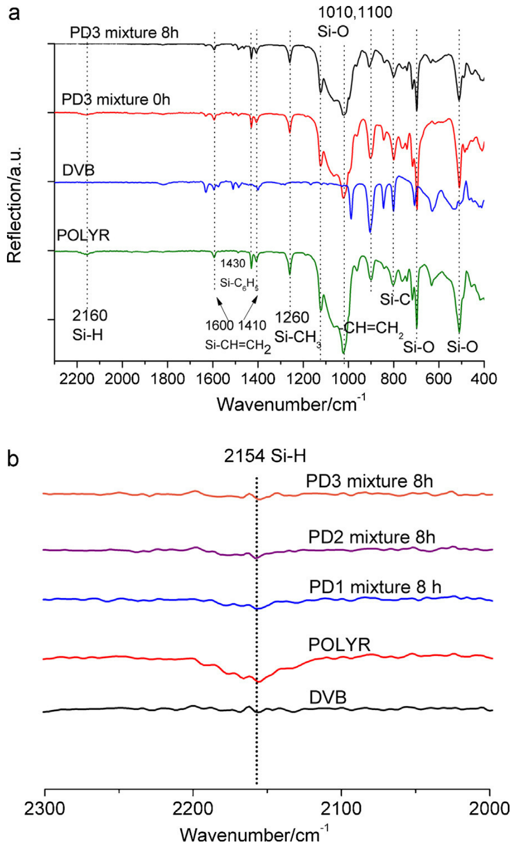

Fig. 2. FTIR spectra of POLYR-based samples.

The FTIR spectra of pure HTT, DVB and cured HTT-DVB mixtures are presented in Fig. 3a. The Si-polymer HTT shows a Si—H band with strong intensity due to the high amount of Si—H groups related to the monomeric unit. The band intensity of Si—H decreases with increasing DVB content from sample HD1–HD3, demonstrating that the hydrosilylation reaction took place. However, for stoichiometric and excess amounts of DVB not all Si—H groups were consumed by the DVB-vinyl groups.

It should be noted that the estimation of DVB amounts might not be directly applicable in the practical case. POLYR has a low fraction of Si—H and the insertion of large DVB units (with voluminous phenyl group) via the hydrosilylation reaction does not encounter much resistance due to steric hindrance, while the insertion of bulky DVB into the polymeric units of Si—H rich HTT could be difficult [27,28]. These molecular features have to be considered to be responsible for the insufficient consumption of Si—H groups in the case of the polymer HTT. Maddocks et al. mentioned that a higher concentration of DVB may cause steric hindrance during the reaction, restricting the number of sites on the polymer available for hydrosilylation and therefore resulting in bonding of only one vinyl group of DVB [28]. Dibandjo et al. reported that the 200% stoichiometric amount of DVB consumed all the Si—H groups

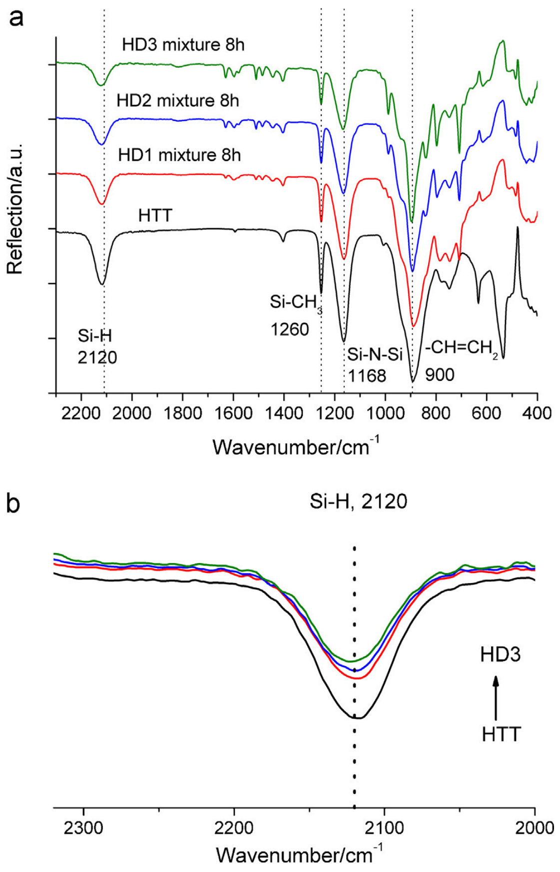

Fig. 3. FTIR spectra of HTT-based samples.

of 1,3,5,7-tetramethyl-1,3,5,7-tetracyclotetrasiloxane (TMTS), but Si—H still remained for polyhydridomethylsiloxane (PHMS200) precursor with this over-stoichiometric DVB amount [27].

To summarize the FTIR study, for both POLYR and HTT, an increasing Si—H consumption with increasing addition of DVB by hydrosilylation reaction was confirmed. The results revealed that the theoretical stoichiometric amount of DVB works for POLYR, while for HTT a significant amount of residual Si—H groups remains, even at 200% stoichiometric excess of DVB to HTT.

3.3. Structure and composition of the pyrolyzed material

For the characterization of the carbon phase formed after pyrolysis of the polymeric samples Raman spectra were recorded (Fig. 4). The characteristic carbon vibrations appear in all spectra: the disorder-induced D band at 1350 cm^{-1}, the G band at 1582 cm^{-1} due to in plane bond stretching of sp^2 carbon, the 2D vibrations at 2440, 2700 and 3200 cm^{-1}representing the overtone of the D mode and the D+G combination band at 2950 cm^{-1} also induced by carbon disorder [29–31]. It is found that the Raman spectra of all ceramics show a similar pattern indicating that the amount of DVB modification did not affect the type of carbon structure. The absolute intensity ratio of the $I(\mathrm{D})/I(\mathrm{G})$ peak was calculated and found to be stable, ranging from 1 to 1.2 for all samples. No trend with the increase in DVB/carbon content is found. The strong intensity of the D band and 2D vibrations outlines the disordered nature of the free carbon within the ceramic microstructure.

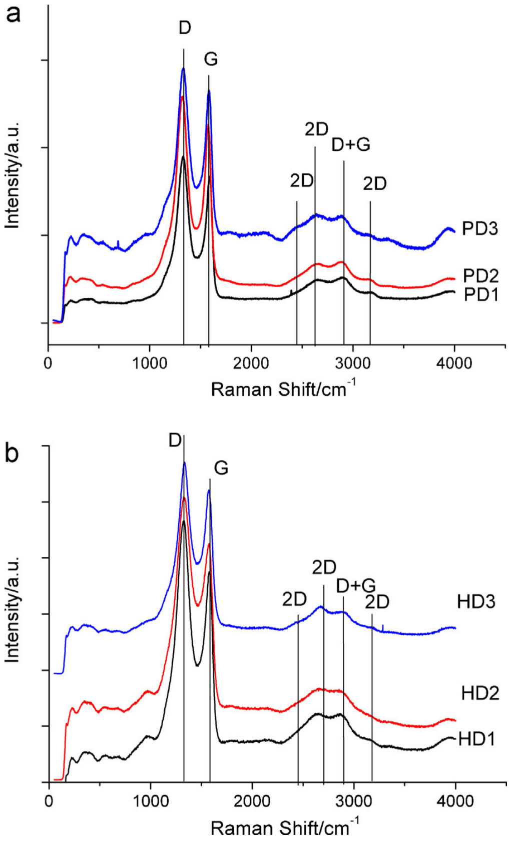

Fig. 4. Raman spectra of (a) POLYR and (b) HTT derived ceramics.

Elemental analysis has been carried out in order to determine the chemical composition of the samples. In Table 2 the results of the elemental analysis and that of the free carbon content as calculated using a common approach of Soraru et al. [32] are listed. With increasing amount of DVB the absolute and free carbon content increase. Fig. 5 presents the dependence of the free carbon content on the DVB addition. For POLYR-derived materials a "saturation"

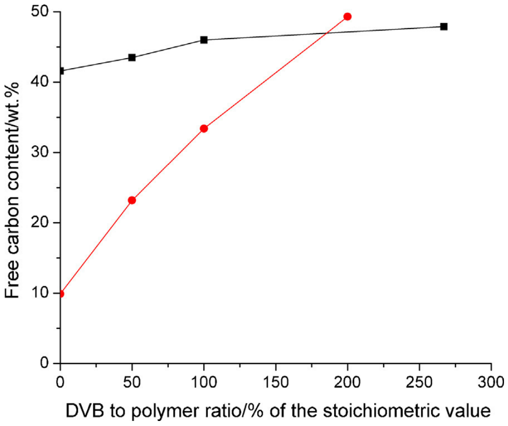

Fig. 5. Free carbon content as a function of DVB to polymer ratio for POLYR and HTT, squares represent POLYR, circles HTT composites.

Table 2
Elemental composition of the investigated materials.

Sample	Composition (wt.%)				Empirical formula	Free Carbon (wt.%)
	Si	C	O	N		
SiOC[a]	33.2	49.2	17.5	–	$SiO_{0.93}C_{3.46}$	41.6
PD1	32.0	50.7	17.2	–	$SiO_{0.95}C_{3.71}$	43.5
PD2	30.3	52.5	17.2	–	$SiO_{1.00}C_{4.05}$	46.0
PD3	29.1	53.9	17.0	–	$SiO_{1.03}C_{4.34}$	47.9
SiCN[b]	56.2	18.8	3.4	21.6	$SiO_{0.11}C_{0.78}N_{0.77}$	9.9
HD1	48.7	32.0	1.4	17.9	$SiO_{0.06}C_{1.54}N_{0.74}$	23.2
HD2	41.7	39.6	1.2	17.5	$SiO_{0.05}C_{2.22}N_{0.84}$	33.4
HD3	32.0	55.2	1.8	11.0	$SiO_{0.10}C_{4.04}N_{0.69}$	49.3

[a] Pure POLYR pyrolyzed at 1100 °C [20].

[b] Pure HTT pyrolyzed at 1100 °C [14].

Table 3
Electrochemical parameters calculated according to the results shown in Figs. 6–9 (HTT not included as found electrochemically inactive [14]).

	SiOC[a]	PD1	PD2	PD3	HD1	HD2	HD3
1st cycle C_{Ch} [mAh g^{-1}]	872	849	977	629	136	477	574
1st cycle C_{rev} [mAh g^{-1}]	536	478	603	344	69	278	347
1st cycle C_{Irrev} [mAh g^{-1}]	336	371	374	285	67	199	227
114th cycle C_{rev} [mAh g^{-1}]	496	198	564	378	88	314	402
1st cycle C_{rev} recovered below 1.5 V [%]	95	89	88	90	78	91	91
η [%]	61.5	56.3	61.7	54.7	50.6	58.3	60.5
η' [%]	92.5	41.4	93.5	109.9	127.5	112.9	115.9

[a] Pure POLYR pyrolyzed at 1100 °C [20].

of the free carbon is found at more than 100% of stoichiometric addition of DVB. This finding corresponds well with the FTIR results demonstrating that the Si—H groups have been almost completely reacted at the calculated 100% stoichiometric DVB content for POLYR. HTT-derived materials, on the contrary, exhibit a strong increase of the free carbon content throughout the investigated composition range. This result is again in agreement with our FTIR results, which revealed that the Si—H groups were not completely consumed.

3.4. Electrochemical characterization

3.4.1. POLYR-derived ceramics

The first galvanostatic lithiation/delithiation cycle of POLYR-based samples measured with a current rate of C/20 is presented in Fig. 6. The corresponding capacity values for the first Li-insertion (charging) C_{ch} and Li-extraction (discharging) C_{rev}, the irreversible capacity C_{irr}, the coulombic efficiency η and the cycling stability parameter η' are summarized in Table 3. The irreversible capacity represents the amount of charge which is not restored during the first discharging process and the coulombic efficiency η is the quantity of charge captured irreversibly within the first cycle and is estimated by the ratio $C_{1st,\,rev}/C_{1st,\,ch} \times 100\%$. In order to evaluate the stability of the material during extended cycling, $\eta' = C_{114th,\,rev}/C_{1st,\,rev} \times 100\%$ is calculated. The percentage of the charge recovered below 1.5 and 1 V, which is important for practical application as anode material, is also included in Table 3. For comparison, the electrochemical values measured for unmodified POLYR are shown as well [20]. The measured 1st lithiation capacities amount 866 mAh g^{-1} for the unmodified SiOC, 849 mAh g^{-1} for PD1, 977 mAh g^{-1} for PD2 and 629 mAh g^{-1} for PD3, while the recovered capacities during the first extraction are 532, 478, 603 and 344 mAh g^{-1}, respectively. These results do not show a clear trend in capacity increase with increasing DVB content, although the best performance has been achieved for PD2 (100% stoichiometric amount of DVB). The best columbic efficiency of 61% for the first cycle and significant charge recovery after prolonged cycling of 93.5% were also found for the sample PD2. Nevertheless, the electrochemical performance of PD2 in terms of cycling stability is lower in comparison to pure POLYR. Although the first reversible capacity is higher (603 vs. 536 mAh g^{-1}), the PD2 sample is less stable during extended cycling when compared to pure POLYR [20].

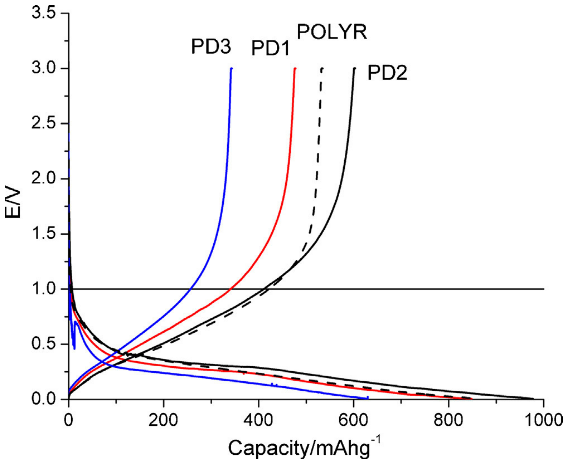

Fig. 6. Comparison of the first lithiation/delithiation cycle for POLYR-based samples at a current rate of 18.6 mA g^{-1} (C/20).

The shape of all insertion/extraction curves in Fig. 7 is similar. The majority of charge (~90%) for all investigated samples has been recovered between 0.005 and 1.5 V during the first discharge, which is consistent with the reports on disordered soft and hydrogen-containing carbon [33,34]. Similar voltage profiles were also analyzed for pure POLYR samples [19,20].

In Fig. 7 the extended cycling behavior at different current rates is shown. The performance at all rates reveals the electrochemical performance in the order PD2 > PD3 = PD1, similar to the first cycle observations (Fig. 6). All materials demonstrate a decrease in the average reversible capacity with increasing rates. The capacity at 1C-rate fades for PD1 and PD3 whereas PD2 presents a stable behavior with a capacity of 200 mAh g^{-1} which is lower than that of 304 mAh g^{-1} reported for pure POLYR [20]. When C/10 current is applied again after high rate cycling, the capacity almost equals or

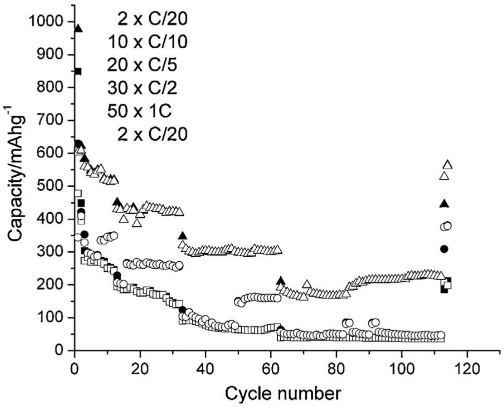

Fig. 7. Extended cycling performance of PD1 (squares), PD2 (triangles), PD3 (circles). Filled symbols are attributed to lithium insertion, empty to lithium extraction, meaning of current rates specified in Section 2.

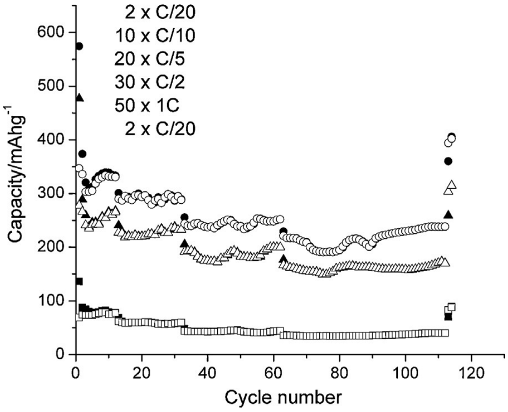

Fig. 9. Extended cycling performance of HD1 (squares), HD2 (triangles), HD3 (circles). Filled symbols are attributed to lithium insertion, empty to lithium extraction, meaning of current rates specified in Section 2.

exceeds the value of the first cycle extraction, which is illustrated by η' of about 93.5 and 110% for PD2 and PD3, respectively. Sample PD1 demonstrates the lowest extended cycling stability of 43.2%.

The measured electrochemical behavior can be explained by the high carbon content of pure POLYR. A further addition of carbon might give rise to structural changes of the SiOC matrix phase which outweighs its possible merits. According to our former observation free carbon is stabilized by the ceramic matrix [14,19,20]. However, once the amount of the carbon exceeds a certain threshold value, the stabilization of the SiOC phase might be lost and the carbon-enriched material does not show an enhanced electrochemical performance as compared to the unmodified ceramic.

3.4.2. HTT-derived ceramics

The first galvanostatic lithiation/delithiation with a current rate of C/20 for HTT-based samples is shown in Fig. 8, while the corresponding capacity and cycling efficiency values are summarized in Table 3. It is already known that SiCN ceramics obtained from bare HTT exhibits nearly no electrochemical activity due to a low carbon content and insufficient electronic conductivity [14]. As a result of DVB addition, charging and discharging capacity and columbic efficiency of the investigated samples were significantly increased.

The improvement of the electrochemical performance is directly attributed to the enhanced carbon content due to the chemical modification of HTT with carbon rich DVB. The best performance, $C_{\mathrm{ch}} = 574\,\mathrm{mAh\,g^{-1}}$, $C_{\mathrm{rev}} = 347\,\mathrm{mAh\,g^{-1}}$ and $\eta = 60.5\%$, was recorded for HD3, the samples with the highest free carbon content (49.3 wt.%).

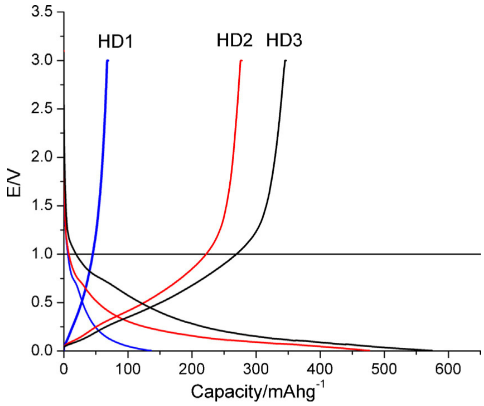

Fig. 8. Comparison of the first lithiation/delithiation cycle for HTT-based samples at a current rate of $18.6\,\mathrm{mA\,g^{-1}}$ (C/20).

Despite different capacities, the first lithiation/delithiation curves for all HTT-based ceramics show a similar profile. Most of the capacity is recovered below 1.5 V. Note that for the best performing sample HD3, the amount of capacity recovered below 1.5 V is similar to PD2, for both about 90%. In comparison, the materials produced without hydrosylilation reaction by Chen et al. [24], consisting of DVB-derived carbon dispersed within the SiCN ceramic, reveal a significantly higher hysteresis, with only ~50% of capacity recovered under 1 V condition.

Fig. 9 presents the extended cycling behavior of HTT-DVB samples at different current rates. In general, an increase in capacity and cycling performance with increasing DVB content is found. Similar to the POLYR-DVB samples, the achievable capacity diminishes with increasing cycling currents. At 1C, HD3 demonstrates an average capacity of $230\,\mathrm{mAh\,g^{-1}}$, which is similar to that of PD2. However, the initial capacity of HD3 at C/20 is much lower than that of PD2, namely 347 vs. $603\,\mathrm{mAh\,g^{-1}}$, respectively. According to elemental analysis HD3 shows a free carbon content of 49.3%, which is slightly higher than that of the POLYR-DVB samples. The free carbon content of HD1 and HD2 amounts 23.2 and 33.4 wt.% respectively. This correlation explains the best capacity performance of HD3 among the HTT-DVB series and similar capacity values to POLYR-DVB samples. Furthermore, this result outlines, that modification of the intrinsically carbon-poor SiCN precursor HTT, with increasing amounts of DVB directly affects the achievable Li-storing capacity. The registered capacities shown in Fig. 9 simultaneously increase with the amount of free carbon incorporated in the ceramic microstructure. In addition, the HD-series demonstrates a significant stability for cycling under high current rates. Moreover, relatively low losses of capacity when switching to higher currents, i.e. C/5 to C/2 and C/2 to C are analyzed for HD-based materials in comparison to PD-derived materials. The capacity of HTT-derived SiCN ceramics diminishes by 10–15% while losses of 25–35%, are registered for POLYR-based SiOC materials. Finally, low charge/discharge current rates applied after the high rates cycling procedure, a capacity higher than that of the initial value is recovered for all samples of the HD-series, as illustrated by the η' values (Table 3).

Fig. 10 presents the voltage–capacity dependences for lithium extraction, registered for 1st and 114th cycle for POLYR-derived (a) and HTT-derived (b) materials. The samples HD2 and HD3 show

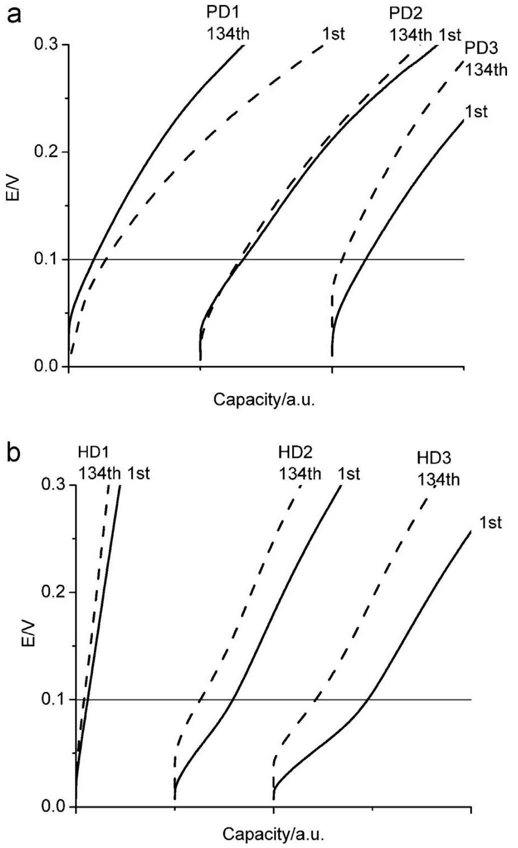

Fig. 10. Comparison of the first and last extraction cycle with C/20 rate for (a) POLYR-derived and (b) HTT-derived samples. For better comparison the graph are shifted with respect to *x*-axis origin for 50 and 100 mAh g^{-1} for PD2, HD2 and PD3, HD3, respectively.

a gently sloping plateau during the first discharge at a voltage lower than 0.1 V whereas POLYR-DVB samples do not show this kind of behavior. This voltage plateau has been reported by Fukui et al. [13] for SiOC based anodes and was attributed to the presence of closed micropores within the ceramic. A similar plateau has been discussed by Reinold et al. [35] for carbon-rich SiCN. No “micropore plateau” was found by Chen et al. [24] for DVB-derived carbons dispersed in SiCN ceramic. The charge recovered in this interval of the potential, i.e. between 0 and 0.1 V vs. Li/Li$^+$, comes from lithium storage in micropores. The highest “micropore capacity” of approximately 50 mAh g^{-1} was found for HD3, while 30 mAh g^{-1} is recovered by the sample HD2. Fukui et al. and Reinold at al. [13,35] found that the plateaus vanish after subsequent cycling so that almost no contribution of the micropores to the capacity can be seen after more than 50 cycles. The fading of the “micropore plateau” with subsequent cycling was attributed to some microstructural changes in the material with ongoing insertion/extraction of lithium ions. Indeed, the samples HD2 and HD3 demonstrate the diminution of “micropore” capacity of more than 50% after 114 cycles (to 12 and 22 mAh g^{-1}, respectively). Nevertheless, much higher cycling stability at higher current rates (C/2, 1C) is measured for HTT-derived materials in comparison to POLYR-based samples, which exhibit no “micropore-plateau”. Our study confirms the findings of Reinold et al. that the presence of micropores leads to an enhanced stability of the material toward prolonged cycling with high current rates.

4. Conclusions

Two different starting polymers providing low (HTT) and high (POLYR) carbon content were chemically modified with lower, equal and higher than stoichiometric amounts of DVB and subsequently converted at 1100 °C into amorphous ceramics. For POLYR-derived SiCO materials a “saturation” of free carbon is found if more than 100% of stoichiometric DVB amount is added. HTT-derived SiCN materials demonstrate a strong increase of the free carbon content throughout the investigated composition range. FTIR spectroscopy measurements show that a complete reaction of all Si—H groups does not occur in the case of HTT, probably due to steric hindrance. Raman spectra revealed no significant difference in the microstructure of the formed carbon phase among all investigated ceramics.

The enhancement of the electrochemical properties in terms of lithium insertion/extraction with increasing amount of DVB is found for HTT-based SiCN materials while POLYR-derived composites perform worse than that of the SiOC ceramic derived from the non-modified Si-polymer. Although the first reversible capacity of the best performing HTT-ceramic (HD3) is lower than that of POLYR-based ceramic (PD2), namely 347 mAh g^{-1} vs 603 mAh g^{-1}, the former one demonstrates an improved cycling stability and significantly lower losses with increasing cycling current rates. Moreover, cycling with the rate C the HD3 electrode recovers the same capacity as the PD2 sample (~230 mAh g^{-1}). The high cycling stability of polysilazane-derived samples may be attributed to the presence of micropores, which stabilize the ceramic microstructure.

Consequently, our study unambiguously demonstrates that increasing the free carbon content via modification of the Si-polymer with DVB improves the electrochemical performance of the resulting SiOC and SiCN ceramics only in the case of intrinsically carbon-poor preceramic polymers. The introduction of carbon to carbon-rich materials might give rise to structural changes of the SiOC matrix phase which stabilizes the free carbon. If the amount of the carbon exceeds a certain threshold value, the stabilization effect might be lost.

Acknowledgements

The authors are grateful for the financial support provided by the Tsinghua University under the program of “Ph.D. student scholarship for overseas graduate study”.

The financial support from the German Science Foundation within SPP1473/JP8 and SFB595/A4 programs is acknowledged. The authors thank to Mahdi Seifollahi Bazarjani, Benjamin Papendorf and Claudia Fasel for their help in the materials characterization.

References

[1] N. Takami, A. Satoh, M. Hara, T. Ohsaki, Structural and kinetic characterization of lithium intercalation into carbon anodes for secondary lithium batteries, Journal of the Electrochemical Society 142 (1995) 371.
[2] J.O. Besenhard, M. Winter, J. Yang, W. Biberacher, Filming mechanism of lithium–carbon anodes in organic and inorganic electrolytes, Journal of Power Sources 54 (1995) 228–231.
[3] W. Xing, A.M. Wilson, K. Eguchi, G. Zank, J.R. Dahn, Pyrolyzed polysiloxanes for use as anode materials in lithium-ion batteries, Journal of the Electrochemical Society 144 (1997) 2410.
[4] A.M. Wilson, J.N. Reimers, E.W. Fuller, J.R. Dahn, Lithium insertion in pyrolysed siloxane polymers, Solid State Ionics 74 (1994) 249.
[5] A.M. Wilson, G. Zank, K. Eguchi, W. Xing, J.R. Dahn, Pyrolysed silicon-containing polymers as high capacity anodes for lithium-ion batteries, Journal of Power Sources 68 (1997) 195.
[6] J.R. Dahn, A.M. Wilson, W. Xing, G.A. Zank, inventors; Dow Corning Corp., assignee. Electrodes for lithium ion batteries using polysilazanes ceramic with lithium. United States Patent US 5631106(A) May 20 (1997).

[7] M. Hara, A. Satoh, N. Takami, T.T. Ohsaki, Structural and electrochemical properties of lithiated polymerized aromatics – anodes for lithium-ion cells, Journal of Physical Chemistry 99 (1995) 16338.

[8] L.J. Ning, Y.P. Wu, L.Z. Wang, S.B. Fang, R. Holze, Carbon anode materials from polysiloxanes for lithium ion batteries, Journal of Solid State Electrochemistry 9 (2005) 520–523.

[9] R. Kolb, C. Fasel, V. Liebau-Kunzmann, R. Riedel, SiCN/C-ceramic composite as anode material for lithium ion batteries, Journal of the European Ceramic Society 26 (2006) 3903.

[10] M. Graczyk-Zajac, G. Mera, J. Kaspar, R. Riedel, Electrochemical studies of carbon-rich polymer-derived SiCN ceramics as anode materials for lithium-ion batteries, Journal of the European Ceramic Society 30 (2010) 3235.

[11] J. Kaspar, G. Mera, A.P. Nowak, M. Graczyk-Zajac, R. Riedel, Electrochemical study of lithium insertion into carbon-rich polymer-derived silicon carbonitride ceramics, Electrochimica Acta 56 (2010) 174.

[12] H. Fukui, H. Ohsuka, T. Hino, K. Kanamura, Preparation of microporous Si—O—C composite material and its lithium storage capability, Chemistry Letters 38 (2009) 86.

[13] H. Fukui, H. Ohsuka, T. Hino, K. Kanamura, A Si—O—C composite anode: high capability and proposed mechanism of lithium storage associated with microstructural characteristics, ACS Applied Materials and Interfaces 2 (2010) 998.

[14] M. Graczyk-Zajac, C. Fasel, R. Riedel, Polymer-derived-SiCN ceramic/graphite composite as anode material with enhanced rate capability for lithium ion batteries, Journal of Power Sources 196 (2011) 6412.

[15] D. Ahn, R. Raj, Thermodynamic measurements pertaining to the hysteretic intercalation of lithium in polymer-derived silicon oxycarbide, Journal of Power Sources 195 (2010) 3900.

[16] P.E. Sanchez-Jimenez, R. Raj, Lithium insertion in polymer-derived silicon oxycarbide ceramics, Journal of the American Ceramic Society 93 (2010) 1127.

[17] D. Ahn, R. Raj, Cyclic stability and C-rate performance of amorphous silicon and carbon based anodes for electrochemical storage of lithium, Journal of Power Sources 196 (2011) 2179.

[18] P. Dibandjo, M. Graczyk-Zajac, R. Riedel, V.S. Pradeep, G.D. Soraru, Lithium insertion into dense and porous carbon-rich polymer-derived SiOC ceramics, Journal of the European Ceramic Society 32 (2012) 2495.

[19] M. Graczyk-Zajac, L. Toma, C. Fasel, R. Riedel, Carbon-rich SiOC anodes for lithium-ion batteries: Part I. Influence of material UV-pre-treatment on high power properties, Solid State Ionics 225 (2012) 522.

[20] J. Kaspar, M. Graczyk-Zajac, R. Riedel, Carbon-rich SiOC anodes for lithium-ion batteries: Part II. Role of thermal cross-linking, Solid State Ionics 225 (2012) 527.

[21] H.J. Kleebe, Y.D. Blum, SiOC ceramic with high excess free carbon, Journal of the European Ceramic Society 28 (2008) 1037.

[22] J. Cordelair, P. Greil, Electrical conductivity measurements as a microprobe for structure transitions in polysiloxane derived SiOC ceramics, Journal of the European Ceramic Society 20 (2000) 1947.

[23] M. Wilamowska, M. Graczyk-Zajac, R. Riedel, Composite materials based on polymer-derived SiCN ceramic and disordered hard carbons as anodes for lithium-ion batteries, Journal of Power Sources (2013) (in press).

[24] Y. Chen, C. Li, Y. Wang, Q. Zhang, C. Xu, B. Wei, L. An, Self-assembled carbon–silicon carbonitride nanocomposites: high-performance anode materials for lithium-ion batteries, Journal of Materials Chemistry 21 (2011) 18186.

[25] X. Liu, M.C. Zheng, K. Xie, J. Liu, The relationship between the electrochemical performance and the composition of Si—O—C materials prepared from a phenyl-substituted polysiloxane utilizing various processing methods, Electrochimica Acta 59 (2012) 304.

[26] Y.D. Blum, D.B. Macqueen, H.J. Kleebe, Synthesis and characterization of carbon-enriched silicon oxycarbides, Journal of the European Ceramic Society 25 (2005) 143.

[27] P. Dibandjo, S. Dire, F. Babonneau, G.D. Soraru, Influence of the polymer architecture on the high temperature behavior of SiCO glasses: a comparison between linear- and cyclic-derived precursors, Journal of Non-Crystalline Solids 356 (2010) 132.

[28] A.R. Maddocks, J.M. Hook, H. Stender, A.T. Harris, Heterogeneously catalysed crosslinking of polycarbosilane with divinylbenzene, Journal of Materials Science 43 (2008) 2666.

[29] A.C. Ferrari, Raman spectroscopy of graphene and graphite: disorder, electron–phonon coupling, doping and nonadiabatic effects, Solid State Communications 143 (2007) 47.

[30] M.A. Pimenta, G. Dresselhaus, M.S. Dresselhaus, L.G. Cancado, A. Jorio, R. Saito, Studying disorder in graphite-based systems by Raman spectroscopy, Physical Chemistry Chemical Physics 9 (2007) 1276.

[31] N. Larouche, B.L. Stansfield, Classifying nanostructured carbons using graphitic indices derived from Raman spectra, Carbon 48 (2010) 620.

[32] G.D. Soraru, S. Modena, E. Guadagnino, P. Colombo, J. Egan, C. Pantano, Chemical durability of silicon oxycarbide glasses, Journal of the American Ceramic Society 85 (2002) 1529.

[33] T. Zheng, W.R. Mckinnon, J.R. Dahn, Hysteresis during lithium insertion in hydrogen-containing carbons, Journal of the Electrochemical Society 143 (1996) 2137.

[34] J.R. Dahn, T. Zheng, Y. Liu, J.S. Xue, Mechanisms for lithium insertion in carbonaceous materials, Science 270 (1995) 590.

[35] L.M. Reinold, M. Graczyk-Zajac, Y. Gao, G. Mera, R. Riedel, Carbon-rich SiCN ceramics as high capacity/high stability anode material for lithium ion batteries, Journal of Power Sources 236 (2013) 224.

Electrochimica Acta 115 (2014) 665–670

Contents lists available at ScienceDirect

Electrochimica Acta

journal homepage: www.elsevier.com/locate/electacta

Determination of the chemical diffusion coefficient of Li-ions in carbon-rich silicon oxycarbide anodes by electro-analytical methods

Jan Kaspar*, Magdalena Graczyk-Zajac, Ralf Riedel

Institut für Materialwissenschaft, Technische Universität Darmstadt, Jovanka-Bontschits-Straße 2, 64287 Darmstadt, Germany

ARTICLE INFO

Article history:
Received 4 October 2013
Received in revised form 23 October 2013
Accepted 24 October 2013
Available online 7 November 2013

Keywords:
Li-ion diffusion coefficient
silicon oxycarbide anode
PITT
GITT
EIS

ABSTRACT

The diffusion coefficient of Li-ions (D_{Li}^{+}) within carbon-rich silicon-oxycarbide ceramic anodes of specific chemical composition $SiO_{0.95}C_{3.72}$ is determined by potentiostatic and galvanostatic intermittent titration technique (PITT, GITT) and electrochemical impedance spectroscopy (EIS). The estimated values for D_{Li}^{+} range between 10^{-9} and 10^{-11} cm^2 s^{-1}, dependent on the applied method. The observed variation of D_{Li}^{+} is in a comparable range as reported for disordered carbons, well reflecting the Li-ion storage in the segregated free carbon phase in the amount of about 43 wt-% within the SiOC microstructure. However, in contrast to graphite and disordered carbons, the diffusion coefficient of lithium within carbon-rich SiOC is less potential dependent. This feature is discussed with respect to the particular morphology of the free carbon phase.

1. Introduction

The electrochemical properties of polymer- and sol-gel- derived silicon oxycarbide (SiOC) ceramics have been studied in the middle of the 1990's by Dahn et al. Accordingly, SiOC was identified as potential host material for Li-ions [1–6]. Within the last few years, among the various chemical compositions of SiOC compounds, stoichiometries with an exceptional high content of carbon (> 50 wt-%) were further considered as perspective anode material in terms of high gravimetric capacity, rate capability and reliable cycling stability [7–16].

The microstructure of carbon-rich SiOC consists of an unique nano-heterogeneous network topology, composed of two interpenetrating amorphous phases: *i)* a Si-O-C glassy phase composed of $SiO_{4-x}C_x$ (x = 1 - 4) mixed bonds, embedding a *ii)* free disordered carbon phase [7,17–20]. In dependence on the amount of free carbon content, either carbon nano-domains (low amount of free C) or a carbon percolation network (high amount of free C) is formed as demonstrated by electrical conductivity measurements and TEM analysis [18,21–24]. The nature of the free carbon can be further described as a mixture of disordered carbon, graphite nano-crystallites and graphene sheets [7,12,13].

Whereas Li-ion intercalation into graphite is a staged process, Li insertion into carbon-rich SiOC compounds occurs majorly in form of adsorption and surface storage within the free carbon phase, similar to the storage in disordered carbon electrodes. Major host sites are the edges of graphene sheets, interstitial and defect sites, micro-pores, graphite nano-crystallites and interfacial adsorption at carbon-crystallite surfaces. The Si-O-C glassy phase on the contrary is considered to play a minor role in terms of the reversible storage process [7,12,13]. Complementary, the storage of Li-ions within the phase-boundary of the Si-O-C glassy and free carbon phase, described by the nano-domain model, is discussed in the literature as well [25,26]. The question of the rate of the Li-ion transport within silicon oxycarbide of chemical composition $SiO_{0.85}C_{1.98}$ was initially addressed by D. Ahn within his PhD work [27]. In this work D_{Li}^{+} values were determined by means of PITT (10^{-7} - 10^{-9} cm^2 s^{-1}) and GITT (10^{-8} - 10^{-10} cm^2 s^{-1}). Weidman et al. evaluated the Li-ion diffusivity within SiOC of the same composition ($SiO_{0.85}C_{1.98}$) by GITT to be 1.8 - 4.2 × 10^{-14} cm^2 s^{-1} [28]. For Si(B)CN-CNT electrodes, a Li-ion diffusivity of 10^{-9} - 10^{-12} cm^2 s^{-1} was analyzed by Bhandavat et al. [29,30].

The work presented in this article, relates to the determination of the chemical Li-ion diffusion coefficient within carbon-rich silicon oxycarbide of the specific composition $SiO_{0.95}C_{3.72}$ by different electro-analytical methods: *i)* potentiostatic intermittent titration technique (PITT), *ii)* galvanostatic intermittent titration technique (GITT) and *iii)* electrochemical impedance spectroscopy (EIS). All three techniques are well-established in the characterization of Li-ion battery electrodes and have been widely applied for a large variety of anode and cathode materials, i.e. graphite, disordered carbons, silicon, Li_xNiO_2, $Li_xCo_{0.2}Ni_{0.8}O_2$, etc. [31–39]. In addition we correlate the chemical diffusion coefficient with the unique morphological features of carbon-rich SiOC.

---

* Corresponding author. Tel.: +49 6151 16 6343; fax: +49 6151 16 6346.
E-mail address: kaspar@materials.tu-darmstadt.de (J. Kaspar).

0013-4686/$ – see front matter © 2013 Elsevier Ltd. All rights reserved.
http://dx.doi.org/10.1016/j.electacta.2013.10.184

Table 1
Elemental analysis data for the Si, O and C content. The weights and molecular fractions of silica, silicon carbide and free carbon were quantified according to reference [40].

	Si	O	C	SiO_2	SiC	Free C
wt-%	31.95	17.28	50.77	32.45	23.96	43.57
mol	1.14	1.08	4.23	0.54	0.60	3.63
mol-%	17.65	16.76	65.59	11.33	12.54	76.14
mol-% normalized	1.00	0.95	3.72			

2. Experimental

Carbon-rich SiOC was prepared by thermal conversion of commercially available polyorganosiloxane, namely *Polyramic RD-684a* (Starfire Systems Inc., USA). The polymer was thermally cross-linked at 350 °C for 2 h and then pyrolyzed at 1100 °C for 3 h under argon atmosphere for ceramization. Heating rates were set to 50 °C h^{-1} for cross-linking and 100 °C h^{-1} for pyrolysis. The heat treatment procedure was performed, using quartz equipment and standard Schlenk-technique. After pyrolysis the obtained sample was hand-ground to a fine powder and sieved < 40 μm for further handling.

The particle size distribution of the ceramic powder was measured by dynamic laser light scattering, using a Fritsch Analysette 22 COMPACT (Fritsch GmbH, Germany). The average particle size (D50-value) amounts 17 μm.

The chemical composition of the sample was determined by hot-gas extraction, using a Leco-200 carbon analyzer and Leco TC-436 N/O analyzer (both Leco Corporation, USA), whereas the amount of silicon in the sample was calculated as the difference to 100 wt-% of the sum of the wt-% values of carbon and oxygen, assuming negligibly amount of hydrogen and no other elements present in the sample. The analyzed composition of Si, O and C is presented in Table 1, including the corresponding molar fractions and equivalents of SiO_2, SiC and free C according to reference [40]. From this data the specific molecular formula $SiO_{0.95}C_{3.72}$ is derived for the compound with a molecular weight of 87.90 g mol^{-1}. Moreover, the density of the material was estimated as described by Martínez-Crespiera et al. and determined to be 2.09 g cm^{-3} [24].

For electrochemical measurements, electrodes composed of 85 wt-% SiOC active material, 5 wt-% Carbon Black SuperP (Timcal Ltd., Switzerland) and 10 wt-% polyvinylidene fluoride binder (PVdF, SOLEF Solvay, Germany) were prepared by tape-casting. The film thickness after drying of the tape was around 60 μm, with a loading of active material of about 2 mg cm^{-2}. Testing-cells of two-electrode Swagelok-type were assembled under protective argon-atmosphere, using metallic lithium (99.9% purity, Alfa Aesar, USA) as reference/counter electrode, 1 M $LiPF_6$ in EC:DMC ratio 1:1 (LP30, Merck KGaA, Germany) as electrolyte and Whatman glass fiber filter (Whatman, UK) as separator. Hermetically closed cells were cycled and analyzed with a VMP multipotentiostat (BioLogic Science Instruments, France) by potentiostatic and galvanostatic intermittent titration technique (PITT, GITT) and electrochemical impedance spectroscopy (EIS). PITT and GITT were performed within the potential range of 2 - 0.05 V, while in former potential steps of 50 mV at a current limit of 37 mA g^{-1} were applied. For GITT the current pulse were chosen to 37 mA g^{-1} for a duration of 15 min, followed by an open circuit voltage period of 4 h. EIS spectra were recorded at different states of charge within the frequency range of 100 kHz - 10 mHz. In order to realize an equilibrium state of the tested cell within EIS-sequences a holding time of 1 h was applied before each measurement.

Due to the little thickness of the tested electrodes of about 60 μm, the influence of Carbon black and PVDF on the electroanalytical response of SiOC could be excluded, since only for μm-thin electrodes PITT, GITT and EIS provide meaningful results for Li-insertion processes, as emphasized by Aurbach et al., [41] and references therein.

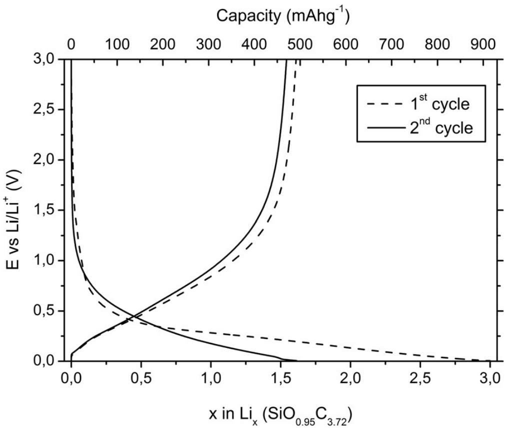

Figure 1. First and second galvanostatic discharge/charge curve of carbon-rich $SiO_{0.95}C_{3.72}$ at a current rate of 37 mA g^{-1}.

3. Results and discussion

General features of the galvanostatic discharging/charging curves (1st and 2nd cycle, 37 mA g^{-1}, 3 - 0.005 V) of $SiO_{0.95}C_{3.72}$ are presented in Figure 1. The obtained profile is in excellent agreement with our previous reports [11–13]. The anodic and cathodic curve progression exhibits significant similarities with the lithiation/delithiation characteristics of disordered soft or hydrogen containing carbons [42–44]. There are no distinct plateaus visible that indicate staged intercalation processes, but pronounced and continuously sloping and rising branches, illustrating Li-ion insertion and extraction within the free disordered carbon phase.

3.1. PITT

In potentiostatic intermittent titration technique, a constant potential is stepwise applied to the working electrode while the current response is analyzed. When the current drops under a defined value, the next potential step is applied. From the change in current and amount of charge transferred at each step (dQ), the Li-ion diffusion coefficient (D_{Li^+}) can be derived. The numerical integration of the transferred change at one potential step represents the differential capacity (C_{int}) according to equation 1.

$$C_{int}(E) = \frac{dQ(E)}{dE} \qquad (1)$$

The corresponding differential capacity plot (C_{int} *vs.* E) of a cycled $SiO_{0.95}C_{3.72}$ electrode is shown in Figure 2. In the cathodic branch of the curve, electrochemical activity starts around 1.1 V, without any characteristic peaks developing during Li-insertion. This observation corresponds well to the cathodic branch of the galvanostatic second cycle in Figure 1. In anodic response two broad peaks appear around 0.35 and 0.7 V during Li-ion extraction, not resolved in the galvanostatic second cycle discharge in Figure 1. Whereas the staged process of Li-ion intercalation into graphite bears characteristic peaks in the differential capacity progression, the Li-ion insertion into carbon-rich SiOC compounds occurs in form of adsorption within the disordered carbon phase. A broad distribution of adsorption site energies leads to the observed curve characteristics and the broad extraction peaks [32,33].

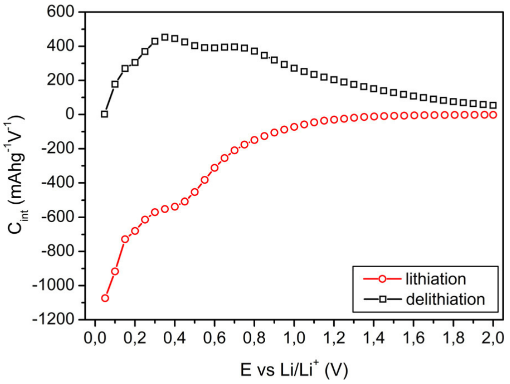

Figure 2. Differential capacity curve of $SiO_{0.95}C_{3.72}$ derived from PITT, resolution 50 mV.

Figure 3 presents the Li-ion diffusion coefficient in dependence of the potential (*log* D_{Li^+} *vs. E*), whereas D_{Li^+} was calculated by the well-established equation (Eq. 2), first derived by Weppner and Huggins [45]. The equation is based on the Fick's second law of diffusion and was specially refined for the processing of PITT data by Levi and Aurbach [46].

$$D = \left[\left(\frac{\sqrt{\pi} l I \sqrt{t}}{\Delta E}\right) / \frac{\Delta Q(E)}{\Delta E}\right]^2 \quad \text{at} \quad t << \tau \tag{2}$$

Here $I\,t^{1/2}$ represents the Cottrell slope obtained from the experimental *I vs. t* curve, $\Delta Q(E)/\Delta E$, quantifies the change in charge at each potential step (representing the differential capacity, according to Eq. 1) and l the characteristic diffusion length, approximated as half of the average particle size (8.5 μm). The equation is valid for sufficiently small time domains $t << \tau$, whereas τ represents the diffusion time constant, which is equal to l^2/D, for ensuring an accurate approximation of the Fickian diffusion principles.

In the relevant lower potential region (< 1 V, Figure 3), the order of magnitude of D_{Li^+} is estimated to 10^{-9} - 10^{-10} cm^2 s^{-1}. For comparison, the chemical diffusion of Li$^+$ in graphite evaluated by PITT is ranging between 10^{-9} - 10^{-11} cm^2 s^{-1} [31,32,36] and for amorphous disordered carbons 10^{-10} - 10^{-11} cm^2 s^{-1} [32,33]. For SiOC of specific chemical composition $SiO_{0.85}C_{1.98}$, the Li-ion diffusivity determined by PITT was estimated to 10^{-7} - 10^{-8} cm^2 s^{-1} [27], two orders of magnitude higher than the results presented in the current study.

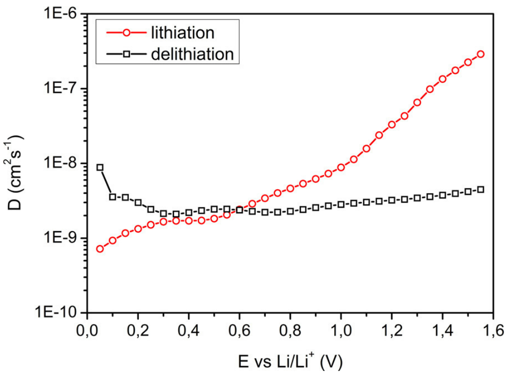

Figure 3. Potential dependent Li-ion diffusion coefficient in $SiO_{0.95}C_{3.72}$, evaluated by PITT, resolution 50 mV.

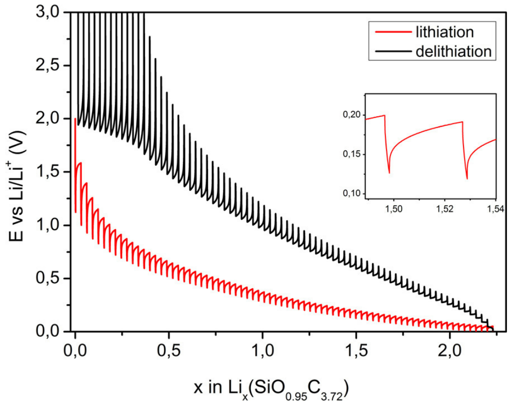

Figure 4. Galvanostatic intermittent titration curve of $SiO_{0.95}C_{3.72}$, current pulse 37 mA g^{-1}.

3.2. GITT

In galvanostatic intermittent titration technique, constant current pulses (I_p) are applied to the working electrode, alternating with open-circuit voltage periods (E_{OC}). During I_p sequences Li-ions insert into the electrode grains, while starting from the surface and building up a concentration gradient. During E_{OC} periods, equilibration occurs by Li-ion diffusion, causing a change in voltage over time. The change in voltage directly correlates with the change in Li-ion concentration and enables the calculation of D_{Li^+} within the active material.

The calculation of D_{Li^+} by GITT was accomplished by using Eq. 3, first derived by Weppner and Huggins. ΔE_t represents the change in potential when I_p is applied, corrected by the ohmic potential drop, ΔE_s quantifies the difference in the open circuit potential at the end of two sequential open-circuit relaxation periods, l equals the characteristic diffusion length (8.5 μm) and Δt_p is the time of pulse duration [45]. The differential capacity as a function of potential ($C_{int}(E)$) can be derived from GITT-data as well, according to Eq. 4 [35].

$$D = \left(\frac{4l^2}{\pi \Delta t_p}\right)\left(\frac{\Delta E_s}{\Delta E_t}\right)^2 at\, t << \tau \tag{3}$$

$$C_{int}(E) = \left(\frac{I \Delta t_p}{\Delta E_t}\right) \tag{4}$$

In Figure 4 the recorded galvanostatic intermittent titration curve of $SiO_{0.95}C_{3.72}$ is shown, from which the differential capacity (Figure 5) and chemical diffusion coefficient D_{Li^+} (Figure 6) were derived as a function of the potential. In the relevant lower potential region < 1 V, the chemical diffusion of Li-ions amounts 10^{-10} - 10^{-11} cm^2 s^{-1}, which is about one order of magnitude less than determined by PITT (10^{-9} - 10^{-10} cm^2 s^{-1}). Similar deviation between the results obtained by both techniques was reported for graphite and SiOC based electrodes before. For graphite, PITT suggested values of 10^{-9} - 10^{-11} cm^2 s^{-1}, whereas the results from GITT revealed diffusivities of 10^{-10} - 10^{-13} cm^2 s^{-1} [47]. D. Ahn determined D_{Li^+} values for $SiO_{0.85}C_{1.98}$ by GITT of 10^{-8} - 10^{-10} cm^2 s^{-1}, likewise one to two orders of magnitude lower than by PITT [27]. Controversially, Weidman et al. evaluated the Li-ion diffusivity within SiOC of the same composition ($SiO_{0.85}C_{1.98}$) by GITT to be 1.8 - 4.2 × 10^{-14} cm^2 s^{-1} [28]. In general a deviation in the order of magnitude of D_{Li^+} evaluated by GITT and PITT can be expected and originates from the methodology of both methods. For details, the interested reader is referred to reference [36].

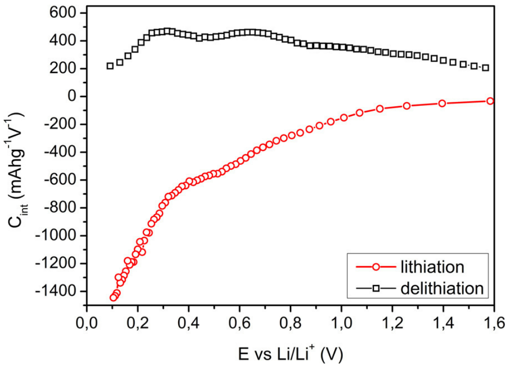

Figure 5. Differential capacity curve of $SiO_{0.95}C_{3.72}$, derived from GITT.

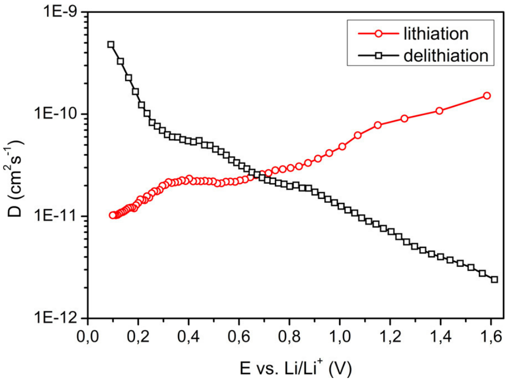

Figure 6. Potential dependent Li-ion diffusion coefficient in $SiO_{0.95}C_{3.72}$, evaluated by GITT.

3.3. EIS

In electrochemical impedance spectroscopy, an AC current of different frequency is successively applied to the testing cell and the dielectric response of the system is analyzed. The obtained data is commonly presented on a complex plane by a Nyquist plot. In general, the Nyquist plot of a Li-ion battery consists of one or two depressed semicircles in the high and middle-frequency range turning into a straight line, the so called Warburg-diffusion element, in the low frequency range with angles around 45°.

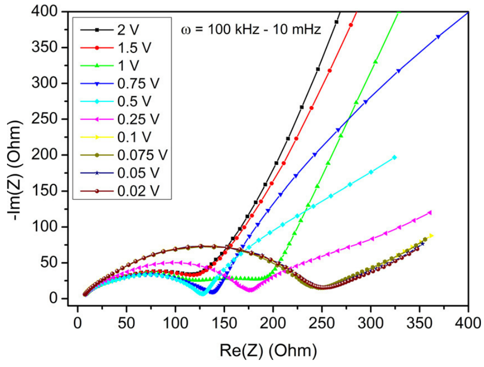

Figure 7. Nyquist plot of $Li_x(SiO_{0.95}C_{3.72})$ at different potentials/charge states.

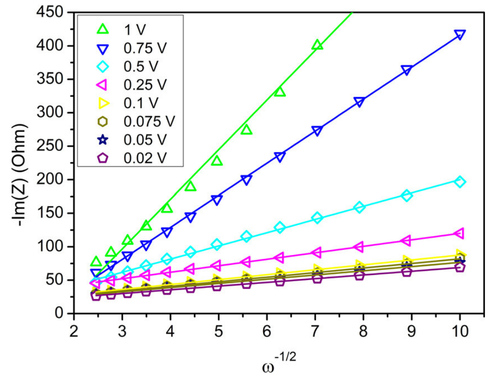

Figure 8. Warburg impedance–*Im(Z)* as a function of $\omega^{-1/2}$ in the low frequency region (165 mHz - 10 mHz) for $SiO_{0.95}C_{3.72}$ at different potentials/charge states.

In Figure 7, the impedance spectra recorded at different potentials for a cycled $SiO_{0.95}C_{3.72}$ electrode during galvanostatic discharging are shown. In all spectra the characteristic semicircle and Warburg-diffusion element appear. The semicircle originates from the electronic charge transfer resistance in the electrode and electrolyte, the double layer capacitance at the electrode-electrolyte interface and a capacitive component relating to the reference electrode, as already reported for various anode materials [31,33,34,39,47]. Within increasing Li-ion uptake and decreasing potential, the diameter of the semicircle changes from 135 Ω at 0.75 V to 250 Ω at 0.1 V. This increase in ohmic resistance correlates well with the progressive Li-storage in the free carbon network throughout the sample, which diminishes the intrinsic electrical conductivity.

The Warburg-diffusion element directly relates to the diffusivity of ionic species (i.e. Li-ions) within the cell and in particular within the working electrode, proceeding on the assumption, that diffusion within the electrolyte is much faster. Thus the Li-ion diffusivity can be calculated according to Eq. 5, derived by Ho et al. [48]. Here, σ presents the Warburg-coefficient, V_m the molar volume of the active material, z the valence state of the diffusing species, F Faraday's constant, A the surface area of the electrode and dE/dx the gradient of the slope of the galvanostatic discharge curve. For semi-infinite diffusion, σ can be extracted from the Nyquist plot, by plotting the imaginary part of the Warburg impedance *-Im(Z)* as a function of $\omega^{-1/2}$ in the diffusion controlled region (165 mHz - 10 mHz). According to Eq. 6, σ equals the slope of the obtained straight line [38].

$$D = \frac{1}{2}\left[\left(\frac{V_m}{\sigma z F A}\right)\left(\frac{dE}{dx}\right)\right]^2 \tag{5}$$

$$Z_w = \frac{\sigma}{\sqrt{\omega}} - i\frac{\sigma}{\sqrt{\omega}} \tag{6}$$

The *-Im(Z) vs.* $\omega^{-1/2}$ plots are presented in Figure 8 and the estimated diffusion coefficient as a function of the potential is shown in Figure 9. The derived D_{Li^+} values are ranging between 10^{-9} - 10^{-10} cm^2 s^{-1}, which is in agreement with the values obtained by PITT and one order of magnitude higher than that obtained from calculations performed by GITT. For a final overview, Figure 10 compares the obtained diffusion coefficients among the applied electro-analytical methods.

Former studies on the lithium diffusion coefficient in carbonaceous materials correlated the shape of the *D vs. E* curve with the nature of the Li-insertion/extraction process and with the extent of disorder in the intercalation host (see reference [33] and references therein). A close correlation between the minima in the

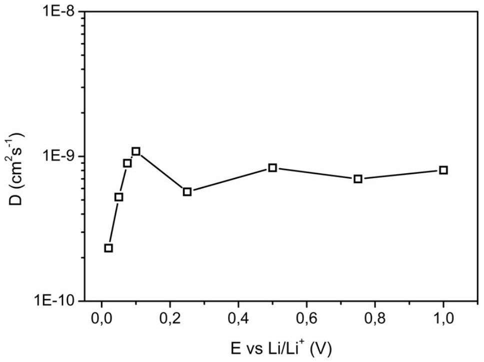

Figure 9. Potential dependent Li-ion diffusion coefficient within $SiO_{0.95}C_{3.72}$, evaluated by EIS.

D vs. E curve and the narrow slow cyclic voltammetry peaks were found for ordered synthetic graphite. It is stated that in the potential range where the phase transitions occurs, i.e. the potential of the voltammetric peaks, the *D* values are significantly low. These studies revealed that the lithium intercalation into graphite is combined with strong attractive interactions between the intercalating species, which slow down the diffusion in these two-phase regions. For disordered carbons broad maxima in the *D vs. E* curve were found and the interaction between inserting species were considered as dominated by coulombic repulsion between neighboring ions. The reason of the different behavior was related to the morphological difference between graphite and disordered carbons. Graphite sheets are assumed to have an infinite length, i.e. their flake size is large in comparison to the healing length of local distortions. Disordered carbons on the contrary exhibit a lateral flake size of ~10 Å, while bearing a healing length of ~5 Å, disabling any attractive interactions between Li species. In consequence, coulombic repulsion is the dominating effect between neighboring Li-ions and amongst the flake interspaces. In addition, there are various different Li-insertion sites in these carbons, in terms of different electrical conductivity, energetics of interaction and redox potentials [34]. Both factors are considered to be responsible for the diffusion maxima at intermediate potentials in the *D vs. E* curves recorded for disordered carbons.

Figure 10 presents the comparison of the Li-ion diffusion coefficients calculated by PITT, GITT and EIS as a function of the potential. Note that we consider the free carbon phase present within the studied sample as major reversible lithium storage host [7–16]. In contrast to graphite and disordered carbons, the obtained *D vs. E* curves exhibit a constant character. In particular, during Li-extraction no pronounced maxima or minima are found. A similar independence of $D_{Li}{}^+$ on the electrode potential was observed by D. Ahn, however this feature has not been analyzed in terms of the sample morphology [27]. This characteristic can be explained by the lateral flake size of the free carbon dispersed within the SiOC. The flake size amounts around 50 Å [13], which is about five times larger than that of disordered carbon discussed in reference [33]. On the other hand, the size of 50 Å is still a small distance in comparison to the ideal infinite length of graphite sheets. The broad extraction peaks found in the C_{int} *vs. E* curves obtained by PITT (Figure 2) and GITT (Figure 5) are not reflected in the *D vs. E* curves, suggesting that no staging mechanism takes place, as it is known for graphite. Neither comparable maxima to those registered for disordered carbons (see reference [33]) are present. We attribute this intermediate behavior to the morphology of the SiOC ceramic, in particular *i)* to the lateral flake size of the free carbon of about 50 Å and *ii)* to the embedded free carbon phase within the stabilizing Si-O-C network. The present flake size is just large enough to support local distortion around adsorbed Li-ions, since their critical healing length is about 5 Å, leading to weak attractive interactions among Li-insertion sites. In addition coulombic repulsion between the ionic species need to be considered as existent, since the carbon flake size is still small compared to the ideal infinitive length of graphite sheets. Both, the attractive and repulsion forces counteract each other excluding significant minima or maxima in the *D vs. E* curve. The second feature to emphasize is the Si-O-C glassy phase and the interface regime between Si-O-C and free carbon. There is a change from oxygen rich $SiO_{4-x}C_x$ (x = 1 - 4) structural units towards carbon rich ones, leading to local bond distortions and formation of voids and defect sites in this transition region [49]. We believe that the interface regime, which is not considered to host the Li-ions, enables a steady ionic transport throughout the material and accounts for a continuous lithium supply to the free carbon over a wide potential range. Hence, the analyzed Li-ion diffusion within carbon-rich SiOC is not strongly influenced by the potential, as it is the case for graphite and disordered carbons.

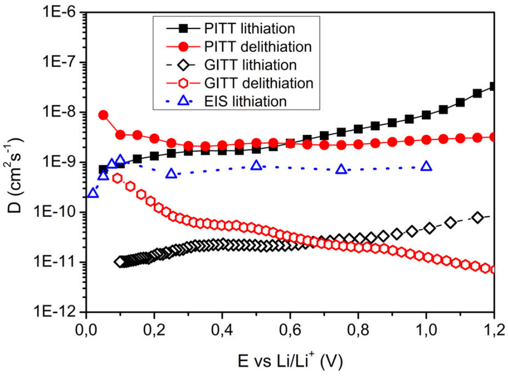

Figure 10. Comparison of the Li-ion diffusion coefficients obtained by PITT, GITT and EIS as a function of the potential.

4. Conclusions

In summary, the evaluation of Li-ion diffusion coefficients ($D_{Li}{}^+$) in carbon-rich SiOC with the specific chemical composition $SiO_{0.95}C_{3.72}$ was accomplished by three different electro-analytical methods, namely PITT, GITT and EIS. The obtained values for the Li-ion diffusivity were ranging between 10^{-9} - 10^{-11} cm^2 s^{-1}, in a similar order of magnitude than that reported for graphitic and disordered carbons. We explain this conformance and the excellent Li-ion transport properties by the beneficial nano-heterogeneous network morphology of the material. The sample comprises more than 43 wt-% of free carbon within its microstructure, determining the diffusion and Li-storage kinetics. Li-ions can easily diffuse within the formed carbon percolation network and be effectively stored. The diffusion of lithium ions in carbon-rich SiOC is less potential dependent as compared to graphitic and disordered carbon electrodes. It lead to the conclusion that the extent of disorder of the free carbon phase is higher than that in graphite but less than found for disordered carbon. Additionally, it should be pointed out that the transition regime between the free carbon and the Si-O-C glassy phase contributes supportively to the fast and steady Li-ion transport into the bulk of the sample by offering voids and a high amount of defect sites.

Acknowledgements

This work was financially support by the Deutsche Forschungsgemeinschaft (DFG), Bonn, Germany within the Priority Program

SPP1473/JP8 and the Collaborative Research Center SFB595/A4. The authors want to acknowledge K. Wissel for her help in the preparation of the electrodes and testing cells and S. Hesse and A. Uhl for their support in the determination of the particle size distribution.

References

[1] A.M. Wilson, J.N. Reimers, E.W. Fuller, J.R. Dahn, Solid State Ionics 74 (1994) 249–254.
[2] W. Xing, A.M. Wilson, K. Eguchi, G. Zank, J.R. Dahn, Journal of The Electrochemical Society 144 (1997) 2410–2416.
[3] W. Xing, A.M. Wilson, G. Zank, J.R. Dahn, Solid State Ionics 93 (1997) 239–244.
[4] A.M. Wilson, W. Xing, G. Zank, B. Yates, J.R. Dahn, Solid State Ionics 100 (1997) 259–266.
[5] A.M. Wilson, G. Zank, K. Eguchi, W. Xing, J.R. Dahn, Journal of Power Sources 68 (1997) 195–200.
[6] A.M. Wilson, G. Zank, K. Eguchi, W. Xing, B. Yates, J.R. Dahn, Chemistry of Materials 9 (1997) 1601–1606.
[7] H. Fukui, O. Hisashi, T. Hino, K. Kanamura, ACS Applied Materials & Interfaces 4 (2010) 998–1008.
[8] H. Fukui, H. Ohsuka, T. Hino, K. Kanamura, Journal of Power Sources 196 (2011) 371–378.
[9] H. Fukui, H. Ohsuka, T. Hino, K. Kanamura, Journal of the Electrochemical Society 158 (2011) A550–A555.
[10] P. Dibandjo, M. Graczyk-Zajac, R. Riedel, V.S. Pradeep, G.D. Soraru, Journal of the European Ceramic Society 32 (2012) 2495–2503.
[11] M. Graczyk-Zajac, L. Toma, C. Fasel, R. Riedel, Solid State Ionics 225 (2012) 522–526.
[12] J. Kaspar, M. Graczyk-Zajac, R. Riedel, Solid State Ionics 225 (2012) 527–531.
[13] J. Kaspar, M. Graczyk-Zajac, R. Riedel, Journal of Power Sources 244 (2013) 450–455.
[14] G. Liu, J. Kaspar, L.M. Reinold, M. Graczyk-Zajac, R. Riedel, Electrochimica Acta 106 (2013) 101–108.
[15] H. Fukui, K. Eguchi, H. Ohsuka, T. Hino, K. Kanamura, Journal of Power Sources 243 (2013) 152–158.
[16] V.S. Pradeep, M. Graczyk-Zajac, M. Wilamowska, R. Riedel, G.D. Soraru, Solid State Ionics (2013), http://dx.doi.org/10.1016/j.ssi.2013.1008.1043.
[17] A. Saha, R. Raj, D.L. Williamson, Journal of the American Chemical Society 89 (2006) 2188–2195.
[18] H.-J. Kleebe, G. Gregori, Y.D. Blum, F. Babonneau, International Journal of Material Research 97 (2006) 699–709.
[19] S.J. Widgeon, S. Sen, G. Mera, E. Ionescu, R. Riedel, A. Navrotsky, Chemistry of Materials 22 (2010) 6221–6228.
[20] E. Ionescu, H.-J. Kleebe, R. Riedel, Chemical Society Reviews 41 (2012) 5032–5052.
[21] J. Cordelair, P. Greil, Journal of the European Ceramic Society 20 (2000) 1947–1957.
[22] H.-J. Kleebe, Y.D. Blum, Journal of the European Ceramic Society 28 (2008) 1037–1042.
[23] H.-J. Kleebe, C. Turquat, G.D. Soraru, Journal of the American Chemical Society 84 (2001) 1073–1080.
[24] S. Martínez-Crespiera, E. Ionescu, H.-J. Kleebe, R. Riedel, Journal of the European Ceramic Society 31 (2011) 913–919.
[25] P.E. Sanchez-Jimenez, R. Raj, Journal of the American Ceramic Society 93 (2010) 9.
[26] D. Ahn, R. Raj, Journal of Power Sources 196 (2011) 2179–2186.
[27] D. Ahn, Electrochemical Insertion of Lithium into Polymer Derived Silicon Oxycarbide and Oxycarbonitride Ceramics, PhD-Thesis, University of Colorado, Boulder, CO, 2010.
[28] P.D. Weidman, D. Ahn, R. Raj, Journal of Power Sources (2013) 1087, http://dx.doi.org/10.1016/j.jpowsour.2013.1009.
[29] R. Bhandavat, G. Singh, ACS Applied Materials & Interfaces 4 (2012) 5092–5097.
[30] R. Bhandavat, G. Singh, ACS Applied Materials & Interfaces 5 (2012) 222–224.
[31] M.D. Levi, D. Aurbach, The Journal of Physical Chemistry B 101 (1997) 4641–4647.
[32] D. Aurbach, J.S. Gnanaraj, M.D. Levi, E.A. Levi, J.E. Fischer, A. Claye, Journal of Power Sources 97–98 (2001) 92–96.
[33] J.S. Gnanaraj, M.D. Levi, E. Levi, G. Salitra, D. Aurbach, J.E. Fischer, A. Claye, Journal of The Electrochemical Society 148 (2001) A525–A536.
[34] D. Aurbach, M.D. Levi, E. Levi, Solid State Ionics 179 (2008) 742–751.
[35] M.D. Levi, K. Gamolsky, D. Aurbach, U. Heider, R. Oesten, Journal of Electroanalytical Chemistry 477 (1999) 32–40.
[36] E. Markevich, M.D. Levi, D. Aurbach, Journal of Electroanalytical Chemistry 580 (2005) 231–237.
[37] B. Markovsky, M.D. Levi, D. Aurbach, Electrochimica Acta 43 (1998) 2287–2304.
[38] P. Yu, B.N. Popov, J.A. Ritter, R.E. White, Journal of The Electrochemical Society 146 (1999) 8–14.
[39] N. Ding, J. Xu, Y.X. Yao, G. Wegner, X. Fang, C.H. Chen, I. Lieberwirth, Solid State Ionics 180 (2009) 222–225.
[40] G.D. Soraru, S. Modena, E. Guadagnino, P. Colombo, J. Egan, C. Pantano, Journal of the American Ceramic Society 85 (2002) 1529–1536.
[41] D. Aurbach, Journal of Power Sources 89 (2000) 206–218.
[42] J.R. Dahn, T. Zheng, Y. Liu, J.S. Xue, Science 270 (1995) 590–593.
[43] T. Zheng, W.R. McKinnon, J.R. Dahn, Journal of The Electrochemical Society 143 (1996) 2137–2145.
[44] T. Zheng, J.S. Xue, J.R. Dahn, Chemistry of Materials 8 (1996) 389–393.
[45] C.J. Wen, B.A. Boukamp, R.A. Huggins, W. Weppner, Journal of The Electrochemical Society 126 (1979) 2258–2266.
[46] M.D. Levi, D. Aurbach, Electrochimica Acta 45 (1999) 167–185.
[47] M.D. Levi, D. Aurbach, Journal of Physical Chemistry B 101 (1997) 4630–4640.
[48] C. Ho, I.D. Raistrick, R.A. Huggins, Journal of The Electrochemical Society 127 (1980) 343–350.
[49] G. Mera, A. Navrotsky, S. Sen, H.-J. Kleebe, R. Riedel, Journal of Material Chemistry A 1 (2013) 3826–3836.

J. Am. Ceram. Soc., **96** [6] 1899–1903 (2013)
DOI: 10.1111/jace.12327

Thermodynamic Control of Phase Composition and Crystallization of Metal-Modified Silicon Oxycarbides

E. Ionescu,[‡,†] C. Terzioglu,[‡] C. Linck,[‡] J. Kaspar,[‡] A. Navrotsky,[§] and R. Riedel[‡]

[‡]Technische Universität Darmstadt, Institut für Materialwissenschaft, Petersenstrasse 32, D-64287 Darmstadt, Germany

[§]Peter A. Rock Thermochemistry Laboratory and NEAT ORU, University of California Davis, Davis, California 95616

Silicon oxycarbides modified with main group or transition metals (SiMOC) are usually synthesized via pyrolysis of sol-gel precursors from suitable metal-modified orthosilicates or polysiloxanes. In this study, the phase composition of different SiMOC systems (M = Sn, Fe, Mn, V, and Lu) was investigated. Depending on the metal, different ceramic phases formed. For M = Mn and Lu, MO_x/SiOC ceramic nanocomposites were formed, whereas other compositions revealed the formation of M/SiOC (M = Sn), MSi_x/SiOC (M = Fe) or MC_x/SiOC (M = V) upon pyrolysis. The different phase compositions of the SiMOC materials are rationalized by a simple thermodynamic approach which generally correctly predicts which type of ceramic nanocomposite is expected upon ceramization of the metal-modified precursors. Calculations show that the thermodynamic stability of the MO_x phase with respect to that of the C–O system is the most important factor to predict phase formation in polymer-derived SiMOC ceramic systems. A secondary factor is the relative stability of metal oxides, silicates, carbides, and silicides.

I. Introduction

Polymer-derived ceramic nanocomposites (PDC-NCs) represent a relatively new class of materials which can be synthesized via polymer-to-ceramic transformation of suitable single-source precursors. In a first step, the pyrolysis of the molecular precursors leads to single-phase ceramics, which subsequently undergo phase separation processes upon high-temperature annealing.[1]

Synthesis and phase formation of silicon-based PDC-NC were studied extensively in the last decade. Pyrolysis of suitable alkoxysilanes, $Si(OR)_4$, or polysiloxanes, $-[Si(R)_2–O]_n$, chemically modified with metal alkoxides was shown to give MO_x/SiOC-based PDC-NCs, as reported for M = Al,[2,3] Ti,[4,5] Zr,[6,7] Hf[8,9] etc. For M = Zr and Hf, a single-phase SiMOC ceramic is obtained upon pyrolysis at rather low temperatures (~700°C), while at higher temperatures amorphous MO_2 nanoparticles precipitate (800°C–1100°C). Upon increasing the annealing temperature to 1300°C, MO_2 nanoparticles crystallize, forming microstructures comprised tetragonal zirconia/hafnia particles finely dispersed within an amorphous SiOC matrix.[7–9]

Metal-modified silicon oxycarbonitrides were also synthesized[10]; however, not only MO_x/SiCNO nanocomposites (M = Ti,[11] Zr,[12] and Hf[13,14]) but also M/SiCNO (for Cu,[15] Ni[16]) and MSi_x/SiCNO (Fe,[17,18] Co,[17] Pd[19]) were reported. In the case of MO_x/SiCNO, a similar polymer-to-ceramic transformation as for MO_x/SiOC was proposed (i.e., formation of a single-phase amorphous SiMCNO at low temperatures and subsequent phase separation of MO_x).[14] However, the phase separation of metals or metal silicides as found in M/SiCN(O) and MSi_x/SiCN(O) compositions has not been clarified so far.

This study shows that the phase composition of the ceramic is thermodynamically controlled by oxidation-reduction reactions which depend on the type of metal used. Although this study only uses data related to the stability of the metal oxides in carburizing conditions (change of the Gibbs free energy as a function of temperature) to understand the phase composition of SiMOC, this rather simple thermodynamic consideration successfully predicts the phase composition formed from SiMOC and SiMCNO upon pyrolysis of single-source precursors.

II. Experimental Procedures

The synthesis of the precursors was performed as described elsewhere for SiZrOC and SiHfOC[7,8] via chemical modification of a polysilsesquioxane (MK Belsil PMS; Wacker, Burghausen, Germany) with $Fe(acac)_3$, $Mn(acac)_3$, $V(acac)_3$, $VO(acac)_2$, $Sn(ac)_2$, and $Lu(ac)_3$ (ac = acetate; acac = acetylacetonate). Thus, each 5 g of polysilsesquioxane PMS was reacted with the corresponding amount of metal precursor at room temperature. For the reactions with the Fe, Mn, V, and Sn containing precursors, xylene was used as a solvent, whereas the reaction with $Lu(ac)_3$ was performed in acetone. The amount of the metal precursor was chosen to obtain after pyrolysis a weight ratio between SiOC and a possible MO_x phase (lowest oxide, which was assumed to precipitate) close to 70:30. To calculate the needed amounts of metal precursors, a ceramic yield of 81 wt% upon conversion of PMS into SiOC has been taken into account.[7,8] In Table I, the amounts of the metal precursors used for the chemical modification of PMS is presented. Thus, the SiMOC-based ceramics were expected to exhibit similar MO_x contents, between 30.9 and 36.7 wt% (see Table I).

After mixing PMS with the metal precursor, the reaction solution was stirred for 2 h at room temperature. Subsequently, the solvent was removed under vacuum (10^{-2} mbar). The metal-modified precursors were cross-linked at 250°C and pyrolyzed in argon at 1100°C. The ceramic yield of the precursor-to-ceramic transformation processes showed values between 51.6 and 71.6 wt% (Table I).

The obtained ceramics were additionally annealed at 1300°C. FTIR spectra were recorded on a Bruker Vertex 70 FT-IR spectrometer (Bruker Optik, Ettlingen, Germany). X-ray diffraction (XRD) was performed on a STOE STADI P X-ray powder diffractometer (transmission geometry, Mo*K*α radiation).

L. Gauckler—contributing editor

Manuscript No. 32561. Received January 8, 2013; approved March 14, 2013.

[†] Author to whom correspondence should be addressed. e-mail: ionescu@materials.tu-darmstadt.de

Table I. Amounts of PMS and Metal Precursors Used as well as Ceramic Yields of the Syntheses of SiMOC Samples

Sample	Metal	PMS (g)	Metal precursor (g)	Expected content of MO_x in SiMOC (wt%)	Ceramic yield (wt%)	Phase composition upon pyrolysis at 1100°C
SiOC	–	5	–	–	81.00	a-SiOC
SiFeOC	Fe(III)	5	7.8	34.1	67.02	Fe_3Si/a-SiOC
SiSnOC	Sn(II)	5	3.1	36.7	71.60	Sn/a-SiOC
SiMnOC	Mn(III)	5	8.6	36.2	61.62	$MnSiO_3$/a-SiOC
SiLuOC	Lu(III)	5	3.2	30.9	71.50	Lu_2O_3/a-SiOC
SiVOC	V(III)	5	9.0	33.1	51.61	V_8C_7/a-SiOC
SiVOC	V(IV)	5	6.9	36.3	64.58	V_8C_7/a-SiOC

III. Results and Discussion

The polysilsesquioxane MK Belsil PMS with the chemical composition $Si_1O_3C_1H_{3.3}$ is commercially available and contains cross-linkable hydroxy and ethoxy groups which can further react with metal alkoxides, acetylacetonates, or acetates. FTIR spectroscopy measurements (Fig. 1) indicate that the reaction of the metal precursors with PMS leads to the formation of Si–O–M units (Fig. 2), as revealed by the appearance of an absorption band at ~950 cm^{-1} and agrees with previously reported results.[7,8]

Pyrolysis of the metal-containing polyorganosiloxanes in Ar atmosphere at 1100°C results in the formation of SiMOC ceramics, which were shown by XRD to exhibit different crystalline phase compositions [Fig. 3(a)]. In SiFeOC, Fe_3Si was observed, while the tin-containing precursor gave a Sn/SiOC ceramic composite. In both cases, Fe(III) and Sn (II) were reduced to Fe(0) (as in Fe_3Si alloy) and Sn(0). It is thought that the reducing conditions during the pyrolysis of the precursors are responsible for the formation of the metallic phases and are mainly due to the release of hydrogen and CO upon ceramization.[7] The Sn/SiOC ceramic did not change phase composition when annealed at 1300°C; whereas in Fe_3Si/SiOC the crystallization of Fe_5Si_3 and β-SiC was found under the same conditions [Fig. 3(b)]. Similar behavior was reported previously for Fe_3Si/SiCNO.[18]

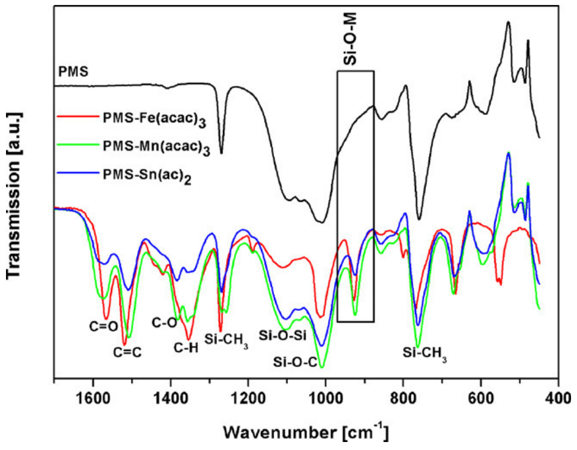

Fig. 1. FTIR spectra of PMS as well as of PMS modified with Fe, Mn, and Sn.

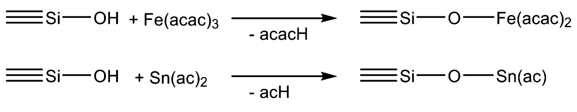

Fig. 2. The reaction of $Fe(acac)_3$ and $Sn(ac)_2$ with the –OH groups of PMS upon formation of Si–O–Fe and Si–O–Sn units, respectively (acac = acetylacetonate; ac = acetate).

Pyrolysis of the Mn-containing precursor led to a poorly crystalline SiMnOC ceramic. The XRD pattern revealed the presence of $MnSiO_3$ [Fig. 3(a)], which was also observed upon annealing at 1300°C [Fig. 3(b)]. It is assumed that the phase separation of MnO (at temperatures between 800°C and 1100°C) and its subsequent reaction with the phase-separated silica at higher temperature leads to the formation of the $MnSiO_3$ phase. Such formation of binary and ternary oxides is analogous to the behavior observed in SiZrOC and SiHfOC.[7,9] However, the formation of $MnSiO_3$ occurs at lower temperatures than those for $ZrSiO_4$ and $HfSiO_4$, which crystallize at temperatures exceeding 1400°C.[7,9]

Similar results were obtained in the case of the lutetium-modified precursor. Thus, at 1100°C poorly crystallized

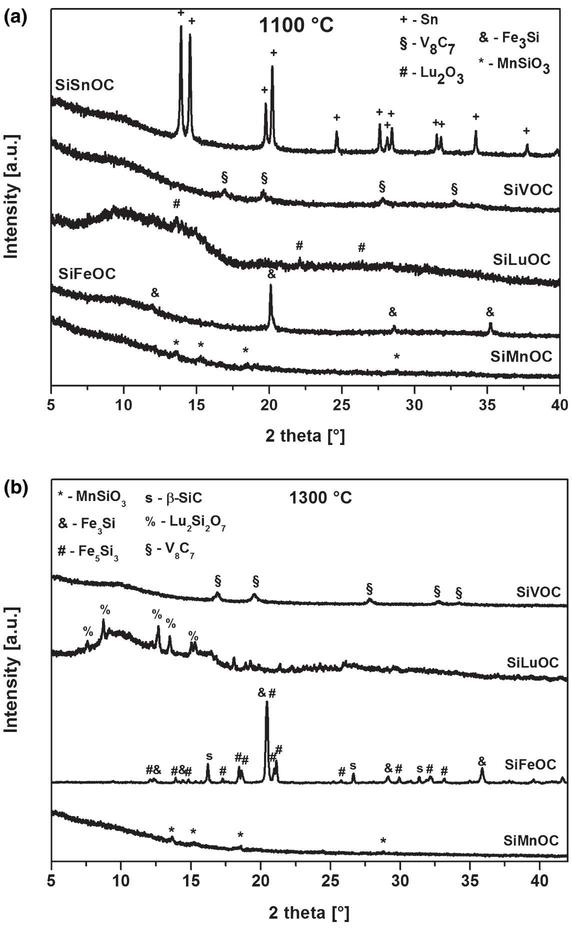

Fig. 3. X-ray diffraction (XRD) patterns for SiMOC (M = Fe, Sn, Mn, Lu, V) pyrolyzed at 1100°C (a) and 1300°C (b).

Lu_2O_3 was identified by XRD, whereas at 1300°C crystalline $Lu_2Si_2O_7$ was found (Fig. 3).

Different behavior was found for the vanadium-modified precursor. At both temperatures a poorly crystalline V_8C_7 was detected, which can result from the reaction of vanadium oxide with excess carbon (Fig. 3, as for SiVOC prepared upon pyrolysis of the V(ac)$_3$-modified precursor). Interestingly, both precursors, i.e., the V(III)- and the V(IV)-modified polysilsesquioxanes led upon pyrolysis to the crystallization of V_8C_7 (i.e., formation of SiOC/V_8C_7 nanocomposites).

The strong effect of the precursor composition on the phase evolution upon ceramization reflects the reducing conditions during pyrolysis and annealing. Thus, it is obvious that the thermodynamic stability of the metal oxides generated during pyrolysis plays a crucial role. To assess this effect in more detail, thermodynamic data for the oxides (MO_x) were used, as depicted in the Ellingham diagrams in Fig. 4. Since all samples were synthesized under the same pyrolysis conditions, the partial pressures of the volatiles (i.e., CO, CO_2, H_2, and CH_4) were not considered explicitly here. However, since carbon is present in all cases, it is appropriate to make a direct comparison between the CO–C and MO_x – M equilibria. Since carbon is present in large amount in the investigated samples, the oxygen fugacity is determined by the equilibrium $2\ C + O_2 \rightarrow 2CO$.

The first conclusion in the case of SiFeOC is that FeO, which is generated upon pyrolysis of the Fe-containing PMS precursor, is unstable and is reduced by carbon to metallic Fe, which (similar to the case of SiFeCNO[18]) subsequently reacts with the SiOC matrix to form Fe_3Si. An alternative process which might occur is the reduction in FeO by carbon to cementite (Fe_3C). As shown in Fig. 5, the Gibbs free energy change for the reaction of FeO with carbon to form Fe_3C is slightly more favorable than that of the formation of metallic iron. Interestingly, the pyrolysis of the Fe-modified PMS at 1100°C did not reveal any crystalline Fe_3C, but already showed the formation of Fe_3Si as crystalline phase. This indicates that Fe_3C, if it is generated, immediately converts into Fe_3Si. However, the possibility that Fe_3C is hard to detect due to its poor crystallinity, whereas the silicide is better crystallized and more easily seen in the XRD pattern cannot be ruled out.

To verify the possible crystallization of cementite upon polymer-to-ceramic transformation of the Fe-modified PMS, the pyrolysis was performed at a lower temperature, i.e., 1000°C. As expected, poorly crystallized cementite (Fe_3C) was detected, proving that the reduction in FeO leads to the formation of Fe_3C (Fig. 6).

Thus, following pathway for the crystallization of Fe_3Si upon pyrolysis of SiFeOC can be assumed: in a first step, phase separation of FeO occurs, which, however, is not stable against carbothermal reduction [see Fig. 4(a)] and converts into Fe_3C (Figs. 5 and 6). As Fe_3C is known to be metastable and to decompose at elevated temperatures even in strongly carburizing conditions[20] and its decomposition rate increases with increasing the temperature beyond 770°C,[21] we assume that Fe_3C either decomposes into Fe and graphite and generates iron for the formation of Fe_3Si (cf. process $3Fe + SiO_2 + 2C = Fe_3Si + 2CO$) or itself converts into Fe_3Si upon reaction with SiO_2 and C (cf. $Fe_3C + SiO_2 + C = Fe_3Si + 2CO$). The proposed mechanism for the formation of Fe_3Si is summarized in Fig. 7.

For the temperature range from 1000°C to 1300°C, the Sn–SnO equilibrium lies above the CO line [Fig. 4(a)]. Tin forms no carbides or silicides, hence these binary equilibria explain why the pyrolysis of the Sn-modified precursor leads to the formation of Sn/SiOC composites.

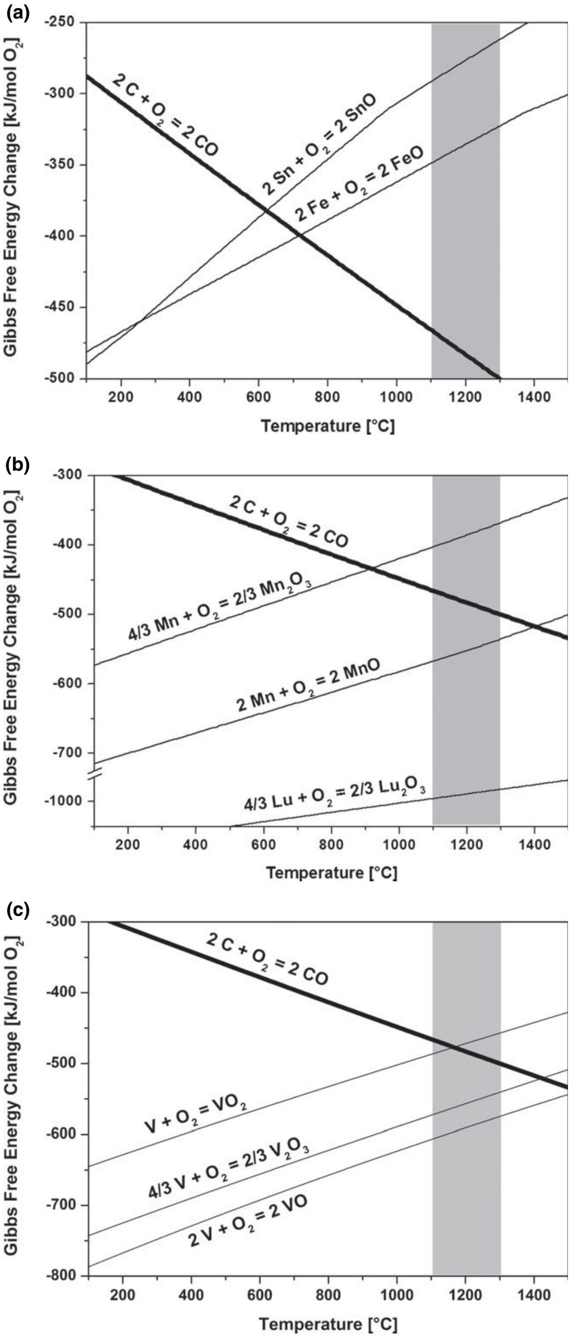

Fig. 4. Ellingham diagrams showing the Gibbs free energy change of different oxides with respect to the system C–O (the gray areas correspond to the temperature range in which our samples were prepared, i.e., between 1100°C and 1300°C). Oxides with Gibbs free energies located in the area above the CO line will get reduced by carbon to their corresponding metals upon CO gas release; whereas those located in the area below the CO line will be stable against conversion into metals (data taken from Ref. [24]).

In the case of SiMnOC, Mn(II) was found by means of XRD and XPS (not shown here) to be present (detailed characterization of SiMnOC will be published in a separate article), although PMS was chemically modified with a Mn(III) precursor. This reflects the fact that the manganese oxide of lowest oxidation state (MnO) is very stable with respect to CO, C, or H_2 reduction (up to temperatures of 1250°C–1300°C).[22]

The temperature evolution of the Gibbs free energy for MnO and Lu_2O_3 agrees well with the XRD results presented above. In both cases, the oxides are stable with respect to reduction by carbon [see Fig. 4(b)]. Once these oxides form, they can react with silica to form silicates, which stabilize them further. Thus, in the case of SiMnOC, the Gibbs free energies of formation of $MnSiO_3$ (−974.7 kJ/mol at 1100°C and −924.0 kJ/mol at 1300°C)[23] are significantly more negative than those of MnO (−564.9 kJ/mol at 1100°C and −535.1 kJ/mol at 1300°C).[24] Also in the case of SiLuOC, Lu_2O_3 is expected to react easily with silica to form silicate phases (e.g., $Lu_2Si_2O_7$, as experimentally observed here), since those processes have been shown to be thermodynamically driven for rare-earth metal oxides, e.g. La_2O_3, Ce_2O_3 etc.[25]

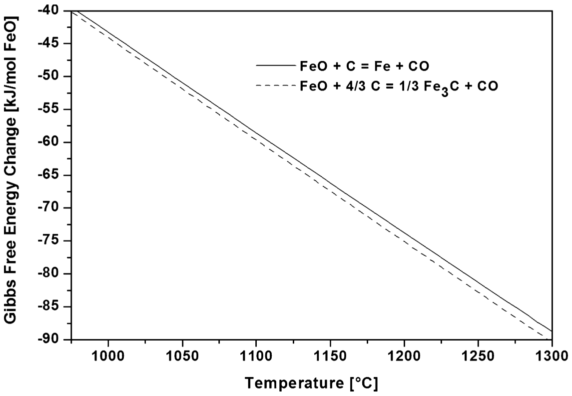

Fig. 5. Gibbs free energy change for the reduction reactions of FeO to Fe (solid line) and Fe_3C (dashed line) (data from Ref. [24]). In the temperature range shown, the formation of Fe_3C seems to be slightly more favorable.

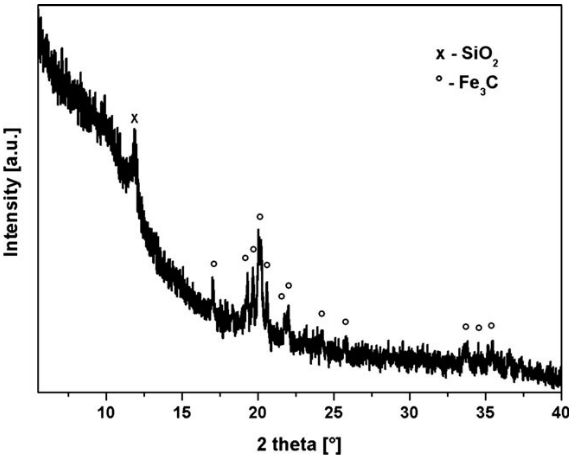

Fig. 6. XRD pattern of the SiFeOC ceramic prepared at 1000°C.

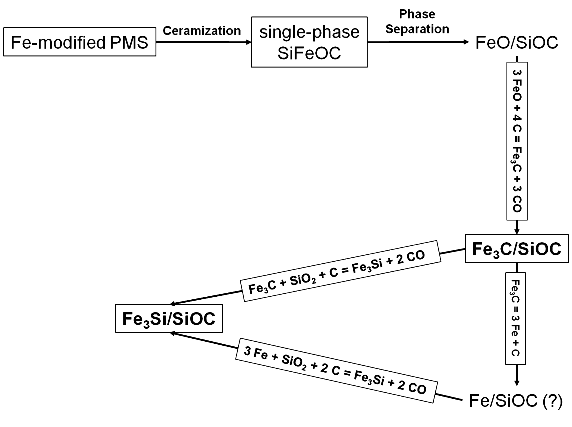

Fig. 7. Proposed mechanism for the formation of Fe_3Si phase upon pyrolysis of Fe-modified PMS at 1100°C.

In Fig. 4(c), the thermodynamic stability of VO_2, V_2O_3, and VO with respect to their carbothermal reduction is represented. At temperatures of 1100°C–1300°C, all three oxides seem to be stable against their carbothermal conversion into metallic vanadium. However, crystallization of V_8C_7 was observed already at 1100°C. The carbothermal reaction of vanadium oxides with nanoscaled carbon was reported in literature to take place at temperatures as low as 900°C–1000°C[26,27] and was shown to lead to the formation of vanadium carbides, as observed also in our samples. Interestingly, the pyrolysis of both our V(III)- and V(IV)-modified samples led to the crystallization of V_8C_7, as shown in Fig. 8. Hence, in the case of the vanadium-modified precursors, vanadium (III) and vanadium (IV) probably get reduced to vanadium (II) and thus VO precipitates *in situ* and subsequently converts into V_8C_7 upon reaction with carbon. This suggests that the carbide is sufficiently stable to overcome the slightly positive free energy of reduction of VO to metallic vanadium.

In Table II, the Gibbs free energies for the carbothermal conversion of VO into metallic vanadium as well as for its carbothermal reduction to V_8C_7 are presented. It is obvious that from the two reduction processes of VO with carbon, the formation of V_8C_7 is favored, since the values of ΔG are strongly negative (−82.3 and −124.8 kJ/mol at 1100°C and 1300°C, respectively); whereas the Gibbs free energy of the formation of metallic vanadium has large positive values.

IV. Conclusion

In this study, we show that the thermodynamic stability of MO_x with respect to the system C–O plays a crucial role within the context of the ceramization process of metal-modified polymers. Based on thermodynamic data of the respective oxides, the phase composition of SiMOC/SiMCNO ceramics upon annealing at high temperatures can be predicted for different metals. The prediction agrees with the experimental results from this study and those reported in the literature for both SiMOC and SiMCNO ceramic composites. However, in addition to the stability of the oxides with respect to reduction, some other aspects must be taken into account for predicting the phase composition of SiMOC/SiMCNO composites, such as thermodynamic stabilization through conversion into silicates (for MO_x being stable with respect to carbothermal conversion into M) or into

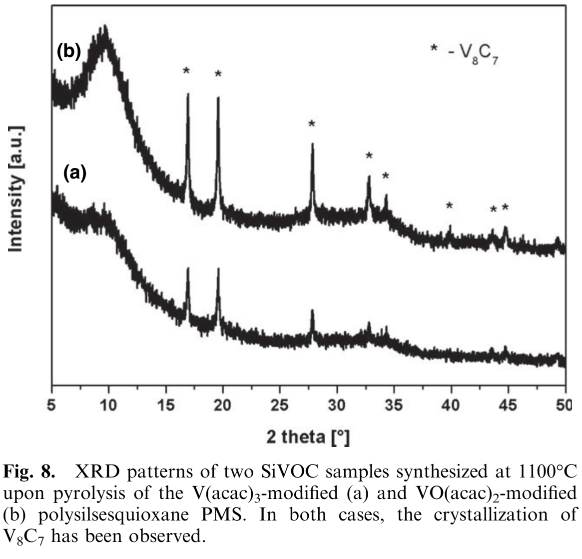

Fig. 8. XRD patterns of two SiVOC samples synthesized at 1100°C upon pyrolysis of the $V(acac)_3$-modified (a) and $VO(acac)_2$-modified (b) polysilsesquioxane PMS. In both cases, the crystallization of V_8C_7 has been observed.

Table II. Gibbs Free Energies of Possible Processes Involved in the Formation of V and V_8C_7 Upon Pyrolysis of the Vanadium-Modified Polysilsesquioxane

Process		
$VO \rightarrow V + ½ O_2$	$\Delta G_{1100°C}$ (1) = +312.70 kJ/mol	(1)
	$\Delta G_{1300°C}$ (1) = +300.36 kJ/mol (Ref. [24])	
$2C + O_2 \rightarrow 2 CO$	$\Delta G_{1100°C}$ (2) = −421.1 kJ/mol	(2)
	$\Delta G_{1300°C}$ (2) = −442.4 kJ/mol (Ref. [24])	
$V + 7/8 C \rightarrow 1/8 V_8C_7$	$\Delta G_{1100°C}$ (3) = −184.44 kJ/mol	(3)
	$\Delta G_{1300°C}$ (3) = −203.99 kJ/mol (Ref. [28])	
$VO + C \rightarrow V + CO$	$\Delta G_{1100°C}$ = +102.15 kJ/(mol VO)	
	$\Delta G_{1300°C}$ = +79.16 kJ/(mol VO)	
$8 VO + 15 C \rightarrow V_8C_7 + 8 CO$	$\Delta G_{1100°C}$ = −82.29 kJ/(mol VO)	
	$\Delta G_{1300°C}$ = −124.83 kJ/(mol VO)	

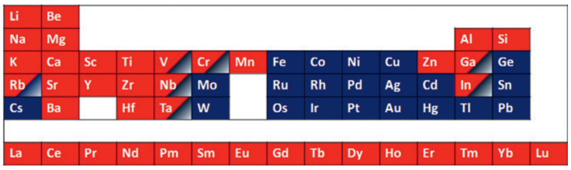

Fig. 9. Predicted phase compositions of SiMOC and SiMCNO upon pyrolysis at 1100°C–1300°C. The oxides of the red marked metals are stable with respect to their reduction and thus SiOC/MO_x nanocomposites are expected. Depending on the stability of the corresponding silicates ($MSiO_x$), solid-state processes between MO and the phase-separated silica may occur, as observed for the case of Mn (crystallization of $MnSiO_3$) and Lu ($Lu_2Si_2O_7$) in this study. The oxides of the blue colored metals are not stable with respect to reduction by carbon. Consequently, SiOC/M nanocomposites are predicted to form here. Also in this case, the relative thermodynamic stability of the corresponding silicides or carbides will determine whether SiOC/MSi_x or SiOC/MC_x nanocomposites will be generated.

silicides or carbides (for MO_x not being stable against carbothermal reduction). These factors are summarized in Fig. 9.

A more rigorous computation of the thermodynamics of crystallization could employ free energy minimization techniques. However, this would require some knowledge or assumptions about the free energies of the metals dissolved in the initially homogeneous ceramics. Such information is not currently available. The main point of this study is that even a very simple thermodynamic approach predicts the observed phases formed with remarkable accuracy.

Acknowledgments

This work was financially supported by the German Research Foundation (DFG) (IO-64/1 (SPP1181, NANOMAT) and IO-64/3) and the Materials World Network (National Science Foundation (NSF MWN-0906070) – Deutsche Forschungsgemeinschaft collaborative project "Nanostructure and thermodynamics of polymer-derived ceramics"). EI thanks M. Vetrecin for his support on calculating Gibbs free energy changes.

References

[1] E. Ionescu, H.-J. Kleebe, and R. Riedel, "Silicon-Containing Polymer-Derived Ceramic Nanocomposites (PDC-NCs): Preparative Approaches and Properties," *Chem. Soc. Rev.*, **41** [15] 5032–52 (2012).

[2] R. Harshe, C. Balan, and R. Riedel, "Amorphous Si(Al)OC Ceramic From Polysiloxanes: Bulk Ceramic Processing, Crystallization Behavior and Applications," *J. Eur. Ceram. Soc.*, **24** [12] 3471–82 (2004).

[3] R. Riedel, L. Toma, C. Fasel, and G. Miehe, "Polymer-Derived Mullite-SiC-Based Nanocomposites," *J. Eur. Ceram. Soc.*, **29** [14] 3079–90 (2009).

[4] S. Dire, F. Babonneau, C. Sanchez, and J. Livage, "Sol-Gel Synthesis of Siloxane Oxide Hybrid Coatings [$Si(CH_3)_2O.MO_x$ - M = Si, Ti, Zr, Al] With Luminescent Properties," *J. Mater. Chem.*, **2** [2] 239–44 (1992).

[5] S. Dire, R. Ceccato, and F. Babonneau, "Structural and Microstructural Evolution During Pyrolysis of Hybrid Polydimethylsiloxane-Titania Nanocomposites," *J. Sol-Gel. Sci. Technol.*, **34** [1] 53–62 (2005).

[6] S. Dire, R. Ceccato, S. Gialanella, and F. Babonneau, "Thermal Evolution and Crystallisation of Polydimethylsiloxane-Zirconia Nanocomposites Prepared by the Sol-Gel Method," *J. Eur. Ceram. Soc.*, **19** [16] 2849–58 (1999).

[7] E. Ionescu, C. Linck, C. Fasel, M. Muller, H. J. Kleebe, and R. Riedel, "Polymer-Derived SiOC/ZrO_2 Ceramic Nanocomposites With Excellent High-Temperature Stability," *J. Am. Ceram. Soc.*, **93** [1] 241–50 (2010).

[8] E. Ionescu, B. Papendorf, H. J. Kleebe, F. Poli, K. Muller, and R. Riedel, "Polymer-Derived Silicon Oxycarbide/Hafnia Ceramic Nanocomposites. Part I: Phase and Microstructure Evolution During the Ceramization Process," *J. Am. Ceram. Soc.*, **93** [6] 1774–82 (2010).

[9] E. Ionescu, B. Papendorf, H. J. Kleebe, and R. Riedel, "Polymer-Derived Silicon Oxycarbide/Hafnia Ceramic Nanocomposites. Part II: Stability Toward Decomposition and Microstructure Evolution at $T \gg 1000$ Degrees C," *J. Am. Ceram. Soc.*, **93** [6] 1783–9 (2010).

[10] M. Zaheer, T. Schmalz, G. Motz, and R. Kempe, "Polymer Derived Non-Oxide Ceramics Modified With Late Transition Metals," *Chem. Soc. Rev.*, **41** [15] 5102–16 (2012).

[11] Y. Iwamoto, K. Kikuta, and S. Hirano, "Synthesis of Poly-Titanosilazanes and Conversion Into Si_3N_4-TiN Ceramics," *J. Ceram. Soc. Jpn.*, **108** [4] 350–6 (2000).

[12] A. Saha, S. R. Shah, and R. Raj, "Amorphous Silicon Carbonitride Fibers Drawn From Alkoxide Modified Ceraset$^{(TM)}$," *J. Am. Ceram. Soc.*, **86** [8] 1443–5 (2003).

[13] B. Papendorf, K. Nonnenmacher, E. Ionescu, H.-J. Kleebe, and R. Riedel, "Strong Influence of Polymer Architecture on the Microstructural Evolution of Hafnium-Alkoxide-Modified Silazanes Upon Ceramization," *Small*, **7**, 970–8 (2011).

[14] E. Ionescu, B. Papendorf, H.-J. Kleebe, H. Breitzke, K. Nonnenmacher, G. Buntkowsky, and R. Riedel, "Phase Separation of a Hafnium Alkoxide-Modified Polysilazane Upon Polymer-to-Ceramic Transformation—A Case Study," *J. Eur. Ceram. Soc.*, **32** [9] 1873–81 (2012).

[15] G. Glatz, T. Schmalz, T. Kraus, F. Haarmann, G. Motz, and R. Kempe, "Copper-Containing SiCN Precursor Ceramics (Cu@SiCN) as Selective Hydrocarbon Oxidation Catalysts Using Air as an Oxidant," *Chem-Eur J*, **16** [14] 4231–8 (2010).

[16] M. S. Bazarjani, H. J. Kleebe, M. M. Muller, C. Fasel, M. B. Yazdi, A. Gurlo, and R. Riedel, "Nanoporous Silicon Oxycarbonitride Ceramics Derived From Polysilazanes *In Situ* Modified With Nickel Nanoparticles," *Chem. Mater.*, **23** [18] 4112–23 (2011).

[17] R. Hauser, A. Francis, R. Theismann, and R. Riedel, "Processing and Magnetic Properties of Metal-Containing SiCN Ceramic Micro- and Nano-Composites," *J. Mater. Sci.*, **43** [12] 4042–9 (2008).

[18] A. Francis, E. Ionescu, C. Fasel, and R. Riedel, "Crystallization Behavior and Controlling Mechanism of Iron-Containing Si-C-N Ceramics," *Inorg. Chem.*, **48** [21] 10078–83 (2009).

[19] M. Zaheer, G. Motz, and R. Kempe, "The Generation of Palladium Silicide Nanoalloy Particles in a SiCN Matrix and Their Catalytic Applications," *J. Mater. Chem.*, **21** [46] 18825–31 (2011).

[20] A. Schneider, "Iron Layer Formation During Cementite Decomposition in Carburising Atmospheres," *Corros. Sci.*, **44** [10] 2353–65 (2002).

[21] R. J. Longbottom, O. Ostrovski, J. Q. Zhang, and D. Young, "Stability of Cementite Formed From Hematite and Titanomagnetite ore," *Metall. Mater. Trans. B*, **38** [2] 175–84 (2007).

[22] A. Salak, M. Selecka, and R. Bures, "Manganese in Ferrous Powder Metallurgy," *Powder Metallurgy Progress*, **1** [1] 41–58 (2001).

[23] J. H. Huang and E. Rosen, "Determination of Gibbs Free-Energies of Formation for the Silicates $Mnsio_3$, Mn_2SiO_4 and Mn_7SiO_{12} in the Temperature-Range 1000-1350-K by Solid-State EMF-Measurements," *Phys. Chem. Miner.*, **21** [4] 228–33 (1994).

[24] T. B. Reed, *Free Energy of Formation for Binary Compounds*. MIT Press, Cambridge, MA, 1971.

[25] M. Bolech, E. H. P. Cordfunke, A. C. G. van Genderen, R. R. van der Laan, F. J. J. G. Janssen, and J. C. van Miltenburg, "The Heat Capacity and Derived Thermodynamic Functions of $La_2Si_2O_7$ and $Ce_2Si_2O_7$ From 4 to 1000 K," *Thermochim. Acta*, **284** [2] 253–61 (1996).

[26] H. Preiss, D. Schultze, and K. Szulzewsky, "Carbothermal Synthesis of Vanadium and Chromium Carbides From Solution-Derived Precursors," *J. Eur. Ceram. Soc.*, **19** [2] 187–94 (1999).

[27] Z. W. Zhao, Y. Liu, H. Cao, S. J. Gao, and M. J. Tu, "Phase Evolution During Synthesis of Vanadium Carbide (V_8C_7) Nanopowders by Thermal Processing of the Precursor," *Vacuum*, **82** [8] 852–5 (2008).

[28] J. C. Hu, C. R. Li, F. M. Wang, and W. J. Zhang, "Thermodynamic Reassessment of the V-C System," *J. Alloy Compd.*, **421** [1–2] 120–7 (2006). ☐

Journal of Power Sources 269 (2014) 164–172

Contents lists available at ScienceDirect

Journal of Power Sources

journal homepage: www.elsevier.com/locate/jpowsour

Silicon oxycarbide/nano-silicon composite anodes for Li-ion batteries: Considerable influence of nano-crystalline vs. nano-amorphous silicon embedment on the electrochemical properties

Jan Kaspar [a, *], Magdalena Graczyk-Zajac [a], Stefan Lauterbach [b], Hans-Joachim Kleebe [b], Ralf Riedel [a]

[a] *Institut für Materialwissenschaft, Technische Universität Darmstadt, Disperse Feststoffe, Jovanka-Bontschits-Straße 2, 64287 Darmstadt, Germany*
[b] *Institut für Angewandte Geowissenschaften, Technische Universität Darmstadt, Schnittspahnstraße 9, 64287 Darmstadt, Germany*

HIGHLIGHTS

- Silicon oxycarbide/nano-silicon composites as new anode material for LIB.
- Polymer-derived SiOC ceramic matrix stabilizes nano-silicon upon cycling.
- Silicon embedment enhances the intrinsic gravimetric capacity of SiOC.
- Stable reversible capacity of 704 mAh g^{-1} for nano-amorphous Si embedment.

ARTICLE INFO

Article history:
Received 5 February 2014
Received in revised form
23 May 2014
Accepted 17 June 2014
Available online 24 June 2014

Keywords:
Li-ion battery
Anode
Silicon oxycarbide
SiOC
Nano-silicon
Polymer-derived ceramic

ABSTRACT

Silicon oxycarbide/nano-silicon composites (SiOC/nSi) are prepared by mixing of nano-sized silicon, either crystalline (nSi_c) or amorphous (nSi_a), with commercially available polyorganosiloxane *RD-684a* and subsequent pyrolysis. The influence of the type of nano-silicon, namely crystalline vs. amorphous, on the electrochemical properties and performance is analyzed and correlated with the corresponding composite microstructure. In the case of crystalline nano-silicon, a high reversible capacity of 905 mAh g^{-1} is registered, whereas that for amorphous nano-silicon embedment reaches 704 mAh g^{-1}. However, regarding the cycling stability, SiOC/nSi_c shows a significant capacity fading upon continuous cycling, related to SiOC matrix failure. The host phase is not able to accommodate the arising mechanical stresses upon Si grain expansion and contraction when alloying/dealloying with Li. SiOC/nSi_a on the contrary, demonstrates a stable cycling performance for up to 100 cycles. This excellent performance is explained by the enhanced matrix integrity of the compound, rationalized by a smaller size of the embedded crystallized Si grains and an intrinsically enhanced electrical conductivity due to the formation of SiC.

1. Introduction

Li-ion batteries are well commercialized and widely used as energy source for all kind of portable electronics. However, there is an unsatisfied need for higher energy and power density devices, for instance, as power sources for electrically driven cars or large scale stationary energy storage [1–3]. Hence, novel electrode and electrolyte materials are required in order to provide a prospective future for Li-ion battery technology; in particular, alternatives to graphite with its limited capacity of 372 mAh g^{-1} need to be found [4–6].

One alternative compound attracting much attention in the last years is silicon, due to its high electrochemical capacity of 3579 mAh g^{-1} for $Li_{15}Si_4$ phase. Unfortunately, Si suffers from large volume changes upon alloying with Li ($\Delta V \approx 280\%$ for $Si/Li_{15}Si_4$), creating strong mechanical stresses, which cause particles to crack and pulverize. In consequence, electrical conduction pathways break down, leading to electrode failure and poor cycle life-time [7–13]. To overcome these drawbacks research efforts have been in progress in order to improve the stability of silicon based anodes.

---

* Corresponding author. Tel.: +49 6151 16 6343; fax: +49 6151 16 6346.
E-mail address: kaspar@materials.tu-darmstadt.de (J. Kaspar).

http://dx.doi.org/10.1016/j.jpowsour.2014.06.089
0378-7753/© 2014 Elsevier B.V. All rights reserved.

The size reduction to the nano-metric scale is intensively explored to overcome the electrode failure [11,14–18]. Various studies have shown a considerable increase in the reversible capacity and lifetime for silicon thin-films [19,20], silicon nano-wires [21–27] and silicon nano-tubes [28,29]. Another promising and efficient approach represents the embedding of silicon within active and non-active matrices, leading to the diminution of the overall capacity but increasing the cycling stability of the composite material. The huge number of scientific report related to this matter has been reviewed by Kasavajjula et al. [30]. Within this context, the preparation of Si-carbon-composites or the selective carbon-coating of silicon has to be mentioned as a particularly successful way to stabilize silicon [31–44].

Besides silicon, polymer-derived ceramics (PDC), that provide a high amount of free carbon within their microstructure, are considered as highly promising anode compounds (SiOC: [45–62], SiCN: [63–66]). In addition to PDC preparation, SiOC can be produced by Sol–Gel process [67–71] or via electrodeposition method [72–74]. Since the early work of Dahn et al. [75–80], continuous research was done in order to introduce SiOC based anodes to commercial Li-ion cells. First investigations on SiOC–CNT composites were addressed by Shen et al. and Bhandavat et al. [81–83] and the synthesis and electrochemical properties of Sol–Gel derived Si/SiOC composites reported by Liu et al. [84]. The modeling of carbon-rich SiOC and its Li-insertion was accomplished by P. Kroll [85–88]. However, for practical application of SiOC anodes, the decrease of the first cycle irreversible capacity still represents a major challenge for this material. In general the charge storage capacity of SiOC ceramics is closely related to their microstructure and phase composition, which can be systematically designed and tailored in the PDC process by selecting suitable precursors, their chemical modification and variation of processing conditions. Concerning the microstructure of carbon-rich SiOC (i.e. compounds in which the content of carbon exceeds 20 wt-% [89]), it is composed of two interpenetrating phases: i) an amorphous silica and/or Si–O–C network comprised of $SiO_{4-x}C_x$ ($x = 1$–4) structural units and ii) a free carbon phase comprised of amorphous or turbostratic-like carbon [90–94]. Depending on the amount of carbon segregation, either carbon nano-domains (low amount of free C) or a carbon percolation network (high amount of free C) exist, as demonstrated by electrical conductivity measurements and TEM analysis [95–97].

Lithium-ion storage in carbon-rich SiOC occurs in form of an adsorption and surface storage within the free carbon phase, similar to the storage of Li-ions in disordered carbons; host sites are the edges of graphene sheets, interstitial and defect sites, micropores and graphite nano-crystallites. On the contrary, the Si–O–C amorphous network is attributed a minor role in the reversible storage process [45,51–53,58–60]. In addition, the storage of lithium ions within the phase-boundary of the Si–O–C network and free carbon phase, described by the nano-domain model, is discussed in the literature as well [81,98–101]. Due to the high amount of free carbon interspersed within the amorphous Si–O–C network, carbon-rich silicon oxycarbide represents a promising electrochemically active matrix to stabilize silicon with respect to continuous lithiation/delithiation. In contrast to graphite, carbon-rich SiOC provides a higher Li-ion storage capacity as host, namely up to 520 mAh g^{-1} [59] instead of only 372 mAh g^{-1}, as known for graphite.

In this paper, we report for the first time, that the combination of nano-scaled silicon and carbon-rich SiOC brings about a promising electrochemical performance of the final composite. In particular it makes possible to i) take advantage of the specific electrochemical properties of both compounds, ii) profit of the elastic properties of SiOC to accommodate the volume changes related to Li–Si alloy formation and thus enhance the materials cycle-ability and iii) ensure a sufficient intrinsically electrical conductivity thanks to the high carbon content in the SiOC ceramic. Moreover, we investigate the role of the embedded silicon crystallinity on the composite electrochemical stability. Thus, crystalline and amorphous silicon particles were mixed with commercially available polyorganosiloxane *RD-684a* and subsequently thermally treated at 1100 °C for SiOC matrix ceramization. The influence of the silicon crystallinity on the microstructure of the composites is analyzed, compared and discussed with respect to the corresponding electrochemical properties and cycling behavior. Surprisingly, the microstructure significantly depends on the embedded silicon, i.e. amorphous Si crystallizes and reacts with free carbon under pyrolysis condition and strong SiC crystallization occurs, while for the composite prepared with crystalline silicon, Si grains of larger diameter and only traces of crystalline SiC are found, as verified by XRD and TEM analysis.

2. Experimental

Silicon oxycarbide/nano-silicon composites (SiOC/nSi) were prepared by mixing of nano-crystalline (nSi_c, 30–50 nm; Nanostructured & Amorphous Materials Inc., USA) and nano-amorphous (nSi_a, ~36 nm; Strem Chemicals Inc., Germany) silicon particles with polyorganosiloxane *RD-684a* (Starfire Systems Inc., USA) in acetone. The amount of solvent was adjusted to the double amount of polymer by weight and removed before pyrolysis by vacuum drying. The mixing itself was accomplished by magnetic stirring with ultrasonic support. Pyrolysis of the mixed batches was performed under Ar-atmosphere at a temperature of 1100 °C using quartz-equipment; holding time at the maximum temperature was 3 h and heating rates set to 100 °C h^{-1}. The amount of Si to polymer of the prepared mixtures was adjusted to generate composites with a weight-ratio of Si:SiOC phase of about 20:80, as suggested beneficial for silicon-based composites for anode purposes [102].

For microstructural characterization, X-ray powder diffraction (XRD) was performed with a Bruker D8 Advance (Bruker, USA), using Ni-filtered Cu Kα radiation. For elemental analysis, a carbon analyzer Leco-200 (Leco Corporation, USA) was used to determine the carbon content and an N/O analyzer Leco TC-436 (Leco Corporation, USA) to determine the corresponding oxygen content. The silicon fraction was calculated as the difference to 100 wt-% of the sum of the wt-% values of carbon and oxygen, assuming no other elements being present in the samples. Raman spectra were recorded with a confocal micro-Raman spectrometer Horiba HR 800 (Horiba, Japan), using an Ar-ion laser with wavelength 514.5 nm. Scanning electron microscopy (SEM) images of uncycled and cycled electrodes were recorded with a Philips XL30 FEG (FEI, Netherlands). Transmission electron microscopy (TEM) studies on powder samples dispersed on a lacey carbon Cu-grid were performed at a JEOL 2100F instrument (JEOL, Japan), operated at 200 keV.

For electrochemical measurements, electrodes composed of 85 wt-% composite material (active mass), 5 wt-% Carbon black (Timcal Ltd., Switzerland) and 10 wt-% Na-CMC binder (Sigma–Aldrich, USA), were prepared by tape-casting. The film thickness after drying of the tapes was around ~36 μm in average, with a loading of the active material of about 1.4 mg cm^{-2}. A detailed procedure of electrode preparation can be found elsewhere [53,59]. Testing-cells of two-electrode Swagelok-type were assembled in an Ar-filled glove-box, using metallic lithium (Li-tape 99.9% purity, 0.75 mm thickness, Alfa Aesar, UK) as reference/counter electrode, 1 M $LiPF_6$ in EC:DMC ratio 1:1 (LP30, Merck KGaA, Germany) as electrolyte and glass fiber filter (Whatman™, UK) as separator. Hermetically closed cells were cycled with a VMP multipotentiostat

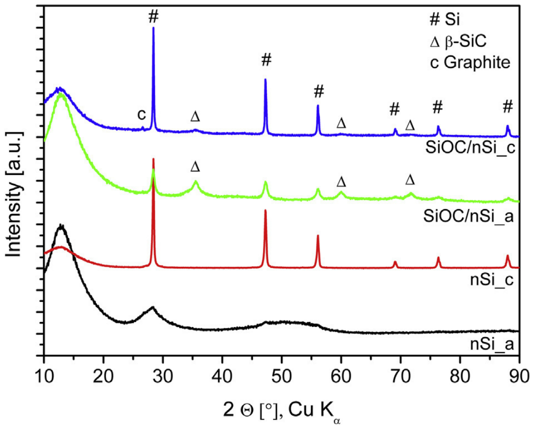

Fig. 1. XRD pattern of SiOC/nSi_c and SiOC/nSi_a composites and pure input silicon nSi_c and nSi_a.

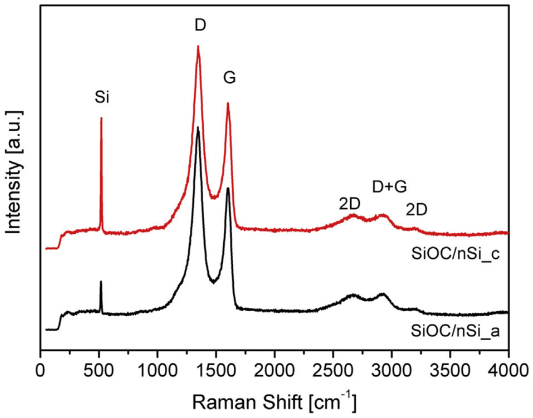

Fig. 2. Raman spectra of SiOC/nSi_c and SiOC/nSi_a composites.

(BioLogic Science Instruments, France) by galvanostatic cycling with potential limitation (GCPL) at a current rate of 74 mA g^{-1} within the potential range of 0.005–3 V (E vs. Li/Li$^+$) and potentiodynamic cycling with galvanostatic acceleration (PCGA) in 50 mV steps with a limiting current of 37 mA g^{-1} and within the potential window of 0.05–3 V (E vs. Li/Li$^+$). For data analysis, the registered capacities were divided by the mass of active material, i.e. the sum of the masses of SiOC and nSi phase.

In the following, composites and electrodes are denoted with respect to the morphology of the initial embedded silicon particles, i.e. SiOC/nSi_c for crystalline and SiOC/nSi_a for amorphous species.

3. Results and discussion

3.1. Material characterization

Fig. 1 presents the X-ray diffraction pattern for the SiOC/nSi_c and SiOC/nSi_a composites, as well as diffractograms of the initially used silicon powders nSi_c and nSi_a. In both composite patterns and for nSi_c, strong Bragg reflections related to crystalline silicon are visible at 28.4°, 47.3°, 56.1°, 69.1°, 76.4° and 88.0° (reference card number [27-1402]). Crystalline silicon carbide (β-SiC) can be identified for the composites at 35.6°, 60.0° and 71.8° (reference card number [29-1129]). For SiOC/nSi_c there is an additional weak reflex visible at 26.5° originating from diffraction at graphitic carbon arrangements within the free carbon phase in the SiOC matrix [53,59]. The pattern of nSi_a reveals the amorphous nature of the material, since no sharp reflexes are observed, but rather broad signals around 28° and in the range of 47–55°. The presence of crystalline silicon in SiOC/nSi_a indicates that the initially amorphous Si crystallizes under pyrolysis conditions, at least partially. A similar behavior was reported for the thermal treatment of pure amorphous nano-silicon by Schierning et al. [103]. The intensity of the SiC signals is much stronger in case of SiOC/nSi_a, suggesting a strong carbothermal reaction of the amorphous silicon with free carbon present in the SiOC matrix. SiC crystallization by decomposition of the matrix itself can be excluded, since pure SiOC derived from *RD-684a* polymer is exclusively amorphous up to 1200 °C [53,59]. In contrast, for SiOC/nSi_c only week SiC intensities are detected, suggesting the formation of minor amounts of SiC. A Riedvelt refinement was applied for the SiOC/nSi_a pattern in order to analyze the phase ratio between the crystallized silicon and silicon carbide. The results indicate a ratio of Si:SiC of 28.5:71.5 by weight and 36.3:63.7 by mole.

The existence of segregated free carbon is outlined by the presence of intense D and G-bands in the Raman spectra of the composites, as shown in Fig. 2. Besides the D and G-intensities, the overtones of the D vibration, the 2D modes, the D + G combination mode and a sharp band relating to crystalline Si-vibration are visible. In particular, the intense D-band specifies the free carbon of amorphous nature, well corresponding to the absence of graphite diffraction intensity in the XRD patterns.

Table 1 presents the chemical composition of the composites and their ceramic matrices. For all species a phase partitioning of SiOC into equivalents of silicon carbide, silica and free carbon is included, according to [71]. For the composites, the phase fractions of crystalline Si and SiC are additionally quantified. In the case of SiOC/nSi_a, the estimated ratio Si:SiC (28.5:71.5 by weight and 36.3:63.7 by mole) is taken as the basis for Si and SiC quantification, assuming the consumption of free carbon from the matrix in the

Table 1
Chemical composition of SiOC/nSi_c and SiOC/nSi_a. The weight fractions of the phase equivalents for SiOC, i.e. silicon carbide, silica and free carbon, are quantified according to Ref. [71].

Sample	Si [wt-%]	O [wt-%]	C [wt-%]	Phase equivalents SiOC			Crystalline Si [wt-%]	Crystalline SiC [wt-%]
				SiC [wt-%]	SiO$_2$ [wt-%]	Free C [wt-%]		
SiOC/nSi_c	43.68	15.25	41.07	14.70	28.63	36.67	20.00	–
SiOC/nSi_c matrix only	29.60	19.06	51.34	18.37	35.79	45.83	–	–
SiOC/nSi_a	42.67	16.15	41.18	12.13	30.32	32.10	7.25	18.20
SiOC/nSi_a matrix only	30.41	21.66	47.93	16.27	40.68	43.05	–	–

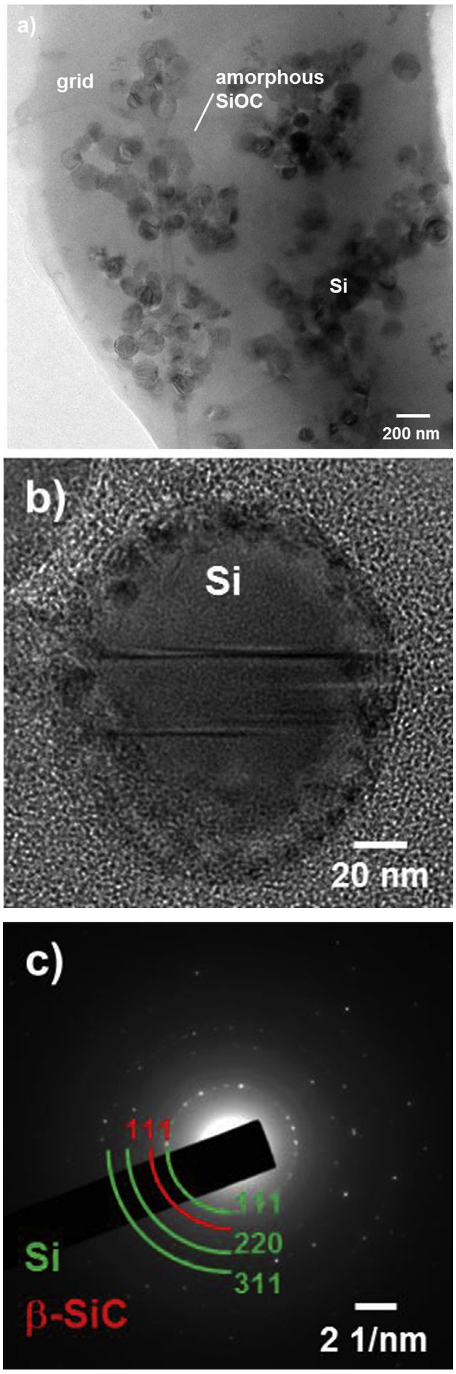

Fig. 3. a), b) TEM micrographs and c) SAED pattern of SiOC/nSi_c.

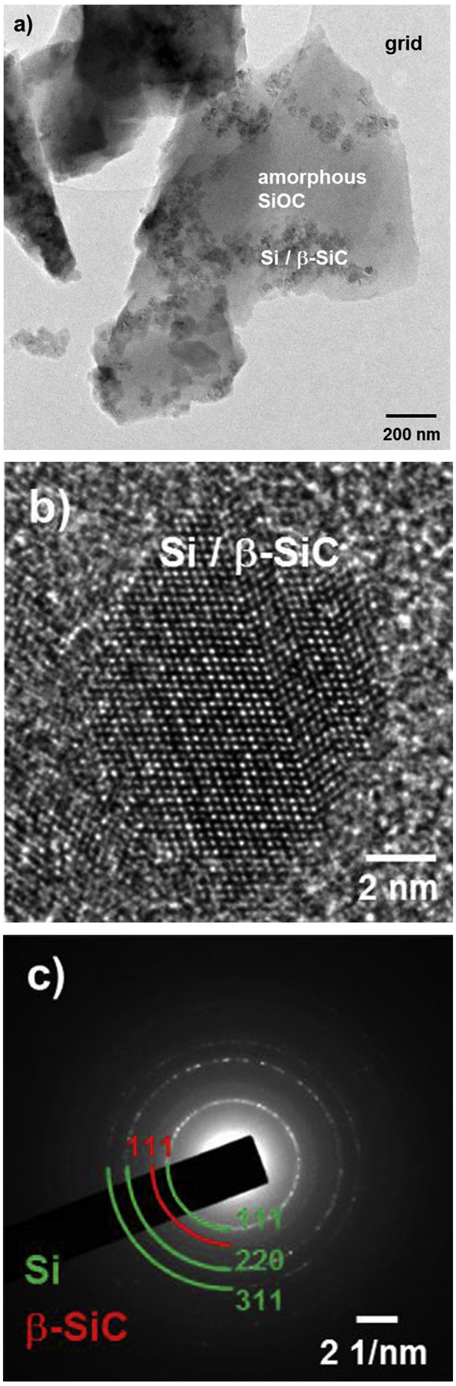

Fig. 4. a), b) TEM micrographs and c) SAED pattern of SiOC/nSi_a; in HRTEM in the present orientation there is no identification between Si and SiC possible.

formation process of SiC. Consequently, the actual amount of crystalline Si phase in SiOC/nSi_a only amounts 7.25 wt-% in contrast to 20 wt-% present in SiOC/nSi_c.

In Figs. 3 and 4, the TEM micrographs and the SAED pattern of SiOC/nSi_c and SiOC/nSi_a are shown. Note that for both composites, the particle distribution within the matrix is inhomogeneous, as a result of sample preparation, since the nano-sized silicon particles already tend to agglomerate before mixing with polyorganosiloxane *RD-684a*. In the case of SiOC/nSi_c, grains of the initially embedded size of 30–50 nm and particles up to 100 nm in diameter are well visible within the amorphous SiOC phase. In contrast, the microstructure of SiOC/nSi_a differs significantly, i.e. Si and SiC precipitates of ~10 nm in size are detected. Due to the similar lattice parameter of Si and β-SiC, HRTEM is not able to distinguish between both species. However, the SAED pattern clearly reveals the presence of both phases, well matching with the XRD results.

Altogether, the prepared SiOC/nSi composites are composed of four major phases: i) the amorphous Si–O–C matrix, including ii) free carbon, iii) crystalline silicon and iv) crystalline silicon carbide.

3.2. Electrochemical characterization

The electrochemical stability of both composites, SiOC/nSi_c and SiOC/nSi_a, upon prolonged galvanostatic cycling performed with a current of 74 mA g^{-1} is compared in Fig. 5. For SiOC/nSi_c, the initial reversible capacity amounts 804 mAh g^{-1} and increases during the first 10 cycles up to 905 mAh g^{-1}. Starting around cycle 15, a continuous capacity decrease sets on and after 50 cycles a capacity of only 314 mAh g^{-1} is recovered. The coulombic efficiency within one cycle ranges between 94 and 98%. It is suggested that the reason of the observed fading is related to the loss of silicon electroactivity, due to a progressive degradation and failure of the SiOC matrix, which is not able to withstand the generated mechanical stresses upon continuous expansion and contraction during Li–Si alloying/dealloying. At a certain point, the matrix ruptures irreversibly, leading to electrically isolated fragments that cannot contribute to Li-ion storage any-longer. For SiOC/nSi_a, the initial capacity is lower compared to that of SiOC/nSi_c (Fig. 5), due to the loss of electrochemically active silicon and free carbon by the formation of inactive silicon carbide [104]. The initial recovered capacity of 555 mAh g^{-1} increases up to a maximum of 704 mAh g^{-1} and remains relatively stable for 100 cycles. Characteristic fading, as observed for SiOC/nSi_c, does not occur, demonstrating superior matrix integrity of the sample. Moreover, the coulombic efficiency after the 5th cycle is continuously above 99.5%.

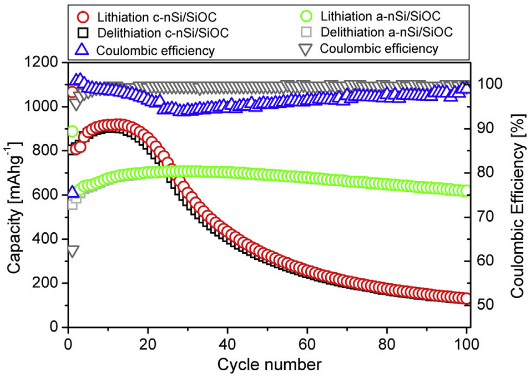

Fig. 5. Comparison of the cycling behavior and coulombic efficiency of SiOC/nSi_c and SiOC/nSi_a in dependence of cycle number at a current rate of 74 mA g^{-1}.

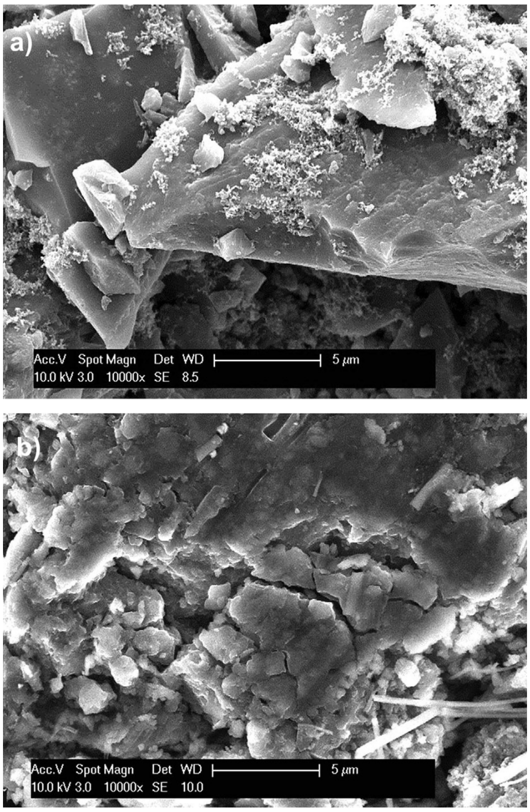

Fig. 6. SEM images of SiOC/nSi_c electrodes a) before and b) after cycling; the fibers present remaining rests of the separator.

SEM micrographs of uncycled and cycled composite electrodes are shown in Figs. 6 and 7 and illustrate the matrix failure of SiOC/nSi_c and matrix integrity of SiOC/nSi_a. The prolonged insertion/extraction of lithium into SiOC/nSi_c causes significant cracking of the electrode particles and in consequence, the composite grains appear broken apart and pulverized after cycling. For SiOC/nSi_a on the contrary, almost no change in morphology is found, when comparing the pristine electrode to that exposed to prolonged electrochemical cycling.

The differential capacity plots for both composites are shown in Fig. 8 and confirm the prior findings. When following the development of the Li–Si alloying/dealloying activity, at 0.22 and 0.08 V for alloying and at 0.30 and 0.45 V for dealloying [10], an initial intensity increase is recognized for SiOC/nSi_c, followed by a rapid decrease after cycle 10 (Fig. 8a). The initial capacity increase relates to cycle-wise silicon activation, suggesting that not all silicon present in the sample is contributing to Li-ion storage right from the beginning of cycling and that the Si phase needs to be activated first. The general intensity decrease in the dq/dV plot over the whole potential range beyond cycle 10, again is attributed to the continuous degradation of the composite material due to matrix failure and matches well with the cycling performance shown in Fig. 5. For SiOC/nSi_a on the contrary (Fig. 8b), the characteristic Li–Si alloying/dealloying signals initially increase in intensity

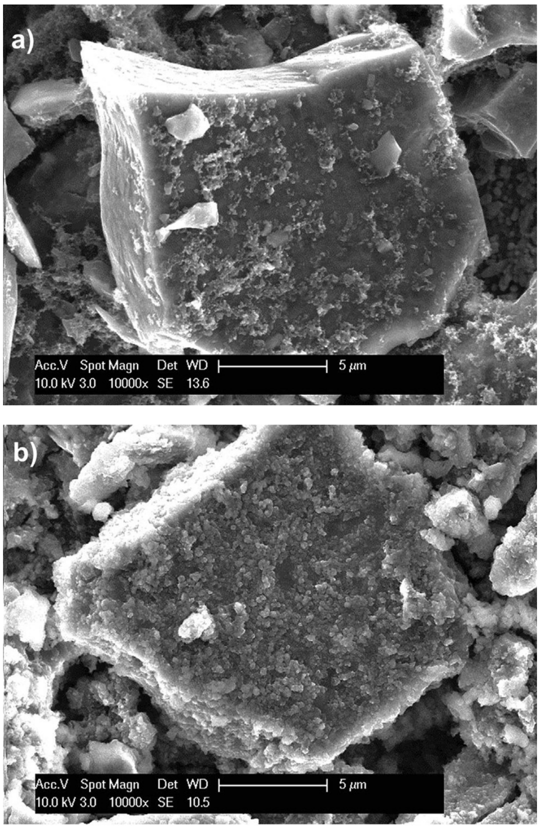

Fig. 7. SEM images of SiOC/nSi_a electrodes a) before and b) after cycling.

within the first 10 cycles and remain stable in following prolonged cycling.

Note that in both plots, there is a difference in the first alloying curve in the cathodic branch, namely for SiOC/nSi_c (Fig. 8a) a peak at ~0.18 V, followed by an intense peak in the range of 0.12–0 V, is visible, while for SiOC/nSi_a (Fig. 8b) a broad wave starting at ~0.22 V, superimposing with a potential peak at ~0.18 V and again followed by a low voltage peak in the range of 0.12–0 V, is identified. The peak at 0.18 V can be attributed to the activity of the SiOC matrix, observed at this potential during the first lithiation [105]. The low voltage peak in the range of 0.12–0.08 V for both samples corresponds to the first alloying of crystalline silicon and the formation of a two-phase region with a-Li_xSi, as described by Obrovac et al. [9] and Li et al. [10] ($Si\_c + xLi \rightarrow a\text{-}Li_xSi$). For SiOC/nSi_a first the activity of the traces of amorphous silicon present in the composite at ~0.22 V is observed, but superimposed within the more pronounced SiOC matrix electroactivity appearing at potentials around 0.18 V.

Within subsequent cycling both composites reveal the high and low voltage peaks of amorphous silicon at ~0.22 and 0.08 V in the cathodic branch [10], while the matrix electroactivity at 0.18 V is replaced by a broad peak with maximum at ~0.45 V [60,105]. This activity remains stable for SiOC/nSi_a, while it almost vanishes for SiOC/nSi_c after cycle 40 (Fig. 8a, yellow curve (in the web version)). This finding matches perfectly to our reasoning that the electrochemical instability of the SiOC/nSi_c composite is caused by the inability of the matrix to withstand the stresses related to the silicon volume changes. Concerning the SiOC activity in the anodic branch, typically peaks are found at potentials of 0.08, 0.34 and 0.68 V [60]. For both composites, not all these signals are well pronounced, but rather broadened and overlapping with the silicon activity intensities. It is however possible to trace the significant fading of the 0.08 and 0.68 V peaks for SiOC/nSi_c with subsequent cycling, emphasizing the diminishing matrix activity.

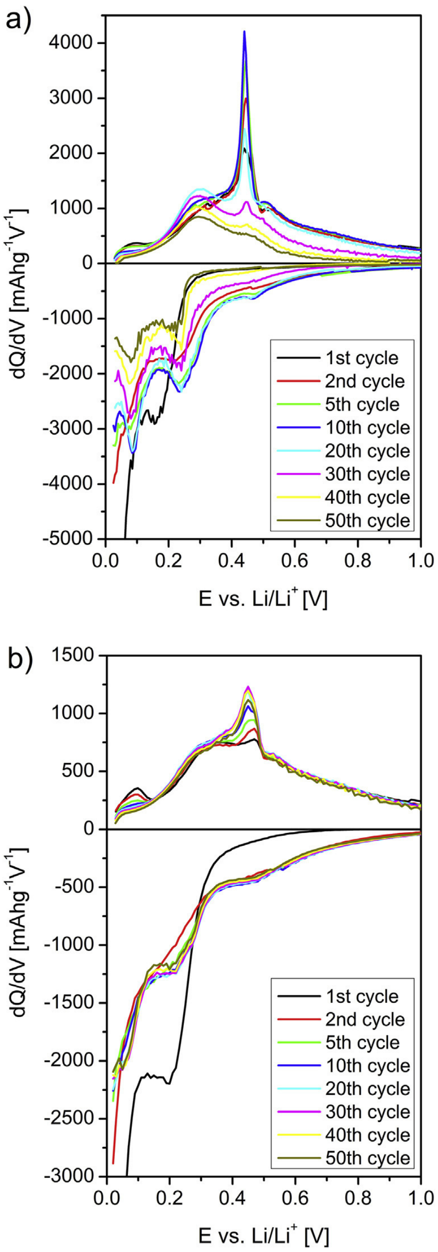

Fig. 8. Differential capacity curves for a) SiOC/nSi_c and b) SiOC/nSi_a.

In Fig. 9, the cycling performance of the composites is compared with respect to pure SiOC and a pure nSi_c reference, representing the general cycling behavior of both, pure nSi_c and nSi_a reference

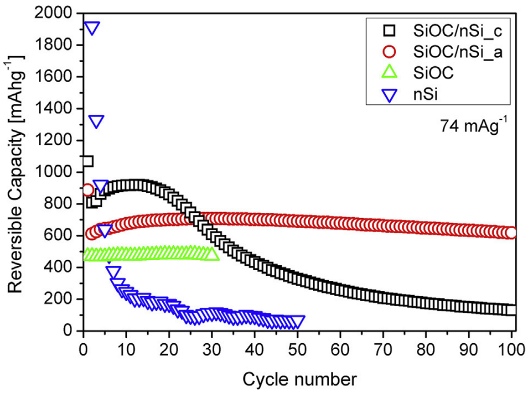

Fig. 9. Comparison of the reversible capacity in dependence of cycle number for SiOC/nSi_c, SiOC/nSi_a, pure SiOC [53,59] and pure nSi at a cycling current of 74 mA g^{-1}.

electrodes. The data for pure SiOC is taken form our previous reports [53,59]. The capacity of the nSi electrode drops instantly and after 10 cycles only about 10% of the initial capacity is recovered. This rapid degradation is a well-known and reported phenomenon, rationalized by the tremendous volume changes upon Li–Si alloying/dealloying (Si/$Li_{15}Si_4$, $\Delta V \approx 280\%$) that provokes amorphization and pulverization of the electrode [7–13]. Pure SiOC demonstrates a stable capacity of about 477 mAh g^{-1}. For both SiOC/nSi composites, the introduction of electrochemically active silicon increases the total capacity up to 905 mAh g^{-1} for SiOC/nSi_c and 704 mAh g^{-1} for SiOC/nSi_a compared to pure SiOC. However, in the case of crystalline silicon embedment, the cycling stability and electrode life-time are significantly reduced. Moreover, with respect to pure silicon, a carbon-rich SiOC host appears suitable to mechanically stabilize the incorporated Si-grains during lithium uptake and release and accounts for an improved cycling stability and reduced capacity fading, especially in the case of SiOC/nSi_a. When comparing the absolute capacities of both composites to the ones reported for Si/Graphite composites by Jo et al. [41], a carbon-rich SiOC matrix offers additional advantage, since the theoretical capacity of graphite is limited to 372 mAh g^{-1}, whereas SiOC exceeds this value with up to 520 mAh g^{-1} [53,59]. Accordingly, slightly lower capacity values of 530 and 568 mAh g^{-1} were registered for the Si/Graphite samples of similar composition of Si:Graphite of 20:80 by weight. Another report in literature is concerned with the electrochemical performance of a Si/SiOC composite prepared by Sol–Gel method [84]. The ratio of Si:SiOC amounts approximately 10:90 by weight, whereas the sample demonstrates a high first cycle reversible capacity of 1372 mAh g^{-1}. Upon prolonged cycling the recovered capacity rapidly decreases, with only 77% capacity retention after 30 cycles (990 mAh g^{-1}). In comparison, the SiOC/nSi_a sample prepared in this work exhibits a slightly lower content of free Si (7.25 wt-%) and hence a lower maximum capacity (704 mAh g^{-1}). However, the synthesized SiOC/nSi_a composite stands out with its superior cycling stability, i.e. 88% capacity retention after 100 cycles with respect to the maximum value, indicating that a carbon-rich SiOC host can better accommodate the arising mechanical stresses upon Li–Si alloy expansion/contraction than carbon-poor SiOC, as prepared by Liu et al. [84]. A similar beneficial stabilization was recently reported for SiOC/Sn nano-composites, in which a carbon-rich SiOC matrix was emphasized of major importance for the non-destructive buffering of Sn-grain related volume changes upon alloying/dealloying with Li [106].

On the one hand, the smaller size of the crystalline nSi grains (~10 nm), causes minor absolute volume changes upon Li–Si alloying/dealloying and in consequence less mechanical load is applied to the matrix. As consequence, critical fracture stress intensities are locally avoided. In addition, the presence of SiC phase, as in the case of SiOC/nSi_a, increases the intrinsic electrical conductivity of the material and supports the internal electrical wiring (σ_{SiC} = ~10^1–10^2 S m^{-1} depending on its form and size, $\sigma_{Si} = 10^{-3}$ S m^{-1}, $\sigma_{SiOC} = 7.14$ S m^{-1} [97,107]). A similar conductivity increase was previously reported for SiC containing SiCN ceramics [108,109]. Finally, both features account for the superior electrochemical cycling stability of the SiOC/nSi_a material.

At last, a comparison between the theoretically expectable and the experimentally registered capacities for the composites is drawn. According to the chemical composition in Table 1, a theoretical capacity can be estimated from the mass ratio SiOC:Si. For silicon, 3579 mAh g^{-1} ($Li_{15}Si_4$ phase) is considered as theoretical value, whereas the capacity contribution from SiOC is adopted from our previous reports [53,59], i.e. 477 mAh g^{-1} for a current rate of 74 mA g^{-1}. In sum, the calculated values for the composites amount 1097 mAhg^{-1} for SiOC/nSi_c and 615 mAh g^{-1} for SiOC/nSi_a. For SiOC/nSi_c the experimental value of 905 mAh g^{-1} is lower compared to the theoretical one, which can be reasoned by two oppositional effects: i) the silicon phase is gradually activated upon cycling and not completely accessible for Li-ions from the first lithiation, but ii) matrix degradation and thus loss of composite active material occurs immediately upon cycling. For SiOC/nSi_a on the contrary, the experimentally found capacity of 704 mAh g^{-1} is higher than the theoretically estimated one (615 mAh g^{-1}), which could be explained by the following. First, the estimation relies on the assumption that the amorphous input silicon completely crystallizes into either silicon or silicon carbide. But it seems that amorphous silicon phase is still present within the SiOC matrix, as traced in the dq/dV plot in Fig. 8b. In consequence, the real capacity is necessarily higher than the calculated one. In addition, the presence of SiC nano-particles increases the electronic conductivity and availability of carbon phase within the SiOC host and might increase the capacity of the sample in a non-linear way with respect to the calculation. A similar phenomenon was previously reported for mixtures of carbon-poor SiCN ceramics and graphite [64,105].

4. Conclusions

Nano-crystalline and nano-amorphous silicon particles were successfully embedded within a polymer-derived, carbon-rich silicon oxycarbide matrix. The composites demonstrated a high gravimetric capacity of 905 mAh g^{-1} and 704 mAh g^{-1} for SiOC/nSi_c and SiOC/nSi_a, respectively. However, strong capacity fading was found for the SiOC/nSi_c material, whereas the incorporation of nano-amorphous Si into the SiOC matrix provided a material with a stable cycling performance up to 100 cycles. Fundamental microstructural differences were identified as the main reason for the difference in the electrochemical behavior. In the case of SiOC/nSi_c, crystalline silicon grains up to 100 nm in diameter are present within the matrix, while in the case of SiOC/nSi_a, silicon and silicon carbide crystallites of ~10 nm in size were found. Due to the smaller size of the Si precipitates, the absolute volume expansion of the formed Li–Si alloy in SiOC/nSi_a is less critical, leading to minor mechanical load locally applied to the matrix. The arising stresses can be well accommodated by the SiOC host without degradation. In the case of SiOC/nSi_c, the expansion of the larger Si grains causes a severe matrix failure and in consequence fading of the capacity is well pronounced. Moreover, nano-sized SiC grains present in SiOC/nSi_a, increase the electrical conductivity and contribute to the superior electrochemical behavior of the composite. Finally, the deviation between the theoretically estimated capacity of SiOC/nSi_a (651 mAh g^{-1}) and SiOC/nSi_c (1097 mAh g^{-1}) and the registered ones of 704 mAh g^{-1} and 905 mAh g^{-1}, respectively, is described. For the sample based on amorphous silicon, it is suggested that the initially amorphous silicon crystallized only partially, leaving electrochemically active amorphous phase unconsidered in the estimation, while for SiOC/nSi_c a slow activation of the available crystalline silicon is assumed to be responsible for registered lower capacity values.

Acknowledgments

This work was financially supported by the Deutsche Forschungsgemeinschaft (DFG), Bonn, Germany within the priority program SPP1473/JP8 and the collaborative research center SFB595. The authors want to acknowledge K. Wissel for her support in the electrode preparation, J.-C. Jaud for his assistance with the XRD measurements and M. Bekheet for the performed Rietveld refinement.

References

[1] H. Kawamoto, Sci. Technol. Trends 36 (2010) 34.
[2] G.L. Soloveichik, Annu. Rev. Chem. Biomol. Eng. 2 (2011) 503–527.
[3] J. Liu, Adv. Funct. Mater. 23 (2013) 924–928.
[4] C.M. Hayner, X. Zhao, H.H. Kung, Annu. Rev. Chem. Biomol. Eng. 3 (2012) 445–471.
[5] J. Chen, Materials 6 (2013) 156–183.
[6] R. Wagner, N. Preschitschek, S. Passerini, J. Leker, M. Winter, J. Appl. Electrochem. 43 (2013) 481–496.
[7] L.Y. Beaulieu, K.W. Eberman, R.L. Turner, L.J. Krause, J.R. Dahn, Electrochem. Solid-State Lett. 4 (2001) A137–A140.
[8] M.N. Obrovac, L. Christensen, Electrochem. Solid-State Lett. 7 (2004) A93–A96.
[9] M.N. Obrovac, L.J. Krause, J. Electrochem. Soc. 154 (2007) A103–A108.
[10] J. Li, J.R. Dahn, J. Electrochem. Soc. 154 (2007) A156–A161.
[11] X.H. Liu, L. Zhong, S. Huang, S.X. Mao, T. Zhu, J.Y. Huang, ACS Nano 6 (2012) 1522–1531.
[12] Y.F. Gao, M. Zhou, J. Power Sources 230 (2013) 176–193.
[13] Z. Ma, T. Li, Y.L. Huang, J. Liu, Y. Zhou, D. Xue, RSC Adv. 3 (2013) 7398–7402.
[14] J. Graetz, C.C. Ahn, R. Yazami, B. Fultz, Electrochem. Solid-State Lett. 6 (2003) A194–A197.
[15] M. Holzapfel, H. Buqa, L.J. Hardwick, M. Hahn, A. Wursig, W. Scheifele, P. Novak, R. Kotz, C. Veit, F.M. Petrat, Electrochim. Acta 52 (2006) 973–978.
[16] D. Arquier, G. Calleja, G. Cerveau, R.J.P. Corriu, C. R. Chim. 10 (2007) 795–802.
[17] J.R. Szczech, S. Jin, Energy Environ. Sci. 4 (2011) 56–72.
[18] C.-F. Sun, K. Karki, Z. Jia, H. Liao, Y. Zhang, T. Li, Y. Qi, J. Cumings, G.W. Rubloff, Y. Wang, ACS Nano 7 (2013) 2717–2724.
[19] J.P. Maranchi, A.F. Hepp, P.N. Kumta, Electrochem. Solid-State Lett. 6 (2003) A198–A201.
[20] V. Baranchugov, E. Markevich, E. Pollak, G. Salitra, D. Aurbach, Electrochem. Commun. 9 (2007) 796–800.
[21] C.K. Chan, H. Peng, G. Liu, K. Mc Ilwrath, X.F. Zhang, R.A. Huggins, Y. Cui, Nat. Nanotechnol. 3 (2008) 31–35.
[22] C.K. Chan, R. Ruffo, S.S. Hong, R.A. Huggins, Y. Cui, J. Power Sources 189 (2009) 34–39.
[23] L.-F. Cui, R. Ruffo, C.K. Chan, H. Peng, Y. Cui, Nano Lett. 9 (2009) 491–495.
[24] Y.F. Gao, M. Zhou, J. Appl. Phys. 109 (2011) 014310.
[25] A. Vlad, A.L.M. Reddy, A. Ajayan, N. Singh, J.-F. Gohy, S. Melinte, P.M. Ajayan, Proc. Natl. Acad. Sci. 109 (2012) 15168–15173.
[26] M. Ge, J. Rong, X. Fang, C. Zhou, Nano Lett. 12 (2012) 2318–2323.
[27] X.H. Liu, F. Fan, H. Yang, S. Zhang, J.Y. Huang, T. Zhu, ACS Nano 7 (2013) 1495–1503.
[28] Y. Fan, Q. Zhang, Q. Xiao, X. Wang, K. Huang, Carbon 59 (2013) 264–269.
[29] Z. Wen, G. Lu, S. Mao, H. Kim, S. Cui, K. Yu, X. Huang, P.T. Hurley, O. Mao, J. Chen, Electrochem. Commun. 29 (2013) 37–70.
[30] U. Kasavajjula, C. Wang, A.J. Appleby, J. Power Sources 163 (2007) 1003–1039.
[31] N. Dimov, S. Kugino, M. Yoshio, Electrochim. Acta 48 (2003) 1579–1587.
[32] Y. Liu, K. Hanai, J. Yang, N. Imanishi, A. Hirano, Y. Takeda, Solid State Ionics 168 (2004) 61–68.
[33] M. Holzapfel, H. Buqua, W. Scheifele, P. Novak, F.M. Petrat, Chem. Commun. 12 (2005) 1566–1568.
[34] S.H. Ng, J.Z. Wang, D. Wexler, K. Konstantinov, Z.P. Guo, H.K. Liu, Angew. Chem. Int. Ed. 45 (2006) 6896–6899.
[35] X.L. Yang, Z.Y. Wen, X.X. Xu, B. Lin, Z.X. Lin, J. Electrochem. Soc. 153 (2006) A1341–A1344.
[36] J. Saint, M. Morcrette, D. Larcher, L. Laffont, S. Beattie, J.P. Peres, D. Talaga, M. Couzi, J.M. Tarascon, Adv. Funct. Mater. 17 (2007) 1765–1774.
[37] M. Alias, O. Crosnier, I. Sandu, G. Jestin, A. Papadimopoulos, F. Le Cras, D.M. Schleich, T. Brousse, J. Power Sources 174 (2007) 900–904.
[38] R. Demir Cakan, M.-M. Titirici, M. Antonietti, G. Cui, J. Maier, Y.-S. Hu, Chem. Commun. 37 (2008) 3759–3761.
[39] C. Martin, M. Alias, F. Christien, O. Crosnier, D. Belanger, T. Brousse, Adv. Mater. 21 (2009) 4735–4741.
[40] Z. Luo, D. Fan, X. Liu, H. Mao, C. Yao, Z. Deng, J. Power Sources 189 (2009) 16–21.
[41] Y.N. Jo, Y. Kim, J.S. Kim, J.H. Song, K.J. Kim, C.Y. Kwag, D.J. Lee, C.W. Park, Y.J. Kim, J. Power Sources 195 (2010) 6031–6036.
[42] H. Xiang, K. Zhang, G. Ji, J.Y. Lee, C. Zou, X. Chen, J. Wu, Carbon 49 (2011) 1787–1796.
[43] R. Yi, F. Dai, M.L. Gordin, S. Chen, D. Wang, Adv. Energy Mater. 3 (2013) 295–300.
[44] R. Yi, F. Dai, M.L. Gordin, H. Sohn, D. Wang, Adv. Energy Mater. 11 (2013) 1507–1515.
[45] H. Fukui, O. Hisashi, T. Hino, K. Kanamura, ACS Appl. Mater. Interfaces 4 (2010) 998–1008.
[46] H. Fukui, N. Nakata, K. Dokko, B. Takemura, H. Ohsuka, T. Hino, K. Kanamura, ACS Appl. Mater. Interfaces 3 (2011) 2318–2322.
[47] H. Fukui, H. Ohsuka, T. Hino, K. Kanamura, J. Power Sources 196 (2011) 371–378.
[48] H. Fukui, H. Ohsuka, T. Hino, K. Kanamura, J. Electrochem. Soc. 158 (2011) A550–A555.
[49] X. Liu, K. Xie, C.-M. Zheng, J. Wang, Z. Jing, J. Power Sources 214 (2012) 119–123.
[50] X. Liu, M.-C. Zheng, K. Xie, J. Liu, Electrochim. Acta 59 (2012) 304–309.
[51] P. Dibandjo, M. Graczyk-Zajac, R. Riedel, V.S. Pradeep, G.D. Soraru, J. Eur. Ceram. Soc. 32 (2012) 2495–2503.
[52] M. Graczyk-Zajac, L. Toma, C. Fasel, R. Riedel, Solid State Ionics 225 (2012) 522–526.
[53] J. Kaspar, M. Graczyk-Zajac, R. Riedel, Solid State Ionics 225 (2012) 527–531.
[54] R. Bhandavat, Z. Pei, G. Singh, Nanomater. Energy 1 (2012) 324–337.
[55] V.S. Pradeep, M. Graczyk-Zajac, M. Wilamowska, R. Riedel, G.D. Soraru, Solid State Ionics 262 (2014) 22–24, http://dx.doi.org/10.1016/j.ssi.2013.1008.1043.
[56] H. Fukui, K. Eguchi, H. Ohsuka, T. Hino, K. Kanamura, J. Power Sources 243 (2013) 152–158.
[57] H. Fukui, H. Ohsuka, T. Hino, K. Kanamura, J. Electrochem. Soc. 160 (2013) A1276–A1281.
[58] G. Liu, J. Kaspar, L.M. Reinold, M. Graczyk-Zajac, R. Riedel, Electrochim. Acta 106 (2013) 101–108.
[59] J. Kaspar, M. Graczyk-Zajac, R. Riedel, J. Power Sources 244 (2013) 450–455.
[60] J. Kaspar, M. Graczyk-Zajac, R. Riedel, Electrochim. Acta 115 (2014) 665–670.
[61] P.D. Weidman, D. Ahn, R. Raj, J. Power Sources 249 (2014) 219–230.
[62] V.S. Pradeep, M. Graczyk-Zajac, R. Riedel, G.D. Soraru, Electrochim. Acta 119 (2014) 78–85.
[63] J. Kaspar, G. Mera, A.P. Nowak, M. Graczyk-Zajac, R. Riedel, Electrochim. Acta 56 (2010) 174–182.
[64] M. Graczyk-Zajac, C. Fasel, R. Riedel, J. Power Sources 196 (2011) 6412–6418.
[65] L.M. Reinold, M. Graczyk-Zajac, Y. Gao, G. Mera, R. Riedel, J. Power Sources 236 (2013) 224–229.
[66] S.-H. Baek, L.M. Reinold, M. Graczyk-Zajac, R. Riedel, F. Hammerath, B. Büchner, H.-J. Grafe, J. Power Sources 253 (2014) 342–348.
[67] G.M. Renlund, S. Prochazka, R.H. Doremus, J. Mater. Res. 6 (1991) 2716–2722.
[68] G.M. Renlund, S. Prochazka, R.H. Doremus, J. Mater. Res. 6 (1991) 2723–2734.
[69] G.D. Soraru, J. Sol–Gel Sci. Technol. 2 (1994) 843–848.
[70] C.G. Pantano, A.K. Singh, H. Zhang, J. Sol–Gel Sci. Technol. 14 (1999) 7–25.
[71] G.D. Soraru, S. Modena, E. Guadagnino, P. Colombo, J. Egan, C. Pantano, J. Am. Ceram. Soc. 85 (2002) 1529–1536.
[72] T. Momma, S. Aoki, H. Nara, T. Yokoshima, T. Osaka, Electrochem. Commun. 13 (2011) 969–972.
[73] H. Nara, T. Yokoshima, T. Momma, T. Osaka, Energy Environ. Sci. 5 (2012) 6500–6505.
[74] H. Nara, T. Yokoshima, M. Otaki, T. Momma, T. Osaka, Electrochim. Acta 110 (2013) 403–410.
[75] A.M. Wilson, J.N. Reimers, E.W. Fuller, J.R. Dahn, Solid State Ionics 74 (1994) 249–254.
[76] A.M. Wilson, W. Xing, G. Zank, B. Yates, J.R. Dahn, Solid State Ionics 100 (1997) 259–266.
[77] A.M. Wilson, G. Zank, K. Eguchi, W. Xing, J.R. Dahn, J. Power Sources 68 (1997) 195–200.
[78] A.M. Wilson, G. Zank, K. Eguchi, W. Xing, B. Yates, J.R. Dahn, Chem. Mater. 9 (1997) 1601–1606.
[79] W. Xing, A.M. Wilson, K. Eguchi, G. Zank, J.R. Dahn, J. Electrochem. Soc. 144 (1997) 2410–2416.
[80] W. Xing, A.M. Wilson, G. Zank, J.R. Dahn, Solid State Ionics 93 (1997) 239–244.

[81] J. Shen, D. Ahn, R. Raj, J. Power Sources 196 (2011) 2875–2878.
[82] R. Bhandavat, M. Cologna, G. Singh, Nanomater. Energy 1 (2012) 57–61.
[83] R. Bhandavat, G. Singh, J. Phys. Chem. C 117 (2013) 11899–11905.
[84] X. Liu, K. Xie, J. Wang, C. Zheng, Y. Pan, J. Mater. Chem. 22 (2012) 19621–19624.
[85] P. Kroll, J. Mater. Chem. 13 (2003) 1657–1668.
[86] P. Kroll, J. Non-Cryst. Solids 351 (2005) 1121–1126.
[87] P. Kroll, J. Mater. Chem. 20 (2010) 10528–10534.
[88] P. Kroll, MRS Proc. 1313 (2011).
[89] P. Colombo, G. Mera, R. Riedel, G.D. Soraru, J. Am. Ceram. Soc. 93 (2010) 1805–1837.
[90] Y.D. Blum, D.B. MacQueen, H.-J. Kleebe, J. Eur. Ceram. Soc. 25 (2005) 143–149.
[91] H.-J. Kleebe, G. Gregori, Y.D. Blum, F. Babonneau, Int. J. Mater. Res. 97 (2006) 699–709.
[92] G. Gregori, H.-J. Kleebe, Y.D. Blum, F. Babonneau, Int. J. Mater. Res. 97 (2006) 710–720.
[93] S.J. Widgeon, S. Sen, G. Mera, E. Ionescu, R. Riedel, A. Navrotsky, Chem. Mater. 22 (2010) 6221–6228.
[94] G. Mera, A. Navrotsky, S. Sen, H.-J. Kleebe, R. Riedel, J. Mater. Chem. A 1 (2013) 3826–3836.
[95] J. Cordelair, P. Greil, J. Eur. Ceram. Soc. 20 (2000) 1947–1957.
[96] H.-J. Kleebe, Y.D. Blum, J. Eur. Ceram. Soc. 28 (2008) 1037–1042.
[97] S. Martínez-Crespiera, E. Ionescu, H.-J. Kleebe, R. Riedel, J. Eur. Ceram. Soc. 31 (2011) 913–919.
[98] A. Saha, R. Raj, D.L. Williamson, J. Am. Chem. Soc. 89 (2006) 2188–2195.
[99] P.E. Sanchez-Jimenez, R. Raj, J. Am. Ceram. Soc. 93 (2010) 1127–1135.
[100] D. Ahn, R. Raj, J. Power Sources 195 (2010) 3900–3906.
[101] D. Ahn, R. Raj, J. Power Sources 196 (2011) 2179–2186.
[102] S.D. Beattie, D. Larcher, M. Morcrette, B. Simon, J.M. Tarascon, J. Electrochem. Soc. 155 (2008) A158–A163.
[103] G. Schierning, R. Theissmann, H. Wiggers, D. Sudfeld, A. Ebbers, D. Franke, V.T. Witusiewicz, M. Apel, J. Appl. Phys. 103 (2008) 084305.
[104] D. Larcher, C. Mudalige, A.E. George, V. Porter, M. Gharghouri, J.R. Dahn, Solid State Ionics 122 (1999) 71–83.
[105] M. Wilamowska, M. Graczyk-Zajac, R. Riedel, J. Power Sources 244 (2013) 80–86.
[106] J. Kaspar, C. Terzioglu, E. Ionescu, M. Graczyk-Zajac, S. Hapis, H.J. Kleebe, R. Riedel, Adv. Funct. Mater. (2014), http://dx.doi.org/10.1002/adfm.201303828 in press.
[107] O. Madelung, Semiconductors Data Handbook, Springer, Berlin, 2004.
[108] C. Haluschka, H.J. Kleebe, R. Franke, R. Riedel, J. Eur. Ceram. Soc. 20 (2000) 1355–1364.
[109] C. Haluschka, C. Engel, R. Riedel, J. Eur. Ceram. Soc. 20 (2000) 1365–1374.

Stable SiOC/Sn Nanocomposite Anodes for Lithium-Ion Batteries with Outstanding Cycling Stability

Jan Kaspar, Caglar Terzioglu, Emanuel Ionescu, Magdalena Graczyk-Zajac, Stefania Hapis, Hans-Joachim Kleebe, and Ralf Riedel**

Silicon oxycarbide/tin nanocomposites (SiOC/Sn) are prepared by chemical modification of polysilsesquioxane Wacker-Belsil PMS MK ($SiOC_{MK}$) and polysiloxane Polyramic RD-684a ($SiOC_{RD}$) with tin(II)acetate and subsequent pyrolysis at 1000 °C. The obtained samples consist of an amorphous SiOC matrix and in-situ formed metallic Sn precipitates. Galvanostatic cycling of both composites demonstrate a first cycle reversible capacity of 566 $mAhg^{-1}$ for $SiOC_{MK}$/Sn and 651 $mAhg^{-1}$ for $SiOC_{RD}$/Sn. The superior cycling stability and rate capability of $SiOC_{RD}$/Sn as compared to $SiOC_{MK}$/Sn is attributed to the soft, carbon-rich SiOC matrix derived from the RD-684a polymer, which accommodates the Sn-related volume changes during Li-uptake and release. The poor cycling stability found for $SiOC_{MK}$/Sn relates to mechanical failure of the rather stiff and fragile, carbon-poor matrix produced from PMS MK. Incremental capacity measurements outline different final Li–Sn alloy stages, depending on the matrix. For $SiOC_{RD}$/Sn, alloying up to Li_7Sn_2 is registered, whereas for $SiOC_{MK}$/Sn $Li_{22}Sn_5$ stoichiometry is reached. The suppression of $Li_{22}Sn_5$ phase in $SiOC_{RD}$/Sn is rationalized by an expansion restriction of the matrix and thus prevention of a higher Li content in the alloy. For $SiOC_{MK}$/Sn on the contrary, the matrix severely ruptures, providing an unlimited free volume for expansion and thus formation of $Li_{22}Sn_5$ phase.

1. Introduction

Li-ion batteries represent the standard power source for portable electronics, such as mobile phones or laptop computers. The tremendous success of Li-ion secondary batteries started in 1991, when Sony Energytec introduced them into the market.[1,2] Since that time, cell design did not change significantly and the most common cell structure still consists of a carbon anode (e.g. graphite) in combination with a lithium metal oxide cathode (e.g. $LiCoO_2$). Over the years, power demands of new generation customer electronics steadily increased, pushing conventional cells to their limits. In addition, automobile industry strongly requests enhanced power supply for electrical and hybrid electrical driven vehicles. Thus, novel high power and high energy density materials are necessary in order to provide a sustainable future for Li-ion technology and to satisfy the emerging customer demands.[3–9]

Within this context, metals which can store lithium via alloying processes attracted attention as alternative anode material.[10–13] Lithium-tin alloy (Li-Sn) for instance has a theoretical capacity of 994 $mAhg^{-1}$ for its highest lithiation state of $Li_{22}Sn_5$, which is almost three times higher than that of the theoretical capacity of graphite (372 $mAhg^{-1}$). However, the major drawback related to tin-based anodes is their poor cycling stability, which emerges from large volume expansion and contraction during Li-uptake and release ($\Delta V \approx 260\%$ for Sn versus $Li_{22}Sn_5$).[14] Especially the tensile stress during contraction commonly initiates grain cracking and local grain pulverization. Consequently, electrical conduction pathways break down, causing capacity loss and poor cycle life time.[15,16]

Intense efforts were made in order to suppress this degradation by adopting nanostructured Sn-based architectures.[17–21] Sn-coated Cu-nanopillars for example, provide sufficient space to accommodate volume changes during the alloying/dealloying process, while demonstrating an enhanced cycle life.[19] However, such type of nano-architectures exhibit low energy density due to a rather low active mass-to-volume ratio. The major drawback related to Sn-nanoparticles is the loss of their initial morphology upon cycling. In consequence, the beneficial properties of the initial nanoscale get lost, including enhanced mechanical integrity towards crack initiation and pulverization.[10,11]

Another approach to prepare Sn-based electrodes with improved cycle stability was demonstrated by Derrien et al., who synthesized Sn/C nanocomposites by embedding Sn nanoparticles into a carbon matrix.[17,21] As the Sn particles are well distributed throughout the matrix, the initial microstructure remains stable during long term cycling. Additionally, the carbon matrix increases the electrical conductivity and ensures electrical wiring, even when cracking and pulverization occur.

J. Kaspar, C. Terzioglu, Dr. E. Ionescu,
Dr. M. Graczyk-Zajac, Prof. R. Riedel
Institut für Materialwissenschaft
Technische Universität Darmstadt
Jovanka Bontschits Straße 2, 64287 Darmstadt
E-mail: kaspar@materials.tu-darmstadt.de;
riedel@materials.tu-darmstadt.de
S. Hapis, Prof. H.-J. Kleebe
Institut für Angewandte Geowissenschaften
Technische Universität Darmstadt
Schnittspahnstraße 9, 64287 Darmstadt

DOI: 10.1002/adfm.201303828

In the present work, the direct synthesis of novel ceramic/tin nanocomposites was achieved by an innovative single-source-precursor approach. Accordingly, polyorganosiloxanes modified with tin(II)acetate were prepared and thermally converted into SiOC/Sn nanocomposites at 1000 °C. Two different commercially available polysiloxanes were used for the modification, namely *i)* polysilsesquioxane Wacker-Belsil PMS MK, which transforms into a silicon oxycarbide matrix ($SiOC_{MK}$) with moderate free carbon content (≈6 wt%) and a Young's modulus of 85–96 GPa and *ii)* polysiloxane Polyramic RD-684a, which converts into a carbon-rich (≈41 wt% free carbon) silicon oxycarbide matrix ($SiOC_{RD}$) with a consequently lower value of the Young's modus of 66 GPa.[22–26] Interestingly, the electrochemical performance of the SiOC/Sn-based nanocomposites prepared within the present study correlates with the phase composition and the stiffness of the silicon oxycarbide matrices. The carbon-poor and stiff matrix (as for $SiOC_{MK}$) is found to not be able to withstand volume changes related to Li-Sn alloying, since a serious damage of the electrodes has been monitored, accompanied by a strong capacity fading. If the matrix is carbon-rich and soft (as for $SiOC_{RD}$), it is able to accommodate the high volume expansion upon alloy formation and thus prevents the electrode failure.

2. Results and Discussion

2.1. Materials Characterization

The pure polysiloxanes PMS MK and RD-684a as well as the $Sn(ac)_2$-modified polymers were investigated by FTIR spectroscopy (**Figure 1** and **Figure 2**).

The spectrum of PMS MK shows absorption bands at ν = 590 cm^{-1} (SiOC-H), ν = 768, 1278 cm^{-1} ($Si-CH_3$), ν = 1030 cm^{-1} (Si-O-C) and ν = 1122 cm^{-1} (Si-O-Si), as previously reported.[27–31] The FTIR spectrum of the $Sn(ac)_2$-modified sample shows additional absorption bands corresponding to the acetate ligands, i.e. ν = 1340, 1572 cm^{-1} (C-O), ν = 1385 ($C-CH_3$) and ν = 1524 cm^{-1} (C=C).[32–34] Furthermore, two new absorption bands were assigned at ν = 689 cm^{-1} (Sn-O)[35,36] and ν = 925 cm^{-1} (Si-O-Sn).[37] Thus, the added $Sn(ac)_2$ undergoes a reaction with the Si-OH reactive groups present in PMS MK (**Figure 3**), upon release of acetic acid and the formation of Si-O-Sn units. The formation of Si-O-M (M = metal) units upon modification of the polymer with metal alkoxides, as well as with acetylacetonates and acetates, was demonstrated previously for metalorganic precursors of other metals, e.g. Fe,[27] Zr[28] and Hf.[29,30]

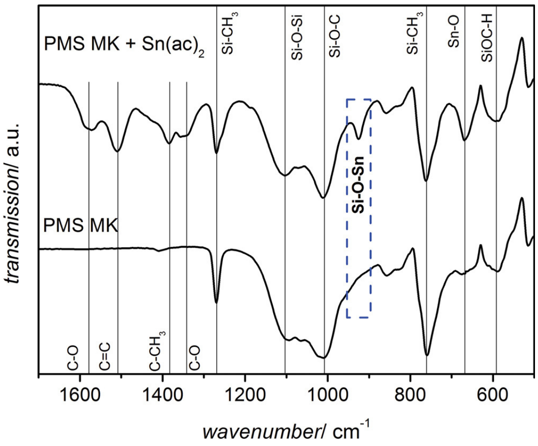

Figure 1. FTIR spectra of PMS MK and $Sn(ac)_2$ modified PMS MK.

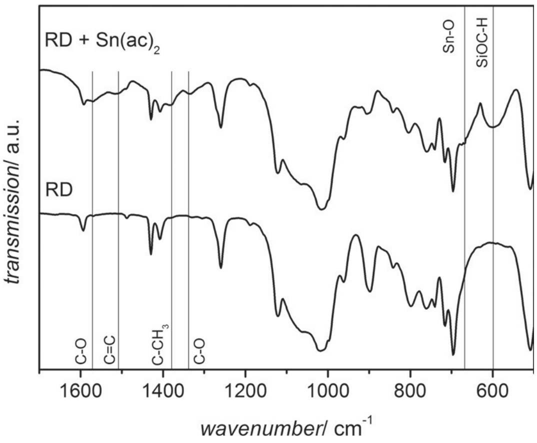

Figure 2. FTIR spectra of RD-684a and $Sn(ac)_2$ modified RD-684a.

The spectra of RD-684a and $Sn(ac)_2$-modified RD-684a (Figure 2) look very similar. Within the polymer there are neither OH nor Si-OR groups to react with $Sn(ac)_2$ as it is the case for

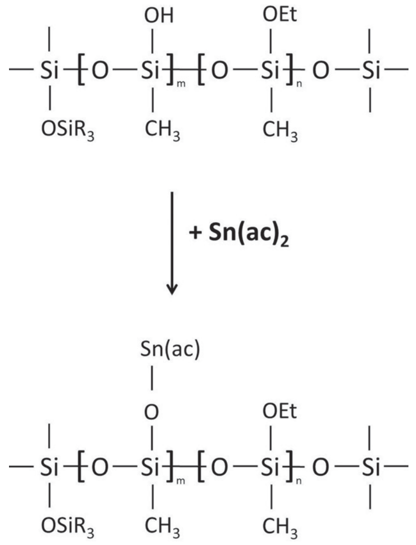

Figure 3. Chemical modification of PMS MK with $Sn(ac)_2$.

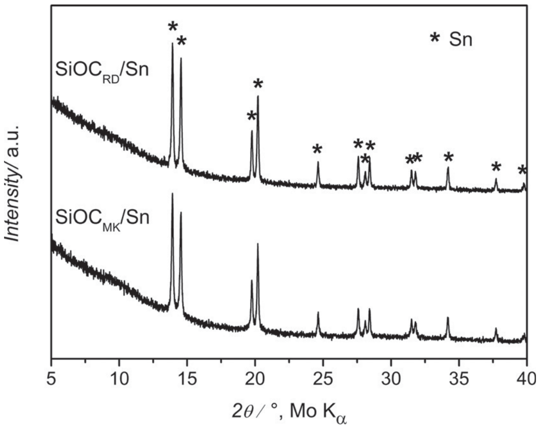

Figure 4. XRD patterns of SiOC$_{MK}$/Sn and SiOC$_{RD}$/Sn after pyrolysis at 1000 °C.

PMS MK. One could expect a reaction of Si-H with Sn(ac)$_2$ upon the formation of Si-Sn units, as it is reported for the reaction of polycarbosilanes with acetylacetonates by Ishikawa et al.[38] and shortly discussed by Ionescu et al.[39] However, the formation of Si-metal units still needs direct proof and thus no Si-Sn vibration could be assigned in the FTIR spectrum of the modified sample. Similar to PMS MK, the spectrum of modified RD-684a exhibits additional absorption bands related to the acetate ligands: ν = 1339, 1570 cm^{-1} (C-O), ν = 1380 cm^{-1} (C-CH$_3$) and ν = 1514 cm^{-1} (C=C) and at ν = 600 cm^{-1} (SiOC-H) and at ν = 667 cm^{-1} (Sn-O).[31–36] Although the exact reaction mechanism between Sn(ac)$_2$ and polysiloxane RD-684a remains unclear, the important finding here is that the transformation of the modified polymer into a SiOC/Sn composite occurs comparable to that of the Sn(ac)$_2$-modified PMS MK.

The X-ray diffraction patterns of SiOC$_{MK}$/Sn and SiOC$_{RD}$/Sn are shown in **Figure 4**. Both ternary silicon oxycarbides are found to be fully X-ray amorphous as previously reported,[22,25,28] whereas the Sn-modified samples exhibit the presence of metallic tin, formed in-situ upon pyrolysis. TEM analysis of both nanocomposites (**Figure 5** and **Figure 6**) illustrates the presence of spherical crystalline Sn inclusions within the amorphous matrices. In the case of SiOC$_{MK}$/Sn (Figure 5) a large number of homogeneously dispersed, ultrafine Sn grains with size below 10 nm and a few ones with larger size that tend to agglomerate are found. For SiOC$_{RD}$/Sn (Figure 6), Sn precipitations with an average diameter of 45 nm are observed, likewise homogeneously distributed throughout the SiOC matrix. In addition a very few ones with lager diameter are present as well. For both composites, the EDS inset in the high resolution micrographs outlines the amorphous matrices as composed of Si, O and C. The Cu-signal originates from the support grid. The round-shaped Sn particles in both nanocomposites indicate that liquid tin shows a poor wettability for the SiOC matrix, as it is known for ceramics with covalent bonding.[40,41] Similar features were recently found in the case of SiCN/Fe-based nanocomposites, which exhibited spherical-shaped Fe$_5$Si$_3$ precipitates dispersed within a SiCN matrix.[39,42]

Interestingly, the crystallization of tin oxide was not found upon pyrolysis of the modified precursors, unlike in other cases, where the modification of polysiloxanes with metal alkoxides, acetylacetonates or acetates was shown to lead to a precipitation and crystallization of the corresponding metal oxides, i.e. to the formation of SiOC/MO$_x$ nanocomposites (M = Al,[31] Ti,[43] Zr,[28] Hf,[29,30] Nb,[44] Ta,[44,45] Mn and Lu,[27] Gd[46]). However, in all cases a similar behavior with respect to the polymer-to-ceramic transformation is expected, which leads in a first step to single phase-amorphous SiMOC intermediates, subsequently partitioning into amorphous SiOC/MO$_x$. Recently we have shown that the phase composition and crystallization of those SiOC/MO$_x$ ceramics strongly depend on the redox stability of the metal oxide towards the C-CO system.[27] As in the investigated

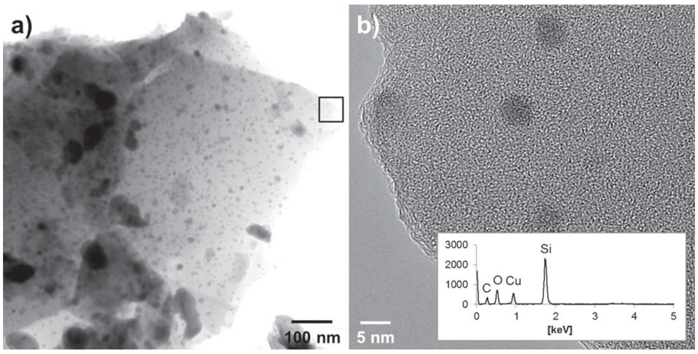

Figure 5. a) TEM micrograph of SiOC$_{MK}$/Sn and b) high-resolution image with EDS pattern of the amorphous SiOC matrix.

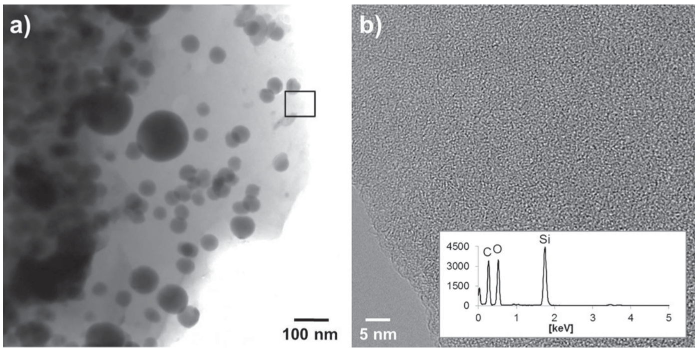

Figure 6. a) TEM micrograph of SiOC$_{RD}$/Sn and b) high-resolution image with EDS pattern of the amorphous SiOC matrix.

Table 1. Elemental analysis data and chemical formulae of $SiOC_{MK/RD}/Sn$, $SiOC_{MK/RD}$ matrices and $SiOC_{MK/RD}$ references. The weight fractions of silicon carbide, silica and segregated carbon were quantified according to the literature.[47]

Sample	Si [wt%]	O [wt%]	C [wt%]	Sn [wt%]	Chemical Formula (normalized to 1 Si)	SiC [wt%]	SiO_2 [wt%]	Free C [wt%]	Sn [wt%]
$SiOC_{MK}/Sn$	34.54	36.04	8.42	21.0	$SiO_{1.83}C_{0.57}Sn_{0.14}$ $(SiO_{1.83}C_{0.08})Sn_{0.14} + 0.49C$	4.15	67.67	7.18	21.0
$SiOC_{MK}$ – matrix	43.72	45.62	10.66	–	$SiO_{1.83}C_{0.57}$ $SiO_{1.83}C_{0.08} + 0.49C$	5.25	85.66	9.09	–
$SiOC_{MK}$[a)]	48.68	39.77	11.55	–	$SiO_{1.43}C_{0.55}$ $SiO_{1.43}C_{0.28} + 0.27C$	19.66	74.68	5.66	–
$SiOC_{RD}/Sn$	24.44	23.85	26.01	25.7	$SiO_{1.71}C_{2.49}Sn_{0.25}$ $(SiO_{1.71}C_{0.14})Sn_{0.25} + 2.35C$	5.01	44.78	24.51	25.7
$SiOC_{RD}$ – matrix	30.94	30.19	32.92	–	$SiO_{1.71}C_{2.49}$ $SiO_{1.71}C_{0.14} + 2.35C$	6.34	56.69	31.02	–
$SiOC_{RD}$[a)]	31.76	21.42	46.82	–	$SiO_{1.18}C_{3.45}$ $SiO_{1.18}C_{0.41} + 3.04C$	18.50	40.22	41.28	–

[a)] Reference data added for comparison.

systems carbon is found to be present in excess, the relative stability of the systems C-CO and M-MO_x determine the phase composition and the crystallization of these SiMOC materials. Zirconia, hafnia or gadolinia are stable with respect to their carbothermal reduction to metallic elements, whereas tin oxide, which is assumed to be generated intermediary upon pyrolysis of the tin acetate-modified polysiloxanes, is not stable under carburizing conditions. As tin does not form any silicides or carbides, the formation of SiOC/Sn nanocomposites is consequently related to the carbothermal reduction of SnO to Sn.

Table 1 presents the chemical composition of the tin comprising composites, their ceramic matrices and pure $SiOC_{MK/RD}$ as reference. The chemical formula of the compounds normalized to silicon and the derived phase composition in terms of silicon carbide, silica and free C, quantified according to the literature,[47] are included.

For both composites, it is evident that the total amount of carbon within the matrix is reduced upon Sn incorporation. For $SiOC_{MK}$(/Sn) it decreases from 11.55 to 10.66 wt% and for $SiOC_{RD}$(/Sn) from 46.82 to 32.92 wt%. This effect of the modification of polysiloxanes and polysilazanes with metal organic precursors has been previously reported and shown to significantly affect the microstructure and physical properties of the resulting nanocomposites.[27–29,31,48] Interestingly, the amount of free carbon in $SiOC_{MK}/Sn$ (9.09 wt%) is higher than that of the reference sample $SiOC_{MK}$ (5.66 wt%), despite the overall content of carbon decreases upon modification. On the contrary, for carbon-rich $SiOC_{RD}$(/Sn) the content of free carbon decreases from 41.28 to 31.02 wt%, following the tendency of the total carbon content.

2.2. Electrochemical Results

Electrodes prepared from the composites were cycled by PCGA protocol in order to follow the incremental capacity as a function of the lithiation/delithiation potential and to trace the electrochemical activity of the embedded tin. Differential capacity plots for the first, second and fifth cycles are shown in **Figure 7**. For both samples, in the cathodic branch cycle two and five, strong and characteristic signals for Li-Sn alloying are visible: For $SiOC_{MK}/Sn$ at 0.64 V (LiSn) and 0.38 V ($Li_{22}Sn_5$) and for $SiOC_{RD}/Sn$ at 0.66 V (LiSn) and 0.42 V (Li_7Sn_2).[14] The presence of these signals reveals the electrochemical activity of the tin phase. Note that there is a distinct difference in the detected final alloy stage between $SiOC_{MK}/Sn$ and $SiOC_{RD}/Sn$. For $SiOC_{MK}/Sn$ the highest alloy phase $Li_{22}Sn_5$ is reached, whereas for $SiOC_{RD}/Sn$ alloying stops with Li_7Sn_2. In the anodic branches, several signals for Li-Sn dealloying appear around 0.44, 0.60, 0.61, 0.70 and 0.78 V. The numerous anodic peaks indicate that dealloying occurs via multifold reactions and stages and cannot simply be considered as the reverse reaction-path of the observed alloying process.[14]

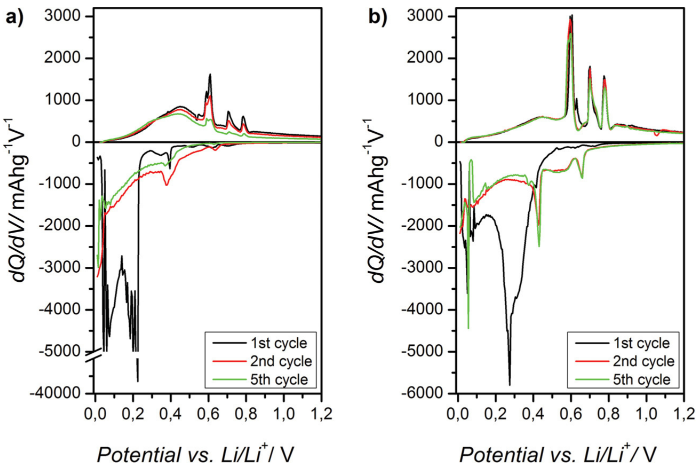

Figure 7. Differential capacity plot for a) $SiOC_{MK}/Sn$ and b) $SiOC_{RD}/Sn$; first, second and fifth cycle are shown.

Table 2. Overview of the first cycle charging, discharging and irreversible capacity and coulombic efficiency (η) for SiOC$_{MK/RD}$/Sn and pure SiOC$_{MK/RD}$ reference electrodes.

	C_{ch} [mAhg^{-1}]	C_{dis} [mAhg^{-1}]	C_{irr} [mAhg^{-1}]	η [%]
SiOC$_{MK}$$^{a)}$	1097	236	861	22
SiOC$_{MK}$/Sn	1190	566	624	48
SiOC$_{RD}$$^{a)}$	978	598	380	61
SiOC$_{RD}$/Sn	1022	651	371	64

$^{a)}$Reference electrodes were prepared and cycled similar to the composites.

The suppression of the formation of Li$_{22}$Sn$_5$ in the SiOC$_{RD}$/Sn composite is related to the restriction of the alloy expansion within the embedding matrix. The volume increase for Li$_7$Sn$_2$ only amounts 75%, as compared to Li$_{22}$Sn$_5$ resulting in less mechanical stress transference to the matrix. This lower load can be well accommodated by the soft SiOC$_{RD}$ without degradation. The stiff and fragile SiOC$_{MK}$ on the contrary, is not able to withstand the alloy expansion and thus ruptures and pulverizes during cycling. Consequently, a considerably higher volume is available for the Li-Sn expansion and the highest known Li-Sn stoichiometry Li$_{22}$Sn$_5$ is finally formed.

From the elemental analysis data (Table 1), a theoretical capacity for the SiOC$_{MK}$/Sn and SiOC$_{RD}$/Sn composites can be calculated, taking the mass ratio SiOC:Sn into account. For the sample SiOC$_{MK}$/Sn, the theoretical capacity of Li$_{22}$Sn$_5$ (994 mAhg^{-1}) and for SiOC$_{RD}$/Sn that of Li$_7$Sn$_2$ (790 mAhg^{-1}) is considered. The capacity contribution of the SiOC matrices is estimated from the reference electrode data (**Table 2**). Accordingly, the expected capacities for the composites amount 395 mAhg^{-1} (SiOC$_{MK}$/Sn) and 647 mAhg^{-1} (SiOC$_{RD}$/Sn). For SiOC$_{RD}$/Sn the estimation is in excellent agreement with the experimentally registered value of 651 mAhg^{-1}. The experimentally found higher capacity of SiOC$_{MK}$/Sn (566 mAhg^{-1}) can be explained by two factors: Firstly, for the calculation of the theoretical capacity of SiOC$_{MK}$/Sn composite the data found for pure SiOC$_{MK}$ was applied. However, the presence of dispersed metallic tin nanoparticles might increase the electronic conductivity and/or the availability of carbon phase within the SiOC matrix and thus increases the composite capacity in a non-linear way with respect to the calculation. A similar phenomenon was reported for mixtures of carbon-poor SiCN ceramic and graphite.[49,50] In addition the free carbon content in the sample was found slightly enhanced, providing additional Li-ion storing sites. Secondly, the higher capacity can be attributed to the partially reversible storage of less-ionic lithium species in micropores[51] as well as in the vicinity of SiO$_4$ units.[52] These reactions take place at the potential E < 0.1 V giving a well pronounced peak (c.f. Figure 7a)). The lithium storage in places close to the oxygen is most probably responsible for the high first lithiation capacity (1190 mAhg^{-1}) but due to a strong interaction between lithium and oxygen it brings about a poor reversibility.

Figure 8 and **Figure 9** present the galvanostatic cycling (GCPL) performance of the composites at different current rates and illustrate their cycling stability. Table 2 summarizes the first cycle charge (C_{ch}), discharge (C_{dis}) and irreversible capacity (C_{irr}), as well as the columbic efficiency (η) of the first cycle; η denoting the charge ratio $C_{ch}/C_{dis} \times 100\%$ and quantifying the amount of charge recovered within one cycle.

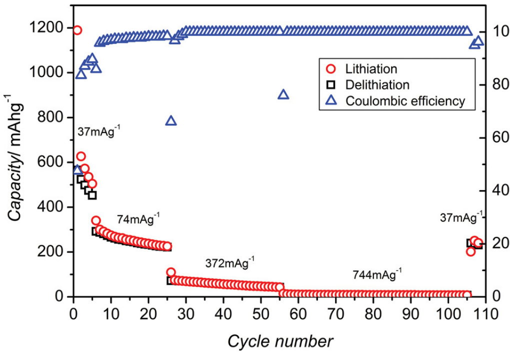

Figure 8. Capacity performance and coulombic efficiency (η) of SiOC$_{MK}$/Sn at different current rates: 5 × 37 mAg^{-1}, 20 × 74 mAg^{-1}, 30 × 372 mAg^{-1}, 50 × 744 mAg^{-1} and 3 × 37 mAg^{-1}.

For SiOC$_{MK}$/Sn, the initial lithiation capacity amounts 1190 mAhg^{-1}, while 566 mAhg^{-1} are recovered during the first extraction, with a coulombic efficiency of 48%. SiOC$_{RD}$/Sn on the contrary provides a lower first cycle lithation of 1022 mAhg^{-1}, but 651 mAhg^{-1} are recovered reversibly, with a significant higher coulombic efficiency of 64%.

The PMS MK-based sample demonstrates a poor cycling stability and continuous capacity fading at all current rates. When increasing the cycling current to 74 mAg^{-1} the capacity drops to 293 mAhg^{-1} and further decreases to 222 mAhg^{-1} within subsequent 20 cycles. At high current (744 mAg^{-1}) almost no electrochemical activity is found. The coulombic efficiency of cycle one to five does not exceed 90%, confirming irreversible losses, caused by two interplaying processes. Firstly, the continuous solid electrolyte interface formation, since new surface is steadily created when the electrode particles crack during Li uptake and release. Secondly, the irreversible Li-ion capture within once broken and electrically insolated grains in the electrode. SEM micrographs of SiOC$_{MK}$/Sn

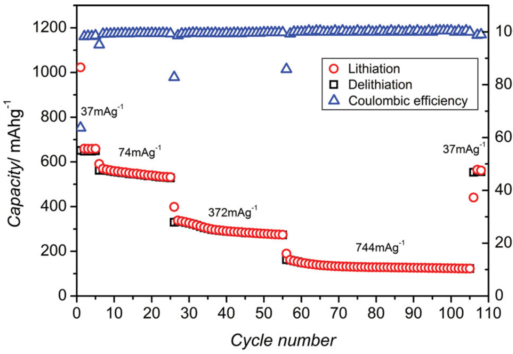

Figure 9. Capacity performance and coulombic efficiency (η) of SiOC$_{RD}$/Sn at different current rates: 5 × 37 mAg^{-1}, 20 × 74 mAg^{-1}, 30 × 372 mAg^{-1}, 50 × 744 mAg^{-1} and 3 × 37 mAg^{-1}.

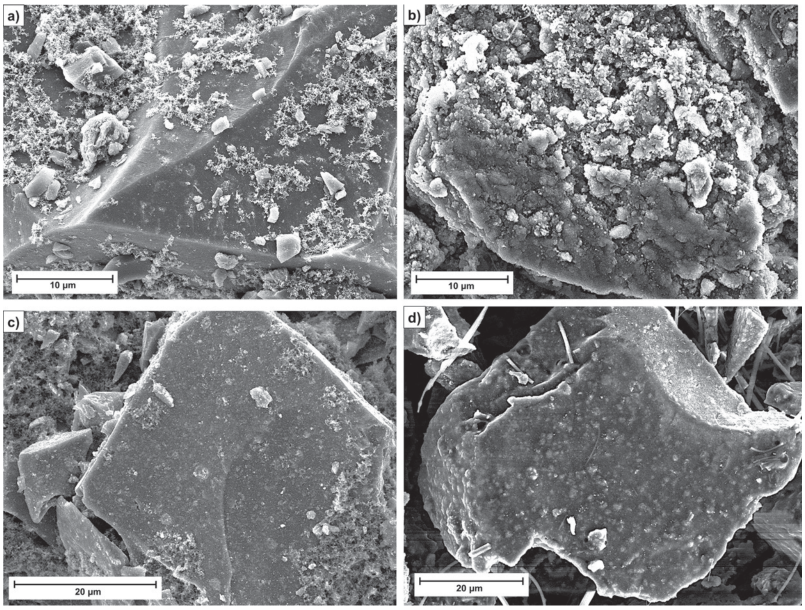

Figure 10. SEM image of a) SiOC$_{MK}$/Sn electrode before cycling, b) after 108 cycles; c) SiOC$_{RD}$/Sn electrode before cycling, d) after 108 cycles (the fibers represent remaining rests of separator).

before and after cycling (**Figure 10**) illustrate this degradation process.

For SiOC$_{RD}$/Sn on the contrary, the reversible capacity remains stable with 651 mAhg^{-1} during continuous charging/discharging with 37 mAhg^{-1}. At a current rate of 74 mAg^{-1}, the registered capacity reduces to 562 mAhg^{-1}, showing little fading over the 20 measured cycles; in average ~1.5 mAhg^{-1} are lost in each cycle. Even at high current of 744 mAg^{-1} a significant electrochemical activity is still detected for SiOC$_{RD}$/Sn, with an average reversible capacity of 133 mAhg^{-1}. When low currents are re-applied at the end of high current series, 562 mAhg^{-1} are recovered for SiOC$_{RD}$/Sn, while for SiOC$_{MK}$/Sn only 232 mAhg^{-1} could be realized.

We explain the superior cycling stability of the SiOC$_{RD}$/Sn sample by its beneficial matrix properties. SiOC$_{RD}$ represents a soft (E = 66 GPa,[25] electrochemically active ceramic with an intrinsically high content of free carbon (>41 wt%).[22–24] Scarmi et al.[53] presented the model structures of carbon-poor and carbon-rich SiOC amorphous ceramics. According to their model, carbon-poor SiOC materials are represented as nanodomains of sp^2 carbon, discontinuously dispersed in silica. Carbon-rich SiOC on the contrary, consists of a cellular network of graphene sheets of sp^2 carbon, where nanodomains of silica are sequestered within cells created by the graphene sheets. Accordingly, the graphene-like network can accommodate the volume change of the Sn nanoparticles upon Li-alloying/dealloying, as it can elastically deform. Consequently, the volume expansion of Sn does not lead to matrix rupture for the SiOC$_{RD}$/Sn composite. In the case of low-carbon SiOC$_{MK}$/Sn, the induced stresses upon Li-Sn alloy expansion exceed the critical fracture strength of the matrix. Cracks evolve and irreversibly damage the stiff and fragile ceramic, with the result of failure. SEM micrographs of cycled electrodes illustrate this feature, revealing cracking and partially pulverized composite-grains for SiOC$_{MK}$/Sn, whereas for SiOC$_{RD}$/Sn almost no degradation is observed (Figure 10).

3. Conclusion

A new method of preparation of SiOC/Sn composite materials with outstanding stability during electrochemical insertion and extraction of lithium ions is presented. The SiOC/Sn nanocomposites were synthesized via pyrolysis of the polysiloxanes PMS MK and RD-684a modified with tin(II)acetate at 1000 °C. Upon pyrolysis, metallic Sn segregates within the SiOC ceramics, forming spherical nanoparticles of different sizes. In the case of modified PMS MK, the composite predominantly contains Sn inclusions below 10 nm, whereas for modified RD-684a an average grain diameter of around 45 nm is found. Electrochemical measurements reveal a superior performance and cycling stability of the carbon-rich and therefore rather soft SiOC$_{RD}$/Sn material (C_{max} = 651 mAhg^{-1} and stable), while fast capacity fading is registered for the carbon-poor and therefore stiff and fragile SiOC$_{MK}$/Sn composite (C_{max} = 566 mAhg^{-1}, not stable). Incremental capacity measurements outlined different final lithium-tin alloy stages, strongly depending on the embedding matrix and its properties. $Li_{22}Sn_5$ and Li_7Sn_2 are formed in SiOC$_{MK}$/Sn and SiOC$_{RD}$/Sn, respectively. Our study emphasizes that a single-source-precursor approach has two crucial advantages for synthesizing Sn-containing nanocomposites as high-performance material for Li-ion battery anode application:

i) it provides the in-situ generation of Sn nanoparticles homogeneously dispersed within the SiOC host and *ii)* the choice of suitable single-source-precursors allows for tailoring of the matrix properties (i.e. carbon-content/stress compliance), to be able to withstand the volume expansion of the Sn precipitates upon alloying with Li.

4. Experimental Section

Materials Synthesis: The synthesis of the single-source precursors was performed upon chemical modification of polysilsesquioxane PMS MK (Wacker-Belsil, Germany) and polysiloxane Polyramic RD-684a (Starfire Systems Inc., USA) with tin(II)acetate ($Sn(ac)_2$, Sigma-Aldrich, Germany). Both reactants were dissolved in xylene and mixed and stirred for several hours for reaction. The solvent was removed and the obtained powders were dried in vacuum (10^{-2} mbar). The ratio $Sn(ac)_2$ to polymer was adjusted to 1:1.5 by weight for $Sn(ac)_2$:PMS MK and 1:2 for $Sn(ac)_2$:RD-684a, in order to achieve comparable tin contents in the SiOC/Sn nano-composites after pyrolysis. The thermal conversion of the single-source precursors was performed in a two-step procedure in a horizontal alumina tube furnace under argon atmosphere: Cross-linking at 250 °C (50 °C h^{-1}; 2 h) followed by subsequent pyrolysis at 1000 °C (100 °C h^{-1}; 3 h).

Characterization Methods: FTIR spectra were collected using a Bruker Vertex 70 FT-IR instrument (Bruker, USA) in attenuated total reflectance geometry. X-ray diffraction (XRD) measurements were performed at a STOE X-ray diffractometer (Stoe & Cie GmbH, Germany) in transmission geometry (Mo K_α radiation). For elemental analysis, a carbon analyzer Leco-200 (Leco Corporation, USA) was used to determine the carbon content and an N/O analyzer Leco TC-436 (Leco Corporation, USA) to determine the corresponding oxygen content. The tin content was measured at "Mikroanalytisches Labor Pascher" (Remagen-Bandorf, Germany) by inductively coupled plasma atomic emission spectroscopy (ICP-AES). The silicon fraction was calculated as the difference to 100 wt% of the sum of the wt% values of carbon, oxygen and tin, assuming no other elements being present in the samples. Scanning electron microscopy (SEM) images of uncycled and cycled electrodes were recorded with a Philips XL30 FEG (FEI, Netherlands). Transmission electron microscopy (TEM) studies on powder samples, dispersed on a lacy carbon Cu-grid, were performed, utilizing a JEOL 2100F instrument (JEOL, Japan) operated at 200 keV. An energy-dispersive X-ray detector XMAX-80 (Oxford Instruments, UK), attached to the instrument, was used for the local chemical analysis.

Electrode Preparation: For electrochemical testing, the pyrolyzed powders (active mass) were ground and mixed with Carbon Black Super P (Timcal Ltd., Switzerland) as conducting additive and polyvinylidene fluoride binder (Solvay S.A., Germany) solved in *n*-methyl-2-pyrolidone (NMP, BASF, Germany) in the weight ratio 85:5:10. The mixture was homogenized and tape casted on the rough side of a 10 µm thin copper foil (SE-Cu58, Schlenk Metallfolien GmbH & Co KG, Germany). The tape (wet-film thickness 150 µm) was dried at 80 °C for several hours in order to remove the solvent NMP. The film thickness after drying was about 80 µm, with an average load of 4.5 mg cm^{-2}. Electrodes of 7 mm in diameter were cut and vacuum-dried at 80 °C for 24 h, before transferred to an argon-filled glove box for cell assembly. Two electrode Swagelok type cells were used, with metallic lithium (Li-tape 99.9% purity, 0.75 mm thickness, Alfa Aesar, UK) as reference and counter electrode, 1 M $LiPF_6$ solved in EC:DMC, ratio 1:1 (LP30, Merck KGaA, Germany) as electrolyte and Whatman glass fiber filter (Whatman, UK) as separator. The prepared hermetic cells were connected to a VMP multipotentiostat (BioLogic, France) and studied by Potentiodynamic Cycling with Galvanostatic Acceleration (PCGA) in order to assess the incremental capacity as a function of lithiation/delithiation potential. The potential window was set to 2.5–0.005 V (E vs. Li/Li^+) with scanning steps of 50 mV and a limiting current of 37 mAg^{-1}. Galvanostatic Cycling with Potential Limitation (GCPL) was performed within the potential range of to 2.5 and 0.005 V (E vs. Li/Li^+) with cycling currents of 37, 74, 372 and 744 mAg^{-1}. Charging and discharging current within one cycle were the same and measured capacities were re-calculated to the amount of SiOC/Sn active mass within the electrodes (85 wt%).

Acknowledgments

This work was financially support by the Deutsche Forschungsgemeinschaft (DFG), Bonn, Germany within SPP1473/JP8, SPP1181 and SFB595 programs. The authors want to acknowledge C. Linck for his support in the sample preparation and assistance in XRD measurements.

Note: The layout of Figure 3 and Table 1 was adjusted after initial online publication.

Received: November 12, 2013
Revised: January 27, 2014
Published online: March 25, 2014

---

[1] T. Nagaura, K. K. Tozawa, *Prog. Batteries Solar Cells* **1990**, *9*, 209.
[2] T. Nagaura, M. Nagamine, I. Tanabe, N. Miyamoto, *Prog. Batteries Solar Cells* **1989**, *8*, 84.
[3] F. Cheng, J. Liang, Z. Tao, J. Chen, *Adv. Mater. Processes* **2011**, *23*, 1695.
[4] R. Marom, S. F. Amalraj, N. Leifer, D. Jacob, D. Aurbach, *J. Mater. Chem.* **2011**, *21*, 9938.
[5] B. Scrosati, J. Garche, *J. Power Sources* **2010**, *195*, 2419.
[6] H. Kawamoto, *Sci. Technol. Trends* **2010**, *36*, 34.
[7] P. G. Bruce, *Solid State Ionics* **2008**, *179*, 752.
[8] P. G. Bruce, B. Scrosati, J.-M. Tarascon, *Angew. Chem., Int. Ed.* **2008**, *47*, 2930.
[9] A. K. Shukla, T. P. Kumar, *Curr. Sci.* **2008**, *94*, 314.
[10] W.-J. Zhang, *J. Power Sources* **2011**, *196*, 13.
[11] W.-J. Zhang, *J. Power Sources* **2011**, *196*, 877.
[12] C.-M. Park, J.-H. Kim, H. Kim, H.-J. Sohn, *Chem. Soc. Rev.* **2010**, *39*, 3115.
[13] M. N. Obrovac, L. J. Krause, *J. Electrochem. Soc.* **2007**, *154*, A103.
[14] M. Winter, J. O. Besenhard, *Electrochim. Acta* **1999**, *45*, 31.
[15] A. D. W. Todd, P. P. Ferguson, M. D. Fleischauer, J. R. Dahn, *Int. J. Energy Res.* **2010**, *34*, 535.
[16] L. Y. Beaulieu, K. W. Eberman, R. L. Turner, L. J. Krause, J. R. Dahn, *Electrochem. Solid State Lett.* **2001**, *4*, A137.
[17] J. Hassoun, K.-S. Lee, Y.-K. Sun, B. Scrosati, *J. Am. Chem. Soc.* **2011**, *133*, 3139.
[18] Z. Du, S. Zhang, Y. Xing, X. Wu, *J. Power Sources* **2011**, *196*, 9780.
[19] L. Bazin, S. Mitra, P. L. Taberna, P. Poizot, M. Gressier, M. J. Menu, A. Barnabe, P. Simon, J. M. Tarascon, *J. Power Sources* **2009**, *188*, 578.
[20] J. Hassoun, S. Panero, B. Scrosati, *Fuel Cells* **2009**, *9*, 277.
[21] G. Derrien, J. Hassoun, S. Panero, B. Scrosati, *Adv. Mater.* **2007**, *19*, 2336.
[22] J. Kaspar, M. Graczyk-Zajac, R. Riedel, *J. Power Sources* **2013**, *244*, 450.
[23] M. Graczyk-Zajac, L. Toma, C. Fasel, R. Riedel, *Solid State Ionics* **2012**, *225*, 522.
[24] J. Kaspar, M. Graczyk-Zajac, R. Riedel, *Solid State Ionics* **2012**, *225*, 527.
[25] S. Martínez-Crespiera, E. Ionescu, H.-J. Kleebe, R. Riedel, *J. Eur. Ceram. Soc.* **2011**, *31*, 913.
[26] C. Moysan, R. Riedel, R. Harshe, T. Rouxel, F. Augereau, *J. Eur. Ceram. Soc.* **2007**, *27*, 397.
[27] E. Ionescu, C. Terzioglu, C. Linck, J. Kaspar, A. Navrotsky, R. Riedel, *J. Am. Ceram. Soc.* **2013**, *96*, 1899.

[28] E. Ionescu, C. Linck, C. Fasel, M. Müller, H.-J. Kleebe, R. Riedel, *J. Am. Chem. Soc.* **2010**, *93*, 241.
[29] E. Ionescu, B. Papendorf, H.-J. Kleebe, F. Poli, K. Müller, R. Riedel, *J. Am. Chem. Soc.* **2010**, *93*, 1774.
[30] E. Ionescu, B. Papendorf, H.-J. Kleebe, R. Riedel, *J. Am. Chem. Soc.* **2010**, *93*, 1783.
[31] R. Harshe, C. Balan, R. Riedel, *J. Eur. Ceram. Soc.* **2004**, *24*, 3471.
[32] R. Frycek, M. Jelinek, T. Kocourek, P. Fitl, M. Vrnata, V. Myslikk, M. Vrbova, *Thin Solid Films* **2006**, *495*, 308.
[33] N. W. Alcock, V. M. Tracy, T. C. Waddington, *J. Chem. Soc., Dalton Trans.* **1976**, *21*, 2243.
[34] K. Ito, H. J. Bernstein, *Can. J. Chem.* **1956**, *34*, 170.
[35] B. N. S. Bhaktha, C. Kinowski, M. Bouazaoui, B. Capoen, O. Robbe-Cristini, F. Beclin, P. Roussel, M. Ferrari, S. Turrell, *J. Phys. Chem. C* **2009**, *113*, 21555.
[36] N. Dharmaraj, C. H. Kim, K. W. Kim, H. Y. Kim, E. K. Suh, *Spectrochim. Acta, Part A* **2006**, *64*, 136.
[37] S. Samanta, N. K. Mal, A. Manna, A. Bhaumik, *Appl. Catal., A* **2004**, *273*, 157.
[38] T. Ishikawa, Y. Kohtoku, K. Kumagawa, *J. Mater. Sci.* **1998**, *33*, 161.
[39] E. Ionescu, H.-J. Kleebe, R. Riedel, *Chem. Soc. Rev.* **2012**, *41*, 5032.
[40] S. K. Rhee, *J. Am. Ceram. Soc.* **1971**, *54*, 332.
[41] O. Dezellus, N. Eustathopoulos, *J. Mater. Sci.* **2010**, *45*, 4256.
[42] A. Francis, E. Ionescu, C. Fasel, R. Riedel, *Inorg. Chem.* **2009**, *48*, 10078.
[43] S. Dire, F. Babonneau, C. Sanchez, J. Livage, *J. Mater. Chem.* **1992**, *2*, 239.
[44] M. Fukushima, E. Yasuda, Y. Nakamura, Y. Tanabe, *J. Ceram. Soc. Jpn.* **2003**, *111*, 857.
[45] M. Fukushima, E. Yasuda, Y. Nakamura, Y. Teranishi, K. Nakamura, Y. Tanabe, *J. Ceram. Soc. Jpn.* **2004**, *112*, S1531.
[46] S. J. Widgeon, S. Sen, G. Mera, E. Ionescu, R. Riedel, A. Navrotsky, *Chem. Mater.* **2010**, *22*, 6221.
[47] G. D. Soraru, L. Pederiva, J. Latournerie, R. Raj, *J. Am. Chem. Soc.* **2002**, *85*, 2181.
[48] B. Papendorf, K. Nonnenmacher, E. Ionescu, H.-J. Kleebe, R. Riedel, *Small* **2011**, *7*, 970.
[49] M. Graczyk-Zajac, C. Fasel, R. Riedel, *J. Power Sources* **2011**, *196*, 6412.
[50] M. Wilamowska, M. Graczyk-Zajac, R. Riedel, *J. Power Sources* **2013**, *244*, 80.
[51] H. Fukui, H. Ohsuka, T. Hino, K. Kanamura, *J. Power Sources* **2011**, *196*, 371.
[52] P. Kroll, *MRS Online Proc. Library* **2011**, *1313*, 1.
[53] A. Scarmi, G. D. Soraru, R. Raj, *J. Non-Cryst. Solids* **2005**, *351*, 2238.

Lebenslauf und Bildungsgang

Persönliche Daten

Name	Jan Hans Kaspar
Geburtsdatum	05. Mai 1984
Geburtsort	Heppenheim

Schulische Ausbildung

1990 – 1994	Grundschule, Peter-Schöffer-Schule in Gernsheim
1994 – 2003	Gymnasium Gernsheim
2003	Abitur

Studium

2004 – 2010	Studium der Materialwissenschaft an der Technische Universität Darmstadt
2006	Vordiplom
2007 – 2008	Auslandsaufenthalt an der University of Illinois in Urbana-Champaign, USA
2009 – 2010	Diplomarbeit im Fachgebiet Disperse Feststoffe des Fachbereichs Material- und Geowissenschaften der Technischen Universität Darmstadt unter der Betreuung von Prof. Dr. R. Riedel Thema der Arbeit: Electrochemical characterization of polymer-derived carbon-rich SiCN anode materials for Li-ion batteries
2010	Studienabschluss zum Diplom-Ingenieur (Dipl.-Ing.) der Materialwissenschaft

Promotion

2010	Promotion am Karlsruher Institut für Technologie (abgebrochen)
2010 – 2014	Promotion an der Technischen Universität Darmstadt am Fachbereich für Material- und Geowissenschaften, Fachgebiet Disperse Feststoffe unter der Betreuung von Prof. Dr. R. Riedel Thema der Arbeit: Carbon-rich silicon oxycarbide (SiOC) and silicon oxycarbide/element (SiOC/X, X= Si, Sn) nano-composites as new anode materials for Li-ion battery application
2014	Disputation zur Erlangung des akademischen Grades Doktor-Ingenieur (Dr.-Ing.)

Beruf

seit 2014	Post-Doktorand und wissenschaftlicher Mitarbeiter am Fachbereich für Material- und Geowissenschaften der Technischen Universität Darmstadt, Fachgebiet Disperse Feststoffe

Danksagung

Mein Dank gehört Herrn Prof. Riedel, der mir die Möglichkeit gegeben hat meine Promotion in seinem Fachgebiet durchzuführen und mich nach mehrmonatiger Abwesenheit in seiner Arbeitsgruppe wieder aufgenommen hat.

Herrn Prof. Soraru möchte ich herzlich dafür danken, dass er die Aufgabe des Zweitgutachters für die Bewertung der vorliegenden Arbeit übernommen hat.

Ein besonderer Dank gilt meiner Betreuerin Dr. Magdalena Graczyk-Zajac. Seit meiner Zeit als „HiWi“ hat Sie mir Ihr umfangreiches fachliches Wissen vermittelt, mich bei Fragen und Problemen aller Art unterstützt und mir mit Ihrem Rat stets zur Seite gestanden.

Bei allen Mitarbeitern, sowie ehemaligen Mitarbeitern des Fachgebiets Disperse Feststoffe, bedanke ich mich für die tolle Zeit, gemeinsamen Erlebnisse und angenehme Arbeitsatmosphäre in unserer Arbeitsgruppe. Insbesondere möchte ich an dieser Stelle meine Kollegen Monika Wilamowska, Yan Gao und Mirko Reinold, sowie Claudia Fasel namentlich erwähnen.

Ein Dank, der sich nicht in Worte fassen lässt, gehört meiner Familie, die mich mein Leben lang unterstützt hat und mir in allen Lebenslagen den nötigen Rückhalt gegeben hat.

Abschließend danke ich Sophie Schneewolf, die nunmehr seit über 5 Jahren an meiner Seite steht und auf die ich mich immer verlassen kann: Danke für alles, denn Du bist alles für mich!

Eidesstattliche Erklärung

Hiermit erkläre ich an Eides statt, dass ich die beigefügte Dissertation selbstständig verfasst und keine anderen als die angegebenen Hilfsmittel genutzt habe. Alle wörtlich oder inhaltlich übernommenen Stellen habe ich als solche gekennzeichnet.

Ich versichere außerdem, dass ich die beigefügte Dissertation nur in diesem und keinem anderen Promotionsverfahren eingereicht habe, und dass diesem Promotionsverfahren keine gescheiterten Promotionsverfahren vorausgegangen sind.

Darmstadt, 01. September 2014

(Jan Kaspar)